The University Of Sheffield.

DEVELOPMENT OF NEW SUPPORTED CATALYSTS FOR DIRECT ETHANOL OXIDATION IN FUEL CELLS

AHMED MOHAMED ALI ELSHEIKH

FACULTY OF ENGINEERING

KROTO RESEARCH INSTITUTE

DEPARTMENT OF CHEMICAL AND BIOLOGICAL ENGINEERING

UNIVERSITY OF SHEFFIELD

THIS DISSERTATION IS SUBMITTED FOR THE DEGREE OF DOCTOR OF PHILOSOPHY

JULY 2020

For the sake of Allah,

Lord of the heavens, earth, and everything in-between.

بِسۡمِ ٱللَّهِ ٱلرَّحۡمَٰنِ ٱلرَّحِيمِ

الٓمٓ (1) أَحَسِبَ ٱلنَّاسُ أَن يُتۡرَكُوٓاْ أَن يَقُولُوٓاْ ءَامَنَّا وَهُمۡ لَا يُفۡتَنُونَ (2) وَلَقَدۡ فَتَنَّا ٱلَّذِينَ مِن قَبۡلِهِمۡۖ فَلَيَعۡلَمَنَّ ٱللَّهُ ٱلَّذِينَ صَدَقُواْ وَلَيَعۡلَمَنَّ ٱلۡكَٰذِبِينَ (3)

سُوْرَةُ العنكبوت

In the name of God The Most Gracious The Most Merciful.

Alif, Lam, Meem (1) Do the people think that they will be left saying "We believe" and they are not tested? (2) But We have certainly tested those before them, and Allah will surely make evident those who are truthful, and He will surely make evident the liars (3).

Surah Al-Ankaboot (The Spider) 29 (1-3)

ABSTRACT

Fuel cells are electrochemical energy conversion devices to be fed with a fuel and oxidant in order to generate electricity. Ethanol has, recently, shown a promising potential to replace hydrogen as a fuel directly fed into the cell due to its liquid state and sustainability. The challenge, however, is the significantly slow ethanol oxidation kinetics. Therefore, an affordable, highly active, and stable catalyst is necessary for activating such reaction. Platinum (and its alloys) is known as the most active metal for fuel cell catalysis, but its scarce presence has made the fuel cell commercialisation non-feasible. Also, it is very susceptible to poisoning by carbonaceous species which considerably decreases the catalyst lifetime. Palladium has shown a good potential to replace Pt. It is more abundant than Pt and has shown a comparable performance. Furthermore, it is more tolerant for poisoning species. In this thesis, Pd nanoparticles (NPs) are prepared by chemical reduction on five different carbon supports all of which are physically characterised and evaluated for ethanol oxidation. Because of a critical balance amongst the physiochemical characteristics (surface area, porosity, crystallinity extent), Vulcan carbon (XC72) has presented the highest support functionality for Pd ethanol oxidation as measured by the obtained current density. Numerous research efforts have co-concluded that adding a 2nd metal to Pd is beneficial economically and technically. Yet, a few groups have given attention to the trimetallic Pd-based electrocatalysts. Therefore, the main target of this thesis is to investigate various trimetallic combinations and synthesis methods to prepare C-supported trimetallic catalysts. Three different borohydride reduction synthetic protocols were deployed to prepare PdAuNi catalysts. The sodium borhydride-2-propanol (SBIPP) method gives the highest performing PdAuNi/C catalyst with 9-A/mg$_{Pd}$ current density peak and - 0.36-V-vs-NHE onset potential while the single Pd counterpart gives only 2 A/mg$_{Pd}$ and - 0.26 V, respectively. The physical characterisation shows enhanced physical alloy structure of this PdAuNi. Using the SBIPP protocol, 12 other catalyst combinations from Pd and two other metals were prepared with 12 wt.% metal loading. PdAu-based catalysts have shown significant enhancement of the Pd activity and stability towards ethanol oxidation. PdAuRh, in particular, produces a remarkable oxidation current peak of 10 A/mg$_{Pd}$ and - 0.4-V onset potential. The PdAuRh and PdAuNi catalysts seem to present serious candidates to replace Pt and facilitate the transition into an affordable low-carbon technology to supply sustainable electricity.

ACKNOWLEDGEMENTS

Firstly, I THANK Allah, Lord of all the worlds, for giving me the power to finish this work. I pray that He accepts this humble effort as an act of worship from me and places it in the scale of my good deeds. Doing this work, I hope my intention is very sincere and pure for the sake of pleasing Him.

To the Prophet *Muhammad* (Peace Be upon Him) for setting the best example and role model - that as a Muslim - I sincerely wish to follow his footsteps with Allah's blessings. And to the Prophets *Noah, Abraham, Moses,* and *Jesus Son of Mary* (Peace Be upon Them) and to all their brothers from Allah's Messengers and Prophets.

To Newton-Mosharafa Fund from The British Council and Egyptian Ministry of Higher Education for sponsoring my PhD studies (Reference No NM*J*8/15).

To my family for their unconditional support and love.

To my supervisor, *Dr. James McGregor*, for his consistent guidance and patient support through the different phases to accomplish this work.

To *Dr. Svetomir Tzokov*, The Electron Microscopy Facility Manager (Dept. Molecular Biology & Biotechnology), for training me on using the transmission electron microscopy (TEM).

To *Dr. Denis Cumming* (The Postgraduate Progression Tutor), for the financial support of physical analyses through the Battery Laboratory financial plan.

To The Dyslexia and Disability Support Services (DDSS) at The University of Sheffield for making some arrangements to help me cope with my physical disability and mental disorder.

To *Dr. Vitor Martins* (PDRA), for liaising with me and commenting on my research approach.

To *Mr. David Wengraf* (Departmental Safety Officer) for his support with the health and safety work.

To *Mr. Thomas Plumpton* for helping me in the lab and making sure that I finish all my experiments during my injury.

To Dr. *Matthew Hobbs* for his support with the writing-up of this thesis.

To *Dr. David Morgan* (HarwellXPS Facility Manager – Cardiff) for helping with performing the XPS analysis of my samples.

To *Mr. John Booth* (Scientific & Medical Products Ltd - Stockport) for helping me with the electrochemical impedance spectra modelling.

To my lab colleagues*: Charles, Yan-Yan,* and *Laura* for their helping and supporting initiatives.

To the technicians: Ms Josie-May Whitnear, Mr. Mark Jones, and Mr. Usman Younis.

LIST OF TABLES

LIST OF FIGURES

List of Abbreviations and Acronyms

EOR:	**Ethanol Oxidation Reaction**
GCE:	**Glassy Carbon Electrode**
EEI:	**Electrode-Electrolyte Interface**
AEM:	**Anion Exchange Membrane**
Ag:	**Silver**
AFC:	**Alkaline Fuel Cells**
Au:	**Gold**
C_2H_5OH:	**Ethanol**
C:	**Vulcan carbon (XC72R)**
CA:	**Chronoamperometry**
CeO_2:	**Ceria**
CH_3OH:	**Methanol**
CNTs:	**Carbon nanotubes**
CNFs:	**Carbon nanofibers**
Cu:	**Copper**
CV:	**Cyclic Voltammetry**
DAFC:	**Direct Alcohol Fuel Cell**
DMFC:	**Direct Methanol Fuel Cell**
DEFC:	**Direct Ethanol Fuel Cell**
EASA:	**Electrochemical active surface area**
EDX:	**Energy Dispersive Spectroscopy**
EIS:	**Electrochemical impedance spectroscopy**
EMF:	**Electromotive force**
FTIR:	**Fourier transform infrared spectroscopy**
KOH:	**Potassium hydroxide**
g:	**gram**
H_2:	**Hydrogen**
ICP-OES	**Inductive coupled plasma optical emission spectroscopy**
Ir:	**Iridium**
LHV:	**Lower heating value**
M:	**Molar**
MCFC:	**Molten carbonate fuel cell**

mg:	**milligram**
mL:	**millilitre**
MOR:	**Methanol Oxidation Reaction**
MWCNT:	**multi wall carbon nanotube**
Ni:	**Nickel**
$NaBH_4$:	**Sodium borohydride**
NaOH:	**Sodium hydroxide**
OCV	**Open circuit voltage**
ORR:	**Oxygen reduction reaction**
PAFC:	**Phosphoric acid fuel cell**
PEM:	**Polymer Exchange Membrane**
PEMFC:	**Polymer Exchange Membrane Fuel Cell**
Pd:	**Palladium**
Pd/C:	**C-supported Pd catalyst**
Pt:	**Platinum**
PdO:	**Palladium oxide**
Rh:	**Rhodium**
Ru:	**Ruthenium**
SEM:	**Scanning Electron Microscope**
SOFC:	**Solid oxide fuel Cell**
TEM:	**Transmission Electron Microscopy**
XRD:	**X-ray diffraction**

Chapter 1: INTRODUCTION

This work focuses on the development of novel materials with potential as active and Pt-free electrocatalysts for the electrooxidation of ethanol in direct ethanol fuel cells (DEFCs). The Pt catalyst alone accounts for more than 50% of the fuel cell construction costs [1,2] and therefore it hinders the commercialisation of fuel cells. Likewise, Pt is very susceptible to poisoning species and therefore the catalyst does not maintain its activity for reasonable time periods. The US Department Of Energy (DOE) is targeting fuel cell durability of 5000h with less than 10% performance loss, cost of 1 kW to be $40, and the Pt-group metal content to be ≤ 0.0125 g/kW by 2020 [3]. Direct ethanol fuel cells have a promising potential to be a key technology in the clean energy generation in terms of curbing CO_2 and other greenhouse gas emissions. Compared to other fuels used to feed the fuel cell anode, ethanol could achieve various technical benefits. For example, unlike hydrogen, ethanol is liquid and could be easily transported and stored. In order to use hydrogen to feed to the fuel cell, it needs either an external reformer unit – that could produce hydrogen from hydrocarbons such as methane and ethanol - attached to the cell or some sophisticated and safe storage and transport arrangement. Also, bioethanol is considered a renewable fuel as it is produced from biomass and agricultural feedstocks. Moreover, compared to methanol, ethanol is more energetic, as each molecule has 12 hydrogen atoms, and it is less toxic too and safer to handle. Additionally, methanol is more capable to crossover the membrane and travel to the fuel cell cathode whilst producing less electricity and decreasing the cell efficiency. However, all fuel cell types working at low temperature need an active noble metal catalyst to activate the redox reactions. Ethanol, rather than H_2 and methanol, is in a higher need for such catalyst as each molecule includes a rigid C-C bond that is not

likely to be broken even if Pt (the commercial metal catalyst) is applied. That is why many research works, including this, are working towards the development of Pt-free catalysts (to reduce the cost) and potentially they can break the C-C bond leading to the complete oxidation of ethanol instead of the prevailing and thermodynamically favoured partial one producing acetic acid. Maintaining the catalyst activity for extended time periods is also a main objective in the area of novel electrocatalyst design which is also applicable considering ethanol oxidation reaction (EOR) which involves a myriad of carbonaceous species.

The thesis is constructed as follows:

The current chapter introduces the technology of fuel cells and broadly classifies their different types. Operating principles of fuel cells and thermodynamics are outlined. Also, a comparison of fuel cell technology to other energy technologies is made. Special attention is paid to the role of catalysis in fuel cell operation.

Chapter 2: holistically reviews the literature related to ethanol electrooxidation and its various pathways. The primary focus is on Pd fuel cell catalysts while Pt catalysts are also abundantly referred to. Also, the different carbons applied as a support and their activation process are thoroughly highlighted.

Chapter 3: lists and explains the experimental techniques (physical and electrochemical) applied to characterise the catalysts investigated in this project. The theoretical principles for each are given a general coverage. Also, the experimental conditions adopted to investigate the current samples are covered. The synthesis methods are not covered in this chapter but in the subsequent chapters individually. The experimental setups of characterisation are explained in detail in this chapter and are referred to thereafter in the subsequent chapters.

Chapter 4: inveestigates the use of different carbons as a support for Pd nanoparticles and their use for ethanol electrooxidation. The applied polyol process is outlined. The physical and electrochemical results are demonstrated. The resulting behaviour is compared and contrasted with reflections from the literature. What is novel in this chapter is the exploratory work to address the collaborative (or contradicting) impacts of carbon support porosity, surface area, and crystallinity on the Pd ethanol oxidation.

Chapter 5: compares the use of different borohydride reduction synthetic routes for preparation of PdAuNi (At. 40:10:50) nanoparticles supported on Vulcan carbon (XC72). The **SBEG** refers to the **$NaBH_4$-etheylene glycol** reduction complex while the **SBIPP** refers to the **$NaBH_4$-2-propanol** reduction complex. **3steps** refers to the consecutive metal reduction of Ni followed by Au and finally

Pd using the SBIPP complex. The physical and electrochemical results are presented and explained with insights and comparative analysis from the literature.

Chapter 6: presents the synthesis using the SBIPP reduction complex of PdMNi (M=Ir, Ag, and Rh) with two atomic ratios (1:1:1) and (4:2:1). Vulcan carbon is applied as a support. The physical and electrochemical results are demonstrated and compared to the monometallic Pd/C with a comparative analysis from the literature. Those trimetallic catalysts are prepared for the first time except PdIrNi and PdAgNi which are reported in two papers.

Chapter 7: explains the synthesis of alternative variety of other trimetallic Ni-free catalysts based on Pd with the inclusion of two other metals from Au, Rh, Ag, and Ir with atomic ratio 1:1:1 each. The physical and electrochemical results are graphically presented and discussed with insightful analysis from the related publications. The 6 catalyst combinations studied for alcohol oxidation in this chapter are prepared for the first time to the best knowledge of the author.

1.1 Background

The climate change growing crises, depleting fossil fuel reserves, and growing worldwide population (and their increasing energy demands) are the big umbrella under which, all forms of renewable energy – including hydrogen and fuel cells – present some potential to respond to those global challenges [4–7]. Photovoltaic, wind, biomass, geothermal, and tidal are different forms of fossil-alternative energies. However, there is a lot of social, economic and political uncertainties and constraints concerning those different technologies. How they could help mitigate the global warming and curb the greenhouse gas emissions is still far from realised and coherently measured. From a climate change motivational angle, the combustion of fossil fuels leads to the generation of greenhouse gas emissions which might be called the anthropogenic greenhouse effect. Besides, there is a natural greenhouse gas effect as those gases (CO_2, H_2O, CH_4, N_2O) exist naturally in the atmosphere. They absorb some of the incident sun light and the other part is absorbed by the earth which is emitted back as infrared (IR) radiation. The greenhouse gases absorb the IR emitted from the earth and emit it back to the space and earth. This natural process keeps the earth surface warm enough for people to live on and the average temperature at 15°C [2].

In this context, the natural presence of the greenhouse gases is beneficial for sustaining human life on earth. However, the growing human-made generation of those gases – over the last 200 years – has led to the global warming due to the thermal energy they could absorb and emit into the troposphere. Also, black carbon (e.g., soot) and other dark particles exist and are also released from

certain industries into the atmosphere but they - absorb the sun rays increasing the overall heat contained in the atmosphere of earth. To give an idea of how serious the climate change is, the CO_2 emissions were 280 part per million per volume (ppmv) upon embarking the industrial revolution in 1860, but it has jumped to 380 ppmv in 2000 and every year, a 2-ppmv increase occurs. The atmospheric CH_4 concentration was only 0.8 ppmv in 1860 but it has increased to 143% to be 1.8 ppmv in 2000. Here, it is noteworthy that the hydrogen produced from incomplete combustion of fossils and biomass burning might have an indirect potential to increase the CH_4 emissions and the average global temperature, consequently [2]. Because of that and the declining fossil fuel resources, it has become necessary to seek and find alternative energy technologies whose operations are eco-friendly and do not generate harmful emissions. Also, the growing worldwide population has inevitably increased and diversified the energy demands especially in this age of information technology and globalisation.

1.2 Definition of fuel cells

Fuel cells could be defined as factories of energy where the input is the fuel and the output is electricity. They could continuously convert the fuel chemical energy into electrical energy for as long as the fuel supply is assured [8,9]. This is the main technical difference between fuel cells and batteries. Both of them depend on electrochemistry to work but a fuel cell is not consumed by its operation. They manufacture electrical energy from a fuel and oxidant. In that sense, heat engines are also energy factories as they convert the fuel chemical energy into either mechanical or electrical energy. In their process, the collision of the high-energy reactant (fuel and oxidant) results in the reconfiguration of electrons in their molecules forming the low-energy products. Initial bonds are broken and new bonds are formed by the electron reconfiguration at picoseconds and subatomic distance. The energy difference between the reactant fuel (H_2 for example) and product (H_2O) is released in the form of heat. Because the process occurs extremely quickly at subatomic distance no useful use could be made from the electrons produced after reactant bond breaking and before product bond formation. Fuel cells address this exact issue by spatially separating the two parts at great distance to enable the harnessing of the electrons in the form of electrical current. Figure 1-1 shows the theoretical principle of fuel cell operation. Fuel cells are a multidisciplinary research topic since they require knowledge of physics, chemistry, electronics, and material science [10]. Therefore, they need collaborative multidisciplinary research efforts from materials scientists, engineers, chemists

and physicists. Also, they have been applied in the sectors of space exploration, portable electronics, transport, residency, and industry [11].

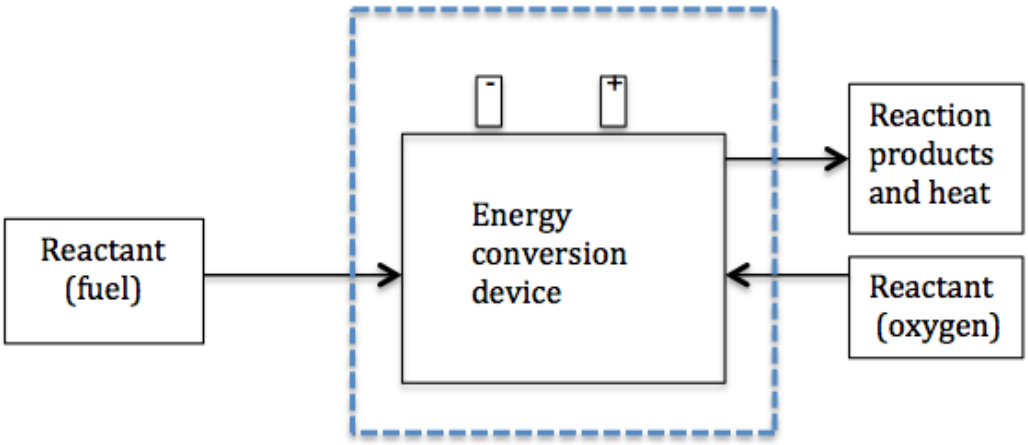

Figure 1-1 Operational layout of fuel cell

1.3 Fuel cell history and functional principles

Historically, the discovery of fuel cell technology goes back to Sir William Grove in the 17th century. First, he was able to split water into hydrogen and oxygen by connecting a power supply to the two platinum electrodes. Then, he found that it is possible to reverse the process by supplying hydrogen and oxygen and replacing the power supply with an ammeter and noticed a small current flowing through it [12]. These two opposite processes are shown in Figure 1-2.

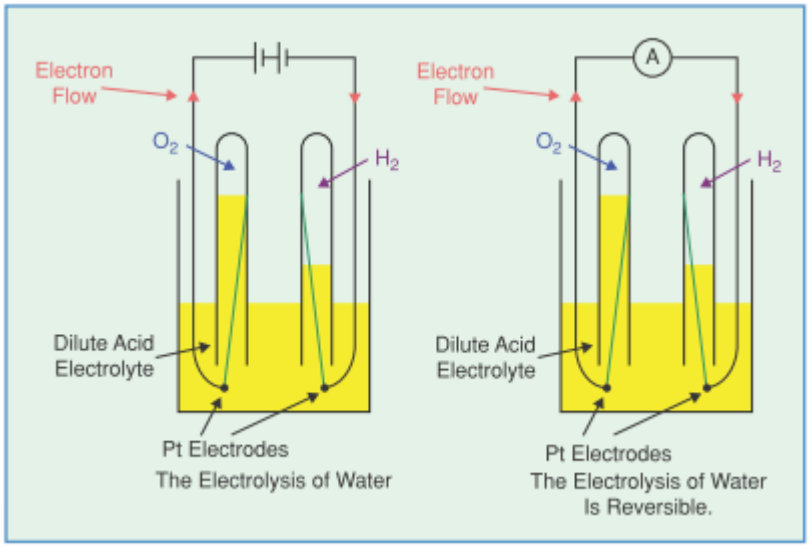

Figure 1-2 William Grove electrolysis cell vs fuel cell [13]

In the fuel cell operation, the fuel is supplied into the anode and consequently would be electro-oxidised while the oxidant is supplied into the cathode and then would be electro-reduced. The released electrons from the fuel oxidation pass through the external circuit while the H^+ ions travel through the electrolyte (or membrane) from the anode to the cathode side [9]. Both the electrons and the H^+ ions react with oxygen on the cathode side producing water. The anode and cathode half-reactions are:

$$2H_2 \rightarrow 4H^+ + 4e^- \quad (anode) \tag{1.1}$$

$$O_2 + 4H^+ + 4e^- \rightarrow 2H_2O \quad (cathode) \tag{1.2}$$

$$O_2 + 2H_2 \rightarrow 2H_2O + \Delta \quad (overall) \tag{1.3}$$

To produce electricity, the liquid electrolyte should only conduct ions and prevent the electrons from passing through it to the cathode. Therefore, the electrolyte should have a zero – or negligible - electron resistance. A small voltage could be obtained from a single cell while drawing a useful current. Therefore, it is worthy to connect multiple cells in series. The series arrangement is called stack in which each anode edge is connected to the next cathode in a line. However, this method is not very efficient since the electrons must be collected at the edge of each electrode (interconnecting cables in Figure **1-3**), which might cause a voltage drop. Therefore, a bipolar plate is used to make

the connection throughout the electrode surface and at the same time to serve as flow channels for both the fuel and oxygen into the anode and cathode, respectively.

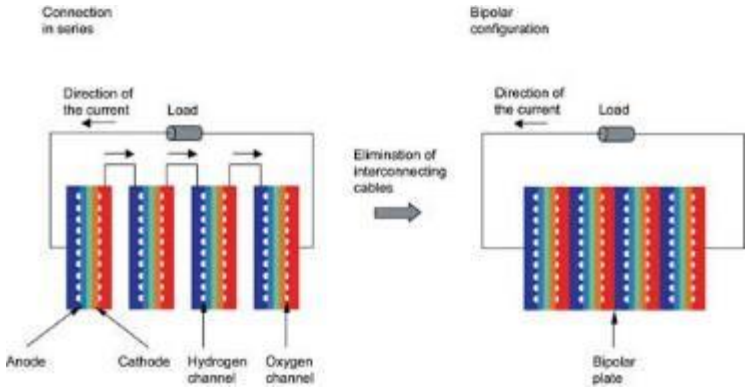

Figure 1-3 Fuel cell stack: (left) series anode/cathode arrangement, (right) bipolar plate/flow field arrangement [14,15]

Considering the design of the bipolar plate, a compromise must be made because it serves two contradicting purposes: feeding the gases through its channels and making an electrical contact to collect the electrons from the whole electrode surface and add up the voltage. The former needs wider channels (less contact with the electrode) to circulate the reactant gases well while the latter needs to have the highest possible contact surface with the electrode [12,16]. Fuel cells often operate at the maximum power density (the product of output voltage × current density). Smaller power density in operation is also possible and it would yield a higher overall efficiency. However, it would require more fuel cell stacks to produce the same voltage output and that is why the smaller-than-maximum-power density is feasible from application perspective [17].

1.4 Advantages of fuel cells

As explained in section 1.2, the molecular collision of the fuel and oxidant leads to electron reconfiguration and bond breaking and formation. The energy difference between the reactant and product is released as a heat. In that sense, both fuel cells and heat engines are energy factories. However, unlike heat engines, fuel cells convert the stored chemical energy – in a fuel – directly into electricity. The process is sustainable as long as the fuel supply is assured [9]. Another condition, that could be added, is the consistent functionality of the catalyst, which is the focus of this project.

The heat engines, on the other hand, combust the fuel producing heat which is converted to mechanical work, and finally an electric generator uses the work to generate electricity [8,16]. Sometimes, the mechanical work is desired is the desired outcome of the heat engine like internal combustion engine. The intermediate thermal/mechanical energy produced imposes a big loss on the efficiency of conversion according to Carnot efficiency. Figure 1-4 shows the steps of electricity production by heat engines combusting fossil fuels.

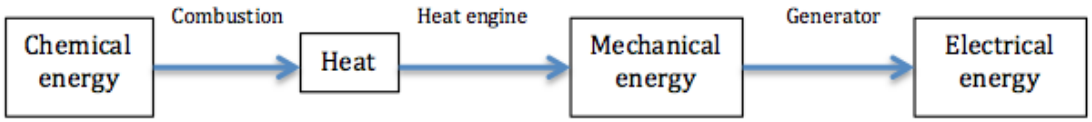

Figure 1-4 Principle of electric power generation using heat engines

Unlike batteries, fuel cells convert – do not store – the chemical energy into electricity, which means they could be used continuously without the need for a replacement or recharging [18]. Fuel cells are considered an efficient technology for energy generation (up to 60%). On the other hand, the cost of fuel cell is generally high compared to the other energy systems due to the need for using noble metal catalysts and sophisticated polymer exchange membranes [18–20]. A simple comparison among fuel cells, solar cells, and batteries is made in Figure 1-5. As fuel cells and solar cells are continuously replenished with the input fuel and photons, respectively, to product the electrical energy output, they are considered open thermodynamic systems.

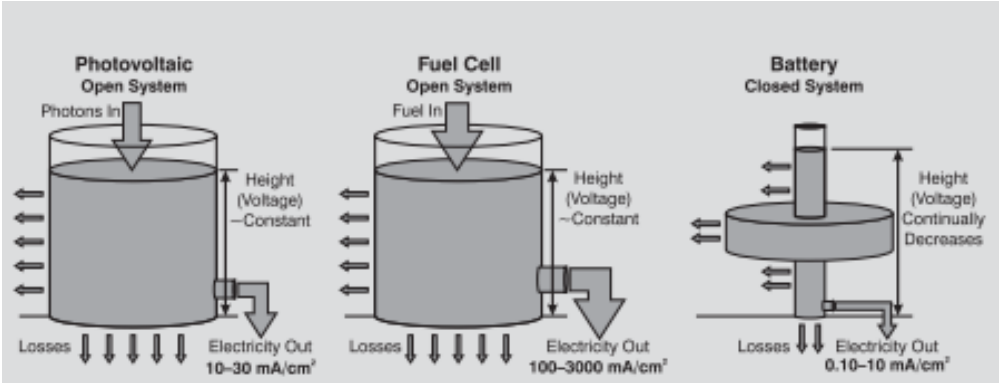

Figure 1-5 Fuel cells versus solar cells versus batteries (Taken from [9]**)**

On the other hand, batteries are gradually depleted from reactants and therefore they are closed systems. That is why the voltage of fuel cell and solar cell is constant while that of a battery

continually decreases. Another differentiation is that fuel cells operate at much higher current densities compared to solar cells and batteries. Because of that, they need materials with low resistance to conduct such high currents. Moreover, the operation of the three devices is noiseless making them suitable for indoor applications. Additionally, their fabrication is easy in terms of the required machinery. In operation, all parts are static, and therefore the mechanical resistance is not an issue and lubricants are not needed [18,21–23]. In their study, Urepti *et al.* have commented on the contributions of reducing the cost and increasing the durability of fuel cells from 2008 to 2012 based on interviews with fuel cell manufacturers in the US, EU, and Japan and on published resources. They argue further reduction in the cost of the system by 2025 is needed for the fuel cells to be a more visible competitor for the traditional technologies. Additionally, the polymer-electrolyte-membrane fuel cells (PEMFCs) have been used to derive new cars instead of gasoline. Still, there is a long walking-way to achieve satisfying cost-performance balance for those fuel-cell-driven cars according to R. F. Service [24].

1.5 Types of fuel cells

The redox reactions and the active species (released – travelling through membrane - ions) vary from one fuel cell system to another. Figure 1-6 shows the reaction direction for the famous five technologies of fuel cells: solid oxide fuel cells (SOFCs), molten carbonate fuel cells (MCFCs), phosphoric acid fuel cells (PAFCs), polymer exchange membrane fuel cells (MEPFCs), and alkaline fuel cells (AFCs) [25]. For SOFC, which operates at 500 -1000°C, the active species are O^{2-} ions travelling from the cathode to the anode, while the CO_3^{2-} ions travelling from the cathode to the anode, are the active species for the MCFC operating at 650°C.

The advantages of both SOFC and MCFCs are: no need for external reforming, no need for noble-metal catalyst, and CO is a fuel not poison. However, the high-temperature operation makes them suitable only for stationary applications and unlikely to be applied for portables or transport vehicles. Hydrogen, carbon monoxide, and natural gas are valid fuels for SOFC and MCFC and water and carbon dioxide are the exhaust products at the anode side unlike PEMFC and PAFC in which water is produced at the cathode side. These systems, particularly SOFCs, are more efficient than the other systems due to the high operational temperature, which reduces the irreversibilities according to Nernst equation; some particular SOFC systems are 80%- or even 90%-efficient.

The active species are H^+ ions in case of both PAFC (200°C) and PEMFC (80°C) and they migrate from the anode to the cathode. However, in case of ACF (70°C), the OH^- ions travelling from the

cathode to the anode, are the active species. Among the crucial differences is the type of electrolyte for each fuel cell. For SOFC, it is solid yttrium-stabilized zirconia (YSZ) and for MCFC, the electrolyte is molten carbonate. Phosphoric acid is the electrolyte for PAFCs. For AFC, the electrolyte is alkaline, and like SOFC and MCFC, water is produced in the AFC anode. An acidic electrolyte is used for PEMFC. The main differences between alkaline and acid electrolytes are discussed in more detail later in this work.

Table 1-1 shows the reactions in both electrodes of the various fuel cells. The most common applications for low-temperature fuel cells (AFC and PEMFC) are stationery and transport vehicles according to Table 1-2. AFCs have been, particularly, used in Apollo and Gemini space missions, while the fuel cells have provided the crew with not only electricity, but drinking water as well.

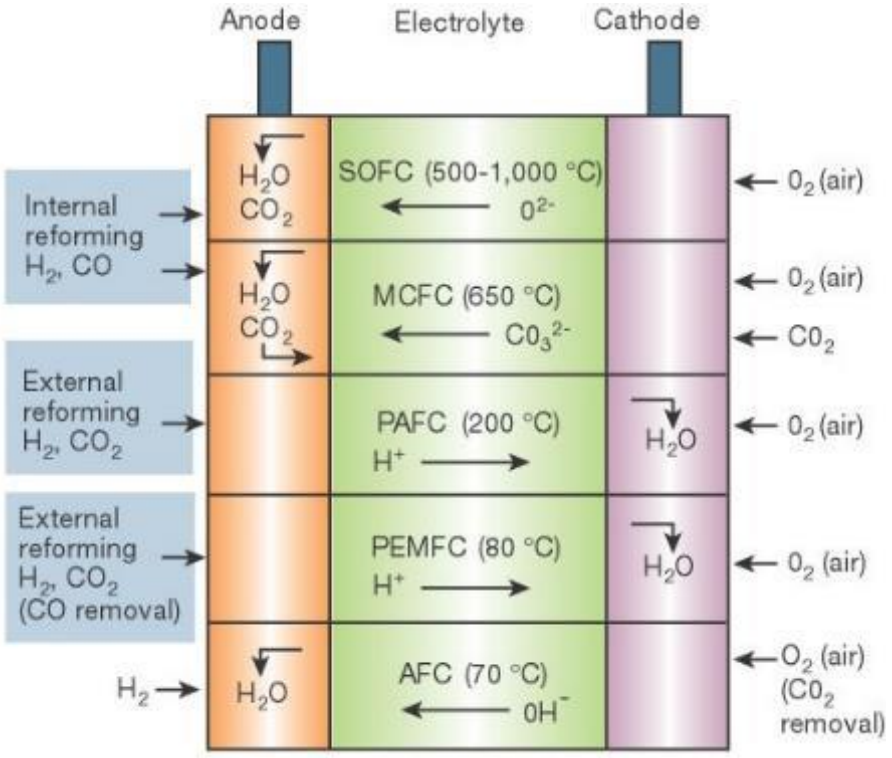

Figure 1-6 The reaction mechanism of different types of fuel cells [25]

The most suitable application for high-temperature fuel cells (SOFC and MCFC) is the stationary power plants competing (and sometimes co-working) with the traditional fuel-combusting plants.

Table 1-1 The anode and cathode reactions in different fuel cell systems

Fuel cell	Anodic reaction	Cathodic reaction
SOFC	$H_2 + O^{2-} \rightarrow H_2O + 2e^-$ $CO + O^{2-} \rightarrow CO_2 + 2e^-$ $CH_4 + 4O^{2-} \rightarrow 2H_2O + CO_2 + 8e^-$	$\frac{1}{2}O_2 + 2e^- \rightarrow O^{2-}$
MCFC	$H_2 + CO_3^{2-} \rightarrow H_2O + CO_2 + 2e^-$ $CO + CO_3^{2-} \rightarrow 2CO_2 + 2e^-$	$O_2 + 2CO_2 + 4e^- \rightarrow 2CO_3^{2-}$
PAFC	$H_2 \rightarrow 2H^+ + 2e^-$	$\frac{1}{2}O_2 + 2H^+ + 2e^- \rightarrow H_2O$
PEMFC	$H_2 \rightarrow 2H^+ + 2e^-$	$\frac{1}{2}O_2 + 2H^+ + 2e^- \rightarrow H_2O$
AFC	$H_2 + 2(OH)^- \rightarrow 2H_2O + 2e^-$	$\frac{1}{2}O_2 + H_2O + 2e^- \rightarrow 2(OH)^-$
DMFC	$CH_3OH + H_2O \rightarrow CO_2 + 6H^+ + 6e^-$	$\frac{3}{2}O_2 + 6H^+ + 6e^- \rightarrow 3H_2O$
DEFC	$C_2H_5OH + 3H_2O \rightarrow 2CO_2 + 12H^+ + 12e^-$	$3O_2 + 12H^+ + 12e^- \rightarrow 6H_2O$

Table 1-2 The advantages, disadvantages, and applications of different fuel cells [21,26,27]

FC Type	Application	Advantages	Disadvantages	Efficiency (%) [20]
SOFC	Stationary	• Fuel flexibility • Cheap catalyst • Solid electrolyte	• Sealing issues • Expensive materials	45-60
MCFC	Stationary	• Fuel flexibility • Cheap catalyst • High-quality waste heat	• Corrosive, molten electrolyte • Lifetime issue • Expensive materials	43-47
PAFC	Stationary	• Developed technology • Good reliability • Cheap electrolyte	• Low CO tolerance (2%) • Expensive catalyst • Frequent electrolyte change	40-42
PEMFC	Portable/ Transport/ Stationary	• Rapid start-up • High power density • Low temperature	• Expensive metal catalyst • Catalyst poisoning • Expensive electrolyte	45-54
AFC	Transport/ Stationary	• Enhanced oxygen reduction • Cheap catalyst • Low-cost electrolyte	• Water management • Progressive carbonization	60
DMFC	Portable	• Easy fuel handling • Low temperature • Rapid initiation	• Low efficiency • High catalyst cost • Fuel crossover	40
DEFC	Portable/ Transport	• Renewable and safe fuel • Low temperature • Fuel transport/storage • High fuel utilization	• Poor anode and cathode performance • Noble metal catalysts • Water management • Catalyst poisoning	43 (complete EOR)

*DEFC and DMFC could apply either PEM or AEM (anion exchange membrane). Accordingly, they would have the advantages and disadvantages of either PEMFC or AFC

1.6 Thermodynamics of fuel cells

For an ideal situation, all the input fuel chemical energy would be converted into a useful electrical work. However, this is not possible for many reasons. First even in reversible (ideal) reaction conditions, the maximum doable work on the external circuit equals the change in Gibbs free energy (Δg_f) which is less than the change of enthalpy at high heating value (ΔH_{HHV}). Furthermore, the reaction produces heat and water. The resultant heat cannot go back and therefore some researchers consider it "a loss" which is not very precise because it could be used for other purposes such heating houses and water in what is called combined power heat (CPH) generation. If the system were reversible (no losses), the output electrical work (W) would be equal to the change of the Gibbs free energy (Δg_f) (the maximum theoretical electrical work) of the input chemical energy according to:

$$\boldsymbol{W = 2FE = -\Delta g_f} \qquad \textbf{(1.4)}$$

Where, E is the open circuit voltage (OCV) of H_2 fuel cell, F is Faraday constant (96485 C/mol), and 2 is the number of electrons transferred for H_2 fuel cell. This is true only if the reactions are reversible which is not practical. Moreover, Δg_f changes with temperature, pressure and other factors. Furthermore, the fuel produced in the external reformer is not 100% pure hydrogen but there are some other gases such as CO_2, CO, and SO_x. In addition to that, it is impractical to assume that all the inlet fuel would be reacting releasing electrons; there is a coefficient known as a fuel utilization factor, which is the ratio of the useful fuel producing electric work by the total inlet fuel.

According to the band theory, the voltage impacts the electron energy in a metal (i.e, Fermi level (E_f)). Therefore, the reaction direction could be manipulated by controlling the voltage. Increasing the voltage in the negative direction (raising E_f), a reduction reaction is more likely to occur and vice versa. The Galvani potential is the reaction potential at equilibrium which means the rate (current) of the forward reaction equals that of the reverse reaction. At this state, not net current output is obtained from the cell and the current is called exchange current (j_o). Figure 1-7 demonstrates how the equilibrium condition is reached considering the hydrogen oxidation example. Initially, the chemical energy profile favours the oxidation of adsorbed M…H. As this happens, the interface electrode side is gradually filled with negative electrons while the electrolyte one is gradually filled with positive H^+ ions until the potential difference ($\Delta\phi$) counterbalances the chemical energy difference favouring

the forward reaction direction. The interfacial potential difference increases the forward activation barrier and decreases the reverse one until both are equivalent. Therefore, it is possible to shift the potential to direct the reaction in one particular direction by applying a potential higher or lower than the Galvani potential. The difference between the Galvani potential and actual potential is called activation overvoltage which is explained further in section 1.9.

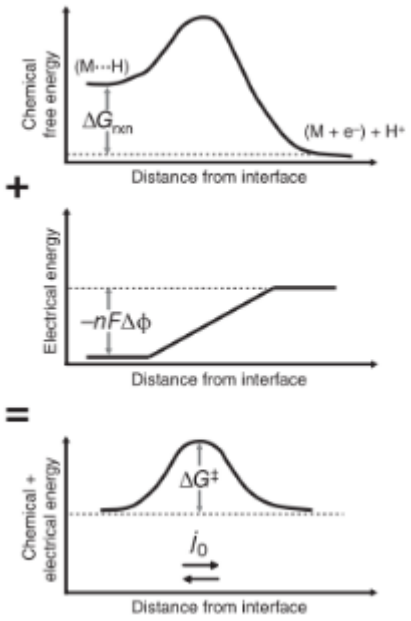

Figure 1-7 The chemical free energy across interface (*a*), the accumulated electrical energy due to reaction (*b*), net zero reaction rate (*c*) [29]

For the above reasons, there are three types of efficiency associated in fuel cell operation: reversible (ε_{thermo}), voltage ($\varepsilon_{voltage}$) and fuel utilisation (ε_{fuel}) efficiency. ε_{thermo} is the ideal thermodynamic efficiency and it is less than 100% since the maximum doable work (Δg_f) is less than the fuel enthalpy. $\varepsilon_{voltage}$ incorporates the voltage losses occurring observed from the *j*-V curve (the voltage losses are explained in detail in section1.9). ε_{fuel} correlates the really utilised fuel to do work to the total inlet fuel. Therefore, the real fuel cell efficiency could be estimated according to:

$$\boldsymbol{\varepsilon_{real} = \varepsilon_{thermo} \times \varepsilon_{voltage} \times \varepsilon_{fuel}} \qquad \textbf{(1.5)}$$

The above equation, therefore, could be written as:

$$\varepsilon_{real} = \frac{\Delta g_f}{\Delta H_{HHV}} \times \frac{V\ (actual\ voltage)}{E\ (OCV)} \times \frac{j/nf\ (utilised\ fuel\ rate)}{v\ (inlet\ fuel\ flow\ rate)} \quad \textbf{(1.6)}$$

The Nernst equation is useful to estimate the actual cell voltage and correlates to the partial gas pressure (activity) and temperature. The below equation is the Nernst equation for a simple H_2-O_2 fuel cell.

$$E = E_o + \frac{RT}{2F}\ln\left(\frac{P_{H_2}.P_{O_2}^{1/2}}{P_{H_2O}}\right) \quad or \quad E = E_0 + \frac{RT}{2F}\left(\frac{a_{H_2}.a_{O_2}^{1/2}}{a_{H_2O}}\right) \quad \textbf{(1.7)}$$

Where, P_{H2} and a_{H2} are the hydrogen partial pressure and activity (concentration), respectively, and E_o is the cell OCV at standard pressure and temperature.

1.7 Heterogeneous Catalysis

Chemical reactions involve collision among the molecules of reactants which results in breaking certain bonds in the reactants and forming new bonds in the products. For example, Figure **1-8** shows the combustion reaction between hydrogen and oxygen molecules. It starts with collision of H_2 and O_2 molecules. Then, the molecules need to gain certain amount of energy in order to be able to break the bonds of H-H and O-O. After that, it is possible to form new bonds of H-O-H.

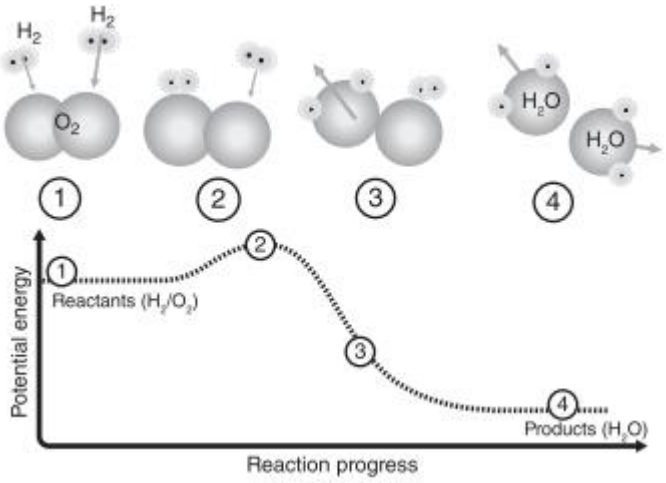

Figure 1-8 H_2-O_2 combustion reaction starting with molecular collision of H_2 and O_2 followed by breaking their associated bonds after gaining energy and finally O-H bond formation [9]

The energy required to break the reactant molecular bond is called the activation barrier which could be reduced by the careful selection of the catalyst material to activate the reactant molecules and facilitate the reaction. In this situation, it is heterogeneous because the catalyst is solid while the reactant are gases. The catalyst surface is the most important aspect because it is the interface that will contact with the reactant molecules.

The ideal crystal surface is evenly packed with atoms at the surface. A gas molecule colliding with the surface atoms could be imagined as a tennis ball bouncing on the surface. The repeated collision with atoms causes the molecule to lose its energy and become attached to the surface. However, the prefect flat surface with evenly order atoms does not exist and there is always one defect type or another. Figure **1-9** shows some of the general surface defects. The terrace is a crystallographic flat surface and steps exist among consequent terraces. Beyond that, a kink is a surface defect at which two different steps meet in a corner. Additionally, other defects may exist on the surface such as vacancy (at the step or terrace) which is an absent atom. Surface sites include any site where the reaction could take place be it surface atom or surface defect. Also, another defect, related to lattice distortion, is the dislocation which could be (edge or screw one).

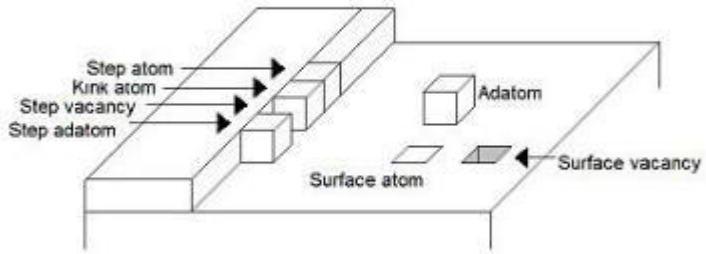

Figure 1-9 Solid surface defects [30]

The attachment of gas molecules into solid surface is called adsorption and the solid surface is called adsorbent or substrate while the adsorbed atom (or molecule) is called adsorbate (adatom in Figure **1-9**). There are two types of adsorption: physisorption and chemisorption. In physisorption, the molecule is adsorbed to the surface under the influence of Van der Waals intermolecular force and does not involve any chemical reaction. In chemisorption, however, the molecule is adsorbed into the surface by forming chemical bonds (usually covalent) with the solid surface atoms. During chemisorption, the adsorbate molecules try to find surface sites to minimise their energy. The enthalpy of physisorption is much less than that of chemisorption and the adsorbent-adsorbate

distance is in the latter is much smaller than the former. Due to the unsatisfied valences of surface atoms, in chemisorption, the adsorbed molecule might be destroyed into molecular fragments which is why metallic solid surfaces catalyse various reactions.

The catalyst ensemble is the minimum arrangement of surface atoms that could be used to model the action of a heterogeneous catalyst. The activity of a catalyst is predominantly determined by the coverage of a catalyst surface with adsorbate gas. Heterogeneous catalysis is a surface phenomenon and therefore, it is important for a catalyst to have a high surface area. Thus, a catalyst support is used to stabilise and disperse the catalyst particles on its surface. Once the gas molecules are adsorbed on the catalyst surface (by occupying one or more surface atoms), the gas molecules are expected to react with other adsorbed molecular species (yet much faster than if the two species to react together without the catalyst). In a heterogeneous catalysis situation, chemical processes are investigated at the surface in two dimensions while the reactant and product molecules must approach and leave the surface in three-dimensional environment.

In case of the supported metal catalysts, surface composition, it is crucially important to maximise the surface content of the active constituent and even when there are some internal pores, reacting molecules should have access to those pores to make use of the active catalytic metal deeply housed. Figure **1-10** shows the processes involved in heterogeneous catalysis situation. The reacting fluid molecules should first travel from the bulk fluid phase into the boundary layer (or interface) between the solid surface and fluid. This mass transport step occurs while the reacting molecules are still moving in the bulk phase and it is impacted by the pressure (or concentration) of the fluid. When the pressure is high, the rate of diffusion will be high and vice versa.

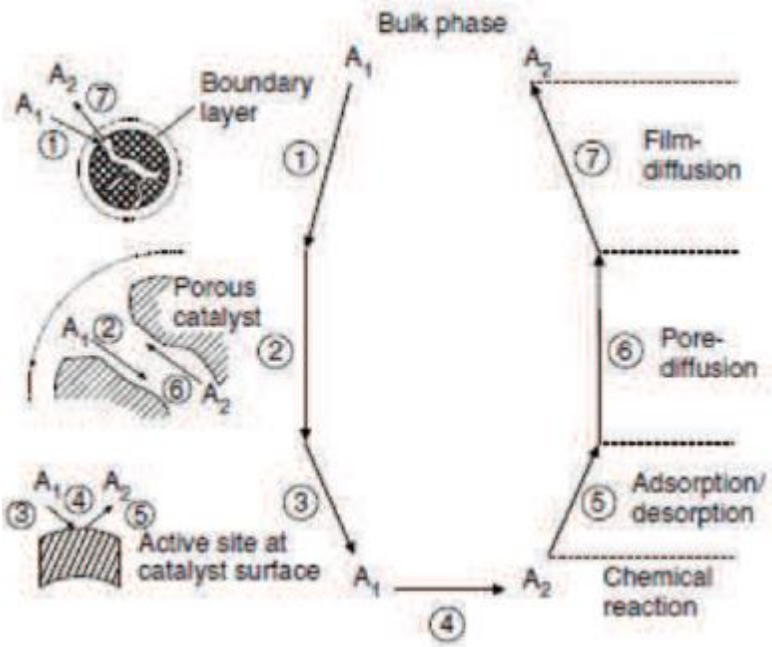

Figure 1-10 Physical and chemical processes in heterogeneous catalysis reactions [31]

Then, follows another diffusion action but through the porous structure of the catalyst. Inside it, the reacting molecules collide with the surface of the composite structure of catalyst (active constituent and inactive support). Once the reactants hit some active metal particle, step 3 occurs in which they are attached (or adsorbed) into it. After that the adsorbed molecule reacts with another adsorbed molecule on another active metal particle moving forward to step 5 through step 4. Figure **1-11** demonstrates the chemisorption vs physisorption. In case of chemisorption the adsorbate-surface sites distance is 1-3 Å while it is 3-10 Å in case of physisorption. Additionally, physisorption is weak (<0.4 eV) but chemisorption is stronger. While physisorption is reversible chemisorption is not. Chemisorption requires surface symmetry but physisorption does not.

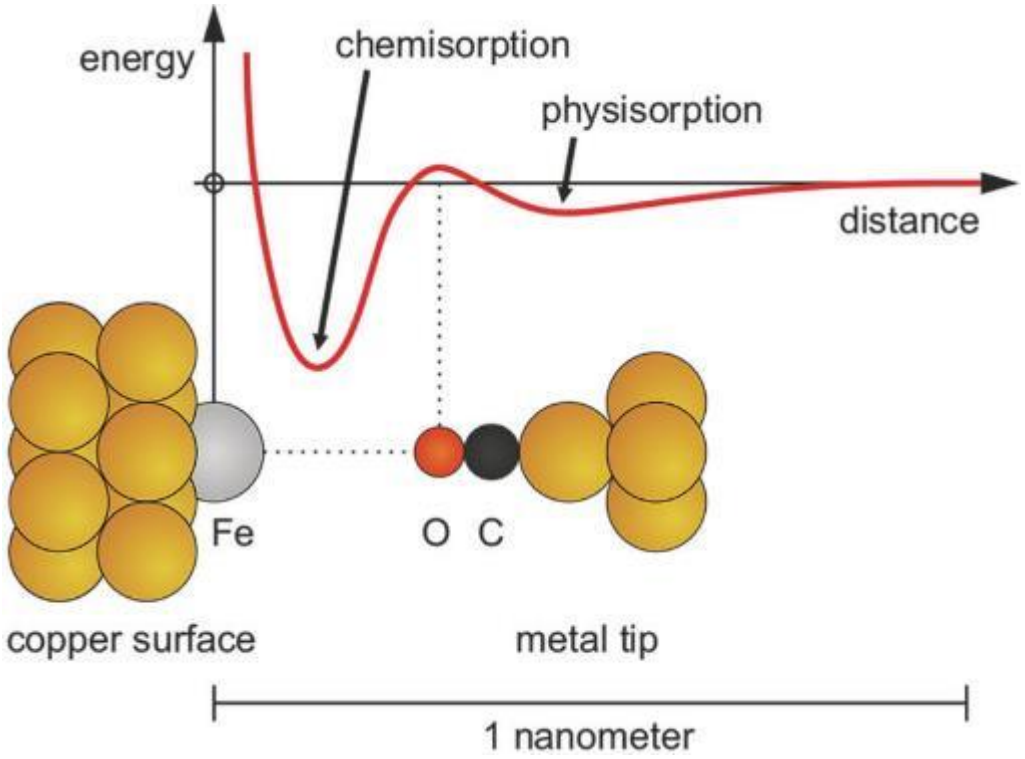

Figure 1-11 The energy and distance in chemisorption vs physisorption

After the surface reaction, the product is to leave the catalyst active site through desorption (step 5). Step 6, the inverse diffusion of step 3, occurs when the product diffuses through the pores of the solid surface. Finally, step 7 is the diffusion of the product through the fluid bulk phase. The reaction rate is controlled and impacted by various actions such as reactant adsorption, surface reaction, and/or product desorption in addition to the diffusion in both the fluid bulk phase and porous solid structure. Thus, it is important to not only have many catalytic reaction sites but also easily accessible inner and outer surfaces. It is also crucial to have decent reactant concentration in the gas stream.

An effective catalyst may (or may not) include different active species which are usually metals, oxides, sulphides, and zeolites. These may serve one individual reaction or collaborate to activate related reactions. One of the prominent factors that contribute to the overall reaction rate is the active surface area, which implies the surface area upon which reaction occurs. To maximise this reaction area, it is crucial to disperse as many small active sites as possible on the support. Figure 1-12 shows how the surface area could be increased by dividing the bigger particles into smaller ones. The surface area of a bulk spherical particle is much less than if it is divided into smaller particles and then added together. The higher surface area of the active catalyst species directly enhances the rate at which a chemical reaction occurs.

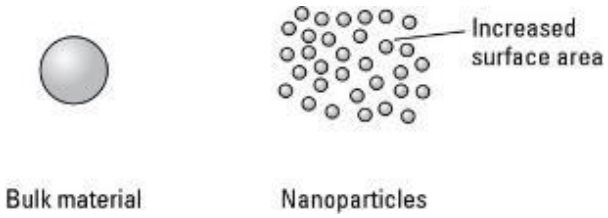

Figure 1-12 increasing surface area by dividing bigger particles into small ones [32]

Yet, it should be mentioned the inverse relation between the surface area and surface energy There is a resistance for the subdivision of bigger particles into smaller ones. In other words, the smaller particles have higher surface energy than the bigger ones and therefore they tend to coalesce together. This process is also called agglomeration, aggregation, and/or sintering and it is entirely undesirable for the catalysis applications though inevitable. It means the small particles will always tend to come together and unite in one bigger particle or at least they will come close to one another. Here is another use of the support inactive constituent is preventing the agglomeration of the small active catalytic species. The functional support helps prevent the particles from aggregation.

1.8 Electrocatalysis

Electrocatalysis is a type of heterogeneous catalysis where electricity is associated with the activated redox reactions. Electricity is either used to derive the reactions such as in water electrolysers or it is produced from the redox reactions such as in fuel cells. Understanding of the processes occurring at the electrode surface is necessary for calculation of the electron transfer between the electrode and electroactive species in the electrolyte. At low current density, the charge transport could possibly be adopted to measure the reaction rate following the Butler-Volmer equations. Yet, this equation fails at high current densities due to the mass transfer mechanisms.

The metal-solution interface is modelled by an electrical double layer which is the accumulation of certain electronic charges on the metal and the opposite-sign charges on the solution side. Due to this charge separation, a potential difference develops which is called the electrode potential. It should be noted this potential develops at the electrode/electrolyte interface even though there is no Faradaic reaction occurring. The exact detailed description of the electrical double layer is not unanimously agreed on. One common model is the Helmholtz layer model in which the solvated ions arrange themselves along the electrode surface, but at a uniform distance that separates them from the

electrode by the action of their hydration spheres. The distance at which the opposite-sign ions arrange themselves is called the outer Helmholtz Plane (OHP) as shown in Figure **1-13**.

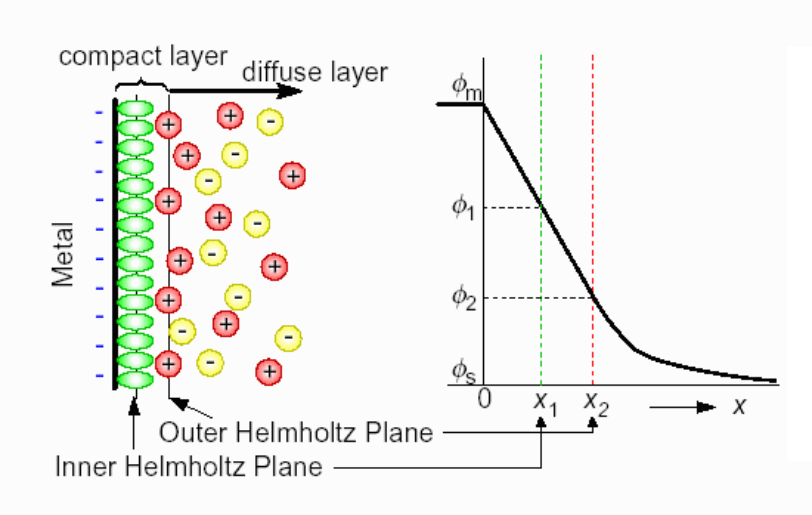

Figure 1-13 Helmholtz double-layer electric model [33]

There is an electrostatic potential drop (ϕ_m-ϕ_s) which develops linearly with the distance from the OHP to the electrode surface. The simple Helmholtz model was further modified by Gouy and Chapman who realised the excess charge in solution are not necessarily concentrated at the OHP by the electrostatic attraction forces [34]. They have claimed the Brownian motion also contributes by pushing the excess charges to disperse in the electrolyte rather being focused at the OHP. The potential difference develops, according to them, through a diffuse layer (expanding beyond the OHP) where the charge density decreases with going further away from the electrode. While the potential drop-distance-from-the-electrode relation is linear in the Helmholtz model, it is curvilinear in case of the Gouy-Chapman one even though the major potential drop is located in proximity to the electrode surface. Another refined scenario was developed by Stern who technically combined the Helmholtz and Gouy-Chapman models. Further development was attained by Grahame who claimed the ions or uncharged species escape or lose their hydration spheres and approach the electrode surface. Eventually they become attached to the electrode surface at the inner Helmholtz plane (IHP).

1.9 Fuel cell overvoltages

There is no single terminology used to express the losses in a fuel cell. Some would call them overpotential/overvoltage, polarisation, irreversibility, losses, or voltage drop. But all these words

mean the same thing in a fuel cell operation, which is the voltage decrease in the actual operating cell below the open circuit voltage with increasing the drawn current (load) from the cell. Figure **1-14** shows the various overpotentials in a working fuel cell: activation (kinetic), Ohmic, and concentration (mass transport) overpotentials. Figure **1-14**, also, shows the power density curve versus the net current. At low current densities, the obtainable power is meaningless from practicality perspective. Obtaining high power requires increasing the current which decreases the actual cell voltage (and therefore the efficiency). Therefore, it is feasible to operate the fuel cell at a current density smaller than - but very close to - the power density peak.

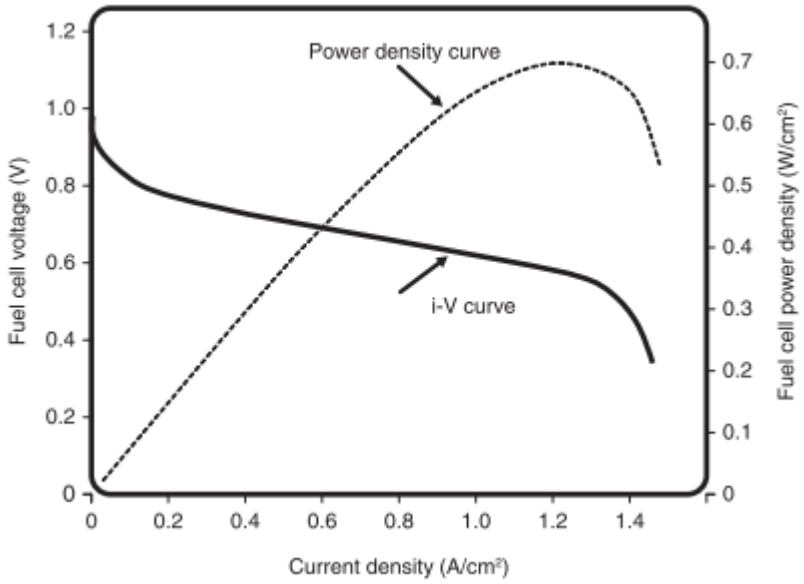

Figure 1-14 Fuel cell overpotential (*j*-V curve) and power density

The first kind of overvoltage experienced in fuel cell operation is the activation overvoltage (η_{act}) which is the voltage lost to overcome the activation barriers against fuel oxidation and oxygen reduction. Looking at Figure **1-14**, the activation overvoltage is the non-linear region while drawing very small current from the cell. The Butler-Volmer equation is applied correlating the current and activation overvoltage (η_{act}):

$$\boldsymbol{j = j_o(e^{\frac{\alpha n F \eta_{act}}{RT}} - e^{-\frac{(1-\alpha) n F \eta_{act}}{RT}})} \qquad \textbf{(1.8)}$$

Where j_o is the exchange current density, α is the charge transfer coefficient, F is the Faraday constant, η_{act} is the activation overvoltage. At high η_{act} values, the Butler-Volmer equation is simplified to the Tafel equation:

$$\boldsymbol{\eta_{act} = a + b.log\, j} \qquad \textbf{(1.9)}$$

Where *b* is the Tafel slope and both *b* and *a* could be estimated by graphically plotting *Log (j) vs* η_{act}. Knowing *a* and *b* helps calculate j_o and α. To minimise the activation overvoltage and maximise the reaction kinetics, the exchange current density needs to be maximised. This could be done by increasing the reactant concentration, decreasing the activation barrier, increasing the temperature, and/or increasing the number of reaction sites. This project focuses on decreasing the ethanol activation barriers and increasing the reaction sites number by trying different catalyst designs. According to the Sabatier principle for catalyst selection, the optimum catalyst activity depends on the strength of adhesion between the catalyst surface and reacting species. If the adhesion is too strong, the reacting species blocks the catalyst surface. And if it is too weak, there will hardly be any reaction occurring. The activity of various materials for oxygen reduction is graphically represented in Figure **1-15** which shows metals such as Pt and Pd achieve the most moderate reactant bonding strength and highest turn-over frequency. While the bonding strength of Fe is very weak, it is very strong with Au. Yet, both of them have a low catalytic activity for oxygen reduction.

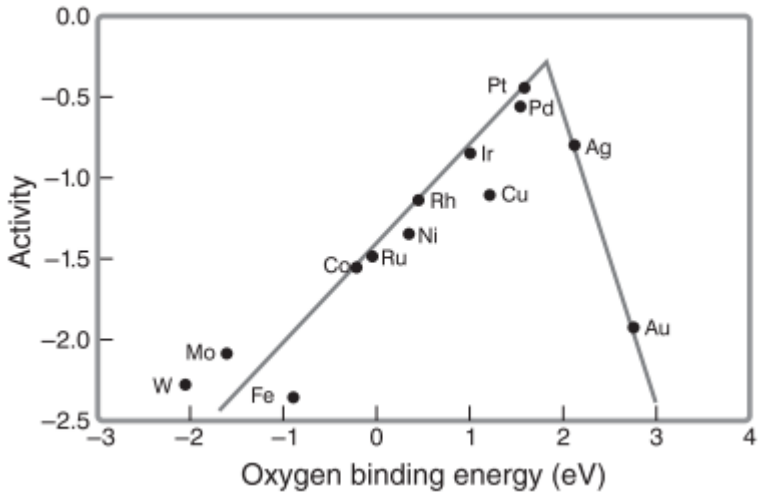

Figure 1-15 The volcano plot comparing the catalytic activity of various materials versus the adhesion strength with oxygen [29]

The second kind of overvoltage encountered in the fuel cell operation is represented by the linear drop in voltage as the current increases in Figure **1-14**. This drop is called Ohmic overvoltage which occurs due to the resistance against the flow of charged species (electrons and ions). Charge transport is driven by a voltage gradient (or conduction) and obeys Ohm's law. While each component in the fuel cell has a certain resistance (Figure 1-16), the major contribution to the Ohmic overvoltage comes from the electrolyte resistance to ion conduction. Ion conductivity, even in good conductors, is 4 – 8 orders lower in magnitude than the electron conductivity in metals [35]. Therefore, the electrolyte development is the main area of research to enhance the fuel cell efficiency by decreasing the Ohmic overvoltage.

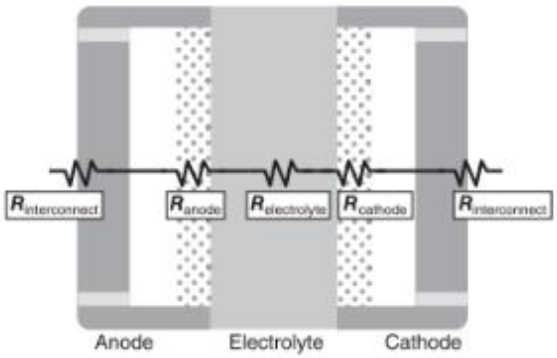

Figure 1-16 The various fuel cell component resistance [35]

The third kind of fuel cell overvoltage is the voltage drop due to mass transfer from the electrolyte bulk into near the electrode surface and inside the electrode structure. Additionally, transferring the products from the reaction sites into contributes to the mass transfer losses. Poor mass transfer leads to performance loss due to reaction depletion or product clogging. It is also called concentration loss. Two mechanisms of mass transfer are encountered in this context. Inside the flow channels of the fuel cell, the mass is transferred from the electrolyte bulk by the action of convection while the diffusion is the working mechanism to transfer the uncharged species inside the gas diffusion layer (GDL) until reaching the catalyst layer (CL). While the diffusive flow is controlled by the concentration gradient in the GDL, the convective flow in the flow channels is impacted by the fluid flow which is characterised by Reynold's number as laminar in most fuel cell cases.

There is a limiting current density (j_L) which is the current of zero-concentration at CL. The limiting current density is expressed by:

$$j_L = nFD^{eff}\frac{C_R^o}{\delta} \quad \textbf{(1.10)}$$

Where, C_R^o is the bulk concentration, D^{eff} is the effective reactant diffusivity within the catalyst layer, and δ is the electrode GDL thickness. Fuel mass transport structure considers the even distribution of reactant ensuring high C_R^o, minimising δ, and maximising D^{eff}. The concentration overvoltage impacts both the Nernstian voltage and reaction rate and in both cases is expressed in terms of the limiting current density (j_L) according to both:

$$\eta_{conc,Nernest} = \frac{RT}{nF}\ln\frac{j_L}{j_L - j} \quad \textbf{(1.11)}$$

And,

$$\eta_{conc,BV} = \frac{RT}{\alpha nF}\ln\frac{j_L}{j_L - j} \quad \textbf{(1.12)}$$

Considering j is always smaller than j_L, both equations could actually be generalised in one term:

$$\eta_{conc} = C.\ln\frac{j_L}{j_L - j} \quad \textbf{(1.13)}$$

Where C equals $\frac{RT}{nF}(1 + \frac{1}{\alpha})$.

1.10 The scope of this project

In the context of growing climate change crises, worldwide population, and energy demands, direct alcohol fuel cells (DAFCs) have a strong potential to supply various energy needs without harming the environment with significant emissions. The advantages of DAFCs include their high energy density. Table 1-3 demonstrates that liquid alcohols such as methanol and ethanol possess a much higher volumetric energy density compared to hydrogen. Besides, DAFCs have a compact configuration and do not need a sophisticated infrastructure as the H_2-fed fuel cells. Yet, it could be understood – by looking at the individual fuel OCV values – that alcohol oxidation is in general more difficult than that of hydrogen. The difference, however, in the overall fuel cell OCV is very small when the fuel oxidation OCV is subtracted for the oxygen reduction reaction (ORR) OCV (1.229 V). And yet, the theoretical energy efficiency of DAFCs is much higher than that of H_2-fed ones. That is why the losses associated with ORR represent around 80% of the losses encountered in PEMFCs.

Table 1-3 Technical data of various fuel oxidation in fuel cells (Credit paid to [36]**)**

Fuels	ΔG° (kJ/mol)	Theoretical OCV (V)*	Energy density (kWh/L)	Reversible efficiency
H_2	0.0	0.0	180 (1000 psi, 25°c)	83.0
Methanol	9.3	0.016	4820	96.7
Ethanol	97.3	0.084	6280	97.1
2-propanol	186.3	0.107	7080	96.9
Ethylene glycol	8.78	0.1122	5800	99.0

*Theoretical open-circuit voltage (this is for only fuel oxidation and the ORR contribution is neglected for fuel comparison)

Therefore, there is a high potential for ethanol – in particular – as a fuel to be fed into the anode of fuel cell. Such technical gains include that its life cycle is neutral which means the carbon dioxide produced by ethanol oxidation is reabsorbed by the cellulose-containing plants used to produce it. This means it is sustainable and eco-friendly. Secondly, it is less likely than methanol to crossover the membrane due to the larger molecular size and eventually it could be more utilised for electricity production in fuel cell. Also, it is more energetic and safer to handle than methanol. Also, the ethanol liquid state gives to high flexibility for small- and large-scale application to the easy transport.

Chapter 2: LITERATURE REVIEW

This chapter surveys the relevant publications of direct ethanol fuel cells (DEFCs) and the ethanol oxidation reaction (EOR). The role of the catalyst is covered and the support function is explained in detail. Various research efforts concerning the carbon functionalisation are reported. The effect of adding a second metal to Pd or Pt is, also, reviewed. Special attention is given to Ni, Au, Rh, Ir, and Ag. The few research efforts concerning trimetallic catalysts are recorded. At the end, the objectives of this work are briefly stated.

2.1 Direct alcohol (methanol, ethanol, ethylene glycol) fuel cells (DAFCs)

Alcohol oxidation reactions generally are very complex involving several steps and pathways such as adsorption, dehydrogenation, electron transfer, and reactions with OH groups [37]. Direct methanol fuel cells (DMFCs) and direct ethanol fuel cells (DEFCs) belong to direct alcohol fuel cells DAFCs and they could use either acid or alkaline electrolytes [21,23,38]. DAFCs operation could be classified as active and passive. In the active setup, there is separate alcohol reservoir from the cell which is not needed in the passive one (fuel migrates in the cell based on the natural conviction and capillary action). This makes the active DAFCs larger in volume and more expensive than the passive one. Therefore, the active DAFC operation is more reliable by controlling fuel flow rate and temperature and therefore it produces more power. On the other hand, the passive DAFC is advantageous looking at its compact size enabling its application for very small application such as mobile phones [39].

Currently, direct methanol fuel cells are very progressive and attracting attention from industrial firms to supply electrical power for various-size portable applications from mobile phones to fork lifts [36]. That is basically of favourable practicalities of methanol for anode oxidation. One key advantage of methanol is that it is 1-C alcohol making its complete oxidation and CO_2 selectivity very high compared to other higher-C containing alcohols. Also, as was pointed out in Table 1-3 the energy density of methanol (4280 Wh/L) is significantly higher than that of hydrogen. Yet, the current main source of methanol is natural gas and therefore it is not considered renewable [36]. Ethanol, on the other hand, is a promising fuel because it is produced from agricultural and biomass by-products. The CO_2 resulting from ethanol oxidation or combustion is believed to be re-consumed by the plants that were deployed to produce it and therefore the ethanol life cycle is considered carbon neutral. Recently, as well, it has been possible to produce bioethanol from wastes and residues containing various amounts of cellulose [40]. This would bring significant economic and ecological benefits because the raw materials to produce biofuels are sometimes biological wastes, which cause pollution and bring diseases and their disposing is needed and sometimes expensive.

Methanol has been considered, and still is, a promising source as a fuel that could be supplied directly in the fuel cell to produce electricity. However, it is toxic, and could easily crossover the membrane to be oxidised in the cathode instead of the anode [41,42]. The crossover problem greatly harms the fuel cell performance by reducing the fuel utilisation, fast cathode degradation, cell voltage reduction, and extra heat generation [36]. Also, methanol is toxic to humans by ingesting, and slightly by inhalation. After ingestion, it is metabolised in the body producing formic acid and formaldehyde, which cause blindness and other diseases. Although this is not a direct motive to replace methanol with ethanol, it imposes some health hazards for humans who should work with methanol. The big issue for methanol is its high membrane crossover rate without producing a useful electric current. This means methanol oxidation and oxygen reduction both occur in the cathode without generating electric power, which reduces the efficiency of the cell. Another alcohol that has some potential for application in the fuel cell anode is ethylene glycol whose technical specifications - such as energy density and toxicity - sometimes makes it intermediate between ethanol and methanol. Moreover, the presence of an OH group bond to each of its two carbon atoms makes its anode oxidation easier than that of ethanol though ethylene glycol oxidation would still be difficult due the C-C bond. Additionally, theoretically, the oxidation of one ethanol molecule releases 12 electrons while only 6 electrons are released by the oxidation of a methanol one. This implies ethanol, theoretically, is able to produce an electric current as twice as methanol [43,44].

Jablonski *et al.* [45] have found that a periodic short circuit of a working DEFC increases the open circuit voltage (70 mV higher) and power density (6%). Heysiattalab *et al.* [46] have studied the key parameters affecting direct ethanol fuel cell performance and have found that increasing the temperature increases ion conductivity of H^+ ions and enhances the reaction kinetics both in the anode and cathode. They also concluded that increasing the flow rate of ethanol and oxygen and varying the oxygen pressure slightly enhances the efficiency of DEFC. Sairsirirat *et al.* [47] have investigated various molarities of ethanol and found that 7 ml of ethanol in 60 mL of water gives the best performance at room.

2.2 Alkaline vs Acidic Medium

The aqueous-media electrochemical performance prominently is correlated to its pH value. One unit increase in the pH shifts the working potential range by -59 mV according to Nernst equation. Changing the electrolyte from a strong acid to a strong base, the working potential is significantly shifted with -830 mV vs SHE [48]. As a result, the electric field at the electrode/electrolyte interface and double layer structure are holistically changed. Traditionally, the applied electrolyte for low-temperature fuel cell is acidic. The first person to replace the acid with alkaline electrolyte was Francis Bacon in 1950 introducing the alkaline fuel cell (AFC) concept at Cambridge. The first application of basic solution for H_2 fuel cells has been space exploration in the mission of Gemini which supplied a lot of drinking water. The use of alkaline media for fuel cell operation has been proven advantageous over the acid one for the following reasons: 1. The possibility to use less or non-noble metals, 2. Faster redox reaction kinetics and enhanced catalyst stability, and 3. Less corrosive ambient [38][39]. Furthermore, according to Li *et al.* [50] Pt is the only acidic resistant-metal that could be used for alcohol oxidation. Further into the stability issue, Zadick *et al*. [51] have found Pd is more stable in alkaline electrolyte than in acidic one.

Additionally, Wang *et al.* [52] have claimed that the solution pH is a key factor that affects the reaction occurring on palladium surface. While Pd is not active for ethanol oxidation reaction (EOR) in acidic media, it is indeed active, comparatively to Pt, for EOR in alkaline ones [41]. However, there are some problems that appear upon using an alkaline electrolyte. For the particular ethanol oxidation, a progressive carbonation of the electrolyte-electrode-interface occurs due to the production of CO_2 and its potential reaction with water. To a large extent, this is resolved by replacing the liquid electrolyte with an anion exchange membrane that conduct the OH^- species from the cathode to the anode. Another problem was reported by Lafforgue et al. [53] who have studied the

degradation of carbon-supported Pt-group metals in alkaline fuel cells and electrolysers. They have noted that Pt/C in alkaline medium is capable to activate the corrosion of the Vulcan carbon support due to the oxidation of oxygen functional groups.

Table 2-1 shows the different pathways for those reactions of fuel oxidation and oxygen reduction in alkaline and acidic media. In alkaline DEFCs, ethanol and OH^- species are adsorbed on the catalyst surface leading to the oxidation of ethanol. In acidic DEFCs, ethanol is adsorbed on the catalyst surface and is oxidised at higher applied potentials producing H^+ ions that will travel to the cathode through the electrolyte membrane. Hydrocarbons' oxidation is generally slower in acidic than alkaline media. Moreover, the oxygen reduction reaction proceeds in basic solutions much faster than the acid ones. It was found the CH_x species are more difficult to strip in an acidic medium than an alkaline one [54]. The oxidation of hydrogen, methanol, and ethanol releases 2, 6, and 12 electrons, respectively. Therefore, presumably, using ethanol alone in a fuel cell would produce more electricity than hydrogen and methanol. This explains the strong potential of ethanol as an energy source through fuel cell direct application.

Table 2-1 The anode and cathode reactions in cases of using alkaline and acid electrolyte

Fuel Cell	**Alkaline Electrolyte**		**Acid Electrolyte**	
	Anode	Cathode	Anode	Cathode
H_2 Fuel cell	$H_2 + 2(OH)^- \rightarrow 2H_2O + 2e^-$	$\frac{1}{2}O_2 + H_2O + 2e^- \rightarrow 2(OH)^-$	$H_2 \rightarrow 2H^+ + 2e^-$	$\frac{1}{2}O_2 + 2H^+ + 2e^- \rightarrow H_2O$
DMFCs	$CH_3OH + 6(OH^-) \rightarrow CO_2 + 5H_2O + 6e^-$	$\frac{3}{2}O_2 + 3H_2O + 6e^- \rightarrow 6(OH^-)$	$CH_3OH + H_2O \rightarrow CO_2 + 6H^+ + 6e^-$	$\frac{3}{2}O_2 + 6H^+ + 6e^- \rightarrow 3H_2O$
DEFCs	$C_2H_5OH + 12(OH^-) \rightarrow 2CO_2 + 9H_2O + 12e^-$	$3O_2 + 6H_2O + 12e^- \rightarrow 12(OH^-)$	$C_2H_5OH + 3H_2O \rightarrow 2CO_2 + 12H^+ + 12e^-$	$3O_2 + 12H^+ + 12e^- \rightarrow 6H_2O$

2.3 Membrane Electrode Assembly (MEA)

Figure 2-1 demonstrates the membrane electrode assembly (MEA) showing the C-supported Pt catalysts for both the anode and cathode. The proton conducting membrane (such as Nafion) is sandwiched between the cathode and anode catalytic layers (CLs) where the redox reactions occur. The catalytic layers are preferentially very thin to facilitate the mass and charge transfer and maximise the electron conductivity. Then, each CL is backed by a gas diffusion layer (GDL) leading to the current collector. The importance of the GDL stems from its ability to distribute reactant gases to the catalyst layer (CL), improve the electrical contact with the CL, and prevent water flooding near the CL [55,56]. GDL connects the bipolar plates with CLs and facilitates the transport of gases from the from the flow fields to the CLs. The porous and hydrophobic structure of carbon, therefore, is of a significant importance. Also, GDL collects the current. The microporous layer (MPL) is the GDL part facing the CL and it is comprised from carbon black aggregates and PTFE. According to [55], The GDL permeability decreases with the increasing the MPL C content, and 2. The GDL permeability increases with increasing the MPL PTFE content between 20% and 50% due the enhanced porosity as the larger PTFE particles rest in the large pores among the C aggregates. However, the GDL permeability decreases with increasing the MPL PTFE content between 10% and 20% by weight, and though not certain, the apparent reason is the increased MPL thickness and reduced porosity and the lowest GDL permeability was achieved at PTFE 20% load by weight.

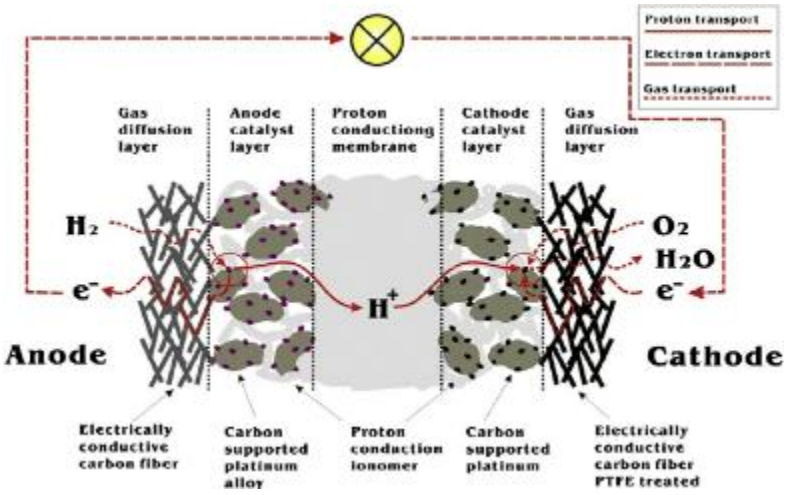

Figure 2-1 The membrane electrode assembly (MEA) and gas diffusion layers (GDL) inside a single fuel cell

Although the fuel oxidation is intended to release useful energy, the reaction, in itself, needs activation energy to occur. That is the reason both reactions need an active catalyst that is capable to reduce the activation barriers and increase the rates of the redox reactions in the anode and cathode

according to Figure 2-2. Here, it might be useful to mention that the active metal particle might be charged during the operation of fuel cells. The charge accumulation on metal particles might be because of poor electrical contact with the carbon substrate or some difficult in the carbon charge transport. The consequence of that the particle will optimise and change its shape during charge transfer step to respond to the increasing free surface energy around it by the accumulating charges. Though this is not solidly proven, there are some observations that support this conclusion and the only way to verify is by deploying more *in-stiu* techniques (such as *in-situ* FTIR and online DEMS) to closely examine the reaction mechanism and define the reaction intermediates and products [17]. The catalyst produces a smaller activation barrier compared to the original uncatalysed reaction and the new activation barrier is called transition state. According to the particular reaction and catalyst, there might be one transition state or multiple ones.

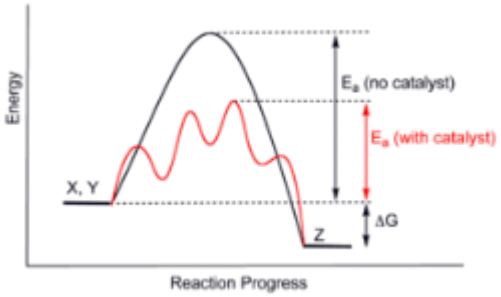

Figure 2-2 The function of a catalyst for a chemical reaction

The function of a heterogeneous catalyst includes physical and chemical steps. The first step is the ability of the catalyst surface to adsorb the different reacting molecules on its active sites. Secondly, a chemical reaction (redox) occurs among the adsorbed reacting molecules. The final step, which is physical, is the catalyst surface let go the adsorbed reaction products on its surface, which depends on the binding energy of those products, and the catalyst surface. In cases of SOFC and MCFC, the high temperature eliminates – or decreases - the need for an active catalyst due to the change in the Gibbs free energy it could make according to Nernst equation. Also, the temperature is inversely related to the activation energy according to the Arrhenius equation:

$$\boldsymbol{k = Ae^{E_a/RT}} \qquad \textbf{(2.1)}$$

Where, k is reaction rate constant, E_a is the activation energy, A is the frequency factor (experimentally determined), R is the universal gas constant, and T is the temperature in K.

2.4 Carbon Support Role

The carbon used as a support for fuel cell electrocatalysts plays a crucial role in the catalytic performance of the electrode. It serves as textural and mechanical support for the metal nanoparticles. Furthermore, it should be stable in acidic and alkaline environments in addition to the corrosion resistance it should have. Also, it should provide high surface area for the dispersion for metal catalyst nanoparticles. Finally, it should be conductive electronically [57–59]. The basic benefits of a support for heterogeneous catalysts are: 1. High specific surface area, 2. Convenient pore structure, 3. Electrical conductivity, and 4. Corrosion resistance [60]. There are unanswered questions in regards to the carbon-based electrodes for energy storage and conversion devices. Some of the common problems are: 1. How to optimise charge/mass transfer, 2. How to enhance the electron transfer kinetics in multiphase boundaries, and 3. How to understand those processes at the recent nanoscale technology [17].

The carbon black with mesoporous structure is of great interest concerning these technical features. That applies to Vulcan carbon (XC72). According to Lazaro *et al.* [58], Vulcan carbon (XC72) is a mesoporous in structure with surface area of 210- to 250 m^2/g and particle size of 30 to 60 nm and is produced by thermal decomposition of some hydrocarbons. Physically, it is constituted from spherical aggregates that agglomerate together [61]. However, a good portion (approximately 30%) of the Vulcan carbon XC72 is microporous [61]. Some metal nanoparticles might be sunken inside those micropores and would show little or no electrochemical activity. The carbon pore size strongly affects the interface between the metal nanoparticles and Nafion® in the catalyst layer in the membrane electrode assembly [62]. Therefore, it is imperative to enhance the textural properties of carbon support to enhance the catalytic activity and stability of the Pd or Pt. Vulcan carbon has an obvious advantage being of the cheapest carbon materials to be used as a support compared to carbon nanofibers, nanotubes and graphene.

The surface treatment of carbon materials in fuel cell application has two main purposes. First, the carbon support materials are hydrophobic, and their functionalisation implies increasing their wettability and consequently facilitating the access of metal precursor into the internal pore structure of carbon during the incipient wet impregnation. Second, the treatment is likely to increase the oxygen functional group content. These functional groups could work as anchoring sites for metal nanoparticles and therefore could reduce the mobility of metal nanoparticles and prevent agglomeration [63]. Some research groups have tried to improve the functionality of XC-72 Vulcan

by acid or gas treatment [64,65] aiming to increase the oxygen functional groups of the carbon support.

Yet, the effect of functionalization is a controversy amongst researchers. Whilst in some cases, the functionalization has led to enhancing the carbon functions; in others, it has reduced the efficacy of the support by having too much oxygenated functional groups that cannot sustain the chemical reaction conditions. Therefore, functionalization treatment is not necessarily always beneficial for the catalytic performance of Pd/XC-72 Vulcan and a compromise should be made to increase the active surface area but not to lose the electronic conductivity of the support consequently. Obradovic *et al.* enhanced the physical and electrochemical properties of carbon black and carbon nanotubes, which subsequently used as a support for catalyst nanoparticles, by acid treatment with HNO_3 and a mixture of HNO_3 and H_2SO_4 [66]. Among their findings is that carbon surface activation by a mixture of HNO_3 and H_2SO_4 is obviously surpassing the single-HNO_3 treatment. On the other hand, the acid treatment, performed by Calvillo *et al.*[63], has had an adverse effect on the textural properties of carbon materials; both the surface area and pore volume have been reduced especially in the severe conditions. An increase in the particle size was detected and attributed to the agglomeration of Pt nanoparticles on the oxidised carbon (conclusion found as well by [58] and explained by the agglomeration of Pt nanoparticles rather than increase in the particle size itself). The authors explained this by the decomposition of the less stable oxygen functional groups during the reduction of metal precursor, and consequently the Pt nanoparticle mobility was enhanced. They also concluded that the higher crystalline grade of carbon support (e.g. nanofibers) would have a strong interaction with the metal nanoparticles producing smaller particle size whereas the lower crystalline grade (Vulcan) would have a weak interaction with the metal producing globular and bigger particle size. Lazaro *et al.* [58] have treated Vulcan carbon with HNO_3 (diluted and concentrated) and a mixture of HNO_3 and H_2SO_4 at room and boiling temperatures for 0.5 and 2h. Their major conclusion is that the oxidation treatment has destroyed the texture of carbon, especially in the severe treatment conditions, which was noticed by SEM and the decrease in BET surface area. In controversy to that, the pore volume has increased in all cases of oxidation treatment. The surface area decrease has also been confirmed by Carmo *et al.*[62] and Jongsomjit *et al.* [67] after treating Vulcan carbon and MWCNTs with H_2SO_4 and a mixture of HNO_3 and H_2SO_4, and yet, both groups have noticed enhancement in the catalytic performance of the functionalised carbon as a support in DMFC and DEFCs.

Yang *et al.* [68] have compared the effects of ultrasonic and reflux acid activation of multi-wall carbon nanotube (MWCNT) and their consequent impact on the electrochemical activity of the supported PtRu catalyst for methanol oxidation. They found the ultrasonic-treated MWCNTs led to higher N_2 sorption and electrochemical active surface areas than the raw and reflux MWCNT. A similar conclusion about the ultrasonic treatment of carbon nanotubes has been found by Murphy *et al.* [69]. Also, the sonication with acid (H_2SO_4 and HNO_3) was found to enhance the electrochemical active surface area and increase the electrochemical mass activity [67]. The 24h-HNO_3 reflux treatment of XC72 seems to have enhanced the Pd/C voltammetry results extensively according to Moares *et al.* [64] though the functionalisation effect on the texture and physical properties seems ambiguous, especially that the activity of binary PdNi and ternary PdNiSn supported on commercial XC72 were better than those on the activated one. Also, the HNO_3 treatment has generally decreased the electrochemical active surface area for the catalysts they synthesized. Silva *et al.* [61] have investigated the textural changes of Vulcan carbon and biocarbon (Eucaliptus grandis wood) after physical treatment with CO_2 at 800ºC for 2h. Their activated biocarbon has very high surface area (787 m^2/g) compared to the activated and non-activated Vulcan (XC72), 230, 216 m^2/g. However, the treatment has resulted in decreasing the pore size in both biocarbon and Vulcan carbon (6.88, 2.41 nm) below the non-activated Vulcan one (8.20 nm). Comparing the three carbons as a support for Pt and PtSn catalysts for ethanol oxidation, the authors have found that the biocarbon-supported PtSn has given the best electrocatalytic performance (compared to PtSn/C and PtSn/C_{CO2}) while the single Pt supported on activated Vulcan XC72 has given the top catalytic activity (compared to Pt/C, Pt/biocarbon).

Other groups have replaced the Vulcan XC-72 by other carbon materials like the carbon nanofibers and nanotubes [70–75]. Although the multi-wall carbon nanotubes and carbon nanofibers have achieved better performance compared to the XC-72, the enhancement is not huge making the Vulcan carbon still feasible option as the most common and affordable support for noble metal nanoparticles synthesis. Carbon activation could be attained either physically or chemically. In the physical route, the raw material is carbonized in an inert atmosphere followed by activation using CO_2 at high temperature. In the chemical route, the precursor is treated with some chemicals which act as dehydrating agents [57,76] In their review, Bianchini *et al.* [77] have concluded the use of MWCNT has been proven to perform a better *j*ob than Vulcan carbon as a support for the Pd nanoparticles for fuel cell electrocatalysts. The claimed reason for the enhancement is the smaller size and better dispersion of Pd nanoparticles in case of Pd/MWCNT than Pd/C. However, it should be mentioned the Vulcan carbon is cheaper than MWCNT, which might raise the fuel cell electrode cost when

added to the noble metal. They also reported the hydrofluoric (HF) acid treatment of MWCNT has had an excellent impact on the Pd/MWCNT$_{HF}$ by doubling the electrochemical activity compared to Pd/MWCNT without HF treatment. They explained the improvement that the enlarged micropores on the HF-treated micropores, can serve as anchoring sites for Pd nanoparticles and can prevent their coalescence and unfastening from the support surface. Kim *et al.* [78] studied the effect of mild acid treatment on the carbon black as a support for Pt catalyst for oxygen reduction reaction. They found the acid functionalisation has increased the electrochemical surface area, but the acid treatment has led to particle agglomeration of the catalyst.

Table 2-2 Parametric impact of carbon physiochemical characteristics

Carbon characteristic	Physical and electrochemical impact
Surface area	The high surface area enables wide dispersion of metal nanoparticles increasing the total number reaction sites and rate (*i.e*, electric current)
Developed porous structure	Enables the convenient housing of the metal nanoparticles, prevents agglomeration by anchoring metal nanoparticles, and makes the metal nanoparticles more accessible to reactants and easier to remove reaction products and intermediates. Thus, a quicker reaction and higher rate are obtained.
Crystallinity	The crystalline nature of the support makes it more conductive for electrons during the reaction. Also, it makes the support more likely to conduct small metal nanoparticles during the synthesis and control the particle growth. Eventually, smaller particles are prepared. With a crystalline support, therefore, a higher electric current is expected.
Functional oxygen groups	Increases the water uptake and decreases the carbon hydrophobicity. Therefore, the metal salt precursors are more likely to stay within the pores during the synthesis. Enable the synthesis of smaller metal nanoparticles.as they could be broken and replaced by smaller metal nanoparticles.

Table 2-2 summarises the parametric effects of carbon characteristics on the electrocatalytic performance. Regarding electrochemical power generation purposes, the porosity of the used carbons is a major concerning technical aspect. The technical specifications of the carbon vary based on the

application. For example, the high surface area is the most concerning property of the carbon for the supercapacitor. On the other hand, the literature informs that the carbon support applied should possess a mesoporous structure and high surface area [58,61,79–83]. The high surface area enables the wide dispersion of the metal nanoparticles which maximises the potential for reactions to occur. The mesoporous structure is necessary to facilitate the transport of reactants onto and products from the catalytic sites. Above that, also a large space around the metal particles is necessary to enable the three-phase (gas-liquid-solid) reaction. However, the significance of the pore size and porous structure development was not addressed in the literature. It is usually stressed that a mesoporous structure is necessary but that means the pore size could be anything between 2 nm and 50 nm. It is not clear if two mesoporous carbons – one with 10-nm and another with 20-nm pore size – would do the exact functional role as a support.

2.5 Synthesis Methods

There are various methods applicable to produce C-supported metal nanoparticles such as chemical reduction, co-precipitation, polyol, microwave, hydrothermal, and microemulsion [84]. The synthesis methods could be classified as physical like sputtering, ion- and electron-beam deposition and laser ablation, hydrothermal ones, electrochemical deposition, and chemical reductions [3]. It is worthy to try various synthesis methods to produce Pd nanoparticles for catalytic applications as the variation in synthetic methods will produce different nanoparticles with varying characteristics. The difference could be in the shape or size of particles or the particle crystal structure all of which impact the electrocatalytic activity of the prepared sample. For example, decreasing the particle size would result in exposing more low-coordinated atoms on the surface to adsorb reagents. It is always beneficial to deposit the noble metal nanoparticles on an electron-conductive support [85]. The polyol method is a famous for the synthesis of metal nanoparticles by chemical reduction of the metallic salt precursors. In this method, a high-boiling-point polyol such as ethylene glycol is used as a solvent and reductant. Hei et al [86] have use the polyol method to prepare monodispersed nanoparticles of Pt, Rh, and Pd involving the ethylene glycol and polyvinylpyrrolidone (PVP) as a reductant and stabiliser, respectively. They have found the particle size increases with increasing the metal precursor concentration. Lazaro *et al.* [82] have compared ethylene glycol, fomic acid and sodium borohydride as reduction agents for Pt nanoparticles supported on carbon nanocoils. They have found the smallest particle size produced by formic acid while the largest one by ethylene glycol.

Furthermore, Adekoya *et al.* [87] have prepared PdAg nanocomposite using PVP as a stabilizer and have compared the influence of using sodium borohydride, ethylene glycol (160°C,3h), diethylene glycol (200°C, 2h), glycerol (160°C,2h), and pentaerythritol (90°C,2h) as a reducing agent. The PdAg by pentaerythritol has given particle size of 11 nm and core (Ag)/shell (Pd) structure. The particle size distribution in case of using diethylene glycol was found much broader with particles as small as 9 nm and others as big as 35 nm. The average particle size of the ethylene glycol-prepared-PdAg was found to 16 nm. The alloy structure is weaker in case of using glycerol as a reductant with Ag concentrated dark spots (15 nm) and Pd brighter conjugates (7 nm).

2.6 Ethanol electrooxidation in fuel cells

The challenge facing ethanol direct oxidation is the slow reaction kinetics of ethanol entailing different reaction pathways, intermediates and products and poisoning species. One main challenge for the oxidation of ethanol is the various reaction pathways the reaction could pursue. While the optimum benefit, from a DEFC performance perspective, is attained when ethanol is completely oxidised producing CO_2 and releasing 12 electrons, the prevailing end product is acetic acid releasing only 4 electrons [54]. While the final product of methanol oxidation is CO_2, it is acetic acid in case of ethanol oxidation. Thus, from a full oxidation perspective, methanol oxidation is easier than ethanol one. This is a major challenge for the fuel cell researchers because even the most active catalyst based on Pt are not likely to break the rigidly stable sp^2 C-C bond of ethanol molecules [88]. That is why the reactions more likely to occur are the breaking of sp^3 bonds of C-H and O-H leading to acetic acid which is a dead end for the reaction.

The ethanol oxidation reaction (EOR) is a complex multistep reaction which goes through two main pathways in parallel (C1- and C2-pathways) according to Shen *et al.*[89], Tsui *et al.*[43], and Liang et al [90]. According to Wang et al [52], the C1 pathway leads to formation of CO_2 by releasing 12 e^- while the C2 one leads to acetic acid by releasing only 4 electrons and consequently losing 2 thirds of the efficiency (Figure 2-3). The C1 pathway in Figure 2-3 describes the complete and more favourite pathway for ethanol oxidation reaction, but it is less probable to occur due to the presence of the C-C rigid bond in ethanol molecules. In case of using Pt catalyst, the C1 yield is below 10% while it is less than 5% in case of Pd catalyst [52]. In the C1 pathway, the ethanol molecule is adsorbed on the catalyst surface. Then, it is oxidised and decomposed into species of CH_x and CO_{ads}, which are oxidized to CO_2 at further higher potentials.

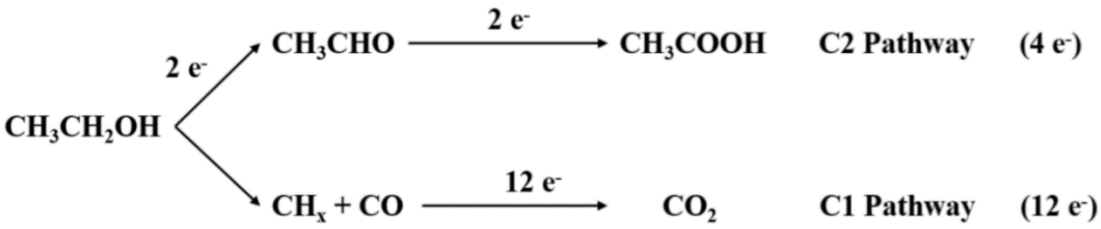

Figure 2-3 Schematic layout of the ethanol oxidation reaction pathways

The C2 pathway represents the incomplete and undesirable, but actual, reaction pathway for EOR, which results in the formation of acetic acid - which cannot be further oxidized to CO_2 [91]. Moreover, Monyoncho et al [92] have compared the electrooxidation of ethanol and acetic acid on Pd/C in alkaline electrolyte and as expected, the acetic acid electrooxidation on Pd produced zero electric current. That means the catalyst was unable to cleave the C-C double bond in acetic acid molecules. In the C2 pathway, ethanol is oxidized to acetyl or acetaldehyde, which is subsequently oxidized to acetate at higher potentials meaning an overall decrease in the generated electricity.

It is usually agreed during EOR there are three intermediates involved, which are acetyl (CH_3CHO_{ads}) through the C2 pathway, poisoning intermediates CO_{ads} and CH_x species through the C1 pathway. Indeed, the CO-tolerance is an advantage of Pd-based over the Pt-based catalysts according to Antolini [41] and Beyhan *et al.* [93]. The same finding has been confirmed about formic acid oxidation on Pt and PtPd catalysts regarding the CO_x tolerance [94]. Moreover, Capon et al [95] noted that Pd/C does not give good performance for methanol oxidation due to the difficulty associated with adsorbing the negatively charged C atom into the Pd sites since Pd has a saturated valence electron structure $4d^{10}$. Additionally, the Pd is 200 times more abundant than Pt and therefore it could clearly reduce the fuel cell construction cost. Liang *et al.*[90] have argued that the dissociative adsorption of ethanol on Pd electrode proceeds fast while the slow step is to remove the adsorbed ethoxy species by the OH_{ads} on the catalyst surface according to the authors. Also, Zhang *et al.* [96] have studied EOR on Pd/C surface by applying the electrochemical impedance spectroscopy (EIS). They have found that the total impedance of EOR decreases by increasing the applied potential from -0.6 to -0.1 V. From -0.1 to 0.1 V, they have found that the impedance appears in the 2nd quadrant – not the first – due to the effect of charge transfer resistance (R_{ct}).

2.7 Pd ethanol oxidation

Palladium and platinum share, to a good extent, many physical and chemical properties such as the *fcc* crystal structure, atomic size, same periodic table group, d-block nature, melting point, oxidation states, electronegativity, ionisation energies, and Van der Waals forces. The Pd reserves, however, are much more than those of Pt which gives Pd an economic advantage [41]. Pd has recently emerged as a more abundant Pt-alternative metal to catalyse ethanol oxidation in alkaline media. Although Pd and Pt are very similar physically, the former is at least 50% more abundant [41]. Pd is also more tolerant for poisons and capable to generate OH at lower applied potential than Pt though Pt is more active for C-C bond breakage than Pd [1]. In their study, Monyoncho *et al.* [92] have combined both the infrared reflection absorption spectroscopy and DFT calculations to investigate the EOR mechanism and final products on Pd surface. Figure **2-4** shows the 5 oxidation steps (losing one electron at each) vs the reaction energy according to that study.

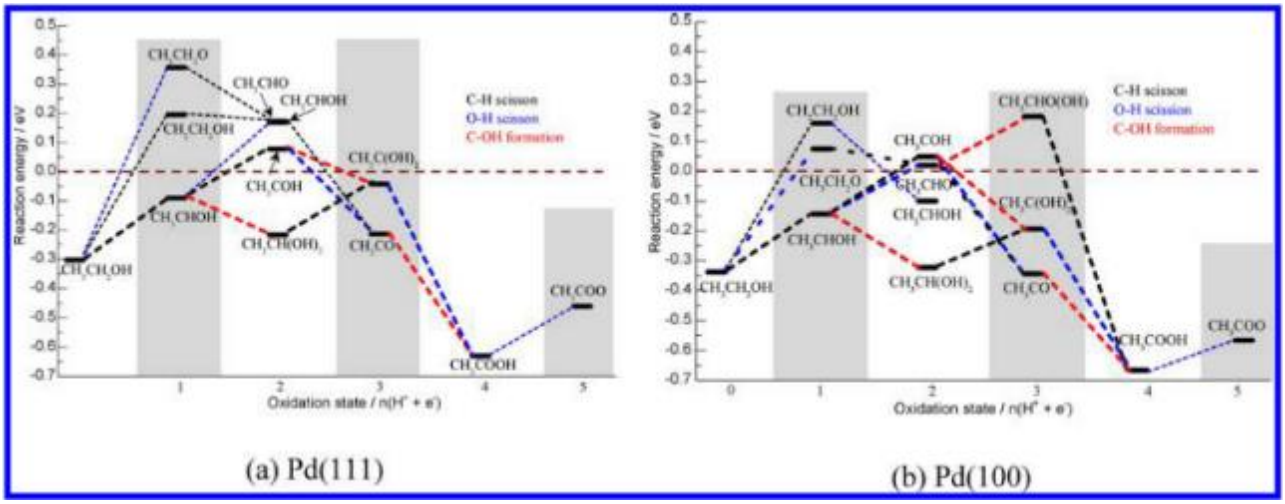

Figure 2-4 DFT calculations of ethanol oxidation reaction pathways and steps on Pd (111) and (100) facets (credit paid to [92])

The very low negative energy of CH_3COOH (and CH_3COO^-) is an indicative of their high chemical stability and therefore they are unlikely to be oxidised on the Pd surface producing CO_2. The main finding is the CH_3CO at oxidation step 3 could have a pivotal role by either producing the more stable CH_3COOH or if a further activation potential is applied (0.9 eV on Pd (100) or 1.4 eV on Pd (111)), it could split the C-C bond and produce C1 fragments. Moreover, the authors concluded the C-C bond could be broken at the second oxidation step but with applying a higher activation potential than the CH_3CO. Torrero et al. [97] have found that the C-C bond cleavage on Pd. PdNi, and PdRu occurs at low overpotential (<30 mV) while acetate is the main product at high overpotentials (>400 mV). Unfortunately, at lower applied potential, the oxygen species generated is not big enough to

remove the CO species adsorbed into the catalyst surface and therefore the current produced is quite small.

2.8 Bimetallic catalysts

Bimetallic NPs have shown a strong potential for many applications due to their unique optical, magnetic, electronic and above all catalytic properties. Their superiority is attributed to the favourable modification in morphology (size, shape), microscopic structure (alloying, core-shell), and electronic configuration (charge transfer, orbital hybridisation) [98]. The catalytic performance of Pd could be enhanced by adding a 2^{nd} metal as a co-catalyst. Adding a co-catalyst metal into Pd or Pt has been proven beneficial for ethanol oxidation in fuel cells. The main functions performed by the second metal are: 1. To activate water and generate oxygen species at a lower applied potential that will facilitate the oxidation and removal of reaction intermediates and liberate catalytic sites, 2. To modify the electronic configuration of Pd so that the adsorption/desorption characteristics of the metal-adsorbate are enhanced, and 3. To modify the geometry of Pd such as particle size and shape, interparticle distance and crystal orientation. Yet, the challenge remaining is the weak alloy formation due to the separative segregation of metals due to difference in cohesive and surface energies of the constituent metals and due to interaction with the support [41].

2.8.1 PdAu catalysts

Yuan-Yuan Feng *et al.* have used the aqueous $NaBH_4$ reduction of metal precursors, K_2PdCl_4 and $HAuCL_4$, to prepare C-supported PdAu NPs supported on C with various Pd/Au ratios (0.1 – 1.5) [99]. All of the PdAu catalysts have shown alloy structure proven by the only one XRD phase with a noticeable shift of the Pd peaks towards Au peaks following the Pd/Au ratio. Their XPS measurement prove the surface is enriched in Pd while the bulk is Au-enriched. The potential reason for this is the Au precursor reduction potential (1.0 V vs NHE) which is higher than Pd one (0.59V) and therefore the NP core is enriched in Au rather than Pd. Moreover, the Au surface energy is 1.6 J/m^2 while that of Pd is 2 J/m^2. That suggests Au tends to segregate into the core while Pd prefers segregating in the surface. The authors also have found the Au incorporation into Pd lattice leads to expanding the Pd unit cell. This expansion results in tensile strain and up-shifting the *d*-band centre which weakens the adsorbate poisons-Pd bond strength.

Shuxian Zhang *et al.* [100] have prepared PdAu NPs supported on MWCNT for formic acid oxidation. They used the aqueous borohydride reduction and produced alloy PdAu catalysts with single XRD phase intermediary between the Pd and Au phases. The Au has promoted the Pd electrocatalytic activity and stability for formic acid oxidation according to the authors. Adrian Geraldes *et al.* [37] have used the electron beam irradiation to prepare Pd, Au, and PdAu NPs supported on carbon for ethanol electrooxidation. The XRD pattern of PdAu shows two separate phases of Au and Pd which suggest the applied method is not suitable for PdAu alloy NPs. Furthermore, the XPS measurements shows a higher Au concentration than the nominal one which corporates the separation of Pd and Au NPs in PdAu/C. Liu et al [98] have found that adding Pd to Au shifts the Au 4f to a lower binding energy values implying electron transfer from the Pd into Au. Also, the smaller PdAu NPs than Au NPs have resulted in broadening the Au 4f peak. It is noteworthy that adding Au into Pd increase the PdAu particle size further than Pd according to the authors and the more Au concentration increases the bigger PdAu particle size is attained according to the authors. Rather than the commonly applied co-reduction,

W. Zhou *et al.*[101] have applied the successive reduction of C-supported Au first and Pd later to produce Au@Pd core@shell structure and applied it for formic acid oxidation. Pure Au/C does not show an activity for either CO stripping or formic acid oxidation. A similar conclusion was found about Au by Adriana Geraldes [37]. Zhen Yin *et al.* [102] prepared various PdAu with varying Pd/Au ratio supported on carbon using the microemulsion method. Using this method, they have found the PdAu particle size increases with increasing the Pd concentration unlike the previous reported methods [37,98,100,101]. Also, the paper confirms the core enrichment with Au and the surface enrichment with Pd through their XPS and EDX measurement. Moreover, the presence of Au results in less PdO formation due to enhancing the Pd air stability. Due to the large electro-potential difference between Pd and Ni and Au and Ni, Chen *et al.* [103] chose the electrochemical dealloying method from the ternary PdAuNi to prepare unsupported PdAu nanoparticles, while controlling the Pd:Au ratio, and have noticed a shift to lower binding energies with increasing the Au content. This have enhanced the stability of PdAu catalyst as the CO-poisoning species would be weakly adsorbed to the catalytic sites. Similar findings regarding the Au addition effect on Pd alcohol electrooxidation [99,104]

2.8.2 PdNi catalysts

Ni has been proven a beneficial co-catalyst when added to Pd because it could generate OH at lower applied potential and modify the electronic structure of Pd [64,67,81,105–107]. The coexistence of Ni and $Ni(OH)_2$ could enhance the alcohol oxidation on transition metals in acidic and basic electrolytes [77,108]. Also, Feng *et al.* [109] prepared unsupported porous Pd and PdNi catalysts for ethanol electrooxidation. They found that the PdNi has shown an upgraded electrocatalytic performance than the monometallic Pd, and this enhancement is ascribed to the electronic and bifunctional effects of Ni. Zhang *et al.* [107] prepared various-proportion Pd_xNi_y/C catalysts for ethanol oxidation reaction. They found that Ni can refresh Pd active sites promoting the ethanol oxidation and their method, microemulsion, could control PdNi particle size and make efficient contact between Pd and Ni. Due to the improvement that Ni could bring to the Pd electrocatalytic performance, Wei *et al.* [110] have added different proportions of CeO_2 into C-supported PdNi catalysts. They found that 5% addition brought the most enhancements on PdNi performance.

2.8.3 Effect of adding Rh

Rhodium (Rh) is a noble and quite expensive metal compared to both Pd and Pt. Therefore, it is best to be avoided in the fuel cell catalyst design provided a more affordable and similarly performing metal exists. Yet, in this particular application of ethanol oxidation, there is a debate among the researchers about the co-catalytic role Rh could play if added to either Pd or Pt. Some groups have found that adding Rh has increased the CO_2 yield by further attacking the ethanol molecule C-C bond. Others have noted that even Rh is a good catalyst on its own. On the other hand, there are some groups have found that adding Rh does not increase the CO_2 selectivity. Adding Rh to Pd has a potential to modify its electronic structure and therefore change its electrocatalytic activity. A. Masic *et al.* [111] have found the Pd ethanol oxidation performance could be enhanced by adding Rh islands on Pd surface through the electrodeposition method. The 50% coverage of Pd surface with Rh has given the highest oxidation current peak according to the authors. Not only Pd, but some researchers have tried to enhance the Pt electrocatalytic performance by adding Rh [112,113]. The C-C scission on PtSn potential is reported to be enhanced by adding Rh [93]. Piwowar *et al.* [114] have challenged the prevailing thought that the Rh-containing catalysts are substantially more active towards the C-C bond scission in ethanol electrooxidation and therefore the reaction is more likely to proceed to produce mainly CO_2 instead of CH_3COOH by using Rh-containing catalysts. They have investigated the ethanol electrooxidation reaction on unsupported Pt, Rh, and PtRh catalysts prepared by the polyol process. According to the authors, the three catalysts have presented similar yields of CO_2

during ethanol electrooxidation which were much less than the CO_2 yields through the CO oxidation. The opposite effect of Rh on Pt EOR was confirmed by H. Lima *et al.* [115] who noticed higher CO_2 and acetaldehyde yields from EOR on PtRh compared to Pt only. The same conclusion about $PtRhSnO_2$ was founded by [116] who explained the role of SnO_2 to activate water and prevent M-OH formation, Pt to dehydrogenate ethanol, and Rh to break the C-C bond. The same conclusion was obtained by [117–119]. Still, the Rh addition effect debate continues regarding the C-C breaking potential as Zhang *et al.* [120] applied the microwave polyol process to produce Pd/C and Rh/C and have found the latter is more active and stable for EOR through the CA and CV measurements especially the oxidation and reduction peaks are shifted to lower potential with Rh compared to Pd while the current value is similar to Pd.

2.8.4 Effect of adding Ir

In light of recent evidence, adding Ir into Pd during synthesis seems beneficial for the electrocatalytic performance of Pd. A. Masic *et al.* Silva's group [121,122] have prepared PdIr/C nanoparticles with different Pd:Ir ratio and applied them for ethanol and ammonia electrooxidation. While the PdIr with (90:10) gives the best catalytic performance for ethanol electrooxidation, the PdIr (70:30) gives the best electrochemical results for ammonia oxidation. The benefit of adding Ir into Pd has also been verified by [123]. Miao *et al.* [124] have claimed – based on DFT calculations – that Ir has a potential to prevent the formation of acetic acid in ethanol electrooxidation. Along the same line, Cao *et al.* [125] have compared ethanol oxidation on Ir and IrSn vs Pt and PtSn which were all prepared using a mixture of $NaBH_4$ and ethylene glycol. They have found that Ir and Ir based catalysts show higher activity and stability for EOR. Ir was also reported efficient for oxygen reduction reaction [48].

2.8.5 Effect of adding Ag

Yo *et al.*[126] have prepared bimetallic PdAg dendrites with various composition and porous structure. They have tried them for ethanol oxidation and the alloying occurring between Pd and Ag has shifted up the Pd d-band centre leading more tolerance for intermediates and poisons during EOR. In the Ag spectrum also, Li *et al.* [14] have prepared PdAg nanoparticles supported on reduced graphene oxide (RGO) and they have noted an occurring promotion on the ethanol and methanol oxidation on PdAg compared to Pd only. Also, Oliveira *et al.* [127] have prepared PdAg alloys and tested them for ORR and EOR. They have noted both reactions' kinetics are promoted on the PdAg

compared to Pd only whilst the alloys maintained higher selectivity for ORR in presence of ethanol. A similar conclusion about the benefit of adding Ag to Pd was reported [104,128].

2.9 Trimetallic catalysts

The attention being paid to developing trimetallic catalyst configurations for alcohol oxidation in fuel cells is scarce compared to the bimetallic ones. A few attempts have been made to develop trimetallic catalysts and of well-chosen metals and with well-considered proportions. For example, Shen *et al.* [123] have prepared two different catalyst architectures of PdAuIr systems: one using the co-reduction of the three metals (7:7:1) and the other by Cu underpotential replacement deposition with Au which covers one third of the PdIr (7:1) surface. They have found the first configuration is less active than (the difference is 10 mA/cm^2) the PdIr one although the situation is reversed after 3000 CV cycles due to the later-occurring stabilising effect of Au. On the other hand, the second configuration - which includes some Au atoms on the surface of PdIr – has shown almost twice the catalytic performance as that of PdIr. Another attempt was made by Zhang *et al.* [129] who prepared trimetallic PdAgSn supported on MWCNTs and have noticed a Pd-Ag alloying potential and significant enhancement on the Pd ethanol oxidation performance. Aiming to enhance the PdSn ethanol oxidation, Zhu *et al.* [130] have added similar individual quantities of Ag, Ni, and Co and the most beneficial was Ag followed by Ni and finally Co. Both groups of Datta [131] and Wang [132] have noted remarkable promotion could be attained by adding both Au and Ni to Pd for ethanol oxidation. Zhu *et al*. [133] have prepared CNT-supported Pd, PdCu, PdSn, and PdCuSn nanoparticles. The trimetallic has achieved a better electrocatalytic activity for ethanol oxidation.

2.10 Objectives of this work

The objectives of this work could be summarised as follows:

- The literature generally dictates the carbon support necessary for fuel cells should have a high surface area, electronic conductivity, and mesoporous structure. Various carbons seem to meet these criteria which makes the support selection a challenge. Aiming to be able to design better catalysts, those factors are explored by applying 5 different mesoporous carbons to support Pd nanoparticles. The five carbons are Vulcan Carbon (C_v), Carbon nanofibres

(CNF), Activated Charcoal (AC), carbon selectivity1 (C_{s1}), and Carbon Selectivity2 (C_{s2}). C_{s1} and C_{s2} are commercial carbon black samples provided by Cabot Corp and identified as conductivity speciality carbons which have a high surface area and mesoporous structure [134]. The other three carbons are also commercial.

- Also, the acid functionalisation impact on the carbon support performance is a controversial topic amongst researchers. Thus, one functionalisation protocol is chosen and applied on Vulcan carbon to produce functionalised Vulcan carbon (C_{vf}) which is, then, used as a support for Pd NPs and tested for ethanol oxidation.
- Based on the results of the work related to the above objectives, the commercial Vulcan carbon (C_v) was chosen as a support for the subsequent trimetallic catalytic systems. The polyol method is replaced by two other borohydride co-reduction routes to prepare C-supported PdAuNi catalysts. Also, one third method (3-step reduction) is applied to produce core@shell Au@Pd/Ni/C structure. The $NaBH_4$-2-propanol (SBIPP) was chosen to prepare Pd/C monometallic catalyst for comparison purposes with the PdAuNi trimetallic to investigate the effect of adding Au and Ni to Pd.
- The $NaBH_4$-2-propanol (SBIPP) is applied to prepare the trimetallic catalysts of PdRhNi, PdIrNi, and PdAgNi each of which having an atomic metal composition with two atomic ratios which are 1:1:1 and 4:2:1 for Pd:M:Ni, respectively.
- Finally, 6 Ni-free trimetallic Pd catalysts of Pd and two other metals (Au, Rh, Ag, Ir) are prepared for the first time using the SBIPP method with 1:1:1 atomic ratio.
- The ultimate objective of this project to design affordable Pt-free catalysts for activating ethanol oxidation in the DEFC anode. Those ethanol-fed fuel cells have a strong potential to supply energy in the electronics, mobile and transport sectors especially that ethanol is readily mixed with gasoline as a fuel for vehicles in some countries. This means ethanol is compatible with the established fuel storage and transport infrastructure. With finding such active, stable, and cheaper-than-Pt catalysts, the DEFC commercialisation could receive a big boost by gaining attention from community, economic and business institutions.

Chapter 3: INSTRUMENTAL CHARACTERISATION METHODS

In this chapter, the physical and electrochemical techniques of characterisation applied in this project are briefly explained. The physical analyses include X-ray diffraction (XRD), transmission electron microscopy (TEM), energy dispersive X-ray spectroscopy (EDX), thermogravimetric analysis (TGA), X-ray photo-electron spectroscopy (XPS), inductive-coupled plasma optical emission spectroscopy (ICE-OES) and Brauner-Teller-Emrete (BET). For each technique, the theoretical principle is explained in addition to the identification of equipment and operational parameters used in this study. The electrochemical ones include cyclic voltammetry (CV), chronoamperometry (CA), Tafel polarisation, and electrochemical impedance spectroscopy (EIS). Once more, the usefulness of each is highlighted and the operational conditions. One type of 3-electrde system was used to perform the electrochemical evaluation. The synthesis methods are not covered in this chapter but are stated individually in the respective following chapters. The author has performed the techniques of XRD, TEM, TGA, EDX, BET, CV, CA, and EIS on his own. The paid techniques are XPS and ICP-OES.

3.1 Physical Characterisation

3.1.1 X-ray diffraction (XRD)

X-ray diffraction (XRD) is used to elucidate crystal structure of the prepared catalyst powder. Figure **3-1** shows the theoretical principle and setup scheme of XRD. To generate X-rays, high-energy electrons should hit a solid/powder surface, some inner-shell electron will be excited to a higher energy state leaving a hole in its original position in the inner shell. This hole is filled by another electron from an outer shell and as that 2nd electron leaves it is position and falls towards the inner shell, it releases X-ray photons with specific energy [135,136]. For example a K-shell hole could be filled with an electron from the L (Kα X-ray) or M (Kβ X-ray) one. Being closer to the K shell, the L electron is easier to fill the K hole than the L one. Thus, the Kα radiation intensity is higher than the Kβ radiation. Thereafter, the produced X-rays are driven to the sample to be analysed. Like visible light, X-rays are electromagnetic radiation but with a much shorter (5000x) wavelength. When an incident X-ray beam- coming from an X-ray tube - hits a solid sample, every atom acts as a centre of scattering for the incident beam and emits a diffracted wave. The scattered waves interfere with one and when this happens constructively (in phase or the order *n* is integer), they produce a diffracted beam detectable by the detector [83]. When the X-ray waves are out of phase or *n* is not integer, they interfere destructively and cancel one another.

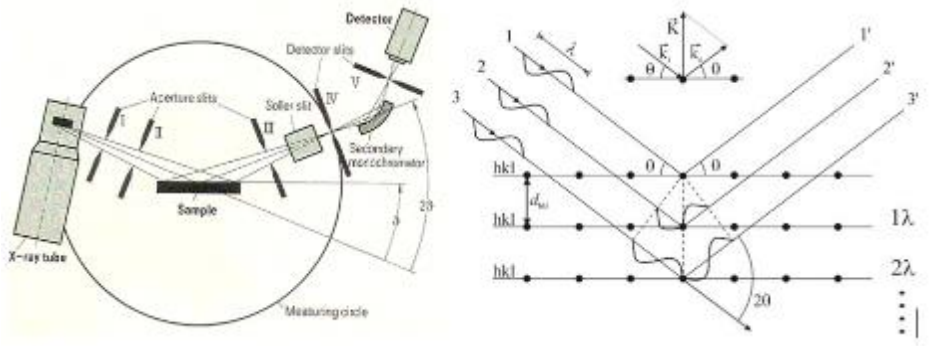

Figure 3-1 Machine setup and principle of X-ray diffraction analysis and Bragg diffraction by crystal planes[135]

The path difference between the initial and diffracted beams – that are in phase – equals $2dsin(\theta)$, where d is the interplanar distance and θ is the diffraction angle. In this work, the Bruker D2 Phaser is used to perform powder XRD operating at 10 mA and 30 kV. It uses a monochromatic Cu Kα radiation (wavelength = 1.54 Å). The scan rate applied is 2°/min. The Bragg's law is used to calculate the atomic spacing of Pd. Ni filter was applied to filter out the non-Kα radiation.

$$\boldsymbol{n\lambda = 2dsin(\theta)} \qquad \textbf{(3.1)}$$

The lattice parameter (*a*, Å), for a cubic system, is calculated according to:

$$\boldsymbol{a = d_{(hkl)} \cdot \sqrt{(h^2 + k^2 + l^2)}} \quad \textbf{(3.2)}$$

It is noteworthy that not all crystal planes are detectable by XRD due to the diffraction intensity even if the Bragg conditions are maintained. While the X-ray wave is scattered by individual atoms in a crystal, the diffraction intensity is controlled by all scattering events from other atoms. Moreover, it is the electron in an atom that scatters the X-ray wave - not the atom itself or nucleus – in all directions. The scattering process polarizes the incident X-ray wave. As each atom contains many electrons round the nucleus, the scattering intensity in one certain angle, is less than the sum of all electrons in the atom due to destructive interference [135]. The structure intensity factor F could be calculated according to the number of atoms per unit cell, their respective locations, and the atomic structure factor *f* according to the following equation:

$$\boldsymbol{F_{hkl} = \sum_{n}^{N} f_n exp[2\pi i(hu_n + kv_n + lw_n)]} \quad \textbf{(3.3)}$$

The usually detectable planes for the metal *fcc* structure are (111), (200), (220), (311), and (222).

Moreover, the crystallite size (nm) could be calculated using Scherrer equation:

$$\boldsymbol{\tau = \frac{K\lambda}{\beta \cos(\theta)}} \quad \textbf{(3.4)}$$

Where, τ is the mean size of the ordered (crystalline) domains, which may be smaller or equal to the grain size (nm), K is a dimensionless shape factor, with a value close to unity (0.9), λ is the X-ray wavelength (1.54 Å), β is the line broadening at half the maximum intensity (FWHM), and Θ is the diffraction angle in degrees.

The XRD is useful because: 1. It shows the crystalline facets of the constituent materials, 2. For multimetallic system, it informs the of potential of alloy formation between the individual metals by checking the diffraction positions of diffraction peaks, 4. It estimates the crystallite size by applying Scherrer analysis (and therefore compare between different catalysts), and 5. It could calculate the lattice constant which explains whether or not lattice expansion/contraction has occurred. There is a

number of error sources, however, associated with the XRD crystallite size. The crystalline peak broadening from contributions of 3 different elements: the crystallite size, instrument-related, and microstrain. Therefore, the peak width applied in Scherrer analysis does not necessarily reflect the true size of crystallites but the microstrain and used instrument could contribute to it. Adding to that, the peak broadening increases with increasing the diffraction angle. The instrumental peak width should be minimum in case of the larger crystallites and vice versa. The microstrain results from non-uniform lattice distortions, dislocations, antiphase domain boundaries, and grain surface relaxation.

3.1.2 Energy Dispersive Spectroscopy (EDX) in SEM

The scanning electron microscope (SEM) is useful to examine the surface of a sample at the micro scale and it has the advantage of higher resolution compared to light microscope (10 nm SEM vs 200 nm LM). SEM applies an electron beam with voltage (5-30kV) – travelling in vacuum - on the sample surface. The electron beam does not pass through the sample but interacts with the sample surface in an interaction volume (less than the sample's thickness), which depends on the sample density (atomic number) and accelerating voltage. The higher the atomic number (Z), the smaller the interaction volume is. For example, the interaction volume (or beam diffusion distance) of a sample containing only heavy metals such as Pd or Pt is bigger than that of a sample containing only light elements such as carbon provided all the operational parameters are the same. In this project, the samples are usually a mixture of heavy metals and carbon which contains functionalised groups (of O, N, H atoms) on its surface. Therefore, the interaction volume could be presumed intermediate due to the impact of its constituents and image contrast is noted due to the atomic number difference. Another important parameter to the interaction volume is the accelerating voltage; increasing the accelerating voltage increases the beam power to penetrate the sample and travel a deeper depth. Low-energy secondary and high-energy backscattered electrons are produced from the electron-matter interaction in addition to other types of signals as shown in Figure **3-2**. In addition to imaging the sample surface at higher magnification than the light microscope, the interaction of the electron beam with the samples generates X-ray from below the surface whose signals are characteristic of the chemical elements present in the sample [137]. The X-ray signals are produced from the sample below the region where backscattered electrons are emitted. It should be mentioned that the catalysts prepared in this work have a very small particle size of 2-5 nm (less than a half of the SEM resolution) for the metals and 50 nm for the carbon. Therefore, the SEM conventional imaging capacity is not helpful for imaging the particle surface and that is why transmission electron microscopy (TEM) is

applied. However, the EDX attached to the Jeol 60100 SEM was found a useful tool for the quantitative chemical analysis and getting elemental distributional maps in this project.

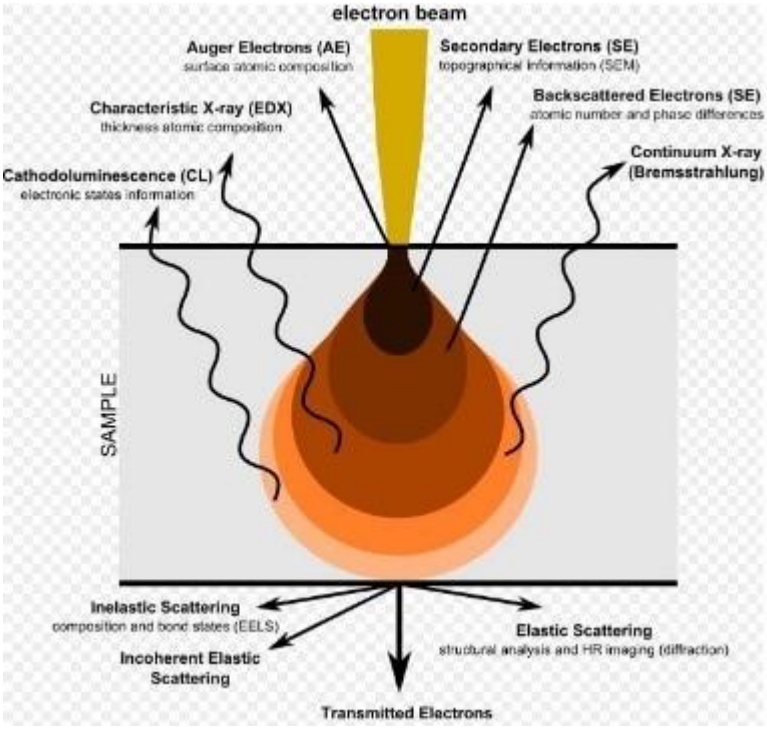

Figure 3-2 SEM electron beam-matter interaction volume and the different emitted signals

To prepare the samples, 5 mg of each catalyst powder were sonicated in 2 mL of ethanol for 1h. Meanwhile, a double-face carbon tape circular piece was glued into a stainless-steel stub. After sonication, 80 µL from the sonicated catalyst suspension were drop-casted on the carbon tape and left a while to dry out. Then, another 80 µL were drop-casted and this was process was repeated one third time. This method produced a uniform-thickness sample, which would be less than if the raw powder were spread on the carbon tape directly. The sample is magnified to 5000x. The spot size is kept high (>70) as it is beneficial for detecting more X-ray signals. EDX quantitative analyses and elemental maps were recorded at 20 kV and 10 kV. The reason for using two voltages is to change to the diffusion distance of the electron beam into the sample. Thus, the elemental composition could studied at different depths from the surface.

3.1.3 Transmission Electron Microscopy (TEM)

Electron microscopes generate images of material microstructure with a much higher magnification and resolution compared to light microscopes due to the approximately 10,000-times shorter wavelengths of electron waves compared to the visible light. Further to that, the TEM resolution (0.05nm) is 200x smaller than the SEM one (10 nm). Therefore, TEM is more suitable for photographing the catalyst surface prepared in those work whose particle size is close to 5 nm. Moreover, if aberration is corrected, the resolution of TEM could reach 0.1 nm [136,138]. A transmission electron microscope contains an electron source, condenser lens, specimen stage, objective lens, projector lens. The lenses are electromagnetic not glass like in light microscopes. Figure 3-3 shows the main differences in the components of SEM and TEM. The transmission electron microscopy samples are much thinner than the SEM ones. Furthermore, the TEM electron beam is more energetic (100-200kV) than SEM. Due to the TEM small thickness of sample and high-voltage of electron beam, the electron beam passes through the sample as shown in Figure **3-3**. Unlike SEM, the TEM beam interacts with both the surface and bulk of a sample.

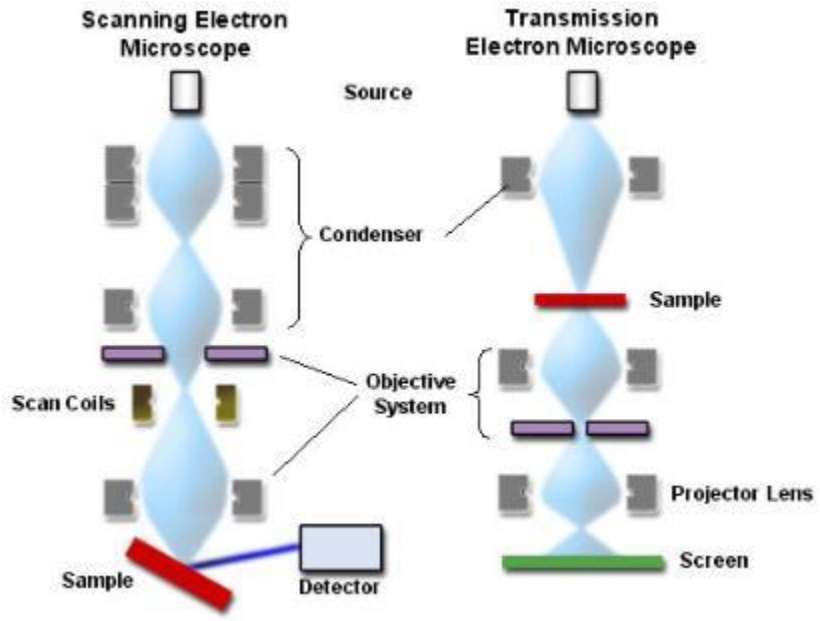

Figure 3-3 Systems of SEM vs TEM

The TEM illuminates a thin sample with a high-energy electron beam, which passes through the sample and gives information about the surface morphology, particle shape and size, and particulate dispersion. Having this kind of information is crucial for understanding the catalyst performance as it is directly impacted by the particle size and shape and the interparticle distance. The smaller particle size would mean more catalytic sites for reaction which ultimately maximises the current drawn. The diffraction mode gives crystallographic information about the sample like lattice parameter and orientation. TEM also studies the morphology of the surface and consequently the dispersion of catalyst nanoparticles on the carbon support. When a high-voltage electron beam is incident on a sample material, the electrons pass

through the sample, which are then detected, and an image of the surface at the nanoscale is obtained though the projection lenses.

To prepare the sample, 5 mg of the Pd/C powder are suspended in 2 mL of ethanol followed by 1-h sonication. Then, 500 - 700 μL were filled in into a spray atomiser. This makes a spray of the slurry and prevent the potentially static aggregation that could occur applying the traditional methods. The Cu grid was hold-up inside a fume-cupboard and facing the slurry spray coming from the atomiser which was manually pressed twice only. Then it was left to dry for at least 3h. The surface morphology was examined by means of transmission electron microscopy (TEM) using Phillips C100 microscope operating at 100kV and using LaB6 filament. Although this equipment has a small resolution, the below-average-100 kV voltage could hinder its imaging capacity occasionally.

The % dispersion (N_S/N_T) is the ratio of the metal atoms on the surface to the total loaded metal atoms in the catalyst. It could be estimated using the Klink's equations [139]:

$$N_T = \frac{2\pi}{3}\left(\frac{d}{a}\right)^3 \quad \textbf{(3.5)}$$

$$N_T = \frac{10}{3}l^3 - 5l^2 + \frac{11}{3}l - 1 \quad \textbf{(3.6)}$$

$$N_s = 10l^2 - 20l + 12 \quad \textbf{(3.7)}$$

Where, N_T is the total number of atoms, N_s is the number of surface atoms, l is the number of layers, a is the lattice parameter in nm, and d is the particle size in nm.

3.1.4 Thermogravimetric Analysis (TGA)

Material properties could be changed following changing its temperature which is known as thermal events. The properties that could be changed include mass, dimension, phase, and mechanical behaviour. For instance, Fe *fcc* structure is converted into *bcc* structure at 910°C which is called solid phase transformation. By increasing the temperature of a solid, the interatomic/intermolecular bonding becomes so weak that certain constituents decompose into the ambient atmosphere. For example, $CaCO_3$ releases gaseous CO_2 and CaO remains a solid at certain temperature range [140].

Glass transition occurs in non-crystalline solids leading to rubber. Thermogravimetric analysis (TGA) is mainly used to study the thermal decomposition of a solid by increasing temperature applied on a sample in a thermobalance. It could be applied in an isothermal mode or scanning mode. The thermal events expected are moisture evaporation, removal of organic residues, oxygen and carboxylic functional groups. The scanning mode was used in this project and was applied to investigate the thermal stability of the different carbon precursors with temperature increase. The TGA analyses were performed in N_2 ambient for characterising the different carbon support specimens at 40 mL/min flow rate between 25°C and 700°C by means of Mettler Toledo.

3.1.5 Brunauer–Emmett–Teller (BET)

The BET method was used to calculate the physical surface area and quantify the pore size and distribution. It is based on the physical adsorption of gas molecules (commonly N_2) on a solid surface to calculate the specific physisorption surface area. The surface area is an important concept to understand and compare the catalyst performance. Also, the porous structure development is an important factor in the catalyst structure-performance interrelation. The BET equation is:

$$\frac{\mathbf{1}}{\boldsymbol{Q}[\left(\frac{\boldsymbol{p_o}}{\boldsymbol{p}}\right)-\mathbf{1}]}=\frac{\boldsymbol{C}-\mathbf{1}}{\boldsymbol{Q_m C}}\left(\frac{\boldsymbol{p}}{\boldsymbol{p_o}}\right)+\frac{\mathbf{1}}{\boldsymbol{Q_m C}} \qquad \textbf{(3.8)}$$

Where,

Q= The adsorbed volume of the gas,

Q_m= The monolayer adsorbed gas quantity,

C= Constant (179 for N_2)

p, p_o = Equilibrium and saturation pressure of adsorbates

To perform the BET analysis, the powder samples were left in vacuum oven overnight to remove dissolved gases and moisture. The BET equipment deployed was 3 Flex Micrometrics porosity meter was deployed. Taken out from the vacuum oven, the samples were further degassed at 250 °C for at least 3h. Then, the samples were installed into the equipment and analysed overnight.

3.1.6 Inductive-Coupled Plasma Optical Emission Spectroscopy (ICP-OES)

The Pd was quantified in the prepared powder of each catalyst using inductive-coupled plasma optical emission spectroscopy (ICP-OES). 10 mg of each powder were first dispersed in 10 mL of HNO_3 (2%) with 1-h stirring and 50°C heating. The samples, then, were 10-fold diluted into 8% aqua-regia to ensure fine precipitates are dissolved.

3.1.7 X-ray photoelectron spectroscopy (XPS)

XPS is a very useful tool for understanding the surface of nanomaterials. The key information that it could elucidate include the surface composition, electronic configuration and d-band structure change, and metal oxidation state. The XPS theory could be stated that a solid sample emits photoelectron from some atom inner-shell when it is hit by a beam of X-ray photons [141]. Figure **3-4** shows how XPS works. The ejected photoelectron has a kinetic energy E_k upon which the binding energy of the photoelectron to the atom could be calculated according to:

$$\boldsymbol{E_B = h\upsilon - E_K - \phi} \qquad \textbf{(3.9)}$$

Where, h is the Planck's constant, υ is the frequency (Hz), and ϕ is a constant related to the energy required in order to e*j*ect the photoelectron from the atom and it is correlated to the sample material and spectrometer. The binding energy values differ from one chemical element to another and therefore XPS is elemental analysis similar to EDX in that perspective. XPS must be equipped with ultra-high vacuum to prevent gas molecules from scattering low-energy photoelectrons and contaminating the sample surface. In analogy to the X-ray tube in XRD, XPS uses a gun that is hit by high-energy electrons and made from Al or Mg to generate characteristic X-ray photons. The X-ray photons applied in XPS have a lower energy (approx. 1.3 keV) than those applied in XRD (> 8 keV) because the XPS ones should have a small line width (<1.0 eV) which enables a high resolution. Examination of the XPS spectrum involves Auger peaks are shown at the highest binding energies while the valence band of 4d is shown at very small background of a few keVs. The XPS background takes a step-like increasing shape with the binding energy. Shake-up satellite peaks usually show up in the spectra and they are extra peaks resulting from the interaction of photoelectron and valence electron causing the photoelectron to lose a few keVs creating satellite peaks. The shake-up satellite peaks are particularly pronounced for some transition and rare-earth metals having unpaired electrons in the 3d and 4f shells. Another type of satellite peak is generated by Plasmon loss which complicates

the spectrum. Plasmon refers to the energy loss due to the high vibration in conduction band of metals.

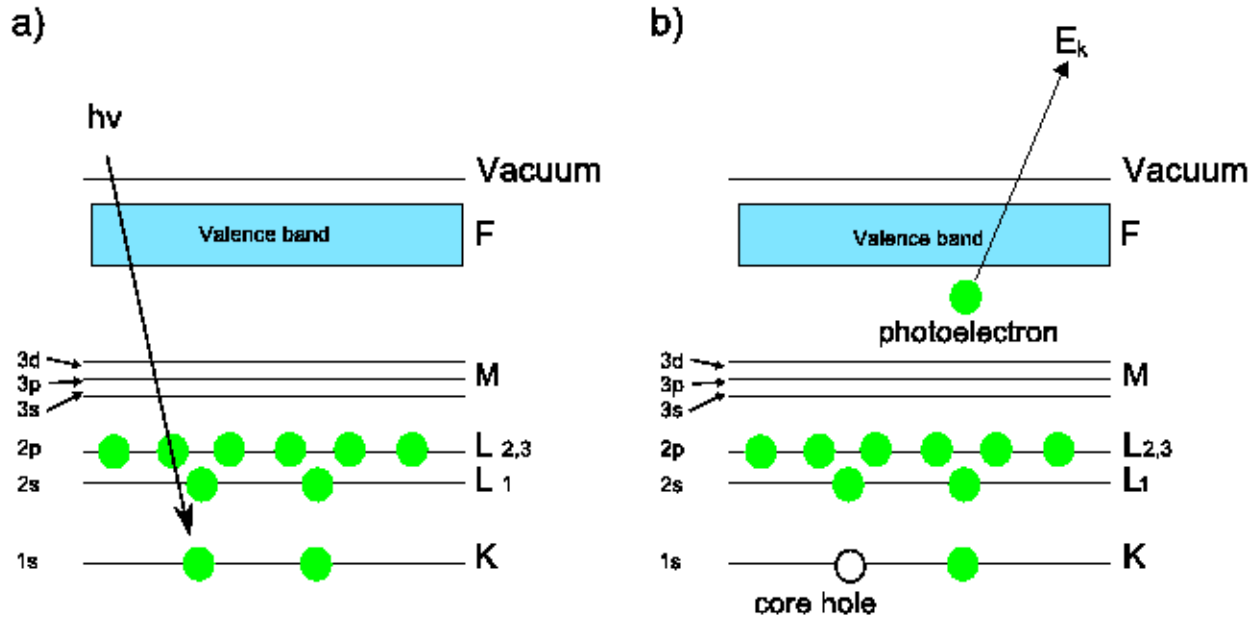

Figure 3-4 X-ray photoelectron spectroscopy (XPS) functional principle

The examination of individual elemental peaks of the samples in this work such as Pd 3d, Au 4f, Ni 2p, and Ag 3d gives an ample of information about the oxidation state of every metal in addition to the possibility of quantification of all constituent metals in the sample surface. It should be mentioned this happens at several nanometres from the top surface. Ultimately, this information are extremely valuable as it could be directly translated into certain catalytic behaviour of the same sample. For instance, metallic Pd present has a different peak from PdO. Furthermore, any small shift in the peak positions of Pd 3d is a very useful concept to compare the electrocatalytic performance of the different Pd catalysts.

XPS was performed on a Thermo Fisher Scientific K-alpha^{+} spectrometer. Samples were analysed using a micro-focused monochromatic Al X-ray source (72 W) over an area of approximately 400 microns. Data was recorded at pass energies of 150 eV for survey scans and 40 eV for a high-resolution scan with 1 eV and 0.1 eV step sizes respectively. Charge neutralisation of the sample was achieved using a combination of both low energy electrons and argon ions. Data analysis was performed in CasaXPS using a Shirley type background and Scofield cross sections, with an energy dependence of -0.6.

3.2 Electrochemical Evaluation

3.2.1 Electrochemical Half-cell testing

A 3-electrode half-cell (Figure **3-5**) is used to perform the electrochemical experiments. The reference electrode, which is used to quantify the applied potential, was either $Ag/AgCl/KCL_{sat}$ or Hg/HgO/KOH (1M). The potential difference between the Hg and Ag reference electrodes is approximately 60 mV and the applied potential is converted into normal hydrogen electrode in Chapters 7) and (Chapter 8). The counter electrode is a Pt-wire and the working electrode is the prepared catalyst pipetted on a glassy carbon electrode (ϕ3 mm). Before running the test, the cell, which includes either KOH only or KOH + EtOH, was purged with nitrogen or argon for 30 min to remove the dissolved gases which might be reduced during the oxidation of ethanol.

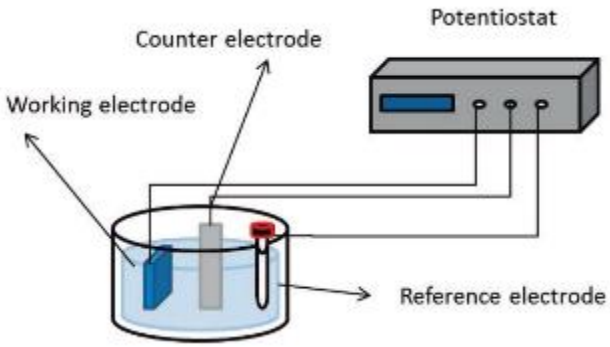

Figure 3-5 The 3-electrode half-cell electrochemical measurement system

3.2.2 Working electrode (WE) preparation

The working electrode was prepared as follows: 5 mg of the prepared catalyst powder were added to a solution of 25 µL Nafion and 2000 µL ethanol. Then, the mixture was suspended in ultrasonic bath for 45 min to prepare the ink slurry. Finally, the ink was deposited on a glassy carbon electrode (Figure **3-6**) (A= 0.0707 cm^2) pipetted.

Figure 3-6 The used glassy carbon electrode

To ensure the uniformity and reproducibility of the deposited electrode surface, some actions were undertaken. First, the glassy carbon electrode was polished in two steps: (1) With 1µm polishing powder and distilled water followed by ultrasonic suspension; and (2) Using 0.05 µm polishing powder and ethanol followed by ultrasonic suspension. Thereafter, the electrode was left to dry in an oven at 60 C. Then, the total volume of pipetted ink was 20 µL, but it was not added in one time. The ink was added to the electrode in 5- µL steps and the electrode was left to dry out after each addition. After the 4^{th} 5- µL addition, the electrode was left a few minutes in the oven to dry out. The instrument used to perform the electrochemical testing is Gamry 600+ potentiostat/galvanostat system.

3.2.3 Cyclic Voltammetry (CV)

Cyclic voltammetry is an essential electrochemical technique to investigate the catalyst activity. It circulates the application of potential between two voltages over the time with a fixed sweep rate. The forward scan is attributed to the oxidation of ethanol and the backward scan is due to the removal of ethoxy incompletely oxidised species if ethanol is present in the solution. In its absence, the CV is applied to investigate the H adsorption and desorption, OH adsorption (in basic electrolyte), and the metal surface oxidation through varying the applied potential. In this thesis, there are two kinds of CV experiments; one in KOH solution to anticipate the electrochemical active surface area and the H and OH adsorption in addition to metal surface oxidation/reduction, and the other in C_2H_5OH + KOH to investigate the ethanol oxidation reaction (EOR). The minimum and maximum applied potentials are -0.9 and 0.4 V vs Ag/AgCl, respectively. The scan rate was 50 mV/s and initial open circuit potential was done before starting CV to ensure the reference electrode functionality. The 50-mV scan rate is relatively fast and was chosen to ensure the distinctive appearance of current peak as it is correlated to the square root of scan rate. The tools that are used to compare the catalyst performance (success measures) are the potential at which oxidation starts (E_{onset}) and the maximum current density achieved in the forward scan (i_{peak}).

3.2.4 Chronoamperometry (CA)

To compare the stability or durability of the prepared catalyst, chronoamperometry measurements (CA) were applied. CA applies a single- or double-step potential and measure the Faradaic current response as a function of time. The current decays exponentially with time, but time is not the only

factor that impacts the CA current. The diffusion coefficient and the concentration near electrode surface increases the current according to Cottrell equation:

$$\boldsymbol{j = \frac{nFAC\sqrt{D}}{\sqrt{\pi t}}} \qquad \textbf{(3.10)}$$

Where, *n* is the number of electrons, *F* is Faraday constant, *A* is the planar electrode area, *C* is the surface molar concentration, *D* is the diffusion coefficient, and *t* is the time.

The same 3-electro cell of cyclic voltammetry with EtOH + KOH is used and the resulting current is measured for the entire period of the test. The objective is to find out how the drawn current reduction proceeds after the initial sharp fall. The higher current is an indication of an active catalyst. Yet, the small current reduction (compared to the first 100 s) in the current by the end of the test period is an indication of more stable and less degradable catalyst. That means an active catalyst could possibly draw a high current throughout the test period but if a steep and consistent current reduction occurs as the time goes by, it indicates the catalyst is not stable and its surface is degraded quickly by some poisoning species. The CA, therefore, gives information of the catalyst tolerance for poisoning.

3.2.5 Tafel polarisation

Looking at the reaction itself occurring at the electrode surface, the rate of electron transfer is expressed by the electric current density (*j*) which expresses how fast the reaction rate is. The Bulter-Volmer equation is commonly applied to measure the relationship between the current density and electrode potential.

$$\boldsymbol{j = j_o\{e^{(1-\alpha)f\eta} - e^{-\alpha f\eta}\} \quad Bulter - Volmer} \qquad \textbf{(3.11)}$$

Where f=F/RT (equals 38.9 V-1 at 298 K), j_o = exchange current density (zero net current flow), α is the charge transfer coefficient which represents the transition state of the electroactive species (if it is reactant-like α=0 and if it is product-like α=1, and typical values are close to 0.5). The η quantity is called the overpotential and equals the difference between electrode potential at current *j* drawn from the cell and the equilibrium potential when there is no net current flow (i.e., the exchange current density (j_o)). Figure **3-7** shows the dependence of the current both on the electrode potential and charge transfer coefficient following Bulter-Volmer equation. When the overpotential is very small

≤ 0.015 V, the exponential factors in Butler-Vomer equation could be expanded by the Taylor series as follows:

$$\boldsymbol{j = j_o\{1 + (1-\alpha)f\eta + \cdots - (1-\alpha f\eta + \cdots)\} \approx j_o f\eta} \qquad \textbf{(3.12)}$$

Therefore, in case of lower applied potential, they behave like a conductor in which the current *j* is proportional to overpotential (η). When the overpotential (η) is large and positive > 0.15 V, the second exponential ($e^{-\alpha f\eta}$) is much smaller than the first ($e^{(1-\alpha)f\eta}$) and therefore could be neglected. This second case is more applicable in fuel cell situations as the overpotential is always a high value.

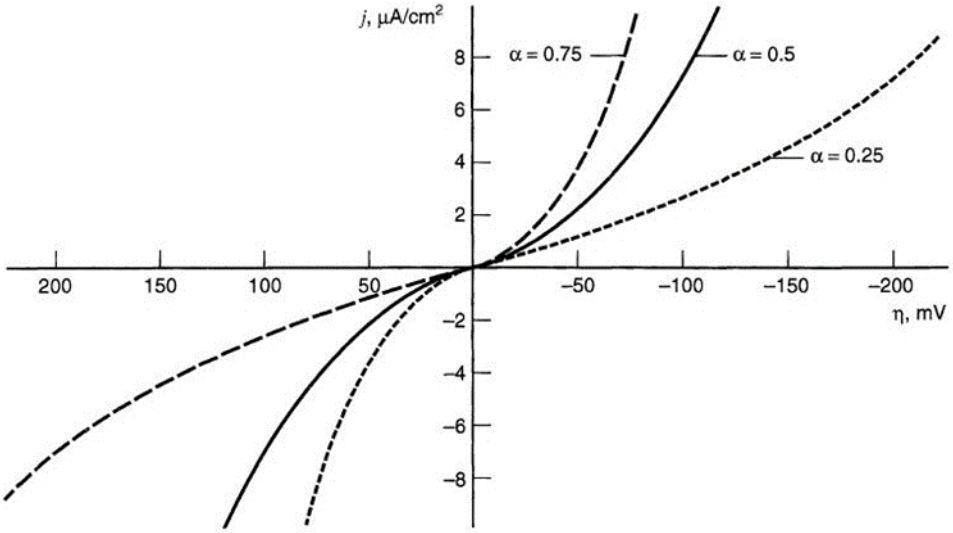

Figure 3-7 Dependence of the current on the overpotential η (mV) and charge transfer coefficient α [9]

Without giving attention to the signs (current direction), the current (*j*) becomes $j=j_o\{e^{(1-\alpha)f\eta}\}$.
By taking the algorithms of both sides:

$$\boldsymbol{ln\, j = ln\, j_o + (1-\alpha)f\eta} \qquad \textbf{(3.13)}$$

The plot of $ln\, j$ versus η is called Tafel plot the slope of which is equal to (1-α)f gives the value of the charge transfer coefficient and its intercept with the vertical axis, at η=0, is equal to $ln\, j_o$.

3.2.6 Electrochemical Impedance Spectroscopy (EIS)

3.2.6.1 EIS Basics

The electrochemical impedance spectroscopy (EIS) is a powerful tool to give insightful information about the different kinds of impeding forces occurring in electrolytic cells. Like the elements of normal electrical circuits such as resistor (R), capacitor (C), and conductor (L), the electrochemical component impedances could be understood and represented. Impedance might refer to any physicochemical barriers that impede the flow of an electric current following an electrochemical reaction. The electrolytic cell has a solution resistance (R_s, **Ω**) associated with the diffusion and mass transfer of active species, charge transfer resistance (R_{ct}, **Ω**) associated with the Faradaic redox reactions, and double layer capacitance (C_{dl}, F) which all could be regarded as electrochemical impedance. C_{dl} is due to the static distribution of opposite-sign charges at the electrode/electrolyte interface which is highlighted in section 1.8. To perform the EIS experiment, the Gamry 600, equipped with frequency response analysis (FRA), was used. The same electrochemical half-cell was used. The frequency applied was 10 kHz to 1 Hz and the AC amplitude was 5 mV. The EIS type is the potentiostat while a fixed potential is applied to monitor and measure the impedances at that potential. Also, to compensate for the current perturbations, before starting the EIS experiment, a potentiostatic scan (at the same EIS potential) was performed for 15 min.

The technique applies sinusoidal voltage perturbations and measure the drawn current from the cell. The current lags behind the voltage with phase shift (ϕ) (Figure 3-8). Both the current and voltage are time- and frequency- dependent, and therefore the fuel cell impedance is time- and frequency-dependent too.

$$\boldsymbol{V(t) = V_o \cos(\omega t)} \qquad \textbf{(3.14)}$$

$$\mathbf{j}(\boldsymbol{t}) = \boldsymbol{i_o} \cos(\boldsymbol{\omega t} - \phi) \qquad \textbf{(3.15)}$$

Where V_o and i_o are the amplitudes of the voltage and current respectively, ω is the frequency in rad/s $2\pi f$ where f is the frequency measured in Hertz.

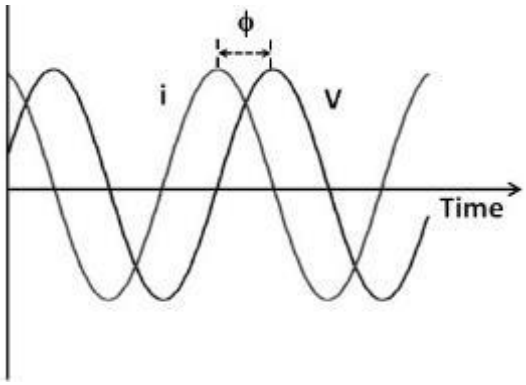

Figure 3-8 Phase shift between current and voltage

As with the Ohmic resistance equivalent to the ratio of voltage to current, the electrochemical impedance is the voltage/current ratio according to:

$$\boldsymbol{Z = \frac{V(t)}{j(t)} = \frac{V_o \cos(\omega t)}{j_o \cos(\omega t - \phi)} = Z_o \frac{\cos(\omega t)}{\cos(\omega t - \phi)}} \qquad \textbf{(3.16)}$$

Where, Z_o is the impedance amplitude. It is also possible to express the values of current and voltage using the complex number as follows:

$$\boldsymbol{Z = \frac{V(t)}{j(t)} = \frac{V_o . e^{(j\omega t)}}{i_o . e^{(j\omega t - j\phi)}} = Z_o . e^{(j\phi)} = Z_o(\cos\phi + j . \sin\phi)} \qquad \textbf{(3.17)}$$

The system impedance is expressed as the real part ($Z_{Re} = Z_o.\cos(\varphi) = Z_o.\cos(\omega t)$) on the horizontal axis and the negative of imaginary part ($-Z_{im} = -Z_o.j\ \sin(\phi) = -Z_o.\ j\ \sin(\omega t)$) on the vertical axis. This graphical representation is called Nyquist plot (Figure 3-9), which also shows an example of it for a hydrogen fuel cell. It shows fuel cell losses *are* dominated by the cathode activation which is much more than the anode activation losses. This explains the higher activation barrier associated with the electro reduction of oxygen molecules.

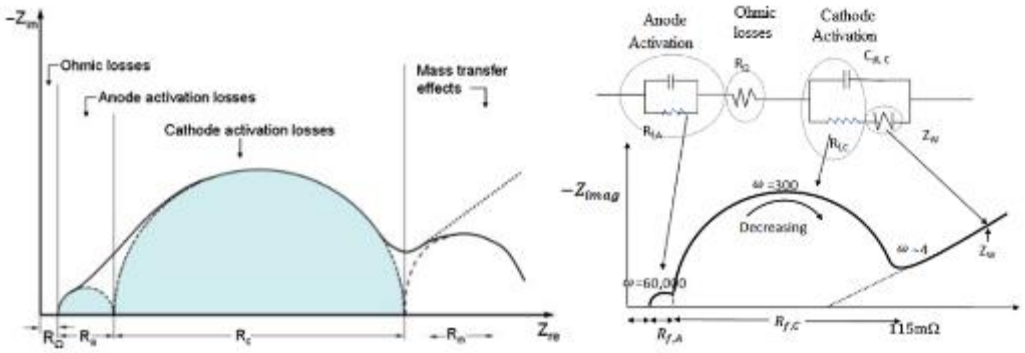

Figure 3-9 The EIS spectra of an example H_2-O_2 fuel cell

The x-axis intercept represents the Ohmic losses, which act as a resistor (V=IR), of the fuel cell. The Ohmic resistance is caused by the electrolyte resistance to the flow of ions added to the electronic resistance of the electrode materials. The resistor representation in the Niquist plot is a single dot on the X-axis as the associated impedance does not change with the frequency. On the other hand, the capacitor representation in the Niquist plot is a single vertical line as its associated impedance (Z_c) is calculated following:

$$\boldsymbol{Z_c = \frac{1}{j\omega C}} \qquad \textbf{(3.18)}$$

Where C is the capacitance in F and ω is the radial frequency in rad/s. At the highest frequency the capacitive impedance is minimum and it is infinity at the very low frequencies.

Figure 3-10 shows the electrolyte/electrode interface including its associated representative impedance elements. The interface where H^+ species reacts with the electrons coming from the anode through external circuit and the cathode oxygen atoms is represented by a double layer capacitor (C_{dl}) and Faradaic resistor (R_f). C_{dl} varies between 30 µF/cm^2 and 300 µF/cm^2 for fuel cells. At the interface an extensive charge separation occurs between the positive ions in the electrolyte side and negative electrons on the electrode side.

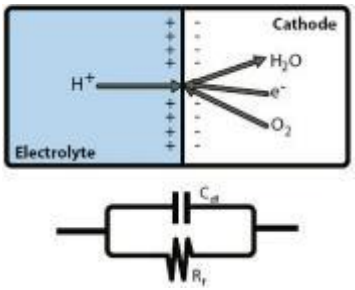

Figure 3-10 Electrode/electrolyte interface of H_2-O_2 fuel cell [9]

The resistance to reaction is (i.e. size of the EIS semicircle) depends on the electrode applied potential, and electronic conductivity of the electrode material and electrolyte. The Faradic resistance (R_f), which is also known as charge transfer resistance (R_{ct}), is due to the resistance to occurrence of redox reaction at the interface. It is due to

the activation barriers associated with the specific reaction to occur. It could be calculated through the Tafel reaction kinetics:

$$\boldsymbol{\eta_{act} = -\frac{RT}{\alpha nF}\ln j_o + \frac{RT}{\alpha nF}\ln j} \qquad \textbf{(3.19)}$$

Where, j and j_o are the current density and exchange current density (A/cm^2), R is the gas constant 8.31 k*J*/kg. K, T is the temperature in K, α is the charge transfer coefficient, n is the number of electrons, and F is the Faraday constant 96485 s.A/mol.

$$\boldsymbol{R_{ct} = \frac{d\eta}{dj} = \frac{RT}{\alpha nF}\frac{1}{j}} \qquad \textbf{(3.20)}$$

Substituting $j = j_o e^{\alpha nF\eta_{act}/(RT)}$ into this equation gives

$$\boldsymbol{R_{ct} = \frac{RT}{\alpha nF}\frac{1}{j_o e^{\alpha nF\eta_{act}/(RT)}}} \qquad \textbf{(3.21)}$$

It should be noted there is no imaginary part in R_{ct} which means it would be represented as a single dot on the X-axis if it is the only impedance component in the electrolytic cell. While the Niquist representation of a series-connected resistor and capacitor is a single vertical line intersecting with the x-axis at the value of resistance, the representation of a parallel-connected resistor and capacitor is a semicircle as shown in Figure 3-11. The imaginary part is zero when the frequency is ∞ and when the frequency is zero the imaginary part is also zero but the total impedance, measured on the real axis, in this case equals the resistor impedance. That is why the arc diameter is equal to value of resistor impedance. The maximum imaginary part is when achieved when the frequency is half-maximum or$\frac{1}{RC}$.

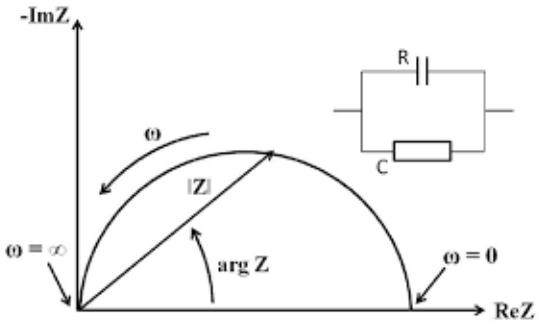

Figure 3-11 Nyquist representation of a parallel connected resistor and capacitor

It is crucial to mention when the electrochemical reaction is very facile, the Faradic resistance is very small and therefore the RC loop is very small too. And when the activation barrier of electrochemical reaction is high, the Faradaic resistance is high and therefor the RC semicircle will be enlarged.

According to Figure 3-12, there is a third type of losses in the fuel cell related to the mass transport which called Warburg losses (Z_w). It depends on the bulk concentration of reacting species (C_i) and diffusion coefficient of reactant species (Di). The higher both Ci and Di, the less Z_w would be. In other words, for a concentrated solution in which the reacting species diffuses easily, the Warburg impedance will be minimal and vice versa. Also, Z_w decreases with increasing ω according to either if the infinite diffusion layer model or porous bounded one as shown in Figure 3-12. The porous bounded model is more applicable and noted in fuel cell operation

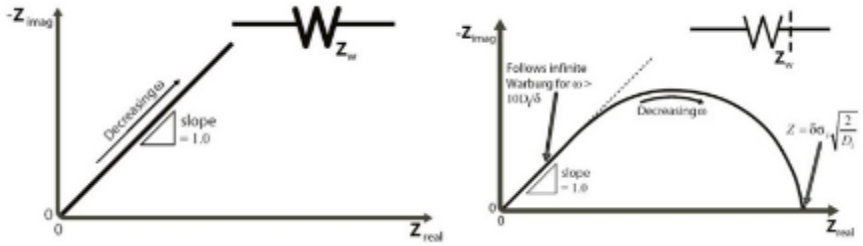

Figure 3-12 EIS representation of mass transport losses in fuel cell flowing infinite diffusion layer model (Left) and finite (porous-bounded) Warburg element model (Right)

Chapter 4: MONOMETALLIC PD ELECTROCATALYSTS SUPPORTED ON VARIOUS CARBONS

Carbon materials have received a considerable attention as building blocks to construct electrodes for energy storage and conversion devices. Some of the properties that make carbon an attractive electrode material, are polymorphism, chemical stability, rich surface chemistry, strong carbon-carbon bonds, and fast electron mobility [17]. As was discussed in the literature review (section 2.4), the carbon support applied in fuel cell electrodes should possess a high surface area to enable the wide dispersion of metal nanoparticles, be conductive electronically to conduct the redox electrons, and have a mesoporous structure to enable the three-phase reactions by facilitating the mass transport and the surface exposure of the catalytic sites. However, the impact of changing those characteristics by using different carbons with varying mesoporous structure has not been investigated. For example, the mesoporous pore size ranges from 2 nm to 50 nm. Changing the pore size within those limits might have some implication on the supported catalyst performance which was not addressed before. Also, whether or not increasing the surface area will always yield an enhanced catalyst performance for ethanol oxidation is a raised question. That is why this chapter investigates the use of 5 different (mesoporous) carbons as a support for Pd nanoparticles deploying the polyol process using ethylene

glycol as a solvent and reducing agent. The reported literature also informs of a controversy about the impact of the physical and chemical activation on the carbon functionality as a support. Thus, this chapter also studies the chemical activation effect by applying an acid functionalisation protocol and the synthesis of Pd on the functionalised Vulcan carbon (Pd/C_{vf}).

4.1 Experimental

The physical and electrochemical characterisation settings could be reviewed in Chapter 3. The section below reports only the synthesis method of Pd and carbon functionalisation.

4.1.1 Carbon oxidation treatment

Acid treatment, of Vulcan (C_v) to give C_{vf}, was performed to enrich the carbon surface with oxygen functional groups, increase the water uptake, and enhance the textural properties following [10,14,15]. Briefly, 2 g of Vulcan (C_v) were dispersed and sonicated in a mixture of HNO3 and H_2SO_4 for 2h. Then, it was left for 24 h to settle down. Sodium carbonate solution was used to neutralize the mixture and then it was washed using deionised water and vacuum filtration. Finally, it was dried in a vacuum oven at 80˚C overnight.

4.1.2 Catalyst synthesis

All chemicals used were of analytical grade and were used without further purification. Sigma-Aldrich supplied all chemicals except Vulcan (Cv) and selectivity (Cs) carbons which were supplied by Cabot Corp. The synthesis protocol follows the polyol process using the ethylene glycol as a solvent and reducing agent [11,21]. The nominal amount of metal precursor (4.415 mL, 0.128M) and each carbon (240 mg) were mixed and sonicated in 36 mL of ethylene glycol for 20 min. The Pd:C weight ratio is 20:80. Then, the pH was adjusted to 10 by adding 1M NaOH. Following, the catalysts' mixtures were stirred at 130˚C for 2.5 hours under refluxing. Mixtures were, then, washed copiously with deionized water until neutralised. Finally, the wet powder was dried at 80˚C in a vacuum oven overnight. The Vulcan-, Selectivity C_{s1}-, Selectivity C_{s2}-, CNF-, acid-Vulcan- and Activated-Charcoal-supported Pd catalysts are named Pd/C_v, Pd/C_{s1}, Pd/C_{s1}, Pd/CNF, Pd/C_{vf} and Pd/AC, respectively.

4.2 Results

4.2.1 Carbon physical characterisation

Figure 4-1 shows the XRD patterns of C_v, AC, CNF, and C_{s1}. The highly intense peak of graphite at 26° in case of CNF stems from its crystalline nature [70]. The high intensity is suggestive of high electron conductivity according to Bianchini *et al.* [77]. C_v has a broader and much less intense peak due to its turbostatic structure with some ordered crystals with length 2nm and height 1.5 nm. The degree of peak broadening increases moving from C_v to C_{s1}. The support having the least crystalline nature is activated charcoal (AC), which shows the broadest carbon peak. According to Calvillo et al. [63] the crystallinity degree of the support promotes the physical and electrochemical characteristics of the supported metal catalysts which means CNF could have a strong support potential from the crystallinity perspective. Yet, caution should be practiced as the surface area and porosity also have important impacts on the electrocatalytic activity.

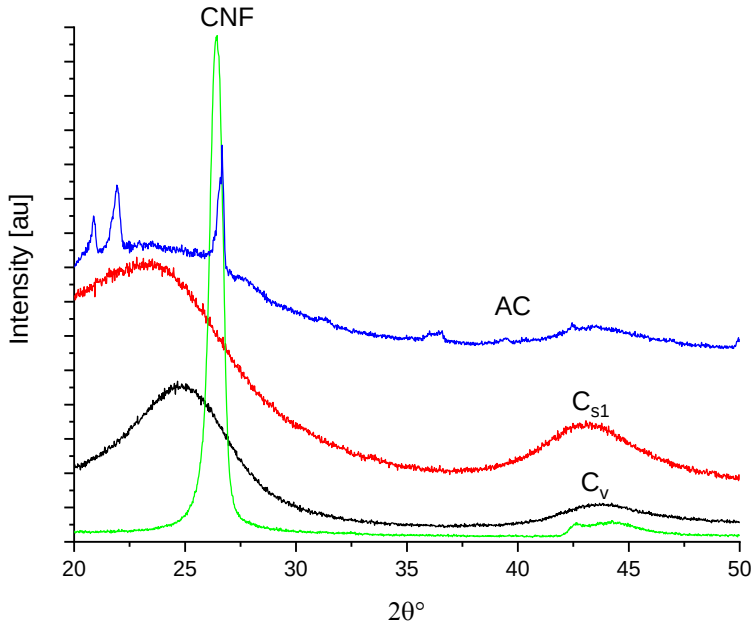

Figure 4-1 X-ray diffraction of Vulcan carbon (C_v), carbon nanofibres (CNF), activated charcoal (AC), and selectivity carbon 1 (C_{s1})

Table 4-1 lists the surface area and porosity measurements of C_{s1}, C_v, AC, and CNF. C_{s1} and AC have much higher surface areas compared to the other two carbons which suggests both have a potential to disperse metal nanoparticles widely and result in enhancing the electrocatalytic performance. On the other hand, both have a smaller pore size (close to half) compared to the other

two carbons. While surface area is an important parameter for enhancing the catalyst performance, pore size is also crucial for this particular application to enable fast and easy transfer of the reactants and products to or from the electrode surface and throughout the electrode surface itself [58]. What has been said about C_{s1} is, to a very good extent, applicable to C_{s2}. On the other hand, in the literature, it is reported that the support should have a mesoporous structure (2nm – 50 nm in pore size) [58,64,142] which is met by all four supports. However, it is not clear what minimum pore size is necessary to support metal nanoparticles without harming its access to the reactants coming from the bulk electrolytes. Therefore, this work aims to develop a more accurate identification of the mesoporous structure. It is noteworthy that the external surface area, in Table 4-1 is less than the BET surface area for all carbons except CNF which has a higher external surface area than its BET area. This could be beneficial for Pd active sites are more likely to be located on the external surface of the CNF and therefore the reactants will easily access the Pd. Additionally, CNF, unlike the other three carbons, does not have micropores and therefore all the pores are large enough and exposed on surface of the cylindrical CNF. Table 4-1 also shows that the micropore area of C_s is approximately 1.5 times as its mesopore area which is the contrary condition of AC whose mesopore area is bigger than its micropore one. Once more, these technical points are suggestive of more enhanced access of Pd on AC than C_{s1}. Figure 4-2 shows the pore size measurement and surface area information of the Cv, Pd/Cv, Pd/Cvf, Pd/Cs1, Pd/CNF, and Pd/AC. It shows that the surface area of support decreases after adding the Pd nanoparticles regardless of the carbon type. Additionally, the pore size of Pd/Cs1 is 13 nm but that of Pd/C_v is 22 nm. Moreover, while the pore size of Pd/CNF is 21 nm, its surface area is only 60 m^2/g.

Table 4-1 Physical textural properties of C_v, C_{s1}, CNF, and AC

Carbon	S_{BET} (m^2/g)	$d_{pore\ size}$ (nm)	V_t (cm^3/g)	$S_{external}$ (m^2/g)	$S_{mesopore}$ (m^2/g)	$S_{micropore}$ (m^2/g)
C_v	230	19	0.25	174	52	55
C_{s1} [134]	1230	X	1.22	x	430	690
CNF	74	20	0.05	80	11	0
AC	845	12.7	0.56	366	475	104

x: Blank data are not reported in the referred reference.

These are interesting findings and they could certainly impact the electrocatalytic performance of Pd NPs supported on them. According to Figure 4-2, the total specific surface area is highest in case of

Pd/Cs1 followed by Pd/AC. Following are the Pd catalysts supported on raw and functionalised Vulcan carbons (Pd/C_v and Pd/C_{vf}). The smallest surface area is that of Pd/CNF. The external surface area – ignoring the bore area – represents a significant part (>90%) form the total specific surface area in case of Pd/C_v and Pd/C_{vf}. It is even higher than the specific area in case of Pd/CNF. On the contrary, the external area is a smaller contribution to the specific surface area in case of Pd/C_{s1} and Pd/AC.

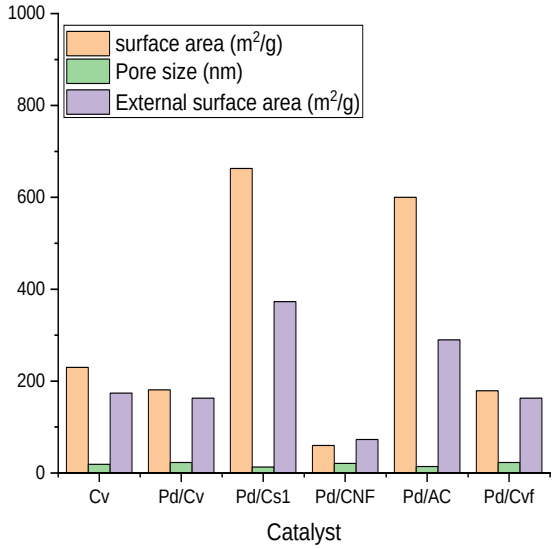

Figure 4-2 BET surface area and pore size measurement of C_v, Pd/C_v, Pd/C_s, Pd/CNF, Pd/AC, and Pd/C_{vf}

Unlike the ascending order of BET surface area from Pd/CNF to Pd/C_{s1}, the pore size changes in a different way. The Pd catalysts supported on high surface area carbons (C_{s1} and AC) have a small pore size (10-12 nm). On the contrary, the ones supported on lower surface area (C_v and CNF) have a higher pore size (20-22 nm). Figure 4-3 shows the pore size distribution of Pd/C_v, Pd/C_{vf}, Pd/CNF, Pd/C_{s1}, and Pd/AC. In case of Pd/C_{s1}, a significant change in the pore volume per gram is attained at low pore sizes (5 nm – 20 nm). This could be explained to the high content of small pores in the selectivity carbon (C_{s1}). Similarly, the pore volume change per gram in case of Pd/AC is also substantial at low pore sizes (5 nm to 30 nm). On the other hand, for the low surface area carbon supported Pd catalysts, the pore volume change per gram is concentrated at higher pore sizes (20 nm – 60 nm). Once more, this could be correlated to the higher pore sizes attained with C_v and CNF.

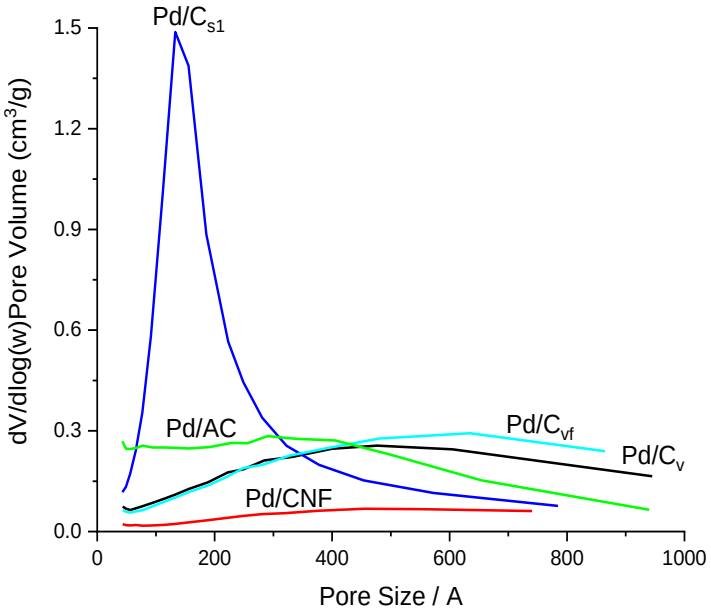

Figure 4-3 Pore size distribution of Pd/C_v, Pd/CNF, Pd/C_{s1}, Pd/AC, Pd/C_{vf}

Figure 4-4 shows the TGA results of C_v, C_{vf}, CNF, $C_{s1,}$ and AC. TGA was applied in an N_2 atmosphere with heating rate of 20˚C/min between 25˚and 700˚C. The significant initial weight reduction (4% of the original weight is lost by reaching 100°C) in case of AC is an indicative of its high moisture content that is lost by reaching 100°C. Following AC in the moisture content is C_{s1} though it is much less (only 0.7 % of the original weight is lost by reaching 100 °C). No observable weight loss could be seen below 100°C in case of C_v and CNF which is due to their hydrophobic nature that does not allow any water. However, C_{vf} experiences an initial weight loss of around 0.5% and the weight reduction below 100˚C which proves the acid treatment has made the Vulcan surface less hydrophobic. Between 100°C and 300°C, the weight loss is more pronounced in case of AC than the other carbons which indicates its higher content of carboxylic groups. The weight loss due to organic residues is barley noted on C_v and CNF. However, the CNF seems to have a lot of carboxylic groups verified by the weight reduction between 300°C and 600°C. Although the Vulcan C_v loses a very small weight fraction, at 200 ˚C, due to decomposition of organic residues, the weight loss of C_{vf} seems much higher at 200˚C and 350˚C due to the decomposition of carboxylic groups added by acid functionalisation. At 650˚C, a more pronounced weight loss is ascribed to the decomposition of anidrides groups which is similar also to the weight loss in AC at this temperature [61,64].

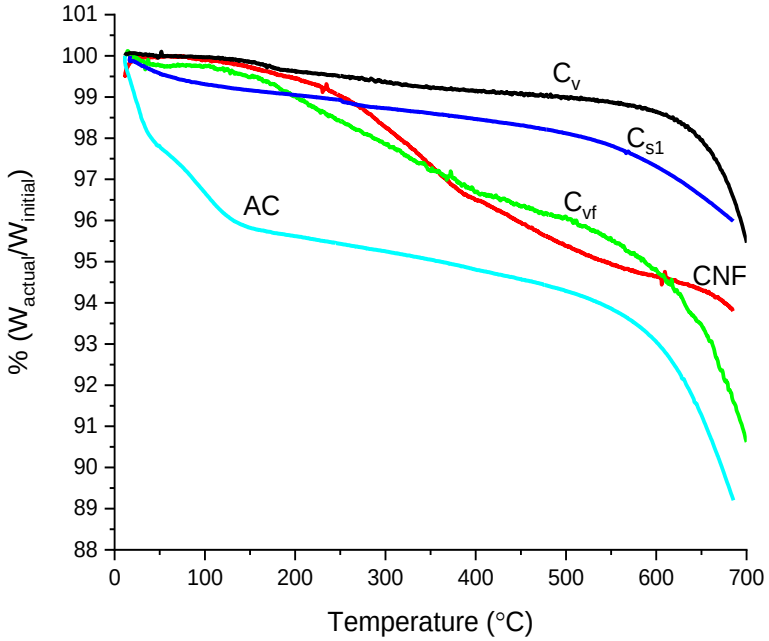

Figure 4-4 Thermogravimetric results of carbon nanofibres (CNF), Vulcan carbon (C_v), functionalised Vulcan carbon (C_{vf}), Selectivity carbon 1 (C_{s1}), and activated charcoal (AC)

The big difference that could be seen between C_v and C_{vf} is an indicative of the higher functional groups that have been added to C_v by the acid functionalisation. On the other hand, no significant transitional weight loss is noted for C_{s1} which indicates it has a small content of carboxylic or anidrides groups.

Figure **4-5** shows the EDX spectrum and quantitate analysis of the Vulcan carbon (XC72). The peak at 0.2 eV, which is not shown completely to show the other very small peaks, is for the C-k line. The Si (1.75 eV), Na (1.05 eV), and S (2.3 eV) peaks are due to some impurities present in the carbon precursor. The O-K peak and the detected Ni quantity are due to the surface functional groups in the carbon. The degree of hybridization increases the number of π sites that act as anchoring sites for the nucleation and growth of metal nanoparticles.

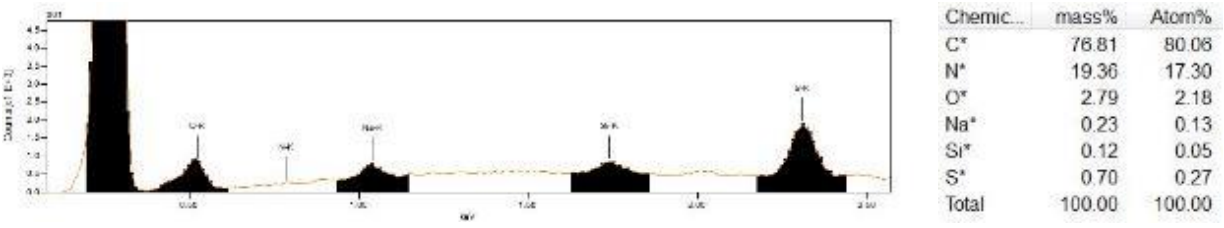

Chemic...	mass%	Atom%
C*	76.81	80.06
N*	19.36	17.30
O*	2.79	2.18
Na*	0.23	0.13
Si*	0.12	0.05
S*	0.70	0.27
Total	100.00	100.00

Figure 4-5 EDX spectrum and quantitative analysis of Vulcan carbon (XC72)

4.2.2 Physical Characterisation of the Supported Catalysts

The Pd metal concentration in each catalyst powder is quantified using ICP-OES which revealed 17.8% and 17.7%, 15.7%, 20.4% and 16.8% for Pd/C_v, Pd/C_s, Pd/AC, Pd/C_{s2}, Pd/CNF, respectively. X-ray diffraction was performed on the prepared catalysts. Figure 4-6 shows the patterns obtained for different catalysts. The peaks are matched using *J*ade software and International Centre for Diffraction Data (ICDD) database. Vulcan carbon (XC72) has a turbostatic structure, which means it is intermediate between amorphous and graphitic crystalline structure verified by the broad peak at 25º while the carbon nanofibres show more crystalline nature evidenced by the sharp peak at 26° in addition to other peaks at 44°, 54°, and 73° matched with C (002), (100), (004), (110) according to PDF no 89-8487 for graphite.

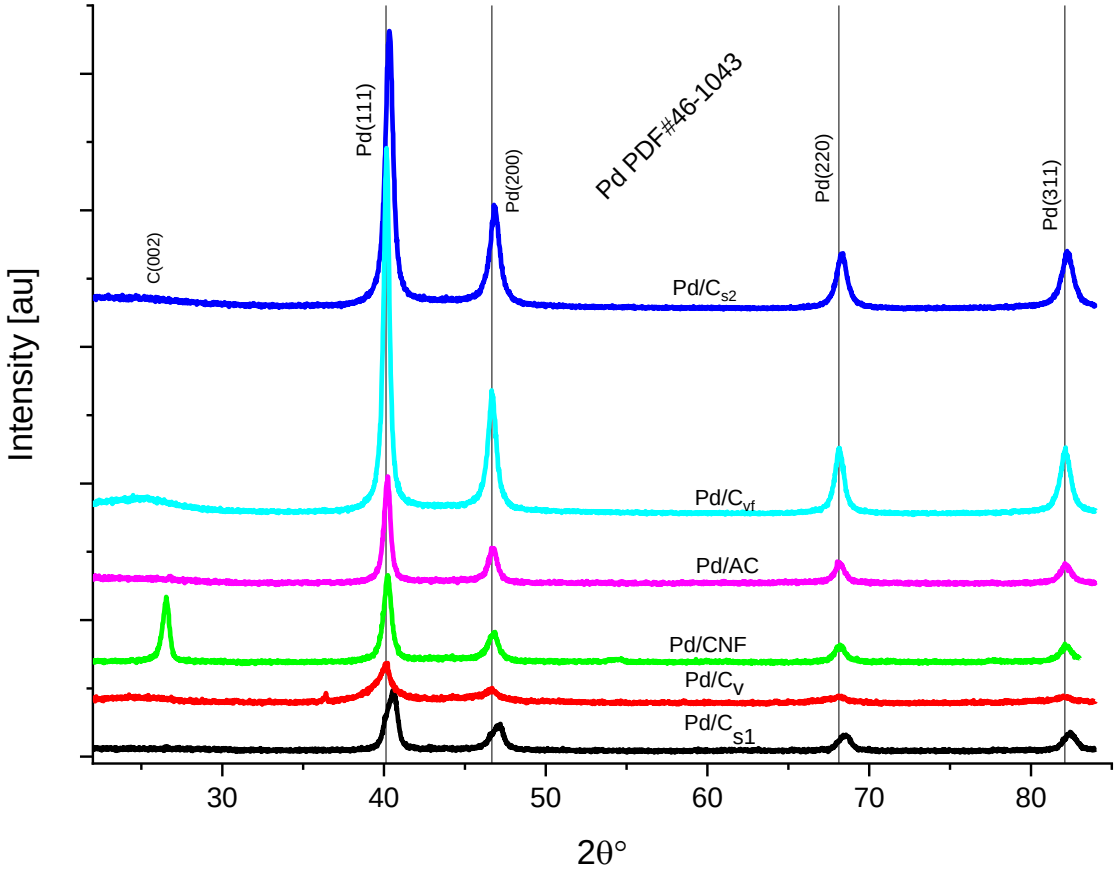

Figure 4-6 XRD patterns of Pd/C_v, Pd/C_{vf}, Pd/AC, Pd/CNF, Pd/C_{s2}, and Pd/C_{s1}

Other carbons are on the contrary of that. Carbons of AC, C_{s1}, and C_{s2} seem to be of a more amorphous nature as they show very broad peak at 25. The other 4 crystalline peaks noted at 40, 46, 68, and 82° are attributed to the *fcc* metallic facets of Pd (111), (200), (220), and (311). The unknown peak at 36.2° for Pd/C_v might be attributed to PdO_2 according to PDF 34-1101. Figure **4-7** shows the enlarged Pd (111) facet peak for the six catalysts. The Pd/C_v, Pd/C_{vf} and Pd/CNF are the closest to Pd only powder diffraction pattern with a small shift to the higher angles. However, the positive peak shift increases for Pd/AC, Pd/C_{s2} and Pd/C_{s1}. The higher positive shift to the right suggests the Pd crystal lattice is sub*j*ected to compressive stress and strain leading lattice contraction indicated by the smaller lattice constant. This might lead to downshift in the *d*-band centre that could increase the adsorption strength between Pd and poisoning species during alcohol oxidation [143].

The interaction between Pd and the AC, C_{s2}, and C_{s2} of Pd/AC, Pd/C_{s2} and Pd/C_{s1} has led to this higher positive peak shift of Pd. It is not fully clear what happened exactly, but the common properties of those carbons – and on the contrary of the other C_v, C_{vf}, and CNF – are the high amorphous content, high surface area and underdeveloped porous structure. The highest peak broadening is noted in case of C_v supported Pd which suggests it is the smallest crystallite size among them. On the other side, the Pd most intense peak is noted in Pd/C_{vf} and Pd/C_{s2} which suggests the Pd crystallite size of those catalysts are comparatively high. The crystal size and interplanar spacing are calculated following Scherrer equation and Bragg's law, respectively, as was explained in Section 3.1.1.

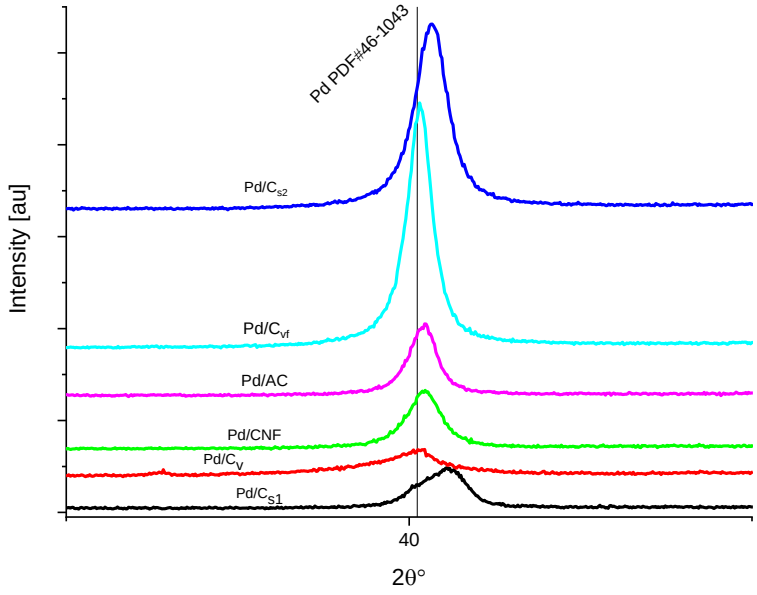

Figure 4-7 Enlarged Pd facet (111).of Pd/C_v, Pd/C_{vf}, Pd/AC, Pd/CNF, Pd/C_{s2}, and Pd/C_{s1}

Table 4-2 shows the crystallographic information obtained by XRD technique for the various carbon-supported Pd catalysts. It, interestingly, shows Pd/C has broadening of the (220) around twice as that of most other catalysts. As a result, the crystal size of Pd/C is less than a half of it for other catalysts. This will impact the catalytic activity of Pd/C compared to other catalysts. There is a strong correlation between the particle (or crystallite) size and catalytic activity of the catalyst. The smaller and well-dispersed crystals should anticipate higher catalytic performance.

Table 4-2 Crystallographic information of Pd NPs on carbons

Catalyst	$2\Theta_{(220)}$	FWHM	τ (nm)	$d_{(220)}$ (Å)	a (Å)	ICDD PDF
Pd/C	67.97	1.76	5.44	1.4	3.9	
Pd/CNF	68.15	0.84	11.44	1.4	3.8	Graphite
Pd/C_{s1}	68.47	0.94	10.22	1.36	3.8	89-8487
Pd/C_{s2}	68.13	0.89	10.77	1.4	3.8	Palladium
Pd/AC	68.18	0.78	12.29	1.4	3.8	46-1043
Pd/C_{vf}	68.22	0.85	11.28	1.4	3.9	

Figure 4-8 shows the TEM micrographs and particle size distribution obtained for Pd/C_v, Pd/C_{s1}, P/CNF, Pd/C_{vf}, and Pd/AC. In case of Pd/C_v, well-dispersed small nanoparticles could be noted by looking across the image. The colour gradient in TEM is usually correlated either to the atomic number and/or the sample thickness. The light elements tend to be bright grey while the heavy ones are dark black. The larger sample thickness causes the image to be darker. In Figure 4-8, the image of Pd/Cv shows large grey aggregates (30 – 60 nm in diameter) and much smaller darker particles (< 5nm). The grey aggregates seem to represent the Vulcan carbon itself while the small dark particles reflect the supported Pd NPs. The average particle size distribution of Pd/C_v (2.3 nm) is the smallest compared to the other catalysts and also its standard deviation is the smallest too. For the Pd/C_{s1}, it is noted the C particle size, itself, is 20 – 40 nm, which is smaller than that of C_v. The image quality was impacted by the low microscope capacity (100 kV voltage) and the initially applied TEM sample preparation which caused individual metal particles to aggregate further than the initial aggregation during the synthesis. The average particle size of Pd/C_{s1} is 6.67 nm. In case of Pd/CNF, the cylindrical shape of CNF could be seen with diameter close to 100 nm. Small black Pd nanoparticles on the surface of CNF could be distinguished with significant agglomeration that is higher than Pd/C_v. For the Pd/C_{vf}, bigger Pd particle or higher Pd aggregation, compared to Pd/C_v, could be seen. The Pd/C_{vf}

average particle size is 2.5 nm. When this is contrasted with Pd/C_v, it highlights the applied acid functionalisation harms the carbon structure by facilitation Pd agglomeration/further growth of particles during synthesis.

As for the Pd/AC, like C_{s1}, the C particle size (<40 nm) is apparently smaller than that of C_v. The average Pd/AC particle size is approximately 7 nm with a high standard deviation of 3.58 nm which once more suggests higher Pd agglomeration occurs on the AC similarly to what happens on C_{vf} and CNF. The TEM results corporate the XRD data about the Pd particle shape and size on the various carbons deployed. The TEM results of Pd/AC and Pd/C_{vf} vs Pd/C_v are in conflict with some literature reports [63,67].

Pd/C_v

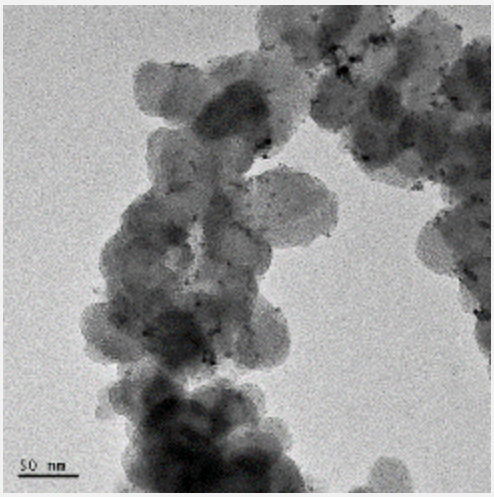

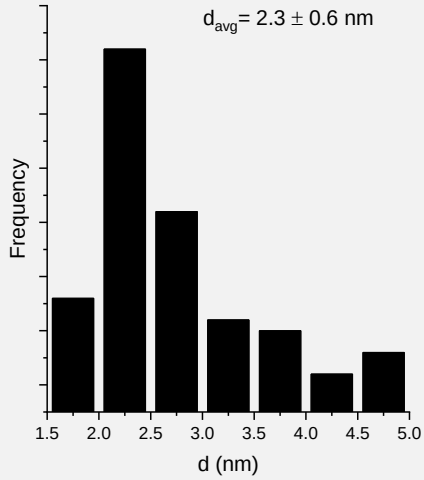

Pd/C_{s1}

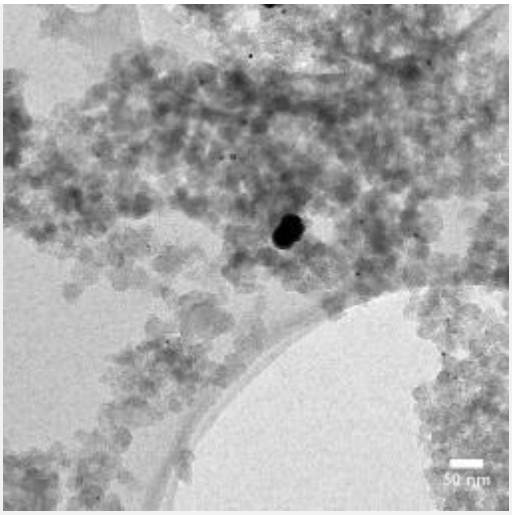

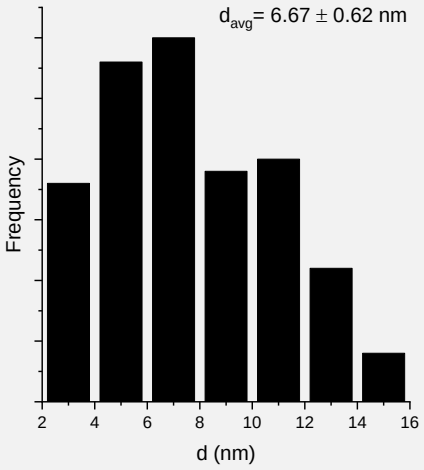

Pd/CNF

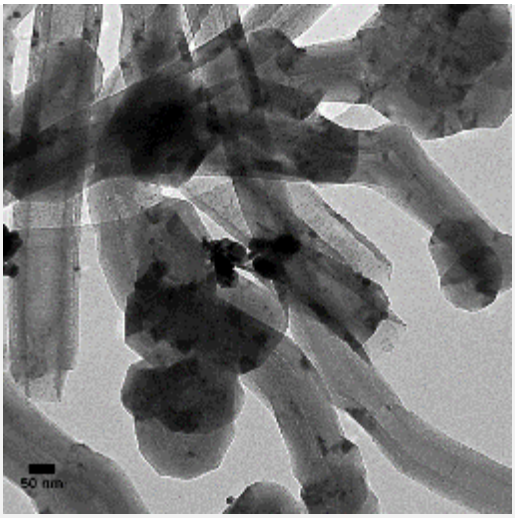

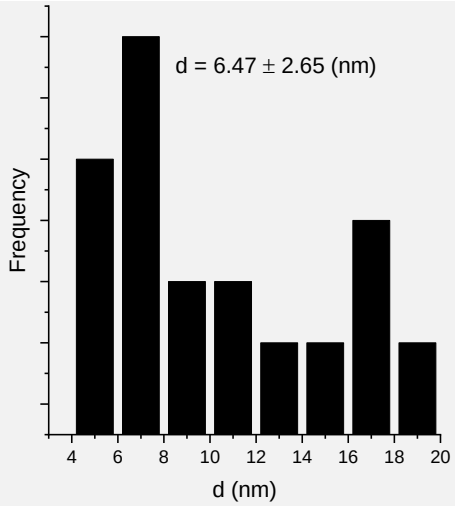

Pd/C$_{vf}$

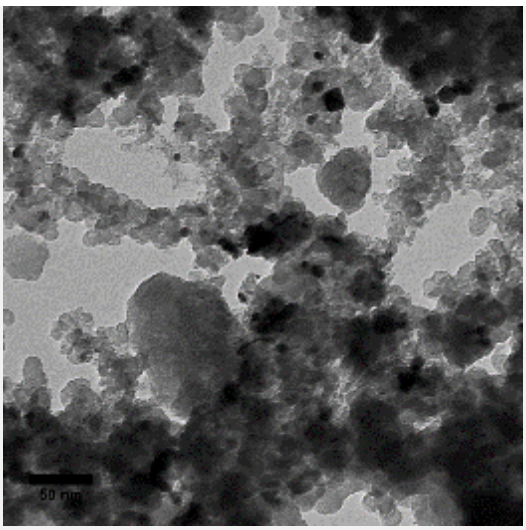

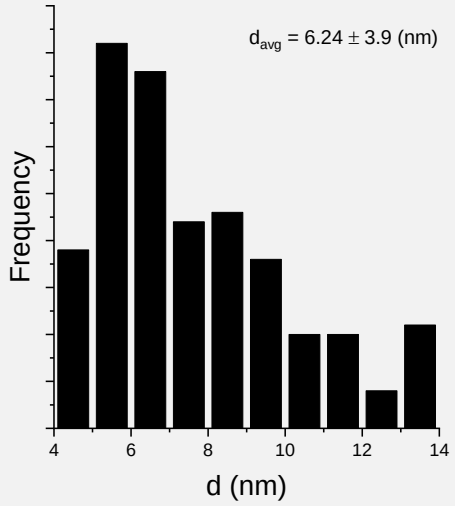

Pd/AC

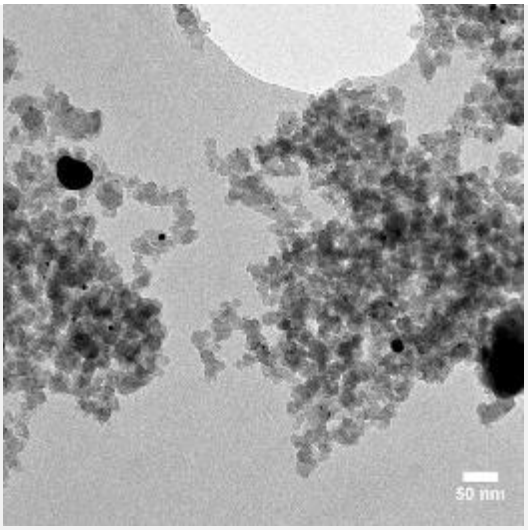

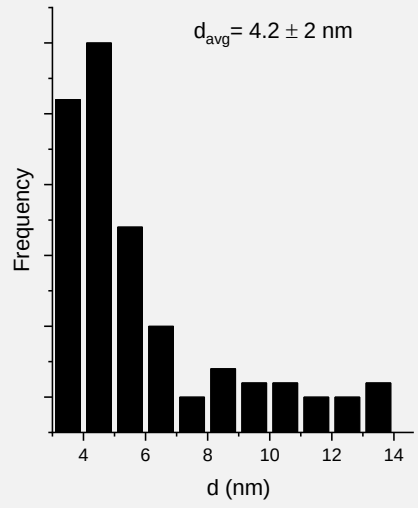

Figure 4-8 TEM Micrographs and particle size distribution of Pd/C$_v$, Pd/C$_{s1}$, Pd/CNF, Pd/C$_{vf}$, and Pd/AC

To investigate the surface composition and Pd oxidation states, X-ray photoelectron spectroscopy deploying Al kα radiation was applied. Table 4-3 lists the elemental compositional quantification of C, Pd, and O in each catalyst. A first note could be made that Pd exists in a metallic state almost on all supports except C_v and C_{s1}. Even further the difference between PdO on Pd/C_v and Pd/C_{s1} is significant with 6:1 atomic ratio. It is not accurately known why Pd has such a low air stability on C_v. Yet, Pd oxidation has probably occurred after synthesis because of reaction with air (it will be seen in the subsequent chapters that adding another metal like Au improves the Pd air stability). A second note could be mentioned about the very high oxygen quantity of Pd/AC – though Pd is metallic – which indicates the high functional oxygen content included in the activated charcoal. Following Pd/AC, in oxygen content, is the Pd/C_{vf} which is anticipated due to the incorporation of surface functional groups into C_v after acid treatment. This further corporates the TGA results regarding those supports in [67] especially Pd is not oxidised on both of them. Moreover, the C content in Pd/AC is only 89% which is approximately 5% less than all other catalysts. Another important note could be made about the surface Pd content in each catalyst.

Table 4-3 XPS surface composition of Pd/C_v, Pd/C_{vf}, Pd/C_{s1}, Pd/AC, and Pd/CNF

Catalyst	At. % C (1s)	At. % O (1s)	At. % Pd (3d)	
			Pd (Metallic)	PdO
Pd/C_v	94.0	4.2	1.1	0.3
Pd/C_{s1}	97.4	2.1	0.2	0.05
Pd/C_{s2}	96.53	2.68	0.61	0
Pd/CNF	95.3	1.9	2.6	0
Pd/C_{vf}	94.8	3.1	1.8	0
Pd/AC	89.4	6.5	3.3	0

For catalysts, such as Pd/C_{s1} and Pd/C_{s2}, the Pd content is very small (0.25 and 0.61) compared to Pd/C_v and Pd/CNF. The exact explanation is not known to the author. However, this finding corporate the hypothesis about the deep burying of Pd in the internal small pores of those two carbons since the Pd quantity detected on their surface is much less that on other supports. A caution is practiced here since AC also has a small pore size similar to C_{s1} and C_{s2}, but the Pd quantity detected on AC is the highest though. Several reasons could have contributed to this conflict such as the metal segregation on the support surface or the accuracy of the XPS device which is less likely due to the

present results of Pd/CNF, Pd/C_v and Pd/C_{vf}. In particular, the high Pd content on CNF supports this hypothesis since CNFs do not seem to have any micropores in their texture according to Figure 4-3.

Figure **4-9** shows the Pd 3d XPS spectra in Pd/C_v, Pd/C_{vf}, Pd/C_{s1}, Pd/C_{s2}, Pd/AC, and Pd/CNF which are convoluted into two doublets of high-energy $3d_{3/2}$ at 341 eV and low-energy $3d_{5/2}$ at 335 eV, both are noted for bulk Pd. All peaks are shifted – with a varying degree – to higher binding energies. Meanwhile, the peaks of Pd/AC, Pd/CNF, and Pd/C_{vf} are intense compared to Pd/C_v and Pd/C_{s2}. The peak broadening might be attributed to the smaller particle size. The peaks of O 1s + Pd 3p and C 1s are shown in Appendix 2.

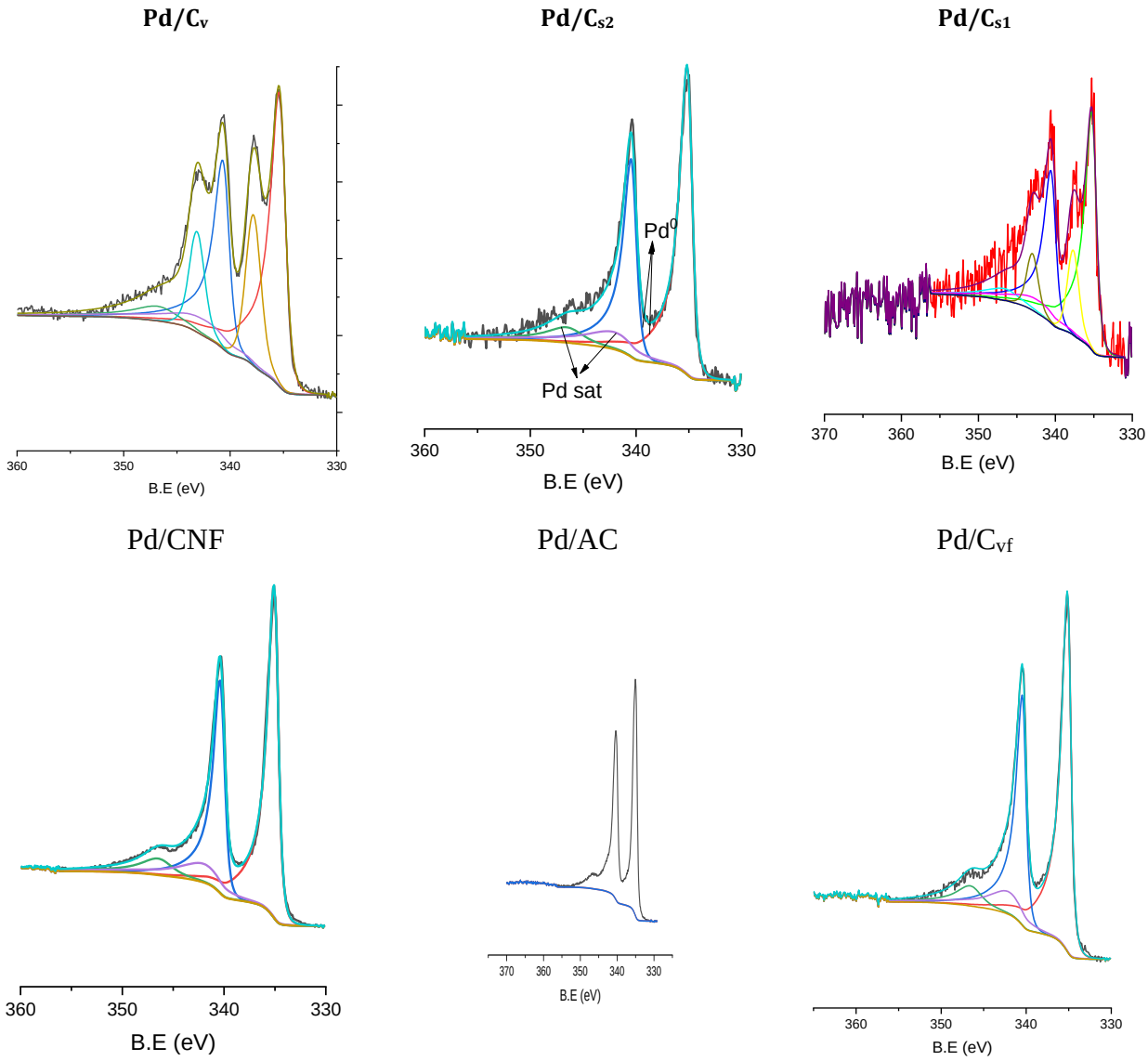

Figure 4-9 XPS spectra of Pd 3d of Pd/C_v, Pd/C_{vf}, Pd/CNF, Pd/C_{s1}, Pd/AC, and Pd/C_{s2}

4.2.3 Electrochemical Catalyst Evaluation

Figure 4-10 shows the cyclic voltammograms of Pd/C_v, Pd/C_{vf}, Pd/C_{s1}, Pd/CNF, Pd/AC and Pd/C_{s2} 1M KOH at 50 mV/s. The AC-, C_{vf}-, and C_{s1}, and C_{s2}-Pd catalysts present higher capacitive current than CNF and C_v, probably because of the larger surface area and highly capacitive behaviour. $H_{abs/des}$ peaks are expected around -0.7 V but are rather difficult to be noted due to the H absorption into the Pd bulk structure added to the mentioned capacitive behaviour of certain supports. The OH adsorption window is between -0.5 V and -0.3 V. In case of Pd/CNF and Pd/C_v, there is a noted increase followed by decrease in the current unlike Pd/C_{vf}, Pd/AC, Pd/C_{s2} and Pd/C_{s1} which do not present an increase/decrease at this potential window. While the OH_{ads} peak is easily recognizable on Pd/CNF and Pd/C_v, it is surpassed in case of the other catalysts. At around -0.1V, starts the surface layer oxidation of both catalysts which continues to the end of the forward scan. Due to that oxidation, a slow gradual increase in the current is noted between -0.1 V and 0.4 V. In the reverse scan, the PdO is reduced between -0.1V and -0.4V. It is worth mentioning the reduction current drawn on Pd/AC and slightly Pd/C_{vf}, Pd/C_{s1} and Pd/C_{s2} is not significant to other potentials due to the higher surface area and oxygen groups contained in AC, C_{s1}, and C_{s2}. However, the PdO reduction peak in case of Pd/C_v and Pd/CNF is more than the other electrocatalysts. This PdO reduction peak area is a reliable measure to quantify the electrochemical active surface area (EASA) per gram of Pd.

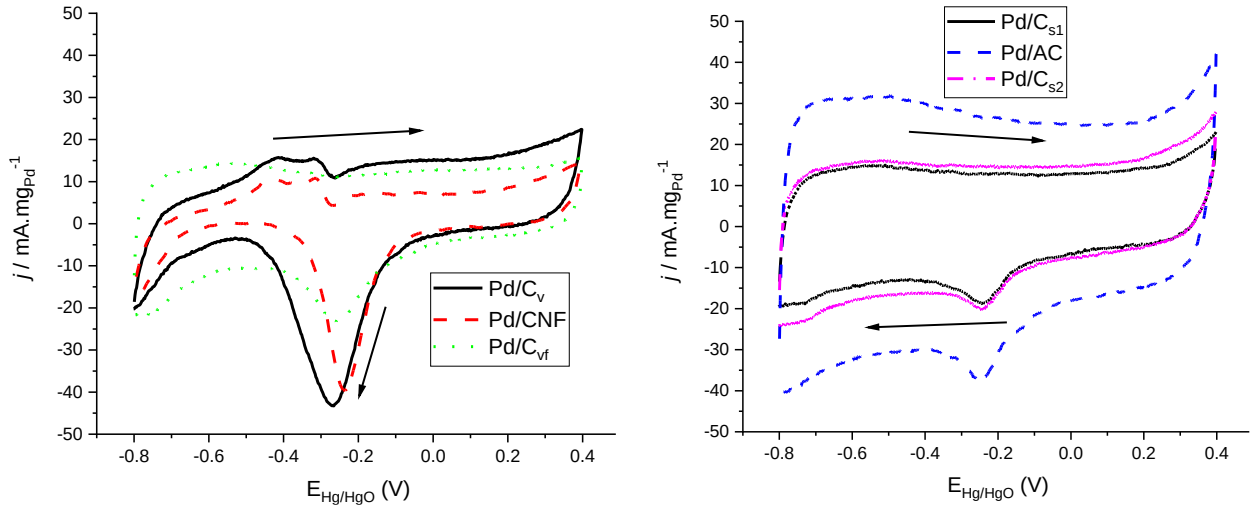

Figure 4-10 CV voltammograms of Pd/C_v, Pd/C_{vf}, Pd/C_{s1}, Pd/CNF, Pd/AC and Pd/C_{s2} in 1M KOH (scan rate = 50 mV/s)

Table 4-4 lists the electrochemical data of the 5 catalysts and among them is the electrochemical active surface area (EASA, m^2/g) which is highest in case of Pd/C_v and lowest in Pd/C_{s1} even though

the physical surface area of C_s is much more (Table 4-1) than all other supports. A similar claim could be made about C_{s2} and AC by looking to the PdO reduction peak in Figure **4-10**. Also, it worth mentioning the EASA of Pd/CNF is the second biggest after Pd/C_v although CNF is the smallest in physical surface area (Table 4-1). The higher EASA of Pd/C_v and Pd/CNF are probably due to the large pore size of CNF and C_v (close to 20 nm) compared to that of AC and C_{s1}, and C_{s2} (close to 12 nm). The surface area measured in this work are close to those reported in literature [61,64].

Table 4-4 EASA measurements of PdO reduction on Pd/C_{s1}, Pd/C_v, Pd/C_{vf}, Pd/CNF, and Pd/AC

Catalyst	-Q (mC)	RSA (cm^2)	EASA (m^2/g)	E_{onset} (mV)	i_{peak} ($mA.mg_{Pd}^{-1}$)
Pd/C_v	3.671	9.064	50.05	-445	185
Pd/C_{s1}	1.557	3.844	22.01	-362	86.4
Pd/CNF	2.026	5.002	35.02	-442	180
Pd/AC	2.068	5.106	28.00	-350	149
Pd/C_{vacid}	2.157	5.326	24.58	-355	99.5

Where -Q (mC) and RSA (cm^2) are the PdO reduction charge and real surface area of electrode, respectively

Moraes *et al*. [64] have prepared Pd-based single, bimetallic and trimetallic catalysts supported on raw Vulcan carbon and functionalised Vulcan carbon. The electrochemical surface area (EASA) they have measured is between 1 m^2/g and 20 m^2/g. Moreover, the EASA recorded for Pd/MWCNT and Pd/CuO_2/MWCNT, obtained in [71], is 3.4 m^2/g and 21.3 m^2/g, respectively. Similar values are obtained for Pd/C, PdAg/C, and PdAu/C electrocatalysts prepared in [144,145] higher EASA values were obtained, for Pd/C and PdNi/C, in [81]. Still, the current EASA values recorded for the various C-supported catalysts are higher than those aforementioned published reports.

The cyclic voltammograms of all catalysts in 0.5M KOH + EtOH is shown in Figure 4-11. The ethanol adsorption has surpassed $H_{ads/abs}$. After adsorbing ethanol, the adsorption of OH starts and therefore the actual ethanol oxidation starts as well. However, Pd/AC and Pd/C_{vf} both draw slightly higher current densities at the ethanol adsorption potentials (-0.8 to -0.6V) in the forward and reverse scans. The probable reason for this is the high oxygen content in both catalysts as confirmed by XPS (Table 4-3). The ethanol oxidation starts early on Pd/C_v and Pd/CNF at -0.442 V and -0.445 V, respectively. It starts later using the other four catalysts around -350V to -365V. The lower E_{onset} in case of Pd/C_v and Pd/CNF is an evidence of smaller activation polarisation in comparison to that in

case of using Pd/C_{s1}, Pd/C_{s2}, Pd/AC, Pd/C_{vf}. In addition to onset potential, the mass activity of Pd/C_v and Pd/CNF are much higher (≥180 mA/mg_{Pd}) than Pd/C_{s1}, Pd/C_{s2} and Pd/C_{vf} (<100 mA/mg_{Pd}). The mass activity of Pd/AC is intermediate with 149 mA/mg due to the rich surface of Pd confirmed by XPS (Table 4-3). Additionally, it is interesting as the higher pore size of Pd/C_v and Pd/CNF assures there is an enough space surrounding the Pd nanoparticles to facilitate reactant/product mass inside the porous structure and accessing the Pd active sites therein.

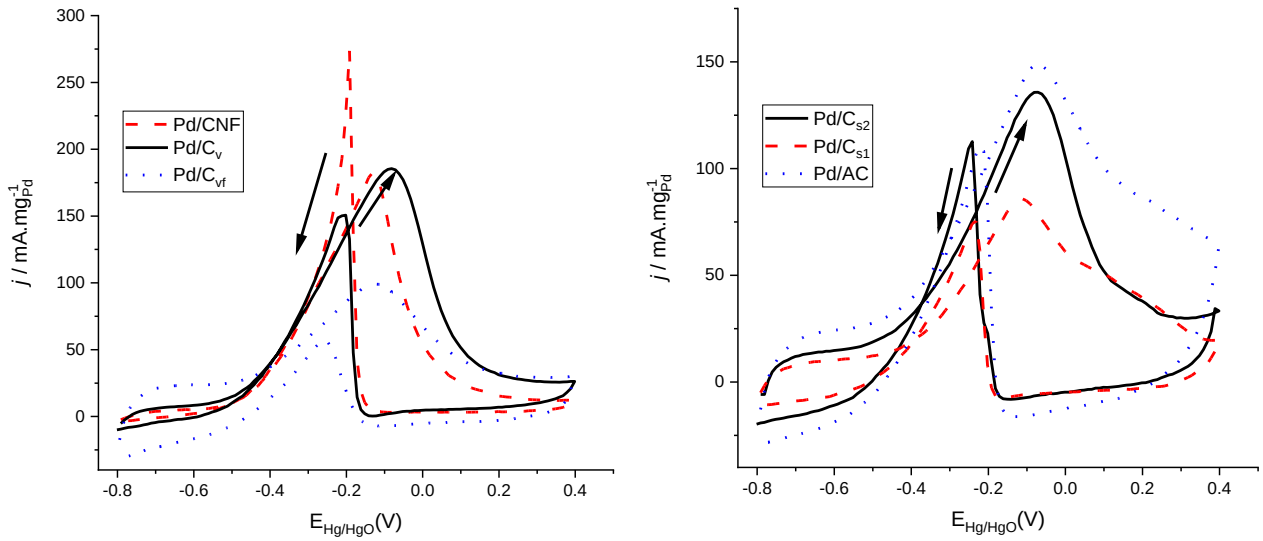

Figure 4-11 CV Voltammograms of Pd/C_v, Pd/C_{vf}, Pd/C_{s1}, Pd/C_{s2}, Pd/CNF and Pd/AC in 1M KOH, scan rate = 50 mV/s

The chronoamperometric scans of all catalysts in 0.5 M EtOH + KOH are shown in Figure 4-12. Several factors contribute the CA current value all the time of scanning. However, the initial fast decays could be mainly attributed to the diffusion of reactive species into the catalysts surface. The slow and gradual reduction in the CA current after the initial 5 mins could be related to the catalyst tolerance for poisoning species such as ethoxy and CO-like species. Some of them are strongly adsorbed to the Pd active sites and hinder their potential to be utilised for further fuel oxidation. As the times goes by, those poisons are expected to increase and therefore a decreasing current is drawn all the way through to the end. Though the 15-min period is not long enough to give a solid evaluation of the catalyst stability, it seems fair to assume no major change would happen if the test period was longer by looking at the currents drawn from all catalysts.

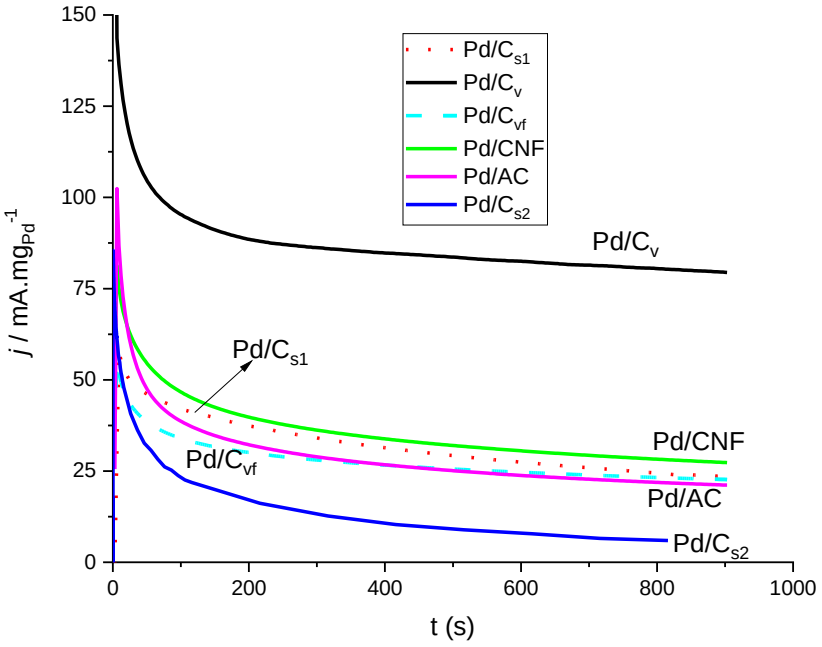

Figure 4-12 Chronoamperometry (CA) scan at -0.5 V of Pd/C_v, Pd/C_{vf}, Pd/C_{s1}, Pd/C_{s2}, Pd/CNF, and Pd/AC in 0.5 M EtOH+KOH

The Tafel polarisation results of all catalysts are shown in Figure 4-13 that were performed between -0.35 and 0.0 V vs Hg/HgO at 0.2 mV/s. This potential window is chosen because it is ethanol oxidation reaction is actively occurring by the consistent adsorption of OH species from bulk electrolyte leading to oxidation of adsorbed ethoxy. Therefore, this is the only part that resembles a straight line. At any other potential window, the data does not give a straight line. It was applied using the linear sweep voltammetry (LSV) measurement with 0.2 mV/s scan rate in 0.5 M EtOH + KOH. The lowest Tafel slope and almost fully linear is noted for Pd/C_v. The other catalysts present similar higher polarisation behaviour with more curvilinear nature and the highest one being Pd/C_{vf} indicates the harm caused the acid treatment on the Vulcan carbon functionality.

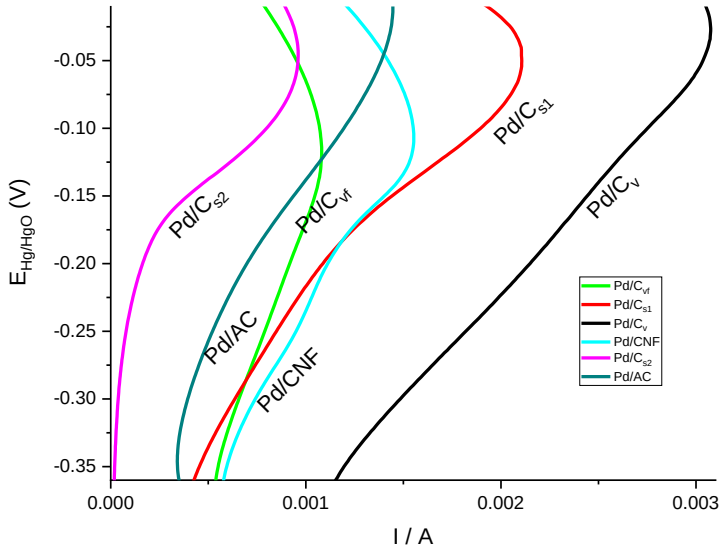

Figure 4-13 Tafel polarisation scan of Pd/C_v, Pd/C_{vf}, Pd/C_{s1}, Pd/C_{s2}, Pd/CNF, and Pd/AC in 0.5 M EtOH+ KOH at 0.2 mA/s

Figure 4-14 shows the electrochemical impedance spectroscopy (EIS) Nyquist plots of all catalysts performed in the same 3-electrode systems with 0.5 M EtOH + KOH. The EIS was performed at fixed applied potential of -0.2 V, -0.01 V, and +0.2 V vs Hg/HgO (NaOH 1M). The frequency range applied was 100 kHz to 0.01 Hz and the AC amplitude was 10 mV. The impedance measurement at -0.2 V are generally the lowest whilst those measured at +0.2 V are the highest. This is an evidence of the sluggish reaction kinetics at +0.2 V. Three phases of Z-V relation have been reported which could correlated to the typical CV Voltammograms [96]. At the activated ethanol oxidation by adsorption of OH from the electrolyte (-0.5 V to -0.1 V), the measured impedance records decreasing values by increasing the applied potential. The same is valid for the high potential region (+0.1 V to +0.4 V) where the catalytic sites are gradually lost by increasing the potential. Yet, between -0.1 V and +0.1 V, it is a controversy. Some researchers have found a negative Niquist plot in the 2nd quadrant and others have still found a first quadrant impedance plots [96,120,146,147].

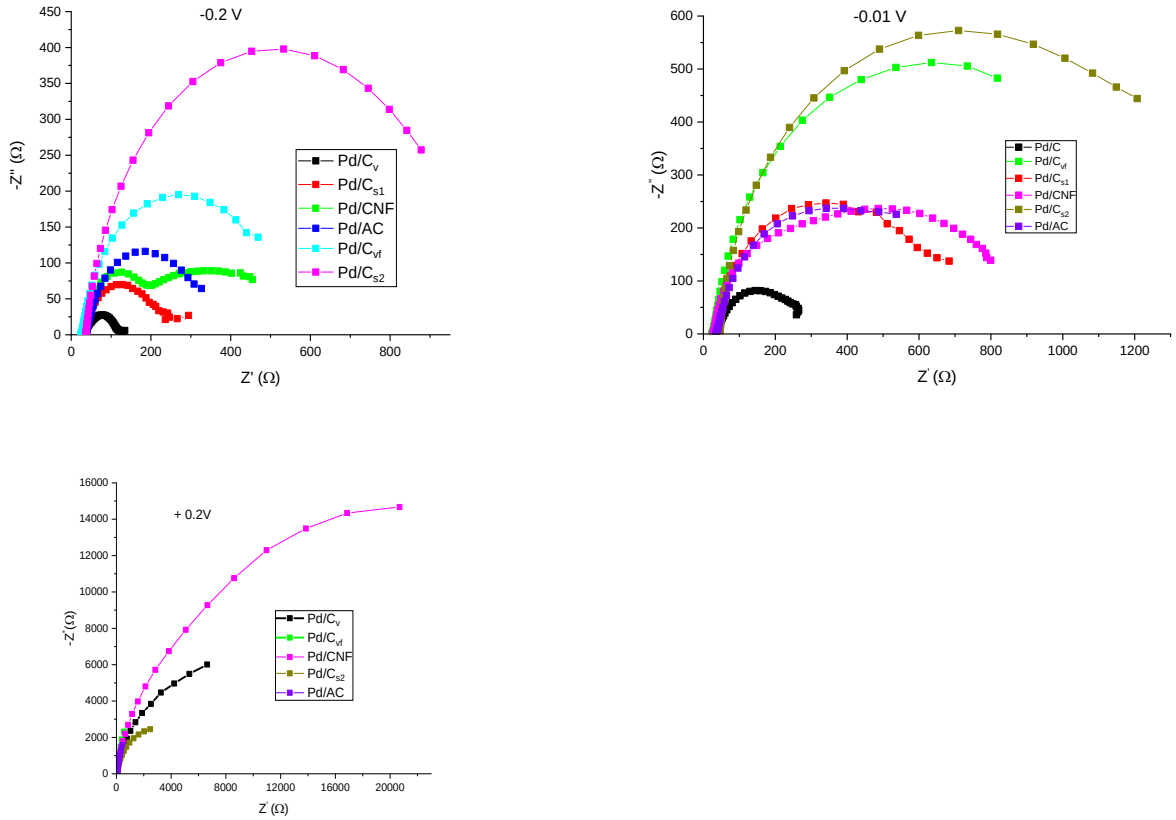

Figure 4-14 Potentiostatic EIS spectra of Pd/C_v, Pd/C_{vf}, Pd/C_{s2}, Pd/CNF, and Pd/AC in 0.5M EtOH + KOH at -0.2 V, -0.01 V and +0.2 vs Hg/HgO

Comparing the 6 catalysts by examining the individual EIS plots, it is clear that Pd/C_v records the lowest impedance values. The smallest semi-circle arc is obtained with applying Pd/C_v almost regardless of the applied potential. This proves the charge transfer resistance (R_{ct}) is smallest on Pd/C_v. R_{ct} is directly linked to the catalyst activity as explained in section 3.2.6 and activation polarisation. Also, R_{ct} is directly impacted by the applied potential unlike the double layer capacitance which barely changes with increasing or decreasing the applied potential. Pd/C_v having the lowest R_{ct} values proves the enhanced reaction kinetics compared to the other catalysts at the same conditions. Pd/C_{s1}, Pd/CNF, and Pd/AC record close impedance values compared to one another at -0.2 V and -0.01 V. This could be explained that high activity contributed by the high surface area of C_{s1} and AC is counter-balanced by the abundantly exposed Pd particles on CNF surface. It should be mentioned here the high conductivity of CNF compared to AC and C_{s1}. It is useful to mention the electric conductivity of amorphous carbon is 1.25 to 2 kS/m while that of graphite increases to 3 kS/m [148]. One challenge facing direct alcohol fuel cells is the progressive

carbonation due the reaction between CO_2 and water. This issue is addressed by applying a solid anion exchange membrane in stead of the liquid electrolyte. However, the carbonation effect is not studied in this work.

Based on the obtained electrochemical and physical results, the support physicochemical properties – such as surface area, pore size, and crystallinity - could be correlated to the electrocatalytic performance of each C-supported Pd catalyst. The electrocatalytic factors that could be considered to reflect the particular catalyst activity are the onset oxidation potential (E_{onset}, V), oxidation current peak (j_p, mA), and the steady state chronoamperometric current (j_{ss}, mA, after 15 min in this case). The lower E_{onset} (V) is suggestive of more efficient oxidation reaction that reveals more *Faradaic* efficiency is obtained applying a certain catalyst. The oxidation current peak (j_p, A/mg_{Pd}) is, also, an important factor that could reflect the number of active sites on a certain surface and the level of their reaction with ethanol. Finally, the steady state current (j_{ss}, A/mg_{Pd}) – obtained from the chronoamperometric scans – is a reflection of the particular catalyst tolerance towards poisoning species. The electrocatalytic performance (ECP) could be approximately expressed as in equation (4.1).

$$\boldsymbol{ECP = \{-E_{onset}\,(\mathrm{V}) + j_p\left(A.mg_{Pd}^{-1}\right) + j_{ss}\left(A.mg_{Pd}^{-1}\right)\} * 10} \qquad \textbf{(4.1)}$$

The onset potential for oxidation reactions is usually negative and therefore the negative sign. Figure 4-15 shows the electrochemical performance (ECP) of Pd nanoparticles supported on various carbons following some physicochemical properties such as surface area, pore size and crystallinity. Looking at the surface area graph, it is interesting that the high surface area carbons (C_{s1}, C_{s2}, and AC) – around 1000 m^2/g - produce lower electrochemical performance than the lower-surface area CNF (60 m^2/g) and C_V (230 m^2/g). This is interesting because it is usually thought the higher surface area could generally promote catalytic performance of any catalyst. The high surface area of AC, C_{s1} and C_{s2}- as the TEM image demonstrate- did not enable wide dispersion and production of small-sized Pd nanoparticles. On the contrary, the Pd particles supported on Vulcan carbon are well dispersed which is noted too on CNF though significant instances of agglomeration could be seen on the latter. Therefore, additional factors seem to play important roles in the support functionality for ethanol oxidation. The effect of pore size shown in the same figure may help explain the contradicting surface area finding. The high-surface-area and low-pore-size carbons (C_{s1}, C_{s2}, and AC) –10 to 12 nm as shown in Figure 4-2– seem to produce low performance with varying degrees. On the other hand, the high-pore-size carbons CNF and C_v (20 – 22 nm) produce enhanced electrochemical performance.

One additional difference is that the XPS measure traces some Pd exists in an oxide state on Vulcan carbon while only metallic state exists on CNF. This in favour for the catalytic functionality of CNF-supported Pd. However, the latter suffers from particle aggregation more than the former. A significant PdO presence was is also noted on Pd/C_{s1}. Geraldes et al. [73] concluded that using a MWCNT presents a better support functionality for ethanol oxidation than Vulcan carbon. Unlike the CNF applied in this work, the MWCNT in that study enable better dispersion of Pd nanoparticles than the C-supported counterpart.

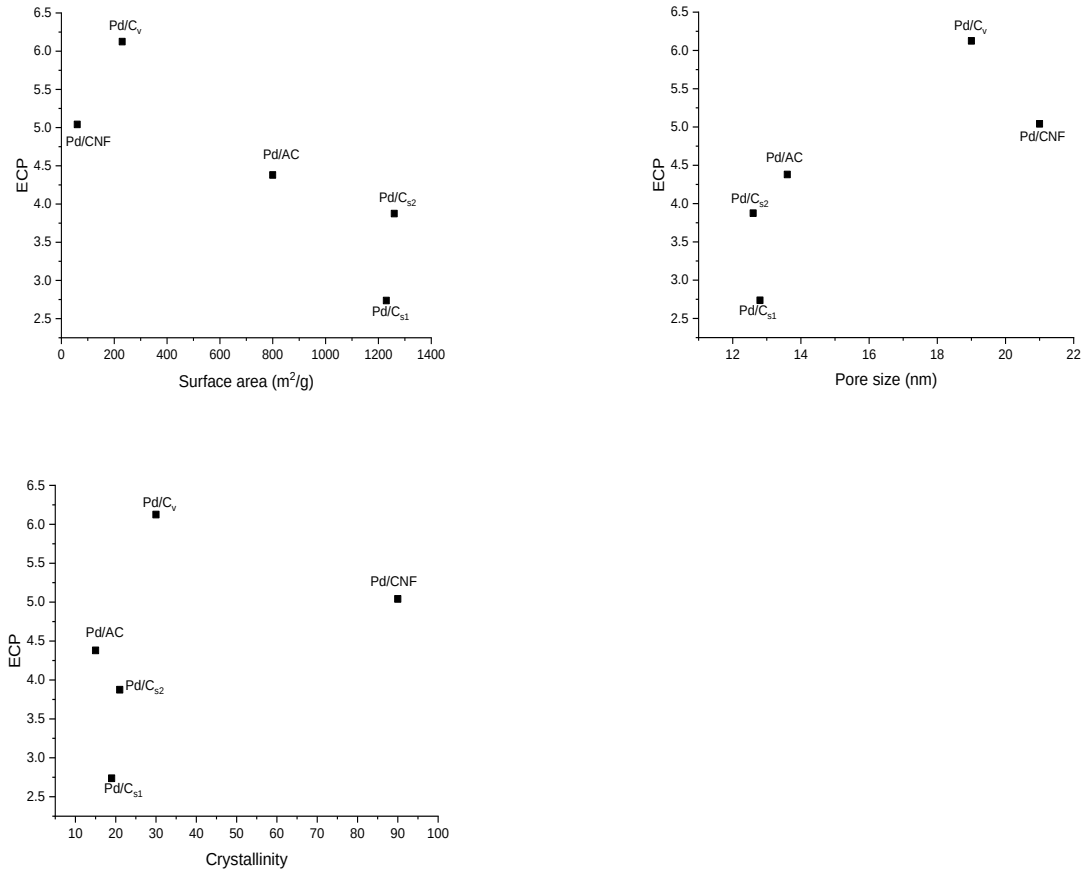

Figure 4-15 The Electrochemical Performance (ECP) vs surface area, pore size, and crystallinity of the supports Cs1, C_{s2}, AC, C_v, and CNF

It should be highlighted the full understanding of the impact of changing the carbon physiochemical properties on Pd ethanol oxidation needs a more accurate knowledge of the mass/charge transport processes occurring at the electrode/electrolyte interface in addition to the housing of that interface on the various carbon structures by making use of a more sophisticated investigation into the fundamentals of physical electrochemistry. Such high-level of expertise should probably be the focus

of some future work. As was reported in the review of Centi *et al.*[17], the multi-phase boundary including reactants, electrons, ions, surface reactive sites forms only a minor fraction of the electrode volume. For instance, while electrons need crystalline order for mobility, molecules need space for moving through the carbon pores. Therefore, the design need is to realise an optimal physical space for the multifunctional electrochemistry. Thus, this work tries to only correlate the ethanol oxidation electrochemical results to the carbon support structure. For example, the XRD measurement of Pd/CNF and Pd/C_v confirms that the shift of diffraction angles to the right is minimal unlike the other high-surface area carbons. That might suggest the high-surface-area carbons have caused a compressive stress/strain on the Pd lattice and that is why the smaller lattice parameter. Like the pore size, the higher degree of crystallinity seems to enhance the catalytic functionality of the support such as CNF. It should be mentioned the degree of crystallinity measurement is not accurate but approximate following the intensity of the C hexagonal peak at 25 degrees. As CNF has a highly intense and sharp peak, it is estimated with a 90% crystalline but all the other carbons generally have a much broader peaks which suggests their degree of crystallinity is between 15 to 25%.

4.3 Conclusions

Based on the presented results and reviewed literature, some conclusions could be drawn. First of all, the key conclusion is that Vulcan carbon (XC72) is the best functioning support from the tested materials. Also, the polyol process could be applied to produce Pd nanoparticles supported on various mesoporous carbons confirmed by XRD, TEM, and XPS analyses. The TEM images and XRD data show that the smallest Pd particles are produced on the Vulcan carbon and the largest particle aggregation is noted on CNF which is shown to be the only highly ordered crystalline support unlike the other carbons. The XRD, also, confirms that the Pd lattice is contracted – compared to the bulk Pd diffraction data - on all carbons though the smallest contraction is noted on the Vulcan carbon and carbon nanofibres. The TGA results confirm that the activated charcoal (AC) contains the highest content of moisture, organic residues and carboxylic groups (XPS supports its high oxygen content as well) and that the acid activation performed on the Vulcan carbon could also increase their content. Also, according to TGA results, raw Vulcan carbon and CNF are the least-containing of them.

The BET measurements confirm that CNF has the smallest physisorption area while the highest are the carbon selectivity 1 and 2. In terms of the surface area, Vulcan carbon is intermediate between CNF on one side and C_{s1}, C_{s2}, and AC on the other. Yet, the pore size of CNF and Vulcan carbon is

close to 20 nm while those of C_{s1}, C_{s2}, and AC are close to 10 nm. XPS measurements show that the Pd atomic concentration in each catalyst is close to one another, but a significant oxide presence is noted only on Vulcan carbon. However, the electrochemical testing has shown the Vulcan carbon presents the highest functionality as a Pd support. CNF is inferior to C_v potentially because of the significantly smaller surface area which has caused particle aggregation. And the small-pore-size carbons (AC, C_{s1}, and C_{s2}) have presented a much lower ethanol oxidation performance even though their high surface area and mesoporous structure.

Thus, the support surface area is an important factor for the catalytic performance but there are other conditions equally important to be met for a functional support. The adequate pore size is also significant promoter to the redox kinetics of ethanol oxidation. A large pore size (a proximately 20 nm) in case of C_v and CNF has clearly outperformed the smaller pore size Cs_1, C_{s2}, and AC (10 nm) as Pd support for ethanol oxidation. The potential reasons for this are the well-exposure of Pd particles on the external surfaces of the former two and also the further facilitated mass transport on them (though this acquires diffusion measurement to be validated). Also, the support crystallinity could enhance the catalytic activity of Pd for ethanol electrooxidation. The crystalline support nature promotes the conduction of smaller Pd nanoparticles and the charge transfer during redox reactions. This helps explain the good CNF potential as a support even though it's small surface area and the Pd particle aggregation tendency on it. It suffices to say that surface area, develop porosity, and crystallinity are three key physiochemical characteristics that must be considered together upon choosing a carbon as a catalyst support. Furthermore, none of them shall be overlooked in favour of another as balance of the three remains a key for the ethanol reaction kinetics.

Chapter 5: ETHANOL OXIDATION PDAUNI CATALYSTS USING DIFFERENT BOROHYDRIDE REDUCTION ROUTES

Many Pd and Pt researchers have focused on the synthesis binary Pd-based catalysts for ethanol oxidation by adding a 2nd cocatalyst metal to prepare bimetallic catalysts. A few, however, have prepared trimetallic combinations such as PdAuNi [131,132] and PdAgNi [149]. In this chapter, 3 different borohydride reduction techniques - SBIPP, SBEG, and 3step - are pursued to synthesize PdAuNi nanoparticles supported on Vulcan carbon (XC72). The monometallic Pd/C by SBIPP is also prepared for comparison. The catalysts are physically analysed by means of XRD, TEM, EDX, and XPS. Moreover, the catalyst is evaluated for ethanol oxidation by running the tests of cyclic voltammetry (CV), chronoamperometry (CA), Tafel polarisation, and electrochemical impedance spectroscopy (EIS).

5.1 Materials and Methods

Three different PdAuNi/C catalysts, which are PdAuNi/C_{SBEG}, PdAuNi/C_{SBIPP}, and PdAuNi/C_{3step}, were prepared using three different protocols. The aimed metal loading was 12 wt. % approximately. Although laboratory research usually loads the carbon support with 20 Wt.% to 40 Wt.% of metal (to ensure a high presence of metal on support), this work aimed to come down close the industrial catalyst loading of 5 Wt.% metal loading [9,150]. The reasons for choosing low metal loading are to consume fewer noble metals, reduce the potential of particle aggregation, and increase the dispersion. The small metal loading will enhance the dispersive separation of metal nanoparticles by reducing the potential for particle agglomeration resulting from less collective surface energy. The SBEG, SBIPP, and 3step refer to reduction by sodium borohydride-ethylene glycol, sodium borohydride-2-propanol alcohol, and 3-step reduction, respectively.

The first protocol (SBEG) is by using the $NaBH_4$-ethylene glycol complex following [151–153] with little modification. Vulcan carbon (202 mg) was dispersed and sonicated in ethylene glycol (10 mL). Then, the respective quantities of the metallic precursor solutions $PdCl_2$, $AuCl_3$, and $NiCl_2$ were suspended in another 10mL of ethylene glycol for a few minutes. Then, a solution of $NaBH_4$ (20 mL) was prepared and added very slowly to the metal precursors' mixture under magnetic stirring. Meanwhile, the carbon suspension was added too. Then, the mixture was heated to 35˚C and kept at that temperature for 3.5h. Then, the mixture was left to cool down and washed copiously with deionized water till neutralisation. Following, it was dried in vacuum oven at 80 ºC for 2h

The second applied $NaBH_4$ reduction protocol (SBIPP) follows [121,154,155]. The Vulcan carbon and metal precursors were sonicated in a mixture of 2-proanol and water (50/50 v/v). KBr was added to act as a capping agent. This is achieved through the anion exchange method which informs the larger Br^- has the potential to replace the smaller Cl^- ion. Then, the Br^- would surround the metal nanoparticles and act as a capping agent. KBr/Metal atomic ratio equals 1.5. Then, the mixture was stirred for 10min followed by adding $NaBH_4$ solution (0.5M, 15mL) in one portion. Then, it was stirred for 30 min. Following, washing by vacuum filtration was undertaken. Finally, the wet powder was dried at 80 ºC in vacuum oven overnight.

The third protocol to prepare PdAuNi/C (3step) aimed to compare the previous co-reductive protocols to the sequential 3-step reduction of metals on carbon surface. The SB-IPP reduction complex was once more used to prepare this catalyst. Initially, Ni was reduced on carbon followed by Au and finally Pd was reduced. The procedure started with sonicating Vulcan carbon (202.4 mg)

in a mixture of isopropyl/water (50/50 v/v). Then, the $NiCl_2$ was added kept in the solution under stirring for 1h as Ni is the most difficult to reduce. Following, $AuCl_3$ was added and kept for 30 min. Finally, $PdCl_2$ was added and kept for 30 min.

After doing most of the physical and electrochemical analyses for the above three catalysts, it was found the best performing catalyst is the one prepared by metal co-reduction using the SB-IPP complex. To elucidate the impact of adding both Au and Ni onto Pd, a monometallic C-supported Pd catalyst (Pd/C_{SBIPP}) was prepared using the same procedure.

5.2 Results and discussion

5.2.1 XRD

Figure **5-1** shows the XRD pattern of the catalyst. The peak at 25º is due to the graphitic structure of Vulcan carbon (XC72). It also shows the crystalline peaks of Pd (111), (200), (220), and (311) facets. Dutta *et al.* have also prepared PdAuNi trimetallic using a different $NaBH_4$ reduction route and have found separate peaks of Pd, Au, and Ni in their XRD patterns. This could be explained by the high segregation occurring in their prepared catalyst that leads to different phases rich in Pd, Au, and Ni giving separate XRD peaks.

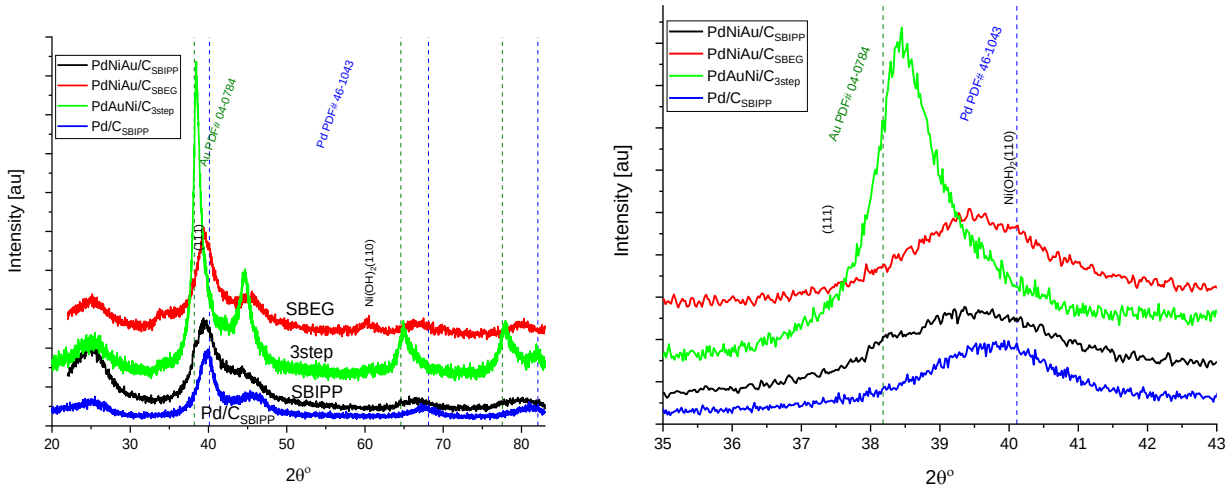

Figure 5-1 XRD Patterns and enlarged (111) peak of $PdAuNi/C_{SBEG}$, $PdAuNi/C_{SBIPP}$, Pd/C_{SBIPP} and $PdAuNi/C_{3step}$

The three trimetallic catalysts prepared, in this work, do not suffer from such high segregation except the shown $Ni(OH)_2$ peak - in the SBEG and 3step samples - which is extensively agreed on for Ni

synthesis. There is a noticed shift to the left in the diffraction angles of Pd peaks and that is because the alloying potential between Ni, Pd and Au. The same finding was reported about the PdAuNi was reported by Wang's group [132] whose PdAuNi catalyst did not present separate Au peaks from the Pd ones.

This is the opposite finding to that of Dutta *et al.* [131] who found the trimetallic system has led to a lattice contraction by simultaneously adding Ni and Au to Pd. The reflections lie between pure Pd (PDF#46-1043) and Au (PDF#04-0784) which suggests a nanoalloy has been formed between Pd and Au. While Au is known to expand the Pd lattice and therefore shift the Pd peaks to lower diffraction angles, Ni is less likely to bring significant changes onto the Pd lattice and shifts the Pd peaks to higher ones (from application point of view according to all PdNi publications reported herein). Theoretically, Ni, having a smaller lattice constant, could contracts the Pd lattice and shift the XRD peaks to higher angles. Yet, the degree of alloying between Au and Pd is known to be stronger than Pd and Ni [99,107,131,132,139]. Using the Pd (220) peak details and Bragg's law, the interplanar distance for the 4 catalysts was found 1.39 Å, 1.40 Å, 1.39 Å, and 1.43 Å for Pd/C_{SBIPP}, PdAuNi/C_{SBIPP}, PdAuNi/C_{SBEG}, and PdAuNi/C_{3step}, respectively. The highest interplane distance (4 Å more than Pd) is noted for the 3-step catalyst is calling for attention as also its XRD peaks are highest to be shifted towards pure Au from Pd peaks. The $PdAuNi_{3step}$ peaks are actually much closer to Au ones unlike the other three samples as shown in Figure **5-1**. The 3-step method involved initially Ni reduction followed by Au and finally Pd. This could explain the high XRD peak shift towards Au as a core@shell of Au@Pd seems to have been prepared. As for the SBIPP and SBEG samples, their XRD patterns suggest both Au and Ni have been incorporated into the Pd lattice since there is almost no change in the interplanar distance from the monometallic Pd. Also, distinguishable peaks of $Ni(OH)_2$ could be noted at 35◦ and 60◦, which is not unusual for Ni synthesis by chemical reduction [107,131,139,156]. The $Ni(OH)_2$ peaks are more pronounced in case of PdAuNi/C_{SBEG} than PdAuNi/C_{3step}. The crystal size is estimated using the Scherrer equation (using the (220) peak details) and is estimated to be 3.00 nm, 3.04nm, 3.84 nm, and 3.04 nm for the Pd/C_{SBIPP}, PdAuNi/C_{SBEG}, for PdAuNi/C_{3step}, and PdAuNi/C_{SBIPP}, respectively. The Au is known to shift the Pd XRD peaks as was reported [37,98–100,102,103,157–161]. This could also be concluded here for the PdAuNi samples.

5.2.2 EDX

EDX quantitative analysis and elemental maps of PdAuNi/C_{SBEG} – shown in Figure 5-2 – are recorded at 20kV and 10kV, respectively. The two voltages are applied to study the sample composition at different depths that could be changed by changing the accelerating voltages. The EDX maps and spectra were recorded at 5000x magnification and over an area of 400 μm^2. It is noteworthy that, as has been discussed in section 3.1.2, the EDX beam penetrates the sample to a certain depth according to the accelerating voltage and the mean atomic number. The atomic number is not a crucial factor in this study since the main constituent (> 80 Wt.%), Vulcan carbon, is applied as a support in all catalysts. The EDX electron beam sample penetration depth could go from 0.2 µm to 2 µm [162,163]. Two accelerating voltages are applied: 10 kV and 20 kV which are expected to impact the penetration depth. As the sample was prepared by drop-casting of the powder + ethanol suspension on the carbon tape, the sample thickness is less than 100 µm. Therefore, the expected depths of both 10kV and 20kV are anticipated to be approximately >0.5 µm and > 1 µm, respectively. The quantitative analysis has shown – applying both voltages the surface is dominated by Ni (3.25% at 20 kV and 3.54 at 10 kV), followed by Pd (0.91% at 20 Kv and 0.81% at 10kV), and the least is Au (0.31% at 20kV and 0.30% at 10kV). Unlike Pd and Au, the Ni concentration at 10 kV is more than its concentration at 20 kV and the reason is the high surface energy of Ni (2.69 Jm^{-2}) compared to Pd and Au whose surface energy values are 1.88 and 1.61 Jm^{-2}, respectively [164]. This is in agreement with the XRD results (Figure **5-1**) which shows distinctive $Ni(OH)_2$ peaks. Looking at the Pd and Au maps (at 20kV and 10kV), it is clear both metal are homogeneously distributed all over the area of the sample. The opposite is noticed looking at the Ni maps where some more intense green areas than others in the sample could be seen. It is found the same spots where the green Ni colour is more intense are the same locations where the O is more intense too. The reason for this match is the fact that almost all Ni exists in the form oxide and hydroxide.

Table 5-1 shows the EDX quantitative analyses of PdAuNi/C_{3step} recorded at 20 kV and 10 kV. Unlike the previous SBEG sample, the Pd content increases in this one and that is probably because Pd was the final metal to reduce after Ni and Au. The interesting thing, also, is the Ni content at 10 kV is still higher than that 20 kV even though Ni was the firstly reduced on C surface. The Au content behaves in the same way as with the SBEG one. The EDX maps (Appendices) show no individual metal segregation occurring of Pd, Au, and Ni.

Table 5-1 EDX quantitative analyses of PdAuNi/C_{SBEG}, PdAuNi/C_{SBIPP}, and PdAuNi/C_{3step}

Catalyst	Acc. Voltage	Pd At.%	Ni At.%	Au At.%
PdAuNi/C_{SBEG}	10 kV	0.88	3.54	0.30
	20 kV	0.91	3.25	0.31
PdAuNi/C_{3step}	10 kV	1.58	2.35	0.66
	20 kV	1.62	1.85	0.67
PdAuNi/C_{SBIPP}	10 kV	1.80	2.90	0.67
	20 kV	1.75	2.52	0.63

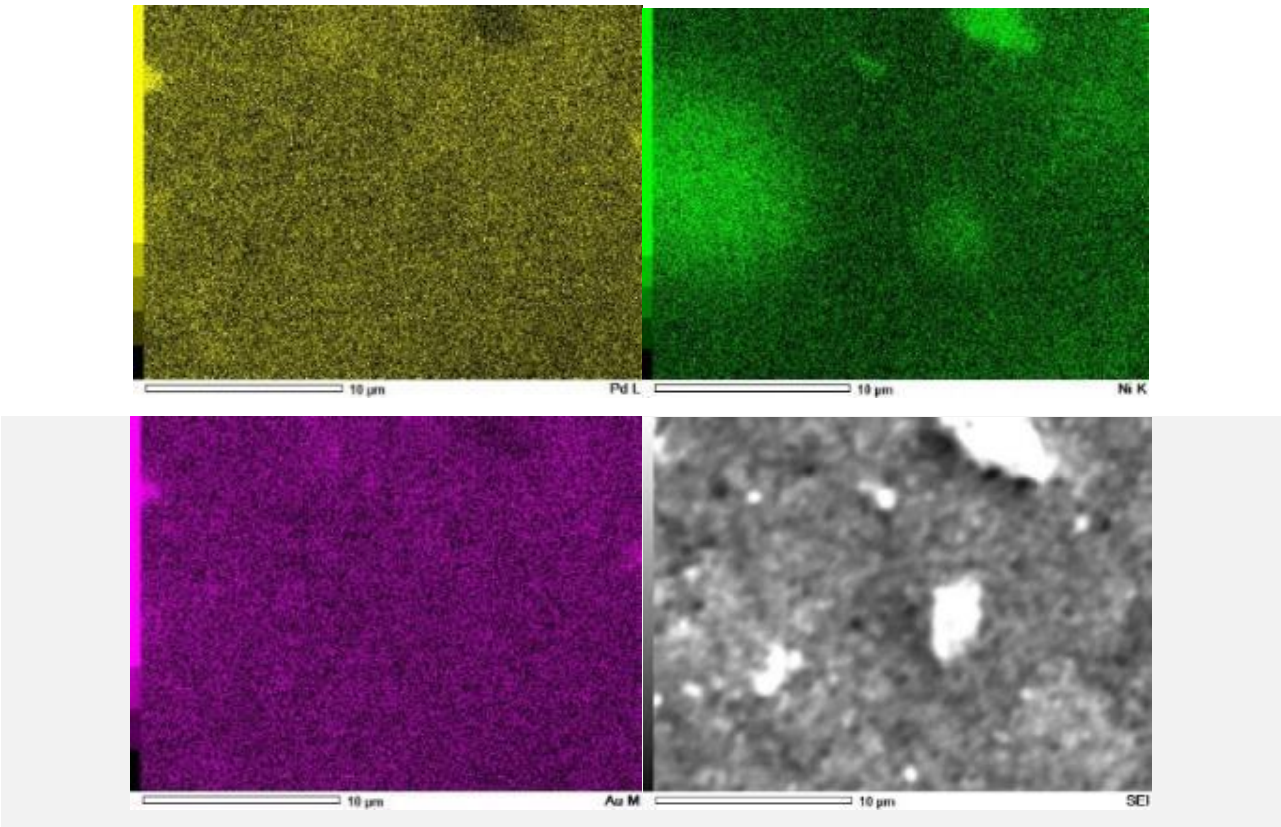

Figure 5-2 EDX elemental maps (Pd, Au, Ni) at 20 kV of PdAuNi/C_{SBEG}

Also, Table 5-1 shows the EDX analysis results of PdAuNi/C_{SBIPP} recorded at 10 kV and 20 kV. Once again, the Ni concentration measured at 20 kV is less than that at 10 kV. However, the Ni increase detected at 10 kV is not significantly higher than that at 20 kV unlike the two other catalysts. The potential reason is the better mixing potential of Pd, Au, and Ni that occurs applying the $NaBH_4$-2-propanol compared to the 3step reduction and $NaBH_4$-ethylene glycol methods. Furthermore looking at the three maps of Pd, Au, and Ni, there are easily seen segregated parts in the three maps but they are unified for the three metals. This could be translated in terms of the good alloying

potential of the three metals applying the SBIPP preparation protocol as also suggested by the shift the XRD peaks pattern (Figure **5-1**). These data, however, may not an enough evidence to suggest an alloy of PdAuNi was, actually, formed.

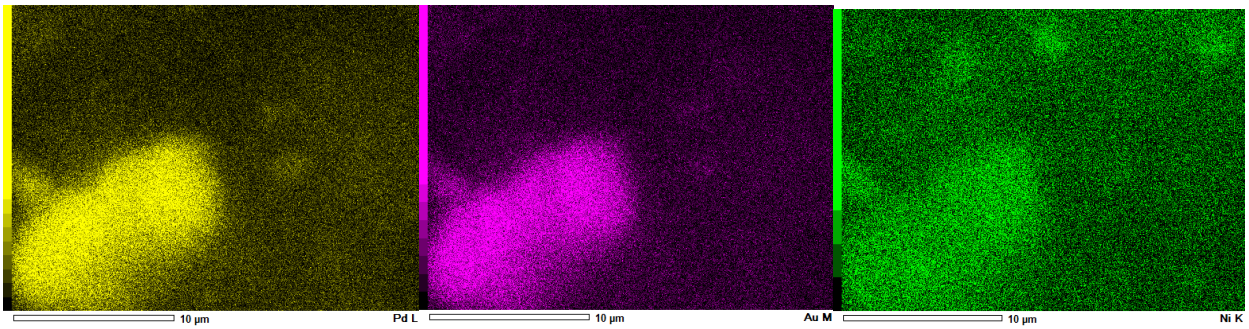

Figure 5-3 EDX Maps (Pd, Au, and Ni) at 20 kV

Table 5-2 lists the different metal concentrations in each catalyst powder quantified by the ICP-OES. These numbers are treated with caution as sometimes the metal nanoparticles are buried in the pores of the carbon in a way making them inaccessible for the oxidation by aqua-regia prior to ICP analysis. Different quantities have been detected for the three intermetallic samples. The SBEG and 3step reduction samples has presented a much higher Ni content compared to the SBIPP protocol. Although the latter procedure shows only 9 mg (Ni), 27 mg (Au), and 51 mg (Pd), its atomic Pd:Au:Ni ratio equals 3:1:1. On the contrary, the atomic Pd:Au:Ni ratios in case of the 3step and SBEG catalysts are 2:1:5 and 9:1:31, respectively. This indicates the SBEG catalyst is highly rich in Ni and is quite poor in Au. Moderate proportions are achieved in the other catalysts. It could be concluded PdAuNi/C_{SBEG} whose surface seems rich in Ni and poor in Pd, but its core seems rich in both Pd. The XPS results in Table 5-3 also seem to support the ICP-OES and EDX results.

Table 5-2 ICP-OES results of metal concentration in Pd/C_{SBIPP}, PdAuNi/C_{3step}, PdAuNi/C_{SBIPP}, and PdAuNi/C_{SBEG}

Catalyst	Pd (mg/1 g powder)	Au (mg/1 g powder)	Ni (mg/ 1g powder)
Pd/C_{SBIPP}	120	-	-
PdAuNi/C_{3step}	75	54	90
PdAuNi/C_{SBIPP}	51	27	9
PdAuNi/C_{SBEG}	57	10	100

5.2.3 TEM

Figure 5-4 shows the TEM micrographs of the prepared catalysts in which some round and quasi-spherical metal particles appear on the carbon support. For the four images, the particle size of Vulcan carbon ranges from 30 to 60 nm. The same finding is abundantly reported in the cited literature in this thesis. For the monometallic Pd/C catalyst, well-dispersed small particles (3.6 nm in average) and yet there are observable segments of particle agglomeration.

Using the same method, a trimetallic PdAuNi/C_{SBIPP} is shown, which shows a smaller particle size (3nm) and better dispersion on the Vulcan carbon. Examining both Pd/C_{SBIPP} and PdAuNi/C_{SBIPP} it could be seen the synthesis of multimetallic system produces a smaller particle size and less particle agglomeration. The potential reason a monometallic system maximizes the surface energy that attracts the particles to one another. In multimetallic systems, the difference in metal surface energies balances the tendency for attraction of monometallic particles. The other two methods have produced small metal nanoparticles of intermetallic PdAuNi, but if compared to the SBIPP co-reduction, more particle aggregation has occurred using them, especially on the SBEG. The higher particle aggregation would have an obvious effect on the electrocatalytic activity of the prepared catalysts. For the SBEG PdAuNi, very high agglomeration could be seen unlike the SBIPP method. This is in part due to the reaction complex of ethylene glycol and $NaBH_4$.

Pd/C_{SBIPP}

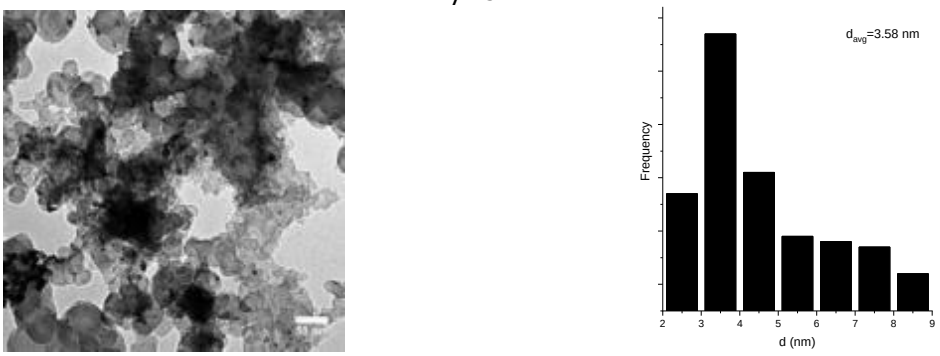

PdAuNi/C_{SBIPP}

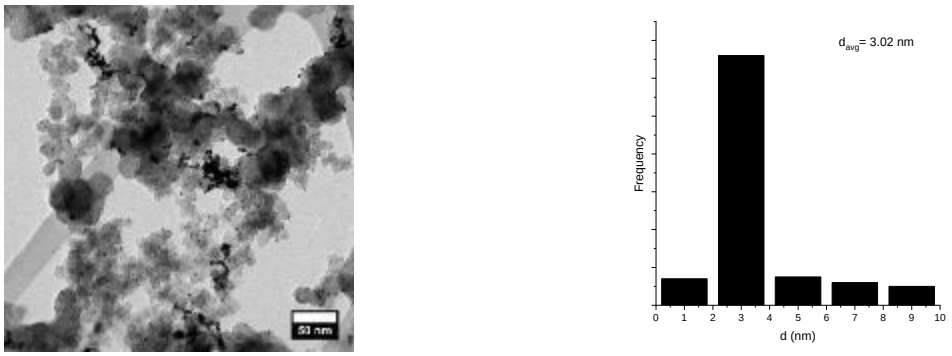

PdAuNi/C_{SBEG}

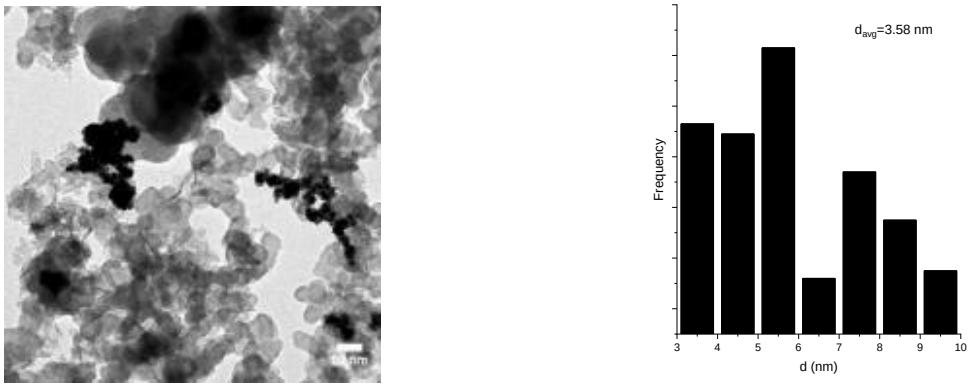

PdAuNi/C_{3step}

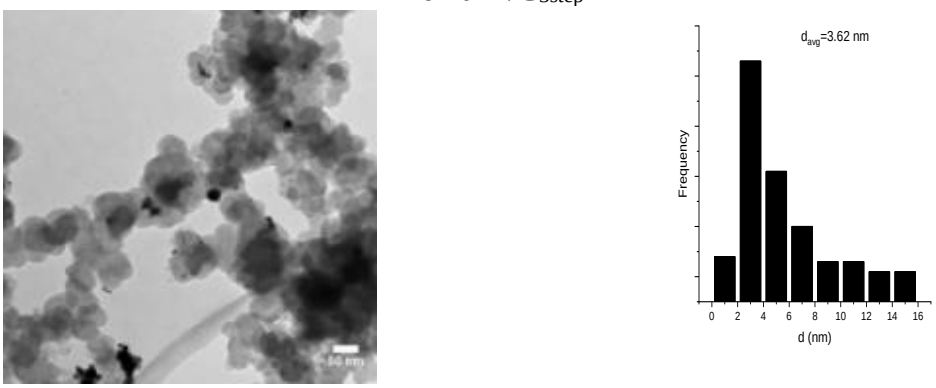

Figure 5-4 TEM Micrographs of Pd/C_{SBIPP}, PdAuNi/C_{SBIPP}, PdAuNi/C_{SBEG}, and PdAuNi/C_{3step}

Also, another thing about the SBEG method that the carbon support was added during the slow addition of $NaBH_4$ to the reactant mixture. The easiest to reduce from the metals is Au followed by Pd and finally Ni. Yet, from the TEM micrograph, it could be seen the metal species are in a state of high coalescence that might have been established even before the addition of carbon support. This might be an indicative that the carbon support is better impregnated with the metal precursors before adding the reducing agent. As was explained in section 5.1, the metal precursors were initially dispersed in ethylene glycol. Then $NaBH_4$ was then drop-wise added and during that the carbon support was added. It could be understood after the initial addition of $NaBH_4$, some (or all) of the metal species were immediately reduced and due to their high surface energy, they segregated into each other. Then, when the carbon was added, the support-metal interaction was not strong enough to separate the metal particles from one another. Therefore, the metal particles endured their aggregating coexistence on the carbon surface. However, the one-step reduction is not likely to produce merely a mixture of metal nanoparticles and carbon. The reduction process includes two steps: nucleation and growth both of which are expected to take place inside the carbon pores. Then, the carbon porous plays a role in preventing the particle agglomeration.

As a result, many carbon big particles could be seen clear of any metal particle. As for the 3-step reduction, the particles are highly segregated - though less than PdAuNi/C_{SBEG} - but more than PdAuNi/C_{SBIPP} and Pd/C_{SBIPP}. The highest particle size was attained with the three steps of reduction. In general, the particle size obtained for the three catalysts is less than those obtained for other PdAuNi nanoparticles reported in other publications [131,132], but higher than PdNi [81,106,107,139] and similar to PdAu nanoparticles [37,100,104,143,158,159,161]. Other higher particle sizes of PdAu are reported in [99,102]. B

5.2.4 XPS

Table 5-3 and Figure 5-5 show the X-ray photoelectron spectroscopy data results of PdAuNi/C_{SBIPP}, PdAuNi/C_{SBEG}, PdAuNi/C_{3step}, and Pd/C_{SBIPP}. It is noteworthy that the sampling depth of XPS is from 1 to 30 nm. In other words, XPS results are suggestive of the composition of the top 10 atomic layers [165]. This is possible although the X-rays could penetrate several millimetres of the sample because the photoelectrons excited from deeper layers lose their kinetic energies due to the long distances they have to travel in the solid [166]. Therefore, it is assumed that only the signals of the external surfaces that are detected and processed [167]. For the monometallic Pd/C, Pd exists in a metallic and an oxidized form (Pd^0/Pd^{2+}= 4/1). Furthermore, the Pd $3d_{5/2}$ of Pd/C_{SBIPP} is located 335.43 eV

which is 0.43 eV higher than the bulk Pd. This shift means Pd has lost electrons and is probably because of the Pd-C strong interaction [98]. This also probably explains the opposite shifted noted in the PdO peak which is located at 335.98 eV which is less than the PdO bulk at 336.7 eV [168].

In case of PdAuNi/C_{SBIPP}, the Pd $3d_{5/2}$ peak is shifted to a lower binding energy than that of Pd/C_{SBIPP} at 335.29 eV and no PdO is detected. With this 0.69 eV shift, a net electron gain into Pd has occurred. the Au $4f_{7/2}$ peak is located at 83.63 eV which is less than the bulk Au of 84 eV. This net negative shift means Au has gained electrons. On the contrary of Au and Pd, the Ni 2p peak (Ni and $Ni(OH)_2$) are shifted to higher binding energies (the shift is close to 1 eV for $Ni(OH)_2$). This suggests Ni has lost electrons and probably its electrons are gained by Au and Pd. In case of the three trimetallic catalysts, Pd exists only in a metallic state. The potential reasons for this is the presence of Ni which is more oxyphilic and the enhancement of Pd air stability brought by Au as well [158,159]. Ni is not only oxyphilic, but it is also reported to enrich the surface - when reduced with Pd - even when Ni is much less than Pd [156]. This could be explained that some Pd surface might be blocked from air contact by the Ni above it. This is also noted in the current work in case of the trimetallic prepared by SB-EG complex, for which a Ni-rich (2.19%) surface and Pd- (0.13%) and Au- (0.02%) rich core has been produced. A similar, but not identical conclusion was found in [169]. However, this contradicts what was found by [132] who have found their PdAuNi surface is rich in Pd. Once again for PdAuNi/C_{SBIPP}, the Pd 3d and Au 4f binding energies are shifted to lower binding energies than Pd/C_{SBIPP} and bulk Au while the Ni 2p is shifted to higher value than the bulk $Ni(OH)_2$.

Table 5-3 XPS elemental surface composition of Pd/C_{SBBIPP}, PdAuNi/C_{SBIPP}, PdAuNi/C_{SBEG}, PdAuNi/C_{3step}

Catalyst	O1s At.%	Pd3d At.%		Pd $3d_{5/2}$ position (eV)	Ni2p At.%	Ni $2p_{3/2}$ position (eV)	Au4f At.%	Au $4f_{7/2}$ position (eV)
		Pd^0	PdO					
Pd/C_{SB-IPP}	1.78	1.78	0.45	335.43	-	-	-	-
PdAuNi/C_{SBIPP}	2.59	1.42	0	335.29	0.42	856.34	0.38	83.63
PdAuNi/C_{SBEG}	5.19	0.11	0	335.13	2.19	855.88	0.02	83.59
PdAuNi/C_{3step}	2.61	1.4	0	335.48	0.71	856.38	0.12	83.83

For the 3step PdAuIr, it is interesting that the Pd 3d peak is shifted to higher binding energy – unlike the SBEG and SBIPP ones - than the Pd/C_{SBIPP}. Also, the Au shift to a lower binding energy is less

than that of the SBEG and SBIPP. Additionally, the Ni shift to a higher potential energy is high and close to that of the SBIPP. The Ni shift is smallest in case of the SBEG with +0.28 eV to the bulk $Ni(OH)_2$.This could be linked to the richness of the SBEG surface in $Ni(OH)_2$ which is 2.19 At.% and much higher than both Pd and Au. Also, an overlap of Pd 4s in the Au 4f spectrum could be seen. There various scenarios that might have occurred during and after the synthesis of the three trimetallics. For example, A net electron transfer might have occured from Pd to Au as the ionization energy of Au (9.2 eV) is higher than that of Pd (8.3 eV). An alternative explanation might be that Ni has given its electrons to both Pd and Au knowing its ionization energy is below both of them (7.6 eV). The XPS surface elemental composition (Table 5-3) shows that this catalyst surface has 2.19, 0.11, and 0.02 atomic % of Ni, Pd, and Ni, respectively. Also the O atomic concentration in the SBEG catalyst is quite high of 5.19 At.%. On the other hand, the XPS atomic concentration of Ni in the other two trimetallic catalysts is much lower; 0.42 % for the SBIPP sample and 0.71 % for the 3step one. Also, the O concentration in the SBIPP and 3-step samples is almost half of that in the SBEG one However, the different methods have played a key role in the resulting Pd shift. It is smallest for the 3step method and highest for the SBEG procedure and it might make sense to correlate that to the abundant Ni presence on the SBEG catalyst surface and much broader peak. This has been reported about adding Ni to Pd [156]. The Ni one is identical to that of $Ni(OH)_2$ suggesting almost all Ni exists in that state, which is supported by XRD pattern. On the other side Pd and Au exist only in metallic state. There is a noted shift to higher binding energies in case of Pd and Au which is a consequence of the alloying and electron exchange between the two metals.

PdAuNi/C$_{SBIPP}$

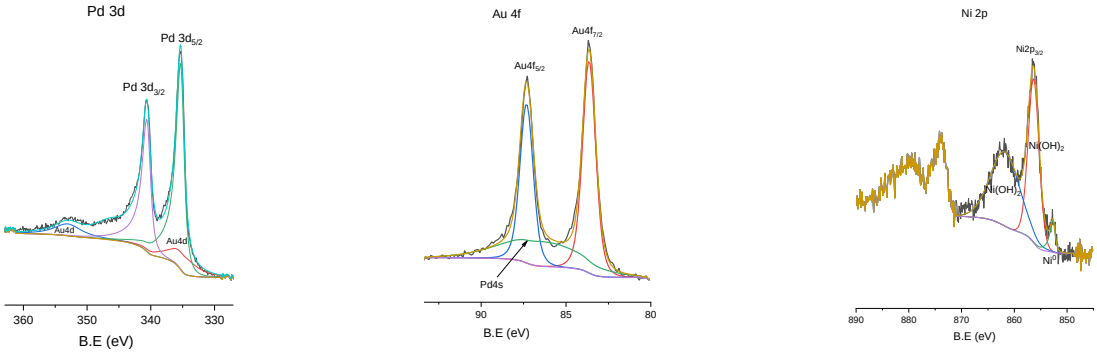

PdAuNi/C$_{SBEG}$

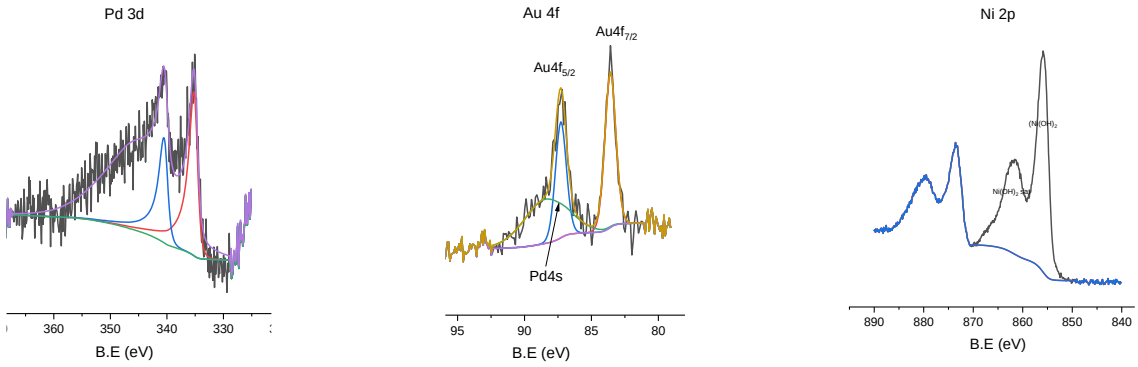

PdAuNi/C_{3step}

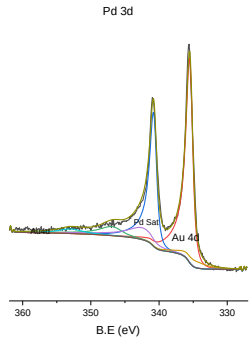

Pd/C_{SBIPP}

Comparative enlarged Pd $3d_{5/2}$

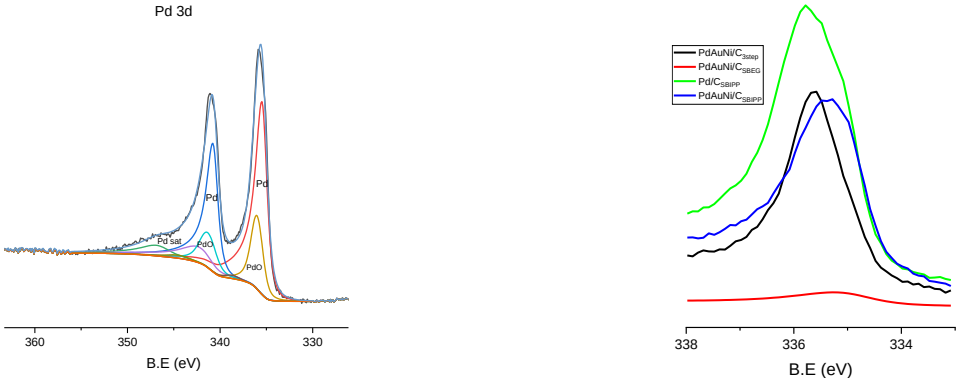

Figure 5-5 XPS spectral peaks deconvoluted of Pd 3d, Ni 2p, and Au 4f in PdAuNi/C_{SBIPP}, Pd/C_{SBIPP}, PdAuNi/C_{SBEG}, and PdAuNi/C_{3step}

To sum this up, it could claimed the three catalysts contain Pd, Au, and Ni in their outer surfaces. However, the Ni-richest and Au-poorest catalyst surface is that of SBEG. Furthermore, the highest Pd binding energy catalyst is the 3step trimetallic followed by Pd/C and a negative shift in the Pd binding energy has occurred by adding Au and Ni in the two other trimetallics. This, overall, means electrons are given to (not taken from) Pd in case of the SBEG and SBIPP catalysts. The presence of Ni^{o} on the SBIPP catalyst surface added to its good binding energy negative shifts of Au and Pd and

positive shift of Ni suggests the good and collaborative presence of the three metals at the outer surface layers which would tune the surface catalytic properties for ethanol electrooxidation.

5.2.5 Electrochemical testing

One of the objectives of this work was to decrease the impact of mass transport losses by helping overcome the reactant/product diffusion barriers due to the concentration gradient near the electrode surface vs the bulk electrolyte. This target has been approached by doing both the CV in both a static 3-electrode half-cell arrangement and a stirred one (50 rpm). The stirring action was accomplished by fixing the 3-electrode cell on top of a magnetic stirrer and inserting the magnetic bar inside the cell. Then, the stirrer is set at 50 rpm and turned on. The 50-rpm is the slowest speed and was chosen to avoid noise signals. The rotating disc electrode (RDE) is the straightforward mean to do this but it was not available to the author. These experiments were performed using the same catalyst of monometallic Pd/C_{SBIPP}. The stirred one has drawn a higher current than the static at any applied potential. Furthermore, some peaks and waves appear in the stirred arrangement that seem to be supressed in the static one. The reason behind such enhancement is probably the facilitated mass transfer of reactants and products that might have contributed to the abundant accessibility of the electrode surface to the reactants by lowering the concentration gradient effect. All the electrochemical experiments reported thereafter are performed in a stirred condition except the static ones in Figure **5-6** in addition to the EIS experiments as the stirring could create a lot of noise signals.

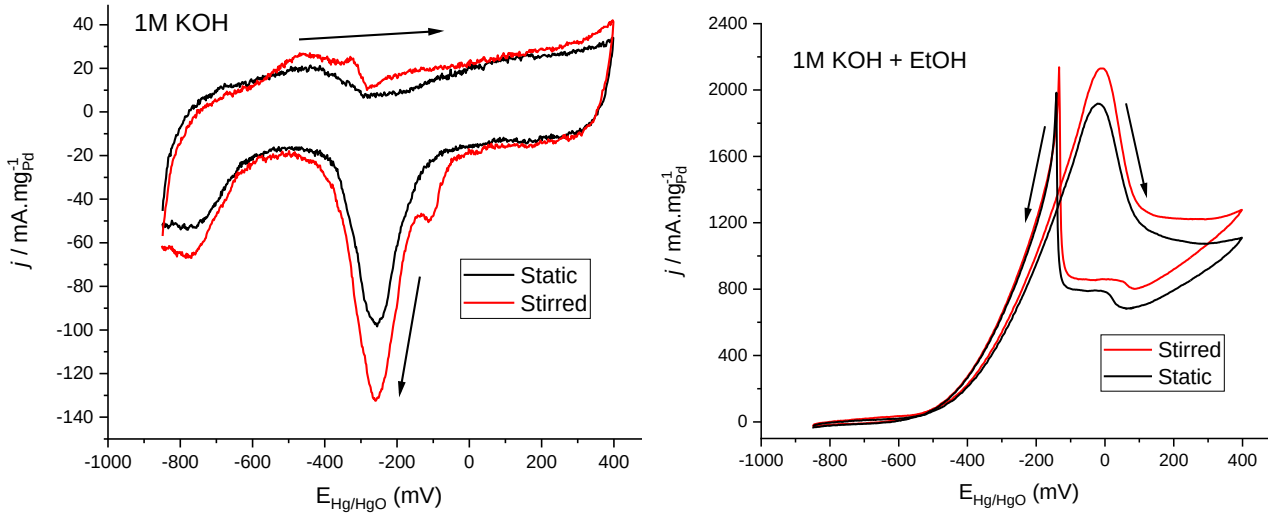

Figure 5-6 CV of Pd/C_{SBIPP} in 1M KOH and 1M KOH+EtOH, static and stirred (50 mV/s)

It is not very clear the reason behind the appearance of the shoulder peak close to the PdO reduction, but it could probably occur because of the reduction of higher Pd oxide. Moreover, the peaks of hydrogen adsorption and desorption, Pd surface oxidation and reduction are all magnified in the stirred condition more the static arrangement. Therefore, there is no doubt that stirring the cell brings some electrocatalytic benefits for ethanol oxidation.

Figure 5-7 shows the cyclic voltammetry results obtained for the prepared and commercial catalysts. This is pursued to study the hydrogen adsorption and absorption, surface metal oxidation/reduction, and to elucidate some information regarding the electrochemical active surface area (ECSA). The results are normalized by metal weight (Pd or Pt) loaded on the working electrode. Each experiment was reproduced 3 times and the chosen cycle is the 25^{th} one at which time the current is stabilized at different applied potentials. For the only KOH solution, it starts with $H_{abs/des}$ region at -700 mV. Here it is noteworthy that Pd has a much higher affinity for hydrogen than Pt. That is why the $H_{ads/abs}$ peak on Pt is much clearer and more intense than those on the Pd catalysts. The hydrogen penetrates the bulk structure of Pd and that is why it is sometimes favoured for hydrogen storage. As this is alkaline solution containing free OH^- free ions, they are expected to be adsorbed on the metal surface as M-OH. Approximately, the adsorption of OH species starts at -550 mV and continues to -100 mV. The Pd (or Pt) surface oxidation starts after that and then is reversed in the backward scan around -250 mV. The clear difference between the two catalysts' performance is because of the high Pt loading in the commercial one and the half-total (Pd+Au+Ni) load in the other ones. That is why the PdAuNi/C cost/g is less than one fifth of that of Pt/C (based the prices of commercial Pt catalyst and metal and carbon precursor prices). The forward peak – on PdAuNi/C_{SBEG} and slightly PdAuNi/C_{3step} - at 400 - 500 mV is due to the oxidation of $Ni(OH)_2$ to NiOOH and the reverse reduction in the cathodic scan is noted at 400-200 mV of NiOOH to $Ni(OH)_2$. Quite similar behaviour was noted by Zhang *et al.* [107] for various proportion Pd_xNi_y/C catalysts prepared by microemulsion method which indicates high segregation of Ni and weak mixing with Pd. A similar behaviour was noted for $Ni(OH)_2$/NiOOH was found by Dutta el al. [139], but only for the monometallic Ni/C while their bimetallic PdNi shows a voltamograms resembling only Pd with enhanced ECSA. The non-existence of the $Ni(OH)_2$/NiOOH peak in case of PdAuNi/C_{SBIPP} is mainly because Ni is probably not separated from Pd and Au as shown by XRD and XPS.

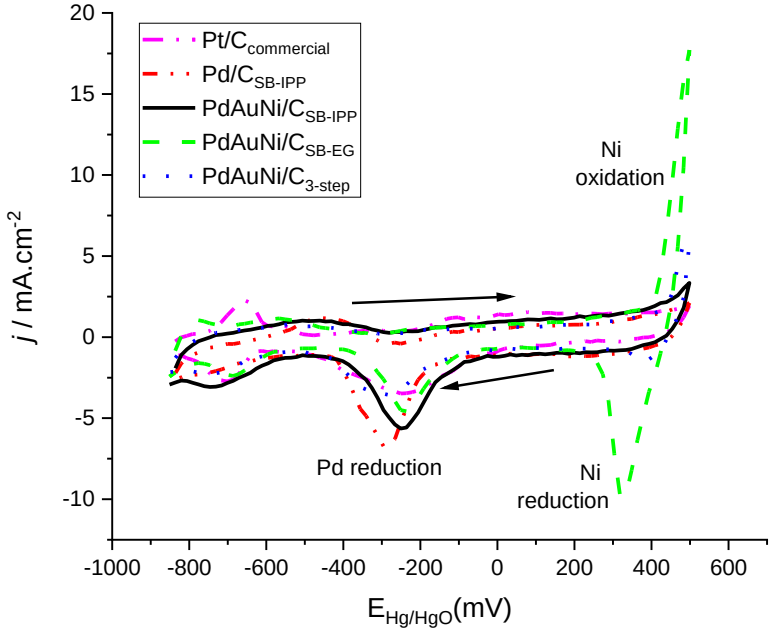

Figure 5-7 Voltammograms in 1M KOH of PdAuNi/C_{SBIPP}, PdAuNi/C_{SBEG}, PdAuNi/C_{3step}, Pd/C_{SBIPP}, and Pt/$C_{commercial}$, (scan rate 50 mV/s)

Also, in case of PdAuNi/C_{3step}, the $Ni(OH)_2$/NiOOH peak exists but much less pronounced than in case of PdAuNi/C_{SBEG}. This is because of the Ni surface content in the 3-step catalyst is more rather than its content in the SBEG (Table 5-3). Nonetheless, the Ni content in the SBIPP catalyst is less than its content in the 3-step one and therefore the $Ni(OH)_2$/NiOOH peak totally disappears in case of the PdAuNi/C_{SBIPP} due to the good alloying potential of the three metals applying the SBIPP protocol. In case of PdAuNi/C_{SBEG}, it is understood that Ni exists only in $Ni(OH)_2$ state. Moreover, the XPS suggests that the particle surface atomic concentration is more than 90% from $Ni(OH)_2$ compared to Pd and Au. In this context, this might mean the top 10 ten atomic layers (30 nm) of PdAuNi/C_{SBEG} are very rich in Ni and very poor in Au followed the 3step and finally the SBIPP sample. That might explain the strong peaks noted in the forward and backward scans of PdAuNi/C_{SBIPP}. Table 5-4 lists the electrochemical active surface area (ECSA, m^2/g) of the prepared catalysts. ECSA was estimated using the charge of PdO reduction peak (normalized by the monolayer reduction charge 0.405 mC/cm^2) in the reverse scan to give the real surface area. Then, it was normalized by the total metal load on the electrode to give ECSA. It is clear that PdAuNi/C_{SBIPP} is much more electroactive (with 150 m^2/g) than the other catalysts. This inevitably would promote EOR remarkably due to the well-dispersed and mixed PdAuNi nanoparticles on the carbon support.

Table 5-4 Electrochemical data of Pd/C_{SBIPP}, PdAuNi/C_{SBIPP}, PdAuNi/C_{SBEG}, PdAuNi/C_{3step}

Catalyst	ECSA (m^2/g)	E_{onset} (mV)	j_p^* (A/mg_{Pd})
Pd/C_{SBIPP}	79	-500	2.34
PdAuNi/C_{3step}	46	-500	2.31
PdAuNi/C_{SBIPP}	150	-650	9.09
PdAuNi/C_{SBEG}	45	-600	3.16

*j_p is the oxidation peak current density.

Figure **5-8** shows the cyclic voltammograms of the 4 prepared catalysts in addition to the commercial Pt/C one in 1M KOH+EtOH solution. This scan helps elucidate the catalyst potential for ethanol oxidation. The crucial data are the onset potential of forward oxidation, oxidation current peak and potential, and the backward current peak and potential. First, the $H_{abs/ads}$ peaks that showed in Figure **5-8** around -700 mV have disappeared for every catalyst due to the attachment of ethanol species into Pd surface. The start of oxidation of ethanol, for PdAuNi/C_{SBIPP}, starts at -650 mV by the recently adsorbed OH species from the electrolyte. The OH adsorption continues and is further increased by increasing the applied potential up to 100 mV. Consequently, the EOR current increases up to that potential reaching to a remarkable current mass density of 9 A/mg_{Pd}. This remarkable oxidation current could be interpreted in terms of the abundant Pd active sites available on the surface. Also, the presence of Ni and Au play an important role to support Pd by recovering its active sites through the generation of oxygen species. The lowest oxidation onset potential and highest current density peak of PdAuNi/C_{SBIPP} are the result of good particle dispersion and higher alloying degree of the three metals in the nanoparticles added to their presence in metallic state (except Ni). Adding Au and Ni has led to modifying the Pd electronic configuration and structure resulting in lower the activation barrier of ethanol oxidation and therefore the enhanced ethanol kinetics. Also, it could be related to the small size of the SBIPP sample verified by TEM and XRD results. It could be confirmed the trimetallic particles are well dispersed and as result a lot of metal active sites (higher ECSA) exist on the carbon surface in case of SBIPP.

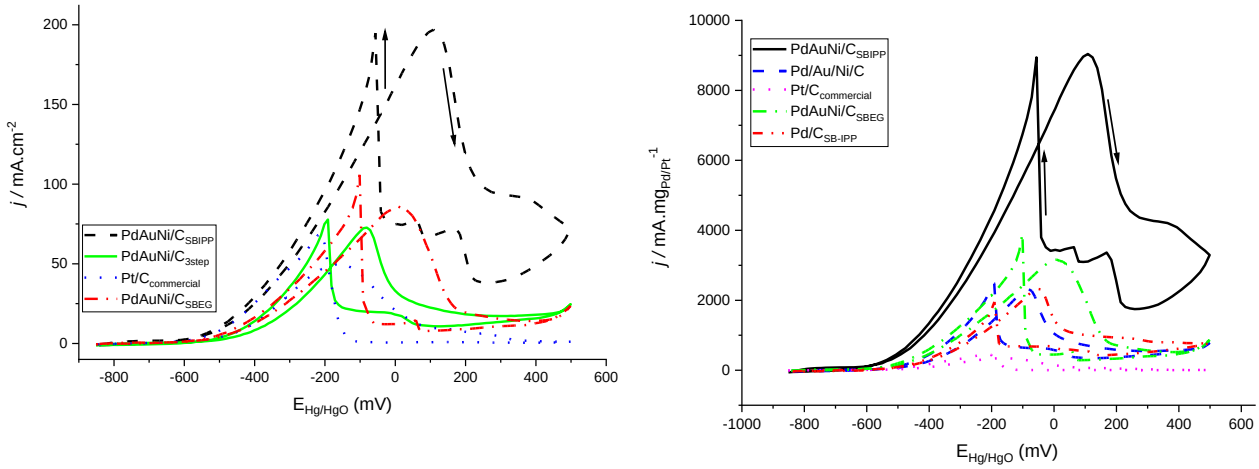

Figure 5-8 Voltammograms of Pd/C_{SBIPP}, PAuNi/C_{SBIPP}, PdAuNi/C_{SBEG}, PdAuNi/C_{3step}, and Pt/$C_{commercial}$ in 1M EtOH + KOH (50 mV/s)

If that catalyst performance is compared to the monometallic Pd/C, with E_{onset} -500 mV and peak current density of, which was prepared using the same protocol, this could explain the indispensable impact of adding both Ni and Au into Pd for ethanol oxidation. The impact of adding Au and Ni to Pd is, also, confirmed, but to a less extent, for the catalyst prepared by the SBEG method with E_{onset} of -600 mV and peak current density of 3.16 A/mg_{Pd}. For that catalyst, the high content of Ni has harmed the ethanol oxidation at this range of applied potential because Ni could oxidize ethanol but at a higher applied potential. Using the 3-step route did not enhance the PdAuNi/C more than the monometallic by the SBIPP one. The potential reason is a weak mixing between the metal nanoparticles since Ni was first reduced and grown for 30 min, followed by Au for another 30 min, and finally Pd for another 30 min. high segregation seems to have happened on the surface that caused some areas are only Pd, Au, or Ni but it looks less probable that a bimetallic or trimetallic has existed. As a consequence, the existence of only Ni or Au has decreased the number of surface Pd sites and were useless for ethanol oxidation.

Looking to the CV in Figure 5-8, it could be seen the forward peak current (j_f)/reverse peak (j_b) ratio is more than 1 for both Pd/C and PdAuNi/C by the SBIPP method while it is less than 1 in case of the 3step and SBEG catalysts. This is an evidence that the former catalysts are more stable tolerant for poisoning species. Therefore, the SBEG and 3-step catalysts would have less durability compared to PdAuNi/C_{SBIPP} because it is less capable to recover its active sites blocked by the reaction intermediates.

Figure 5-9 shows the chronoamperometry scans of the prepared catalysts which were performed for 1h at -400 mV vs Hg/HgO to evaluate the individual catalyst stability for ethanol oxidation. This test helps inform of each catalyst ability to resist degradation - by tolerating the poisoning species - over the operation time. The higher and more stable current decay are, the better the catalyst. Looking at this potential in the CV voltammograms (Figure 5-8,), it could be noted this potential is slightly higher the onset oxidation potential. In other words, the catalyst surface is predominantly covered by adsorbed ethanol species and a small surface fraction is covered with OH that oxidizes and removes the ethanol and its intermediates. For the CA curves (Figure 5-9), there is a noted fast decay in the current during the initial 10 min followed by a slower one for the following 50 min. The highest CA current noticed in case of PdAuNi/C_{SBIPP} is an evidence of a very small quantity of poisoning species blocking the respective active sites of that catalyst compared to the others. Therefore, the active sites for EOR on PdAuNi/C should be more than that on Pt/C. Additionally, PdAuNi/C should have a higher tolerance for poisoning intermediates such as CO or CH_3CO species, which are more strongly adsorbed on Pt surface [1]. On the other hand, looking at the XPS results (Figure 5-5), the higher binding energies for Pd after adding Ni and Au is informing of higher adsorption strength for OH and poisons equally.

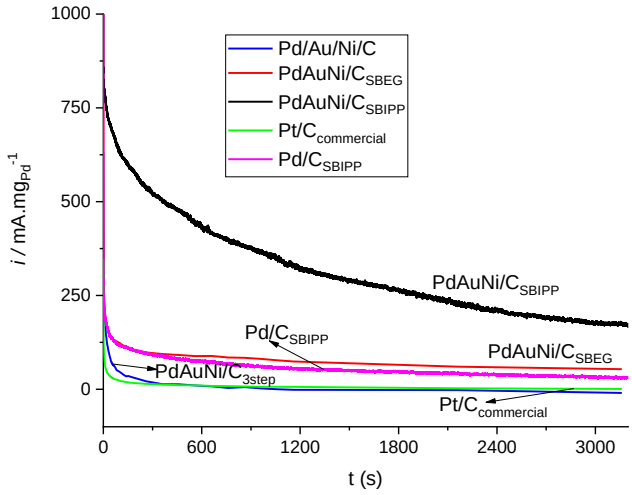

Figure 5-9 Chronoamperometry (CA) Scans of Pd/C_{SBIPP}, PAuNi/C_{SBIPP}, PdAuNi/C_{SBEG}, PdAuNi/C_{3step}, and Pt/$C_{commercial}$ in at -400 mV vs Hg/HgO

Although the j_f/j_b ratio of Pd/C_{SBIPP} than that of PdAuNi/ in Figure 5-8, the CA steady state current of the of the latter surpasses that of the former most probably due to the synergistic effects of Ni and Au that facilitates the removal of blocking species from Pd sites.

Figure 5-10 shows the electrochemical impedance spectroscopy (EIS) results for catalysts. The maximum and minimum frequencies are 10,000 and 0.02 Hz, respectively while the AC voltage amplitude was set to 10 mV. The applied potentials are -0.4 V and -0.2 V vs Hg/HgO, respectively. The Ohmic resistance which is the intercept with the real (horizontal) axis seems to have a negligible change as it is the electrolyte is the same 0.5M EtOH + KOH for all EIS measured spectra and the current was fixed for 10 min before running EIS to not interfere with the current perturbation due to voltage sinusoidal change. None of the catalysts has achieved a full semicircle but an arc with a specific radius. Each arc gives an idea about the double layer capacitance C_{dl} and charge transfer resistance (R_{ct}) resisting the redox reaction on the catalyst reaction sites. The Warburg mass transport impedance (Z_w) has not contributed to any of the measured spectra in Figure 5-10 since the solution is stirred facilitating the diffusion of the reacting species. Within the applied frequency range, therefore, the shown spectra represent only C_{dl} and R_{ct}. The smallest are was obtained for PdAuNi/C and that indicates with catalyst the charge transfer resistance (or resistance to Faradaic reactions) is smallest upon using this catalyst. This result agrees with CV and CA results about this catalyst. It seems Au and Ni have promoted ethanol electrooxidation and also facilitated the removal of blocking species such as CO, CH_x, and intermediates. With the other catalysts, bigger impedance arcs are obtained and that indicates a more resistance is acting against ethanol oxidation reaction. It is noteworthy that the cost of the PdAuNi/C_{SBIPP} is the least of all catalysts and it is 10 times cheaper than the Pt commercial catalyst.

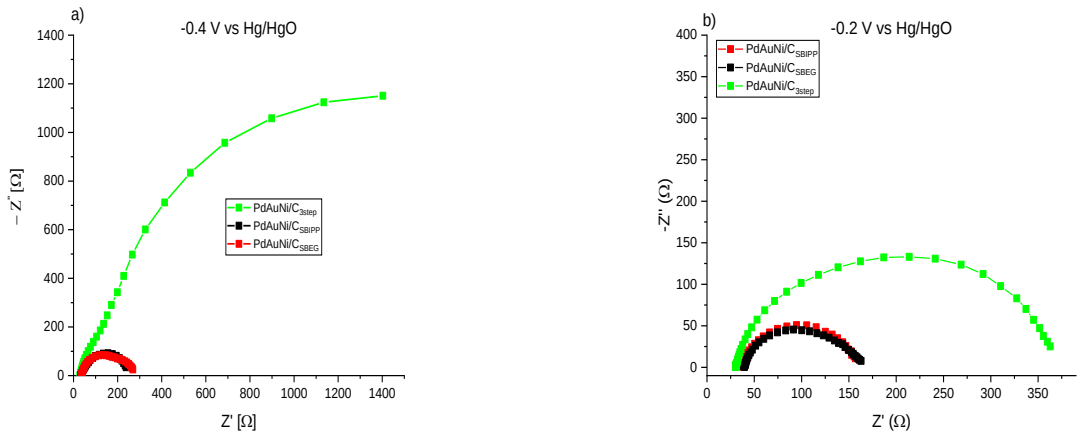

Figure 5-10 Potentiostatic EIS spectra of PdAuNi/C_{SBEG}, PdAuNi/C_{SBIPP}, and PdAuNi/$C_{3\text{-step}}$ at a) -0.4 V and b) -0.2 V vs Hg/HgO

The obtained EIS spectra are fitted using The Gamry Instruments Echem Analyst Software attached to the EIS300 Electrochemical Impedance Software which includes a graphical Model Editor. Two models were constructed tried to simulate the physiochemical impedances encountered in the 3-electrode cell with EtOH+KOH. The first mode (The RC one in Figure 5-11) is the straightforward comprised of solution resistance (R_s), double-layer capacitance (C_{dl}) due to charge separation, and the charge transfer resistance (R_{ct}). As was explained in section 3.2.6.1, the R_{ct} directly reflects the catalyst activity for the redox reaction and the potential catalyst degradation through the poisoning of catalytic sites. The second model (The RCRC one in Figure **5-11**) is more complex as by adding another resistance inside the pore structure (R_p) and another double-layer capacitance inside (C_p).

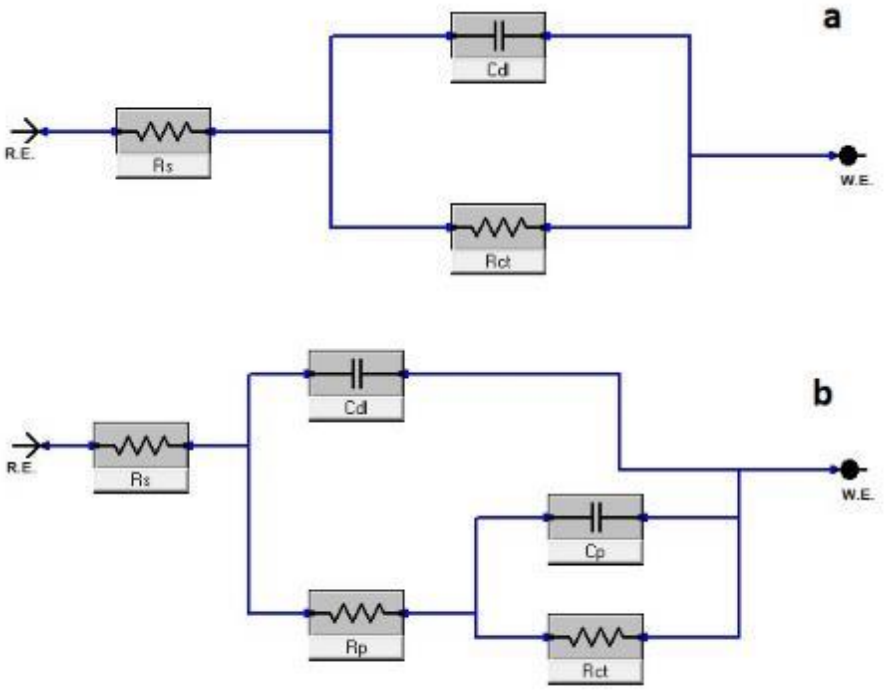

Figure 5-11 Two EIS models (RC and RCRC) of the electrode/solution edited by EIS300

Those two models were tried to fit the experimental data obtained at -0.2V vs Hg/HgO as shown in the Bod plot (Figure **5-12**). In this plot, the value of the total impedance (Z, **Ω**) is plotted versus the frequency (Hz). It is clear the RCRC model gives a fitted curve that is more resembling to the experimental data. However, this is not always the case. Because of that, every Potentiostatic EIS curve in this work is fitted using the two models. Then, the more accurate model is chosen to estimate the value of the charge transfer resistance (R_{ct}, **Ω**).

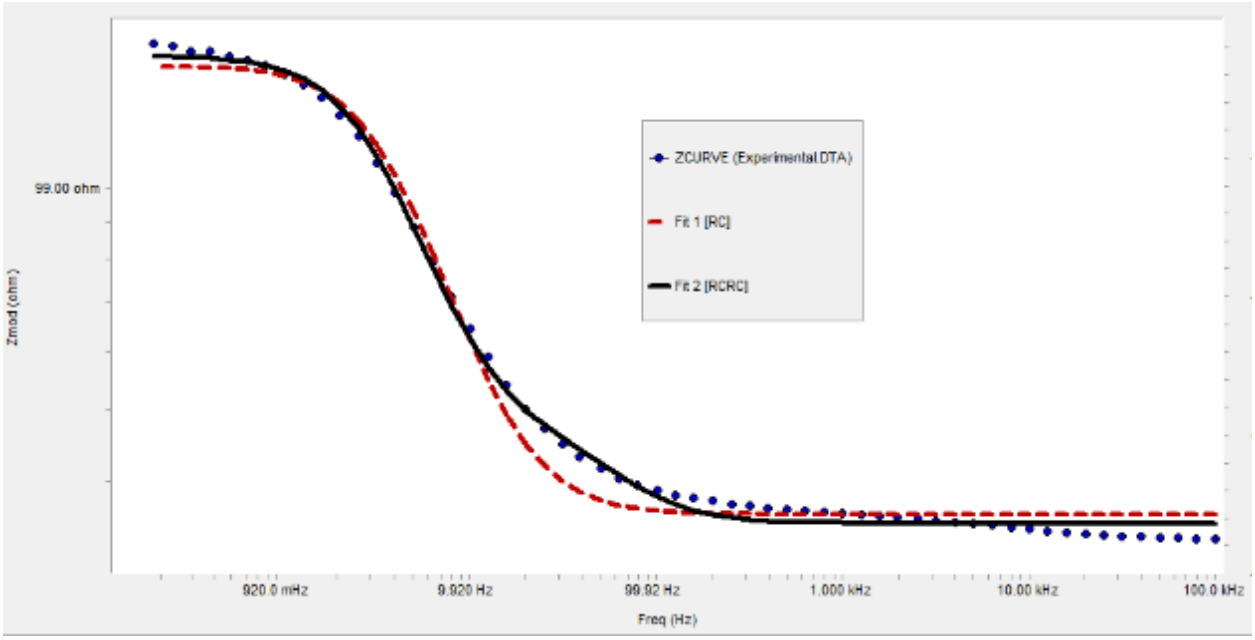

Figure 5-12 Two model fits (RC and RCRC). The RCRC one is more resembling to the experimental EIS data measured at -0.2V

The simple model was found more accurate at low and high potentials to calculate the charge transfer resistance (R_{ct}). At the intermediate-potential, the more complex RCRC one was found more accurate. The reason behind is the complex processes which are the high OH adsorption, starting surface oxidation, and increasing blocking of Pd active sites by poisons. The explanation of the RCRC model could be understood there are one external and one internal electrolyte/electrode interfaces. The external one is the visible glass carbon electrode/electrolyte one while the internal one occurs inside the porous structure of the catalyst. R_p could be explained by the diffusion resistance of electrons and active species in the pores of the carbon. The exact explanation why the diffusion of electrons and ions inside the pore structure at the intermediate voltage is not very clear to the author, however, it is known this potential is the interface between active ethanol oxidation and surface layer oxidation.

Figure **5-13** shows the changes of charge transfer resistance versus the applied potential for PdAuNi/C_{3step}, PdAuNi/C_{SBIPP}, and PdAuNi/C_{SBEG}. Though the R_{ct} change is small by increasing the applied potential from -0.4 V to -0.2 V in case of PdAuNi/C and PdAuNi/C, it is significant in case of PdAuNi/C_{3step}. The higher activity of both SBIPP and SBEG could be explained in the facilitated redox reactions and removal of poisoning species. The controversial enhanced EIS result of

PdAuNi/C_{SBEG} could be attributed to the surface enrichment with Ni and the respective redox Ni reactions compared to the other catalysts.

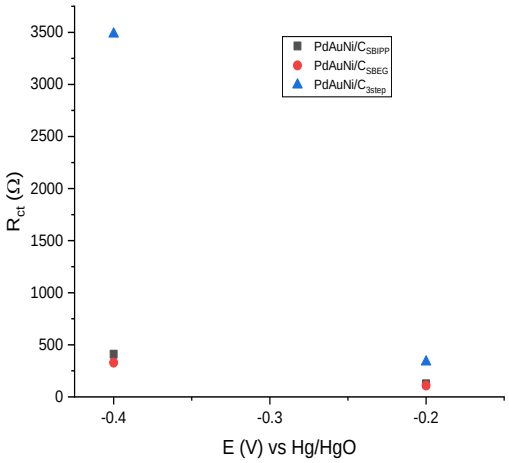

Figure 5-13 R_{ct} values of PdAuNi/C_{SBIPP}, PdAuNi/C_{SBEG}, and PdAuNi/C_{3step} versus the applied potential

The remarkable ethanol oxidation of PdAuNi/C_{SBIPP} could be fairly understood and reflected upon its unique physical characteristics verified by XRD, TEM, EDX, and XPS. This protocol of metal co-reduction and applying the NaBH4-2-propanol complex complemented with applying KBr as a capping agent has produced PdAuNi alloy nanoparticles that no individual metal peaks are shown – in the XRD – separate from the other two metals. Also, though the peaks are closest to the pure Pd peaks, they are slightly shifted towards pure Au peaks which suggest the Au and Ni atoms have been incorporated into the Pd lattice structure. Also, this shift has expanded the Pd crystal lattice and upshifted the *d*-band centre as it is under tensile stress and strain. The mixing *vs* segregation potential – as verified by EDX and XPS – is shown to be highly tuned in case of PdAuNi/C_{SBIPP}. Due to the high alloying and mixing potential in this sample, it is the only one in which Ni was detected in a metallic state in addition the usually oxide one as was verified by the XPS measurements. Furthermore, the PdAuNi/C_{SBIPP} have the highest dispersion and smallest particle size in comparison to the other samples. For all these physical features, the oxidation current density peak and onset potential are more than 9 A/mgPd and -575 mV vs Hg/HgO. Comparing the PdAuNi/C_{SBIPP} ethanol oxidation performance to the monometallic Pd/C_{SBIPP} – which is prepared by the same method – could clearly explain the impact of adding Au and Ni as cocatalysts to Pd. A smaller particle size is obtained and a nanoalloy structure is produced with enhanced electronic configuration that could lead to reducing the ethanol oxidation activation barrier reduction in case of the trimetallic catalyst. The ethanol oxidation performance of the monometallic Pd/C_{SBIPP} is far below that of PdAuNi/C_{SBIPP} with

2 A/mgPd current density peak and -500 mV onset potential of ethanol oxidation. The lowest ethanol oxidation performance is obtained with the 3-step PdAuNi with 2 A/mg_{Pd} current density peak and -450 mV onset potential of oxidation. The XRD peaks of this sample to a high extent resemble Au being farthest away from pure Pd peaks. It is likely the consecutive reduction of Au first and Pd later have produced a core@shell (Au@Pd) structure. The particle size of PdAuNi/C_{3step} is the highest from the four catalysts and it could be assumed – with caution – a few active sites exist on the catalyst surface of that sample. It is noteworthy that the 3-step sample at low applied potential (-0.4 V vs Hg/HgO) experiences a very high resistance (3500 Ω) against the redox reaction as shown in Figure **5-13**. This value is very much more than those values obtained with PdAuNi/C_{SBIPP} and PdAuNi/C_{SBEG}. The probable reason for this is the surface covered in Ni in addition the probable separation among the three metals and Pd potentially buried inside the internal pores. That is why it draws a very small current at the voltage supposed to adsorb a lot of oxygen species to remove the adsorbed ethoxy. The SBEG catalyst performance is intermediate between the other two trimetallic samples (SBIPP and 3step). With an oxidation performance of 3 A/mg_{Pd} current peak and -510 mV onset potential. The physical features of that catalyst are clearly linked to its electrocatalytic performance. For example, the EDX, XRD, and XPS have shown this sample is highly segregated in Ni species on its surface and also the CV in KOH has also revealed a significant reduction and oxidation peaks of $Ni(OH)_2$/NiOOH. Ni is not active for ethanol oxidation but at very high overpotential which is not applicable. Therefore, the ethanol oxidation on the SBEG catalyst –whose surface is densely populated with Ni – is less efficient than that on SBIPP one.

5.3 Conclusions

Three methods are applied to prepare PdAuNi nanoparticles supported on Vulcan carbon and the three samples are evaluated for ethanol electrooxidation. The $NaBH_4$-2-propanol method (SBIPP) has presented the highest activity for ethanol electrooxidation with oxidation lowest onset potential of -575 mV and highest peak current density of 9 A/mg_{Pd}. This performance could be attributed to both the goodness of the SBIPP and also to the effect of adding Au and Ni to Pd (if compared to Pd/C_{SBIPP}). The mixed PdAuNi alloy nanoparticle structure (verified by XRD, EDX and XPS) and smallest particle size of 3 nm (from TEM images) added to the tuned electronic structure have co-worked to promote the ethanol oxidation by reducing the activation barrier and increasing the number of active sites. This PdAuNi catalyst is 4 times more active than its monometallic Pd/C counterpart and yet it is much more affordable. Furthermore, this trimetallic is 10 times more active than the

tested Pt commercial sample and yet its associated cost shall be 0.2 to 0.4 of the latter. Moreover, it is noteworthy that the SBIPP method is very straightforward with 30 min overall synthesis time and also the use of the KBr has probably helped overcome the metal nanoparticle tendency to agglomerate. Unlike other organic stabilisers and capping agents, KBr could be easily washed off from the catalyst particles. It could be claimed the SBIPP protocol is suitable for catalyst mass production. The 3-step reduction which aimed to produce a core@shell structure of Au@Pd-supported Ni/C did not work out very well in terms of electrocatalytic performance of ethanol oxidation. The onset potential is comparatively high of -450 mV and the peak current density is close to that of the Pd/C_{SBIPP} (2 A/mg_{Pd}). The TEM reveals the particle size of this catalyst is highest and therefore it could assumed less active sites exist on its surface. Also, its XRD pattern highly resembles pure Au with Ni segregation. Those physical features could probably explain the low catalytic performance. The SBEG PdAuNi surface suffers from high Ni segregation on the surface verified by XRD, XPS, EDX, and KOH CV. Therefore less Pd actives sites exist on the surface if compared to $PdAuNi/C_{SBIPP}$. Furthermore, this catalyst suffers greatly from metal particle segregation probably due to the initial metal reduction prior to adding the carbon support. Thus, the ethanol oxidation activity is slightly higher than that of $PdAuNi/C_{3step}$ with -550 mV onset potential and 3 A/mg_{Pd}.

Chapter 6: SYNTHESIS OF PDRHNI, PDIRNI, AND PDAGNI CATALYSTS FOR ETHANOL OXIDATION

The $NaBH_4$-2-propanol (SBIPP) co-reduction method was found the most successful synthesis method from the three methods pursued in Chapter 5. Also, based on Chapter 4, Vulcan carbon (XC72) is decided the highest performing support for metal nanoparticles for ethanol oxidation reaction. Therefore, in this chapter, the SBIPP method and XC72 are chosen to prepare C-supported PdNiM (Me = Ir, Rh, Ag) trimetallic catalysts. Two atomic ratios are applied for each catalyst (1:1:1) and (4:2:1). Those catalysts are prepared and investigated for ethanol oxidation reaction for the first time except PdAgNi [149] and PdIrNi [170]. Each metal of those was proven beneficial for ethanol oxidation if added as a co-catalyst to Pd. Ni has been reported abundantly as beneficial co-catalyst because Ni is oxyphilic and capable to generate oxygen species. The catalytic benefit is not only benefit attained by adding Ni to Pd, but also it is much more abundant than Pd adding a significant

economic benefit in terms of the catalyst cost. Therefore, adding a 3rd metal to Pd and Ni might enhance the performance even further.

6.1 Preparation Method

The applied preparation method is similar to the SBIPP method reported in Chapter 5.The variations that were adopted are: 1. Decreasing the alkalinity of the KOH by adding 0.5 M instead of 1M solution to the $NaBH_4$ solution to increase the potential of producing non-oxidised Ni metal and 2. Replacing Au with Ir, Rh, or Ag. Other than those two changes, the processing steps are the same. Table 6-1 lists the weights of carbon and metal precursors for each respective catalyst to produce 150 mg of final catalyst powder. KBr was added for each catalyst with a molar ratio of 1.5:1 (KBr: total molar metal). The washing and drying is similar to what was reported in Chapter 5. For each trimetallic, two catalyst molar compositions of Pd:Me:Ni are produced: the first is 1:1:1 and the second is 4:2:1.

Table 6-1 The weights of added carbon and respective metal precursor of Pd/C, PdRhNi/C, $Pd_4Rh_2Ni_1$/C, PdAgNi/C, $Pd_4Ag_2Ni_1$/C, PdIrNi/C, and $Pd_4Ir_2Ni_1$/C

	C (mg)	**$PdCl_2$ (mg)**	**$NiCl_2$ (mg)**	**$AgNO_3$ (mg)**	**$IrCl_3$ (mg)**	**$RhCl_3$ (mg)**
PdRhNi/C	132	11.91	8.67	x	x	11.51
$Pd_4Rh_2Ni_1$/C	132	18.40	3.4	x	x	10.89
PdAgNi/C	132	11.69	8.54	11.21	x	x
$Pd_4Ag_2Ni_1$/C	132	18.32	3.37	8.83	x	x
PdIrNi/C	132	8.83	6.46	x	14.94	x
$Pd_4Ir_2Ni_1$/C	132	14.19	2.58	x	11.94	x

It is noteworthy that Rh is added even though it is more expensive than Pd. As was explained in section 2.8.3, the effect of adding Rh as a co-catalyst or its sole use to activate ethanol is a controversy. It is not agreed if Rh is active for ethanol oxidation on its own or not. Enhancing the CO_2 selectivity and the C-C bond breaking potential are even more controversial.

6.2 Physical Analyses

6.2.1 XRD

Figure 6-1 shows the XRD patterns of monometallic C-supported Pd, Ni, Ag, Ir, and Rh catalysts prepared using the NaBH4-2-propanol reduction method. XRD patterns were obtained by using Bruker D2 Phaser operating at 30 kV and 10 mA and the scan rate was 2 degrees/min. The powder was fully ground and mounted on the low background stub. The broad peak noted at 25 degrees is due to the tubrostaic nature of Vulcan carbon (XC72). The Ni/C does not show any crystalline peaks of Ni metallic but Ni oxide and hydroxide at 34, 43, and 60 degrees. This is because Ni is oxidised at room temperature upon contacting air after the synthesis. The much higher carbon peak than Ni oxide is also attributed to the small quantity of Ni oxide/hydroxide in the powder (12 wt. %). Ni is known to be the most difficult to reduce from the reported metals and it is, also, the most oxyphilic metal. The evidence of Ni oxidation after synthesis is abundantly reported regardless of the synthesis protocol [81,109,110,139,156,171,172]. The C peak is more intense than the Rh and Ni ones. However, it is less intense than the peaks of Pd, Ag, and Ir. This is indicative of more successful preparation of Pd, Ir, and Ag to produce polycrystalline particles. As for Ni and Rh, the oxide constituent is probably more than the metal constituent. However, Rh was successfully prepared by glycol intermittent wave reduction and shows XRD peaks at 42, 46.5, 72.1 corresponding to the Rh facets of (111), (200), and (220) and has given crystal size of 3.8 nm calculated by Scherrer equation [120]. It is also noteworthy the V-shape at the Ag (200) peak at 45.5° which is not known why it was produced. For instance, some Ag metal and oxide peaks overlapping or something else. This is not also reported in the reviewed literature.

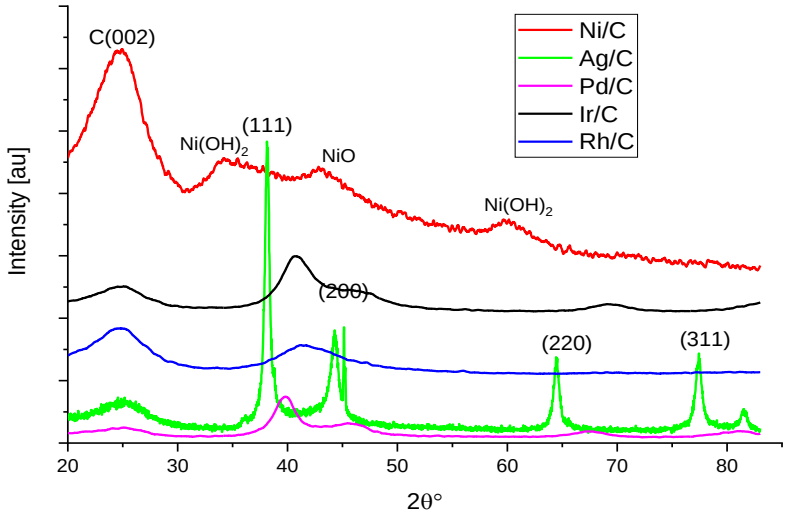

Figure 6-1 XRD Patterns of Pd/C, Rh/C, Ir/C, Ni/C, and Ag/C

Also, it noteworthy that the Ag peaks are positioned at lower diffraction angles than those of Pd. On the other hand, the peaks of Rh and Ir are positioned at higher diffraction angles than those of Pd. The Ag (200) peak is divided into two overlapping peaks which is not understood. Finally, it should be mentioned the most intense crystal peak are of Ag. On the other side, the other metal peaks are much broader than Ag which probably suggest large Ag crystals are produced compared to Pd, Ir, and Rh. Figure 6-2 shows the XRD patterns of Pd/C, PdRhNi/C, $Pd_4Rh_2Ni_1$/C, PdAgNi/C, $Pd_4Ag_2Ni_1$/C, PdIrNi/C, and $Pd_4Ir_2Ni_1$/C. Pd/C pattern is shown for comparison. As for PdAgNi and $Pd_4Ag_2Ni_1$, the XRD patterns show sharp peaks overlapping with broader peaks at higher diffraction angles. The lower-angle sharp peaks are probably due to Ag and the broader ones are apparently due to Pd. The observation of two phases suggests the weak alloying potential between Pd and Ag using the SBIPP method. Other methods have been found to give only one phase of PdAg alloy [126,127,129,130] and the opposite outcome was also reported [87]. The Pd broad peaks in PdAgNi systems are barely shifted to lower diffraction angles compared to the Pd/C according to Figure 6-2 which once more suggests a weak alloy between Pd and Ag has been formed. Ulas *et al.* [149] have prepared various PdAg bimetallic alloy catalysts and they have noticed a higher shift to the Ag peaks with the Ag content. As for the PdRhNi/C and $Pd_4Rh_2Ni_1$, further broadening of the Pd crystal peaks could be noted. Additionally, the diffraction angles are shifted to higher values (Figure 6-3) which is probably due to the alloying potential between Pd and Rh.

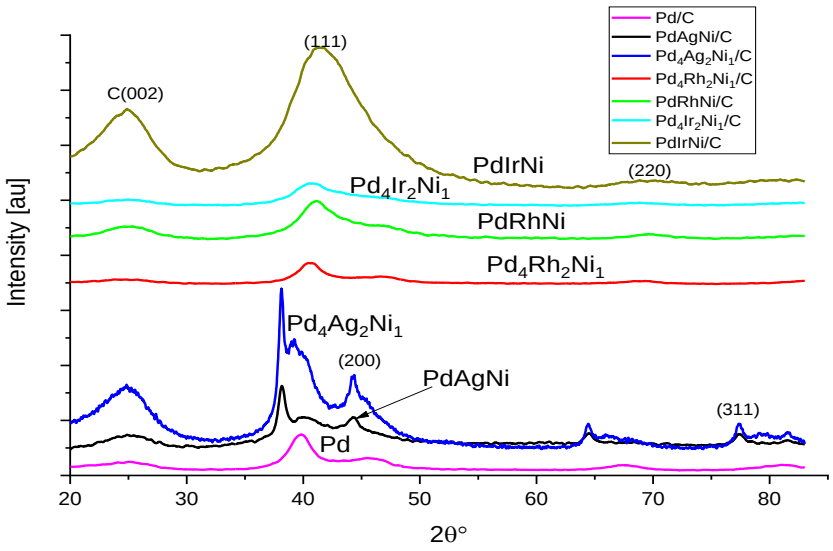

Figure 6-2 XRD Patterns of Pd/C, PdRhNi/C, $Pd_4Rh_2Ni_1$/C, PdAgNi/C, $Pd_4Ag_2Ni_1$/C, PdIrNi/C, and $Pd_4Ir_2Ni_1$/C

As for the PdIrNi/c and $Pd_4Ir_2Ni_1$, only one metallic phase is present which is indicates a PdIr alloy formation on C surface. Also, a shift to higher angles could be noted in both catalysts compared to the monometallic Pd/C. A similar – but not identical – PdIrNi crystal structure was reported [170] which showed high segregation $Ni(OH)_2$ peak at 60° which is also noted in case of PdIrNi catalysts prepared in [170]. It should be mentioned for the six catalysts – especially the 3 with 1:1:1 atomic ratios – that no Ni hydroxide peak is detected as could be seen in the monometallic Ni/C (Figure 6-1). This is probably because the applied method is capable of mixing Ni and Pd which was found in the XRD pattern of $PdAuNi/CS_{BIPP}$ unlike the trimetallic PdAuNi prepared by the SBEG protocol. Ulas *et al.* [149] have prepared various PdAg bimetallic alloy catalysts and they have noticed a higher shift to the Ag peaks with the Ag content. As for the PdRhNi/C and $Pd_4Rh_2Ni_1$, further broadening of the Pd crystal peaks could be noted. Additionally, the diffraction angles are shifted to higher values

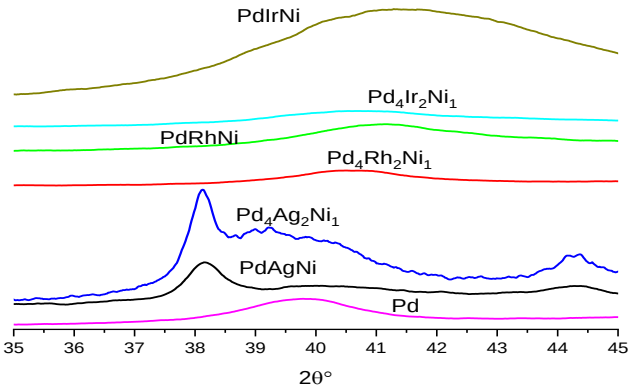

Figure 6-3 Enlarged Pd (111) facet of Pd/C, PdRhNi/C, $Pd_4Rh_2Ni_1$/C, PdAgNi/C, $Pd_4Ag_2Ni_1$/C, PdIrNi/C, and $Pd_4Ir_2Ni_1$/C

As far as this work is concerned, the preparation of PdAgNi or PdRhNi was not reported before. This makes it difficult to compare the structure to the published data except the bimetallic PdAg and PdRh. For Ag, it brings a similar effect to that of Au by shifting the XRD peaks to lower diffraction angles [104,128,144]. From a crystal structure perspective, the effect of adding Rh into Pd is similar to that of Ir. As shown in Figure **6-2** and Figure 6-3, the two PdRhNi catalysts peak positions are shifted to higher diffraction angles. The probable reason is that diffraction peak positions of pure Rh lie at higher diffraction angles than those of pure Pd. It is, also, suggestive of the formation of PdRhNi alloy since no individual metallic peaks are separated from the other.

6.2.2 EDX

Table 6-2 shows the EDX elemental quantification data of PdRhNi/C, $Pd_4Rh_2Ni_1$/C, PdAgNi/C, $Pd_4Ag_2Ni_1$/C, PdIrNi/C, and $Pd_4Ir_2Ni_1$/C. For the PdRhNi system, the detected Ni is less than Pd and Rh at 20 kV though the nominal metal quantities are equal. And Rh is the highest detected with 0.76 At.%. However, the situation is reversed at 10 kV with Ni concentration of 0.51 At.% and those of Pd and Rh are 0.39 and 0.43 At.% respectively. For the $Pd_4Rh_2Ni_1$, though the nominally added Ni is a quarter of Pd and half of Rh, its concentration atomic concentration is doubled by decreasing the voltage from 20 kV to 10 kV.

Table 6-2 EDX spectra and quantification at 10 kV and 20 kV of PdRhNi/C, $Pd_4Rh_2Ni_1$/C, PdAgNi/C, $Pd_4Ag_2Ni_1$/C, PdIrNi/C, and $Pd_4Ir_2Ni_1$/C

Catalyst	Acc. Voltage	Pd At.%	Ni At.%	Me (Rh, Ag, Ir) At.%
PdRhNi/C	10 kV	0.39	0.51	0.43
	20 kV	0.47	0.39	0.76
$Pd_4Rh_2Ni_1$/C	10 kV	0.95	0.25	0.68
	20 kV	1.23	0.12	0.82
PdAgNi/C	10 kV	0.88	1.90	0.46
	20 kV	0.94	1.24	0.55
$Pd_4Ag_2Ni_1$/C	10 kV	1.02	0.38	0.25
	20 kV	1.09	0.26	0.42
PdIrNi/C	10 kV	0.80	1.23	0.57
	20 kV	0.73	0.62	0.50
$Pd_4Ir_2Ni_1$/C	10 kV	0.97	0.28	0.52
	20 kV	0.90	0.14	0.46

The opposite behaviour is noted for Pd and Rh. For those two systems, it could be claimed that Ni has a tendency to segregate into the surface more than Pd and Rh. For the PdAgNi, the Ag quantity at 20 kV is half of its theoretical value – which is close to that of Pd and Ni – and it is further decreased at 10 kV. This suggests the Ag has a high opposite-to-Ni tendency to segregate into the core especially that the Pd and Ni values are close to the theoretical ones. It might suggest some Ag species are deep buried in the carbon pores and not accessible to the electron beam to emit X-ray signals.

The other possibility is that the method applied is not efficient enough to reduce all Ag from the $AgNO_3$ precursor which is unlikely because the Ag quantity in $Pd_4Ag_2Ni_1$/C at 20 kV is close (0.42 %) to its nominal value. Once more, the Ni concentration increases significantly (1.24 to 1.90 At. %) by decreasing the accelerating voltage from 20 kV to 10 kV for the PdAgNi. The conclusion of those two systems could mentioned as Ag having the lowest tendency of surface segregation and Ni the highest one. As for the PdIrNi system, the measure concentration of Ir at 20 kV is slightly less than the theoretical values although its concentration in the $Pd_4Ir_2Ni_1$ one is close enough to theoretical calculation. In both systems, however, Ir has a tendency to segregate to the surface (very close to Pd). For the 5^{th} and 6^{th} times, a significant Ni concentration increase is detected (0.14 to 0.28 for

$Pd_4Ir_2Ni_1$) by decreasing the accelerating voltage from 20 kV to 10 kV. The Ir concentration at 10 kV is usually higher that at 20 kV which might be reasoned that Ir – like Ni – has a surface segregation tendency.

6.2.3 TEM

Figure 6-4 shows the TEM micrographs of PdIrNi/C, PdAgNi/C, PdNiRh/C, $Pd_4Ir_2Ni_1$/C, $Pd_4Ag_2Ni_1$/C, and $Pd_4Rh_2Ni_1$/C. These images demonstrate the highly dispersed trimetallic nanoparticles (small spherical ones) on the Vulcan carbon support. It should be mentioned that a high enhancement has occurred on the TEM images was obtained in this chapter compared to the previous two chapters. This is mainly due to applying an advanced TEM sample preparation which involves first the sonication of catalyst powder (5 mg) in 2 mL of ethanol for 1h and second the usage of a spray atomizer to paint the C-coated Cu TEM grid with the catalyst paste. The second step ensures the separation of powder particles from one another that occurs applying the conventional pipetting or dipping techniques in previous chapters. Carbon multilayers (single C particle size is close to 50 nm) could be seen resting on one another. The good dispersion (32-45%) of the small-size nanoparticles could be seen especially when only a single or double carbon layer is visible following the grey scale. The good dispersion of particles is due to the work of the stabilizing complex produced by the $NaBH_4$-2-proanol mixture added to the capping agent of KBr which helps produce fairly clean metal-C composite compared to other organic stabiliser such as PVP[48,173]. The particle size ranges from 2 to 5 nm as shown in the images and quite a few particle aggregations could also be noticed in each image. This proves the well-dispersed and small-sized particles of PdRhNi that have been produced using this quick synthesis route. While the average particle size of $Pd_4Rh_2Ni_1$/C equals 3.6 nm, it is 0.6 nm smaller in case of PdRhNi/C. The higher content of Ni and Rh might have contributed into the decrease of the trimetallic particle size. The potential reason for this is the smaller geometrical characteristics of pure Rh and Ni compared to Pd (e.g., smaller unit cells and atomic radii).The same trend is also noticed for the PdIrNi systems in which the average particle size of PdIrNi is 2.36 nm is 0.10 nm smaller than that $Pd_4Ir_2Ni_1$. A similar but not identical behaviour is noted in case of both PdAgNi systems. While the average particle size of PdAgNi is less than that of Pd4Ag2Ni1 – like PdRhNi and PdIrNi systems – the particle sizes conceived for both PdAgNi catalysts are higher than those of the PdRhNi and PdIrNi four catalysts. The most probable reason is due the impact of adding Ag to Pd and Ni. Unlike Ir, Rh, and Ni, the geometrical features of Ag are larger than those of Pd. However, both catalysts achieve particle size ranging from 3 to 5 nm which

is 3nm smaller than that particle size obtained for PdAgNi samples prepared by [149]. The method applied in that paper is a traditional $NaBH_4$ reduction without 2-propanol and KBr which might further support the goodness of the devised protocol due to producing smaller particles. Also, The particle size of PdIrNi systems is 2.26 and 2.36 in average which is slightly less than that reported in [170].

$Pd_4Ag_2Ni_1/C$

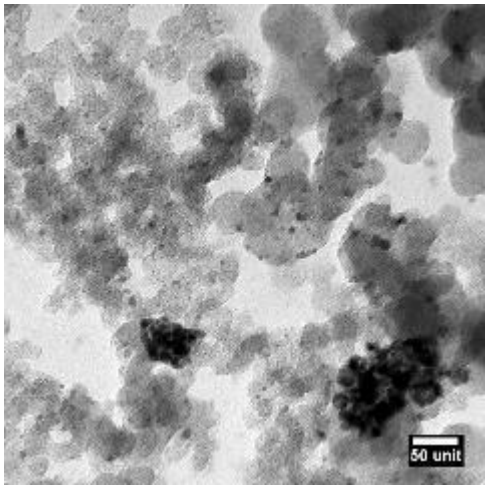

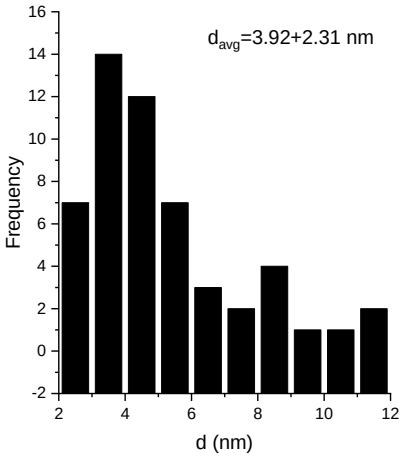

PdAgNi/C

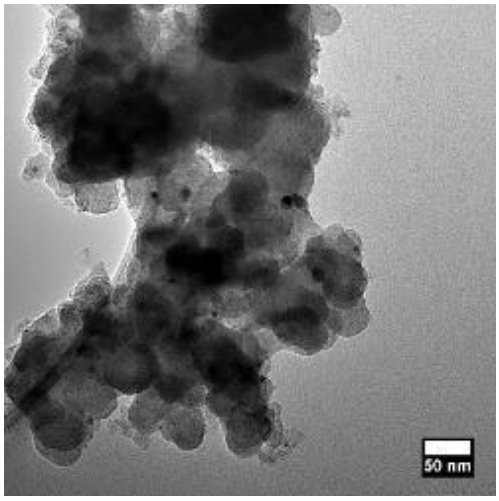

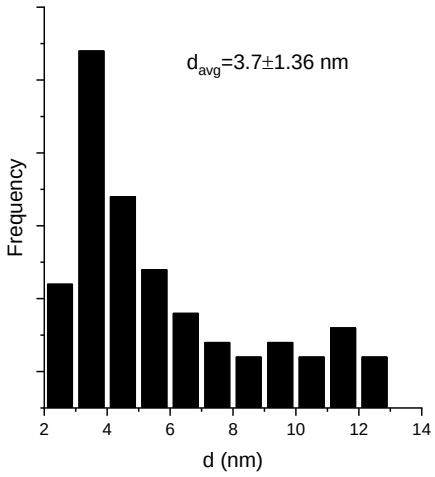

PdRhNi/C

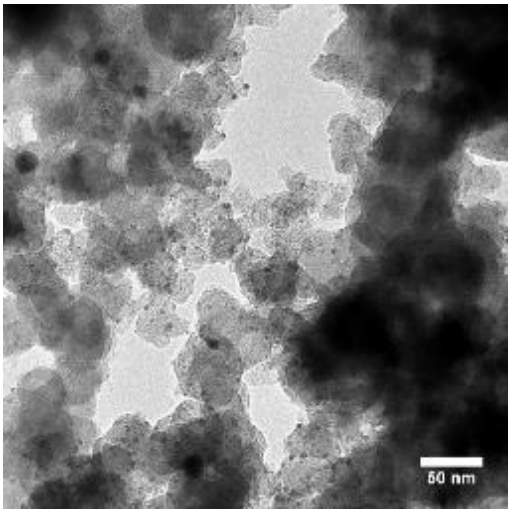

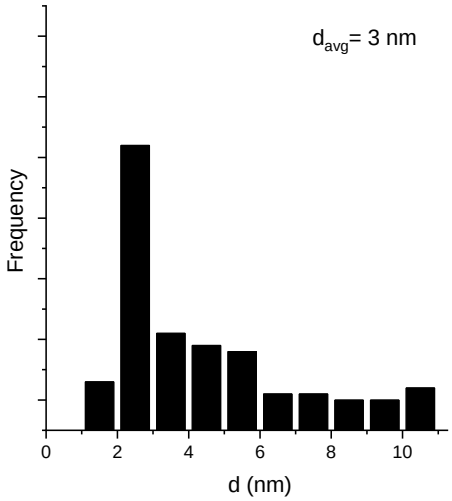

$Pd_4Rh_2Ni_1/C$

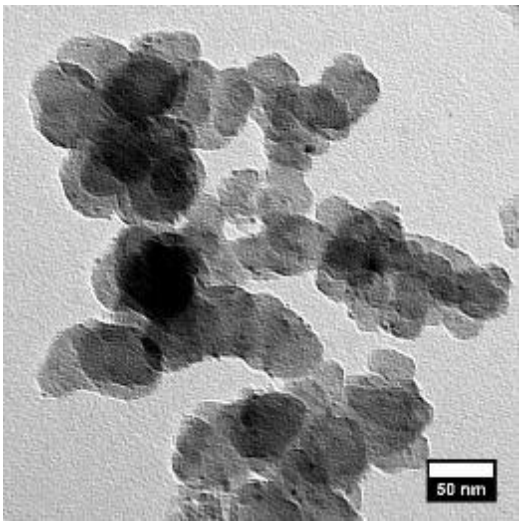

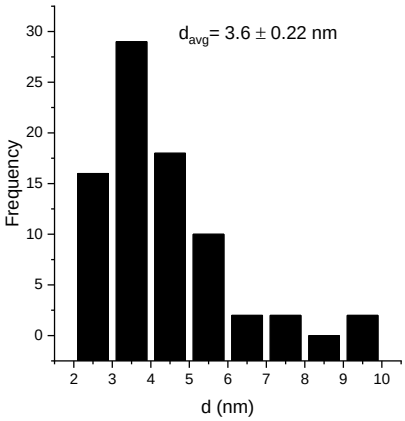

$PdIrNi/C$

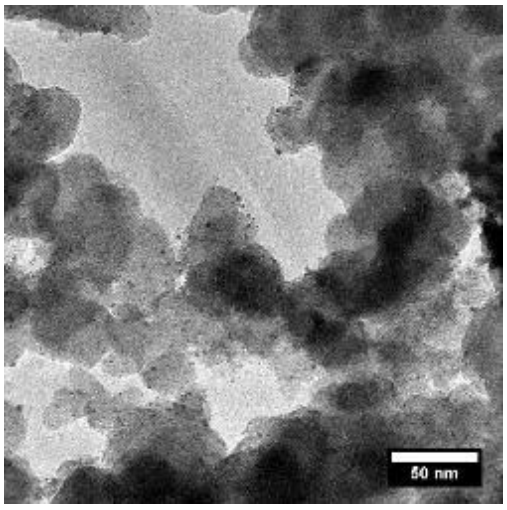

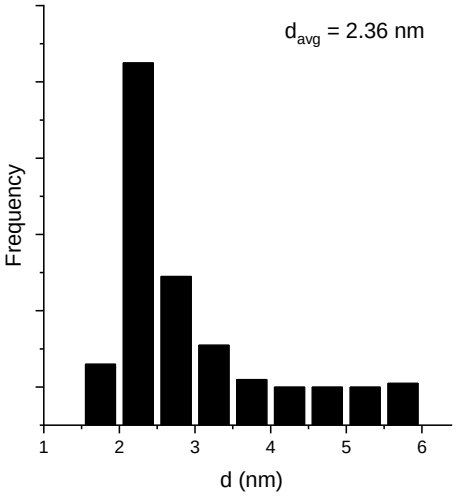

$Pd_4Ir_2Ni_1/C$

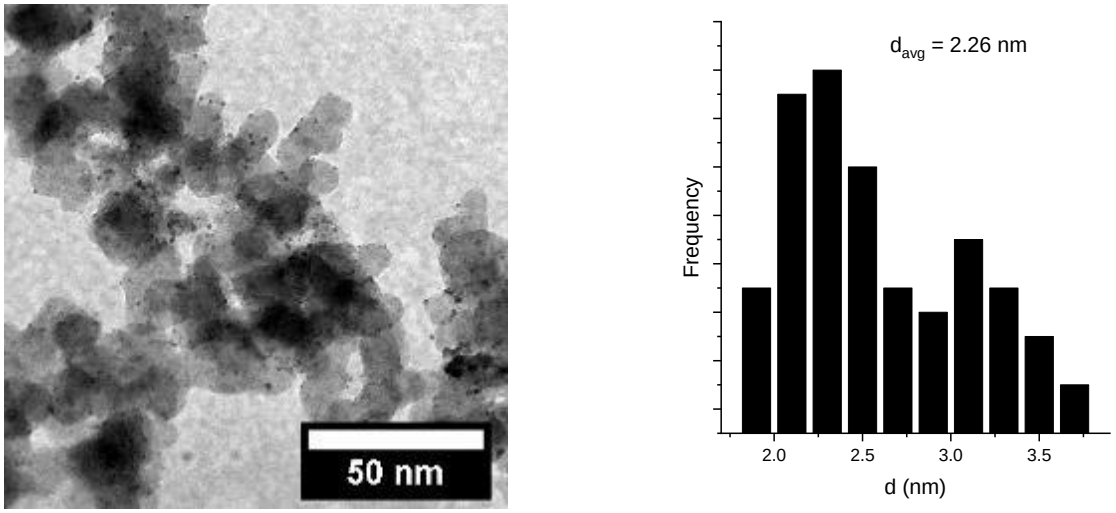

Figure 6-4 TEM Micrographs of PdIrNi/C, PdAgNi/C, PdNiRh/C, $Pd_4Ir_2Ni_1$/C, $Pd_4Ag_2Ni_1$/C, and $Pd_4Rh_2Ni_1$/C

6.2.4 XPS

Table 6-3 lists the XPS surface concentration of each metal in the prepared catalysts. Moreover, for each metal, the metallic and oxide states are also quantified. Unlike the three PdAuNi systems in Chapter 5 in which no PdO was detected in the trimetallic systems, in this chapter, PdO is detected in all catalysts except $Pd_4Ag_2Ni_1$ (Appendix 2). However, The PdO concentration in case of the monometallic Pd/C is 0.45% while it is much less in case of all other trimetallics (less than 0.13%) in Table 6-3. This still indicates the enhanced air stability of Pd when alloyed with Ni and Ag, Ir, or Rh. Another observation from Table 6-3 is that the Pd 3d peak position is shifted to higher binding energy values than the monometallic Pd/C for all of the trimetallic catalysts.

This is also the opposite of the lower shift for PdAuNi/C_{SBIPP} and PdAuNi/C_{SBEG} compared to Pd/C in Chapter 5. This suggests a net electron loss from Pd. It is noteworthy also that the lowest shift (+0.05 eV) happens in the PdAgNi systems and the highest occurs for the PdIrNi systems (+0.10 eV). The Rh $3d_{5/2}$ peak is located at 307.12 and 307.22 eV for PdRhNi and $Pd_4Rh_2Ni_1$ (Appendix 2), respectively. Both of them are shifted to lower binding energies compared to the bulk Rh (307.6 eV) which indicates a net electron gain has occurred into Rh. For those catalysts, also, the Ni 2p shift higher binding energies is significant (0.4 eV) compared to both of the bulk and other catalysts in Table 6-3. This suggests a net electron loss from Ni has occurred which is noted for the other trimetallic systems as well though the shift is less than that of PdRhNi systems.

For the PdIrNi systems a clear positive shift of the Pd 3d binding energy value is noted with > 0.06 eV which informs of a net electron loss of Pd and potentially a strong bonding with the reaction adsorbates. The Ir 4f peak position for PdIrNi is very close to the bulk Ir but that of $Pd_4Ir_2Ni_1$ is shifted +0.08 eV to higher values. Moving along, the Pd 3d peak position has the same location on both PdAgNi systems which is shifted 0.05 eV to higher values than the monometallic Pd/C. Once again this indicates a net electron loss has occurred from Pd. Like Pd, the Ag peak is also located at the same position (368.28 eV) on both PdAgNi systems. Again, this is slightly shifted from the bulk silver at 368.2 which indicates a net electron loss from Ag.

Table 6-3 XPS surface quantification of PdIrNi/C, PdAgNi/C, PdNiRh/C, $Pd_4Ir_2Ni_1/C$, $Pd_4Ag_2Ni_1/C$, and $Pd_4Rh_2Ni_1/C$

Catalyst	Pd at. %		Pd $3d_{5/2}$ (eV)	Rh at. %		Rh $3d_{5/2}$ (eV)	Ir at. %	Ir $4f_{7/2}$ (eV)	Ag at. %	Ag $3d_{5/2}$ (eV)	Ni at. %		Ni $2p_{3/2}$ (eV)*
	Pd^0	Pd^{2+}		Rh^0	Rh^{2+}						Ni^0	Ni^{2+}	
Pd/C	1.63	0.45	335.43	x	x	x	x	x	x	x	x	x	x
PdRhNi/C	1.15	0.08	335.54	0.56	0.15	307.12	x	x	x	x	0.06	0.64	856.00
$Pd_4Rh_2Ni_1/C$	1.61	0.08	335.49	0.42	-	307.22	x	x	x	x	0.04	0.14	856.19
PdIrNi/C	1.18	0.13	335.54	x	x	x	1.48	60.88	x	x	0.32	0.93	855.87
$Pd_4Ir_2Ni_1/C$	1.39	0.10	335.51	x	x	x	1.16	60.98	x	x	0.12	0.18	855.60
PdAgNi/C	0.64	0.12	335.48	x	x	x	x	x	0.32	368.28	-	2.01	855.78
$Pd_4Ag_2Ni_1/C$	1.59	-	335.48	x	x	x	x	x	0.40	368.28	0.05	0.73	855.78

*The Ni peak position is based on the $Ni(OH)_2$ since it is the major Ni form.

The measured Ni oxide concentration is usually much more than its metal one. The Ni oxide species are very small in size and tends to segregate into the surface. However, for the PdRhNi system, the measured atomic concentration of Ni and Rh are 0.7% and 0.71, respectively. Yet, the Pd concentration is 1.23% even though it is noteworthy that the stoichiometric added metal precursors are 1:1:1. Also, in case of $Pd_4Rh_2Ni_1$/C, the theoretical atomic ratios of Pd: Rh: Ni is 4: 2: 1, but the measured concentration is 1.71 : 0.42 : 0.18. For both PdRhNi catalysts, it seems – from an XPS perspective –the surface is densely populated with Pd. This is contradictory to the EDX measurements reported in Table 6-2 which shows the atomic ratios are close to the theoretical ones. The reason is probably due to the depth of surface measured by both techniques. Yet, based on the XPS results, the top surface of PdRhNi two catalysts are rich in Pd which is unusual when Ni is present with Pd. For the PdIrNi system, the XPS measured Pd : Ir : Ni ratio is 1.31: 1.48 : 1.25 which is close to the theoretical values. A similar trend was found for $Pd_4Ir_2Ni_1$. Once more, the EDX measurement are in a slight disagreement with the XPS. As far as the PdAgNi catalyst is concerned, the Ag and Pd atom concentrations are 0.32 and 0.76 At.%, respectively. On the other hand the Ni concentration (all oxide) is 2.01 At.%. A similar trend is noted with $Pd_4Ag_2Ni_1$ in which the Ag and Pd concentrations are 0.40 and 1.59 At.%, respectively. The Ni concentration, on the other hand, equals 0.78 At.%. The Ag measures in both catalyst are less than their theoretical expectations which suggests and corporate the EDX measurements – that it has a high tendency to segregate into the core. On the contrary of Ag, Ni has – as was seen with other catalysts – this high surface segregation potential which also agrees with the EDX. The Pd is in transitional behaviour among Ag and Ni.

Figure **6-5** shows the XPS spectral peaks of Pd, Rh, Ag, Ni, and Ir for PdRhNi, PdIrNi, and PdAgNi catalysts. The peaks of the other 4.2.1 catalysts are included in (Appendix 2).The Ir and Ag peaks do not present any oxide formulation. On the other hand, Rh shows metal and oxide presence but the Rh metallic peaks are much less intense than the oxide ones. It is interesting that the presence of both Ni and Rh together has almost prevented any Pd oxidation. The Ni peaks are mainly oxide ones. The Ni metallic peaks – are significant – in comparison to $Ni(OH)_2$ – only in PdRhNi and PdIrNi systems. The PdO peaks are barely noticed in case of $Pd_4Ag_2Ni_1$ and $Pd_4Rh_2Ni_1$.

PdRhNi/C

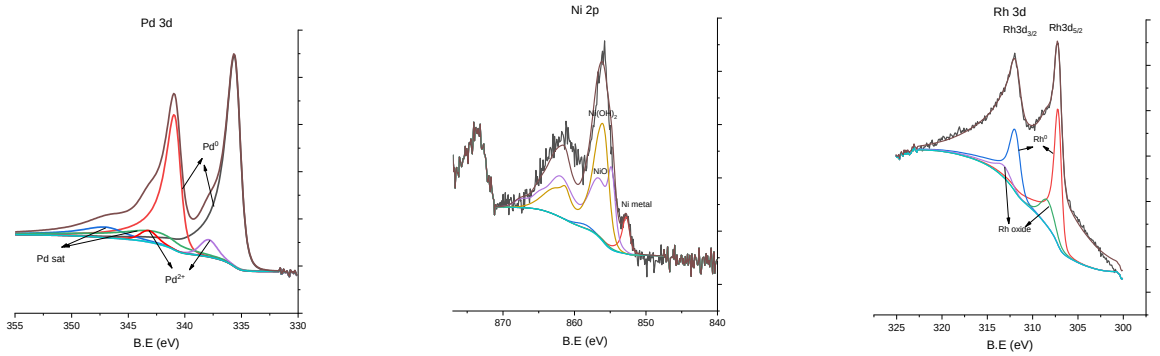

PdIrNi/C

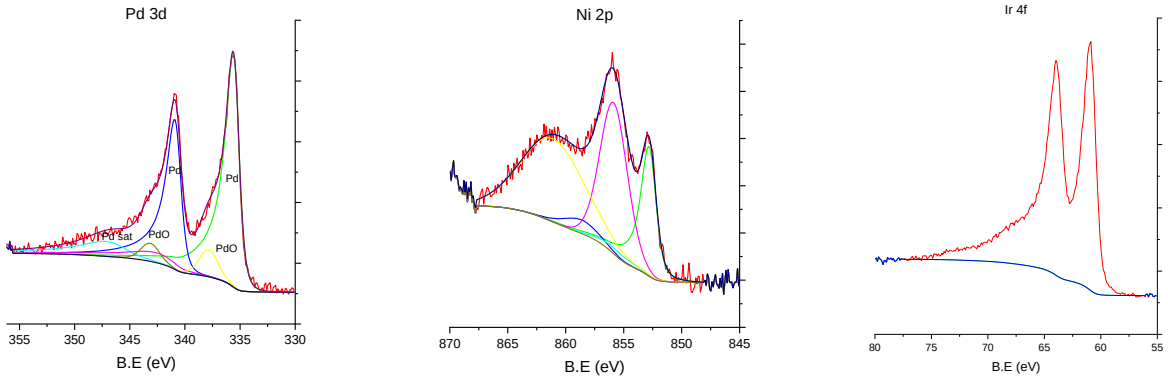

PdAgNi/C

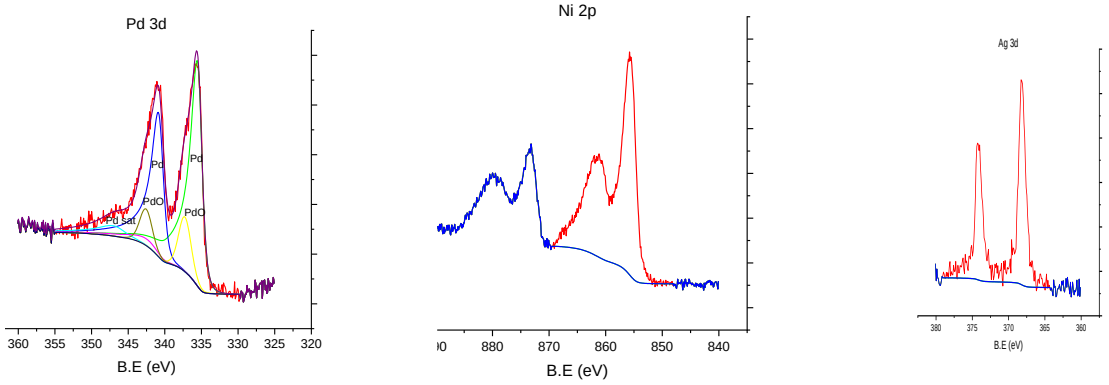

Pd 3d spectra and enlarged Pd $3d_{5/2}$

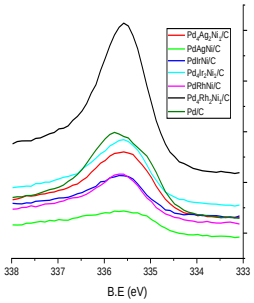

Figure 6-5 XPS peaks of Pd 3d, Ag 3d, Ir 4f, Ni 2p, Rh 3d of PdNiRh/C, $Pd_4Rh_2Ni_1/C$, PdIrNi/C, $Pd_4Ir_2Ni_1/C$, PdAgNi/C, and $Pd_4Ag_2Ni_1/C$ and enlarged Pd $3d_{5/2}$

Though it is beneficial to add Ni into Pd for alcohol oxidation, the high Ni quantities would lead to a surface almost totally covered with Ni which results in preventing ethanol oxidation. Also, a similar – but not identical to Ni – tendency of surface segregation is noted for Ir [121,123]. The Ag 3d peak is located at 367.78 and 368.28 eV for PdAgNi and $Pd_4Ag_2Ni_1$, respectively. The 3d peak position of Ag 3d is 368.3 eV and the noticed shift from higher to lower binding energies could be understood in terms of electron donation Ag into Pd. A similar finding was reported about Pd, PdAg, and PdAgNi [149]. On the contrary of Ag 3d, the Ir 4f is shifted to higher binding energies in case of PdIrNi systems – though the shift is less than 0.1 eV – which might suggest an electron loss on the side of Pd in favour of Ir. Unlike the traditional $NaBH_4$ reduction reported in [170] for PdIrNi, no IrO was detected in both PdIrNi systems in Table 6-3 and Figure **6-5** which might further proves the full reduction of Ir especially some PdO exists in both PdIrNi systems. That is probably why the shift to higher binding energies in the Pd 3d in case of both PdIrNi systems.

6.3 Electrochemical Characterisation

6.3.1 CV

Figure **6-6** shows the cyclic voltammetry scans of the monometallic catalysts in 1M EtOH + KOH at 50 mV/s in which the current is normalized by each metal weight. The left figure compares the current draw applying Pd to other metals (Ag, Rh, Ir, and Ni) and Pd current is taken out from the right one. This is performed to investigate whether any of the cocatalyst metals (Ag, Ni, Ir, and Rh) has some potential for ethanol oxidation on their own without Pd or not. The reported applied potential is counted versus the normal hydrogen electrode (NHE) but the experiments were actually performed versus Ag/AgCl (sat KCl) reference electrode which was converted to NHE afterwards. It is only Pd which draws an observable oxidation current at reasonably low applied potential (-0.4 V to 0.4 V vs NHE). This indicates ethanol oxidation occurs only on Pd. On the other hand, Rh, Ni, Ag, and Ir do not seem to produce any oxidation current which proves those metals are not active for ethanol oxidation on their own. Only Ni, and at very high applied potential (+0.5 V), that draws a noticeable oxidation current due to the $Ni(OH)_2$/NiOOH redox pair.

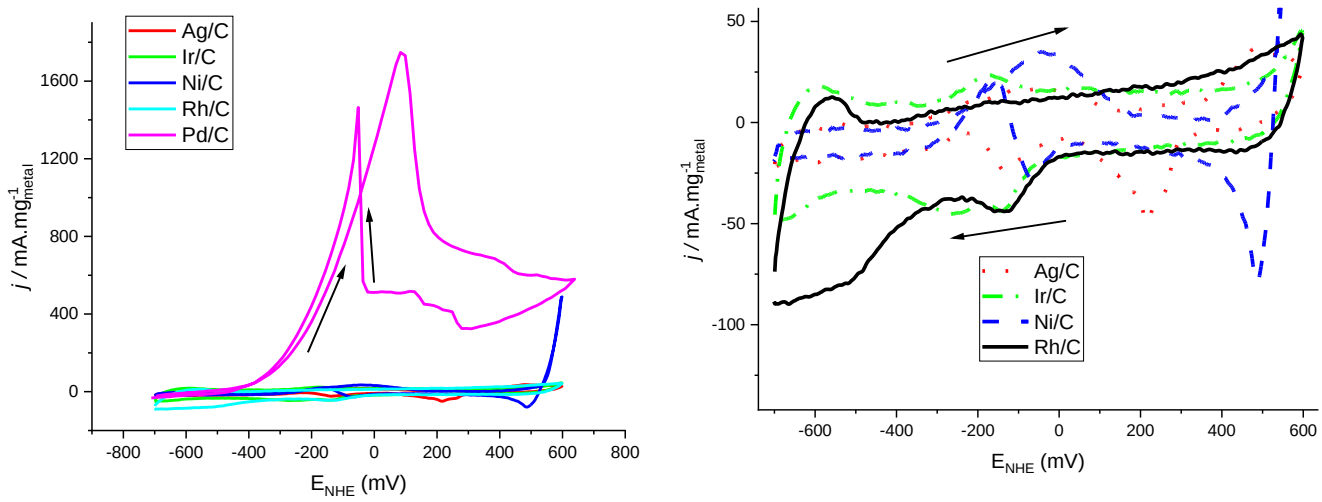

Figure 6-6 Cyclic voltammetry (CV) in 1M EtOH + KOH (*right*) and 1M KOH (*left*) of Pd/C, Rh/C, Ag/C, Ir/C, and Ni/C at 50 mV/s

In the reductive sweep, high positive current is noted on Pd due to the removal of incompletely oxidised species from Pd active sites. As the other metals do not interact with ethanol they do not draw any positive current in the reductive backward scan, but small reduction currents could note on them especially Ni and Ag. Once again those are due to the reduction of Ni and Ag oxides as reported in Figure 6-7. The potential explanation is that metal sites on Ag, Ni, Ir, and Rh are oxidised in the forward scan and consequently reduced in the reverse one. The Rh, in particular – is interesting because the Rh potential to break the C-C bond is a controversy. Comparing Pd and Rh – according to [120] – using the CV, they have found the E_{onset} of ethanol on Rh/C is 280 mV less than Pd/C. Also, in the reverse scan they have found a shoulder close at the peak current density. The forward current peak is attributed to the oxidation of freshly chemisorbed species and the reverse current peak is due to the removal of the incompletely oxidised species during the forward scan.

Figure **6-7** shows the CV graphs of PdIrNi/C, PdAgNi/C, PdRhNi/C, $Pd_4Ir_2Ni_1$/C, $Pd_4Ag_2Ni_1$/C, and $Pd_4Rh_2Ni_1$/C in 1M KOH at 50 mV/s scan rate. The CV of Pd/C is shown for comparison. This test informs of the electrochemical processes that occur on each catalyst such hydrogen adsorption/absorption, metal surface oxidation, hydrogen evolution, in addition to showing the electrochemical active surface area (ECSA). Occasionally, the 421 and 111 terms are used to describe the trimetallic catalysts following their respective metal atomic content. The $H_{ads/abs}$ peak (-700 to -500 mV) is significant – but broad – on PdRhNi/C, PdIrNi/C, $Pd_4Rh_2Ni_1$/C, and $Pd_4Ir_2Ni_1$/C. On the contrary of those catalysts, the $H_{ads/abs}$ peak is greatly suppressed in case of Pd/C due to the ability of Pd to absorb hydrogen into its bulk structure. The PdAgNi/C and $Pd_4Ag_2Ni_1$/C catalysts are in

transitional state between Pd and the other trimetallics in case of hydrogen adsorption and absorption. The OH_{ads} (-400 mV to -200 mV) is clearest on Pd while it disappears on PdRhNi/C, PdIrNi/C, $Pd_4Rh_2Ni_1/C$, and $Pd_4Ir_2Ni_1/C$. Once more, the PdAgNi/C and $Pd_4Ag_2Ni_1/C$ is in transitional behaviour regarding the OH adsorption. The surface oxidation follows – and sometimes overlaps – the OH adsorption. For the PdRhNi, PdAgNi, and PdIrNi systems, the Ni surface oxidation peak is noted at the far end of the oxidation forward scan above -500 mV.

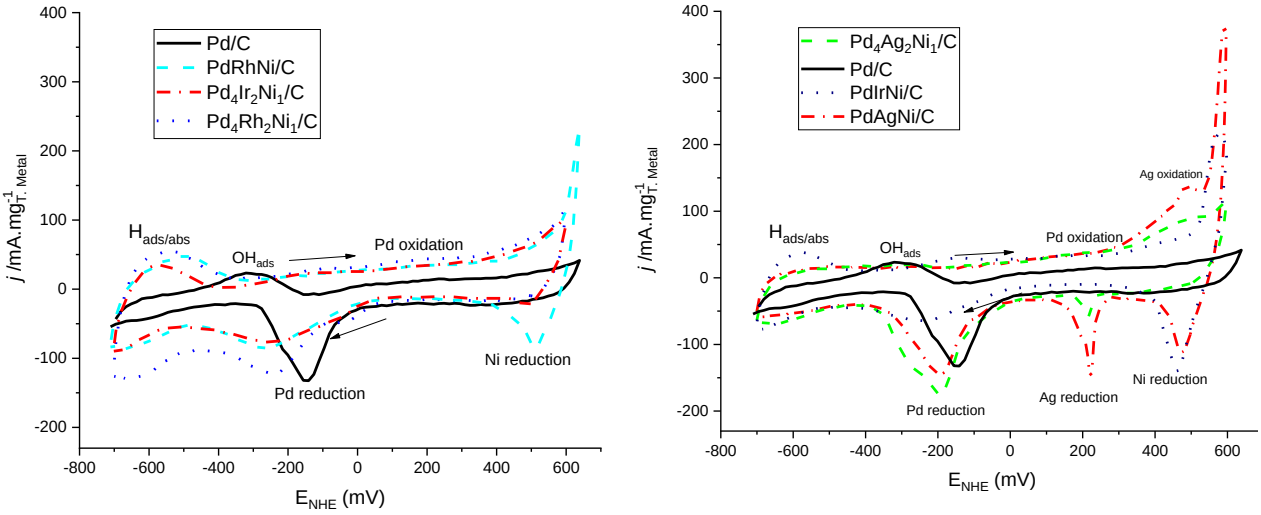

Figure 6-7 CV voltammograms of (*left*) Pd/C, $Pd_4Ir_2Ni_1/C$, $Pd_4Rh_2Ni_1/C$, PdNiRh/C (*right*) Pd/C, PdAgNi/C, PdIrNi/C, $Pd_4Ag_2Ni_1/C$, and in 1M KOH at 50 mV/s

Yet, the Ni oxidation peak is significantly smaller in case of $Pd_4Rh_2Ni_1/C$, $Pd_4Ir_2Ni_1/C$, and $Pd_4Ag_2Ni_1/C$ than their respective counterparts with 1:1:1 atomic ratio. The apparent reason of this reduction is the significantly smaller Ni quantity present in the 421 catalysts compared to the 111 ones. The Pd surface oxidation – in all catalysts – starts at a much lower potentials (0.0 V). The surface oxidation of Ir and Rh seems to go similarly to that Pd. On the contrary, Ag oxidation peaks are easily noted at -500 mV on PdAgNi and $Pd_4Ag_2Ni_1$ though in the latter, it is much smaller than the former most probably because the Ag quantity in the 421 one is less than the 111 one.

In the cathodic sweep, the Ni reduction peak in the 111 catalysts (PdRhNi, PdIrNi, and PdAgNi) is significantly shown around 500 mV which is smaller in their 421 counterparts. The Ag reduction is also noted on PdAgNi and $Pd_4Ag_2Ni_1$ at 240 mV. Like the Ag oxidation, the peak is significantly small in the 421 catalyst compared to the 111 one. The PdO reduction peak in on Pd/C is larger than all other trimetallic catalysts except PdAgNi/C and $Pd_4Ag_2Ni_1/C$. The higher PdO reduction area of the two PdAgNi/C catalysts is an evidence of enhanced electrocatalytic activity in comparison to

Pd/C. On the other hand, the PdO reduction peak – on PdRhNi and PdIrNi systems – is smaller than Pd/C. This suggests the Pd/C is more electroactive than PdIrNi and PdRhNi catalysts (both 111 and 421 compositions).

Figure 6-8 shows the cyclic voltammetry in 1M KOH+EtOH for the 6 trimetallic catalysts and monometallic Pd. This in-situ potential-controlled scan helps verify the activity of each catalyst for ethanol oxidation at certain potential window and applying a fixed scan rate. The oxidation onset potential, oxidation current peak and potential are the key factors to evaluate the catalyst activity. The ethanol oxidation kinetics is faster on the PdAgNi systems compared to the Pd single catalyst. The onset oxidation potential on PdAgNi systems is approximately -500 mV while it is shifted to the right around 100 mV in case of Pd/C. Also, the oxidation current peak on PdAgNi and $Pd_4Ag_2Ni_1$ is 2600 and 2225 mA/mg_{Pd}, respectively. Yet, that peak on Pd is 1700 mA/mg_{Pd}. This suggests a higher rate of ethanol oxidation – and a larger number of Pd active sites that are engaged with ethoxy species. Also, the oxidation peak potentials on PdAgNi systems are shifted to lower values compared to Pd which once more suggests an enhanced electrocatalytic activity. The enhanced electrocatalytic performance of PdAgNi could be attributed to the impact of Ag and Ni could contribute in the Pd ethanol oxidation. For once, Ag is similar to Au in various aspects upon mixing with Pd. For instance, the Ag crystal peaks as could be seen in Figure 6-1**,** are located at lower diffraction angles just like Au. Also, the EDX measurements (Table 6-2) confirms Ag tends to segregate into the core of PdAgNi nanoparticles which is the particular behaviour of Au and the opposite of Ni. Also, the XPS Ag measured concentrations (Table 6-3) confirm its tendency to escape to the core of PdAgNi. Other interesting XPS findings (Figure 6-5) about the PdAgNi systems is that Ag exists only in metallic on both the 111 and 421 catalysts which suggests a good potential of mixing and alloying with Pd. It is similar to Au which exists only in a metallic state in PdAuNi nanoparticles as was found in chapter 5. Another similarity is that adding Ag and Ni to Pd has shifted its XPS binding energies to lower values (Figure 6-5) which is similar to what happened with PdAuNi (Figure 5-5). The main difference between the two PdAgNi and PdAuNi prepared is the XRD patterns which show one sharp peak of Ag and another overlapping Pd one in case of PdAgNi (Figure **6-2**) and only peak reflective peak of PdAuNi (Figure 5-1). On the contrary of PdAgNi systems, the simultaneous addition of Ni and either Ir or Rh in both the 111 and 421 systems has been proven detrimental to the electrocatalytic activity of Pd for ethanol oxidation. For example, the PdIrNi systems achieve oxidation peak current density of 500 and 400 mA/g_{Pd} which are less than half that of the monometallic Pd/C. The EDX and XPS measurements confirm the higher tendency of Ir and Ni to segregate into the surface in comparison to Pd. It is interesting that the 421 achieves less oxidation current than the 111 one. This indicates the lower content of Ir and Ni – applying this method – decreases the Pd electrocatalytic activity for

EOR even further. On a positive note, though, the onset oxidation potential (E_{onset}) on the PdIrNi systems is less than that of Pd which indicates an enhanced catalytic activity. As for the PdRhNi ones, the less-containing Rh and Ni catalysts (421) starts to oxidise ethanol at a higher potential than the 111 one.

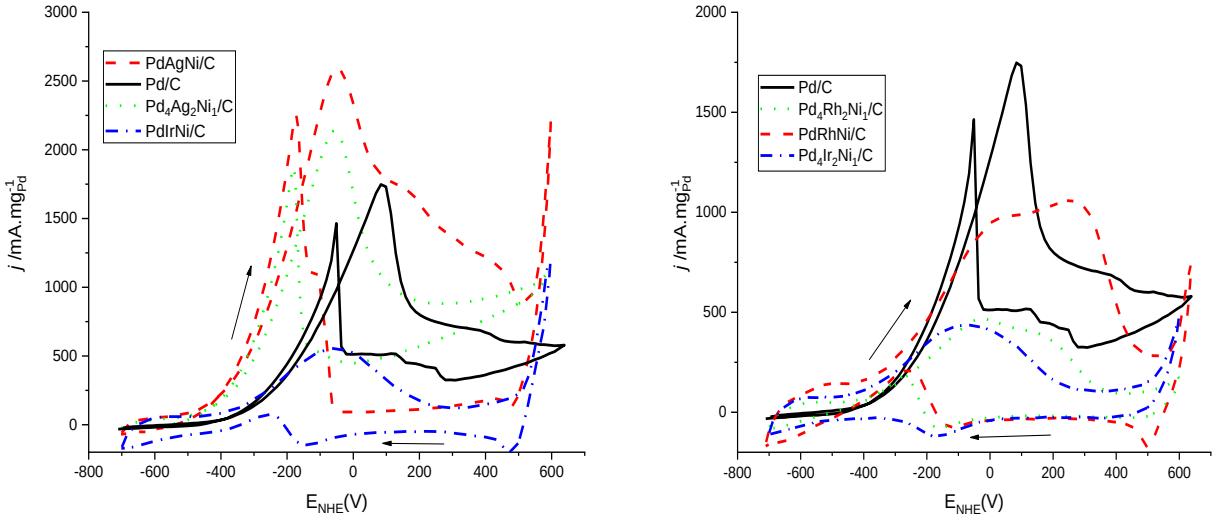

Figure 6-8 CV voltammograms of (*left*) Pd/C, PdAgNi/C, $Pd_4Ag_2Ni_1$/C, PdIrNi/C, (*right*) Pd/C, $Pd_4Rh_2Ni_1$/C, PdRhNi/C, and $Pd_4Ir_2Ni_1$/C in 1M KOH + EtOH at 50 mV/s

Furthermore, the oxidation current on the 111 system is less than that of the 421 one. However, the CV shape of PdRhNi catalysts has a unique feature in comparison to Pd/C and other catalysts. The other catalysts – including Pd/C – achieve a single oxidation peak in the forward CV sweep, but the two PdRhNi systems seem to have two overlapping peaks: at -0.0 V and 300 mV vs NHE. The overlapping peaks could be attributed to the oxidation of different species such as CO-like species at the lower applied potential and some ethoxy CH_3COOH at the higher one. If this analysis is true, it will be a result from the presumed – but debated - Rh potential to promote the CO_2 selectivity through breaking the C-C bond [93,111,112,119,120,174,175]. Relooking at the physical characteristics of PdRhNi systems would tell through the EDX and XPS that the measure XPS Rh concentration (Table 6-3) is less than the theoretical one, but the EDX chemical analysis (Table 6-2) reveals Rh quantities are close to the nominally added Rh precursors. On the contrary of Ir and Ni, Rh does not seem to segregate to the surface which is suggestive of exposing higher Pd quantities on the surface. On the other hand, the XRD patterns of PdRhNi systems (Figure 6-3) are shifted to higher diffraction angles than the Pd/C which is understandable as the Rh diffraction angles are located at higher diffraction

angles. The crystal peaks' shift to higher diffraction angles is an evidence of contracting the lattice parameters compared to Pd/C. This contraction is due to the incorporation of small Rh and Ni atoms into the Pd lattice which applies compressive stress and strain on the Pd unit cells which down-shifts the *d*-band centre and strengths the adsorption binding of the adsorbates (including poisons).

6.3.2 CA and Tafel measurements

Figure 6-9 shows the chronoamperometric (CA) scans – which is done to study the tolerance of each catalyst for poisoning species and ability to maintain the activity – of Pd/C and the trimetallic systems performed at -0.3 V (30 min) and +0.1 (30 min) V vs NHE in 1M KOH+EtOH. Looking at the cyclic voltammetry (Figure 6-8), at -0.3 V, the ethoxy species mainly cover the surface of the catalytic surface though the adsorption of OH has already started at lower applied potential and as the potential increases more OH is adsorbed leading to oxidising and removing the adsorbed ethoxy. The small quantity of OH and high quantity of ethoxy leading to different current values on the catalysts, but the differences are less than those noted at +0.1 V. Also, the current decrease – after initial decay – is steady and gradual which is indicative of less poisoning species blocking the active sites as the time goes by. Apparently, the Ag addition to Pd expands its crystal lattice and causes tensile stress and strain which up-shifts the *d*-band centre which causes weakening of the Pd-adsorbates bonding. That might have impacted the poisoning tolerance of PdAgNi, and therefore the higher CA currents measured on them. The opposite is noted on the other trimetallic systems looking at the CA currents. At +0.3 V, however, that decrease in the current is more noticed and falling with the time. The PdIrNi and PdRhNi systems draw smaller current values than Pd/C both at -0.1 V and +0.3 V though the difference is paramount at +0.1 V. The interesting finding – which is expected from the CV – is about the PdAgNi catalysts which draw significantly higher ethanol oxidation CA currents in comparison to Pd. Unlike the PdAgNi, adding Ni and either Rh or Ir to Pd – using the applied method – contracts its crystal lattice and causes compressive strain down-shifting the *d*-band centre and as the result the smaller CA currents. The falling currents on Pd and PdAgNi catalysts – at + 300 mV – are due to the generally enhanced kinetics at this high potential on one side. On the other, the PdAgNi and Pd catalysts are naturally more electroactive than the other catalysts at other potentials. Therefore, it could claimed that $Pd_4Ag_2Ni_1$ catalyst is the most stable catalyst but PdAgNi is the most active for ethanol oxidation. And both of them are more active and stable for ethanol oxidation than the other four catalyst in addition to the monometallic Pd/C.

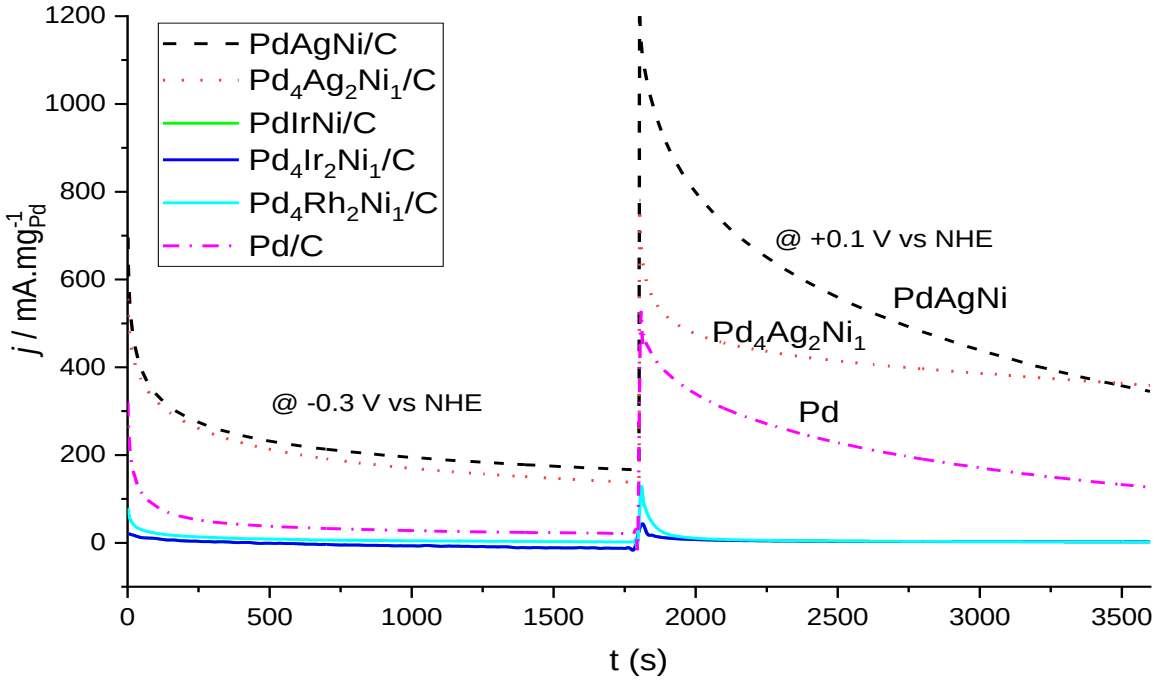

Figure 6-9 Chronoamperometric scans (CA) of PdIrNi/C, PdAgNi/C, PdNiRh/C, $Pd_4Ir_2Ni_1/C$, $Pd_4Ag_2Ni_1/C$, and $Pd_4Rh_2Ni_1/C$ in 1M KOH + EtOH at -0.3 V and +0.1 V vs NHE

Figure **6-10** shows the Tafel polarization obtained by performing the linear sweep voltammetry (LSV) scan at 0.2 mV/s in 1M KOH+EtOH and the Tafel plot extracted from them. The potential window chosen is between -0.3 V and +0.2 V vs NHE and it was picked up to monitor the physiochemical phenomena such as OH adsorption, oxidation of ethoxy species, and catalyst surface layer oxidation. Yet, for the tafel plot this window was restricted to 0.0 V maximum as applied potential because above that it does not resemble a straight line. Also, the study of the lower applied potential and OH adsorption window is more meaningful for the purpose of this work.

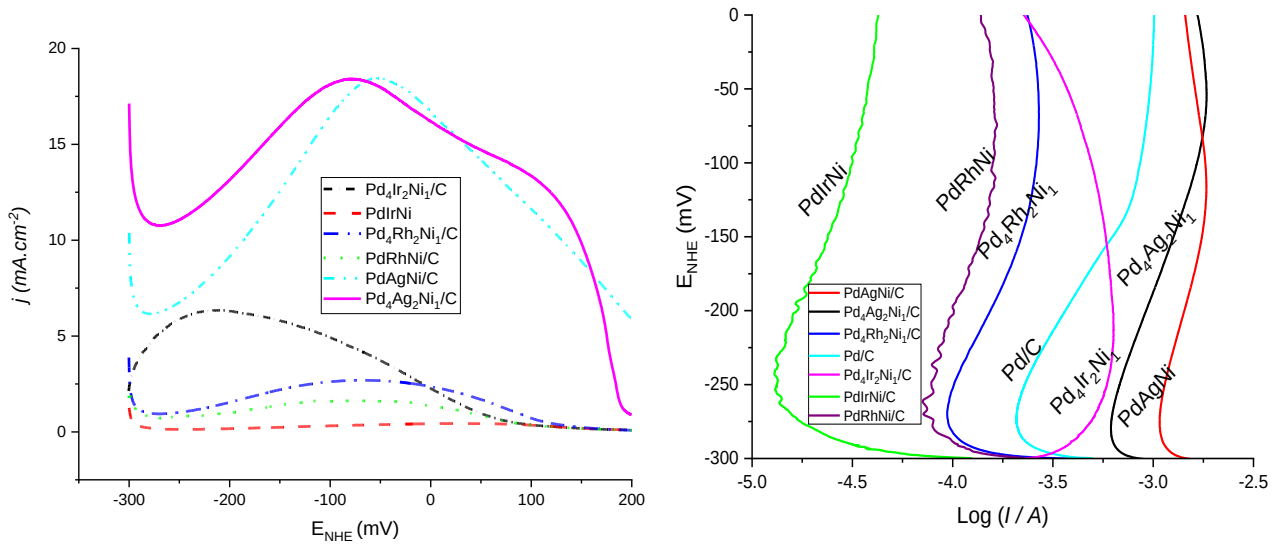

Figure 6-10 (*left*) Linear sweep voltammetry and (*right*) Tafel plots of PdIrNi/C, PdAgNi/C, PdNiRh/C, $Pd_4Ir_2Ni_1$/C, $Pd_4Ag_2Ni_1$/C, and $Pd_4Rh_2Ni_1$/C in 1M EtOH + KOH (scan rate = 0.2 mV/s)

The PdAgNi and Pd systems present linear characteristic behaviour compared to the other catalysts. The lowest Tafel slope is that of PdAgNi followed by $Pd_4Ag_2Ni_1$ and finally Pd. It is noted, however, that the linear behaviour of PdAgNi starts at a potential smaller than the Pd which might be explained by the noticed smaller E_{onset}. Furthermore, it is worthy to note there are two regions on Pd: one between -300 mV and -150 mV and the other between -150 mV and 0.0 V. There is an observable difference in the Tafel slope among the two areas. The first is representative of the OH adsorption, but the latter represents the Pd surface oxidation. With the PdAgNi, it is noted the end of OH adsorption and start of Pd surface oxidation is extended to a potential higher than -150 mV. The opposite behaviour is noted on PdIrNi and PdRhNi catalysts. Also, they present comparatively high Tafel slopes and less linear characteristic performance. The worst performance is achieved on $Pd_4Ir_2Ni_1$ which presents a very high Tafel slopes even at the low potential window which suggests very sluggish ethanol oxidation kinetics on it. The kinetics of PdRhNi ones and PdIrNi.

6.3.3 EIS

For the EIS that, it was reported, for ethanol oxidation on Pd, by increasing the potential from -0.6V to -0.1 the arc size decreases as an indication of enhanced electrode kinetics and these potentials where OH is still being adsorbed [120]. They explained the negative impedance, at -0.1 to 0.1V

potential, in case of Pd catalyst by the strongly adsorbed intermediates on Pd that block the active sites from activating the reaction. Yet, for all Rh EIS spectra, the arcs are all located in the first quadrant [120]. EIS was performed on the six catalysts of this chapter. The objective is to estimate the value of the charge transfer resistance (R_{ct},Ω) and make a comparison among the different trimetallics and the monometallic Pd/C. Figure 6-11 shows the Potentiostatic EIS spectra performed in 1M KOH+EtOH applying Pd/C and the 6 trimetallic catalysts. 4 applied potentials (-0.46, -0.16, +0.14, and 0.44 V) were applied on PdRhNi which was prepared before the other catalysts. Also, the frequency range applied on PdRhNi is 100 kHz to 0.01 Hz but on the other catalysts a smaller range (10 kHz to 0.1 Hz) was applied. On the other catalysts, 3 other potentials (-0.3, 0.0, and +0.3 V) were applied. Considering the PdRhNi, the EIS arc measured at -0.46 and 0.44 V are the highest compared to -0.16 and 0.14 V. At -0.46 V, no effective ethanol oxidation occurs but only the adsorption of ethoxy that may or may not be dissociative. At +0.44 V, the surface of Pd is predominantly blocked by the ethanol reaction intermediates and poisons. The smallest impedance arc is obtained upon applying -0.16 V which is close to the potential where the oxidation peak is noted in the CV (Figure 6-8). On $Pd_4Rh_2Ni_1$/C, the EIS graph does not resemble a part of a semi-circle which indicates a significantly high charge transfer resistance on it. A similar trends is noted on PdIrNi. On $Pd_4Ir_2Ni_1$, the applied potentials of -0.3 and 0.0 V present a semi-circular arc being the smallest at 0.0 V. The impedance values obtained for PdAgNi are higher than those for $Pd_4Ag_2Ni_1$ which suggest smaller charge transfer resistance is attained on the latter.

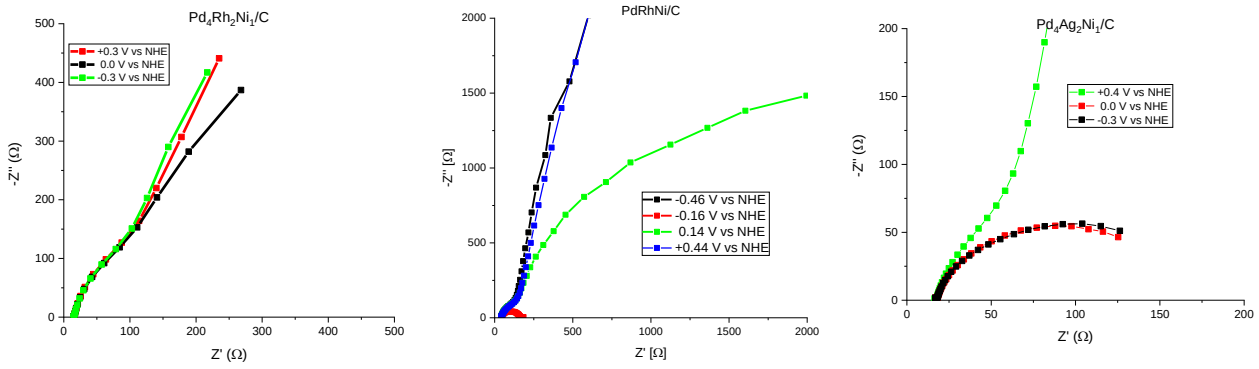

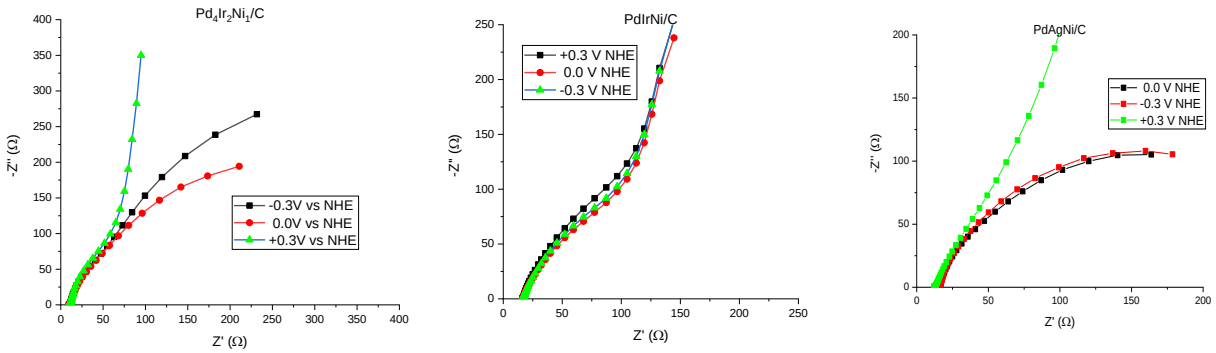

Figure 6-11 EIS spectra of PdIrNi/C, PdAgNi/C, PdNiRh/C, $Pd_4Ir_2Ni_1$/C, $Pd_4Ag_2Ni_1$/C, and $Pd_4Rh_2Ni_1$/C at -0.3 V, 0.0 V, and +0.3 V vs NHE

This might seem controversial to the results of CV and CA which reveal higher catalytic functionality for PdAgNi. The controversy might be explained that more Pd active sites exist on $Pd_4Ag_2Ni_1$ which leads more ethanol oxidation current. Figure 6-12 shows the charge transfer resistance according to the two electrode-electrolyte interfaces EIS model (shown in Figure 5-11). The PdIrNi systems, unlike other catalysts – estimates significantly high R_{ct} values. Also, on the contrary of other catalysts, the R_{ct} increases with increasing the applied potential on PdIrNi and $Pd_4Ir_2Ni_1$ systems. The potential explanation for this is the small Pd active sites (especially on PdIrNi) exposed on the surface as both Ir and Ni have a higher tendency of surface segregation than Pd. On the contrary of PdIrNi, the PdAgNi systems expects the lowest charge transfer resistance due to the enhanced ethanol oxidation kinetics. The reason is the opposite to that of Ir that Ag is less likely than Pd to segregate into the surface. Additional Ag expands the Pd crystal lattice. Finally the Pd active sites on $Pd_4Ag_2Ni_1$ are higher than those on PdAgNi/C and that is why the lower R_{ct} values.

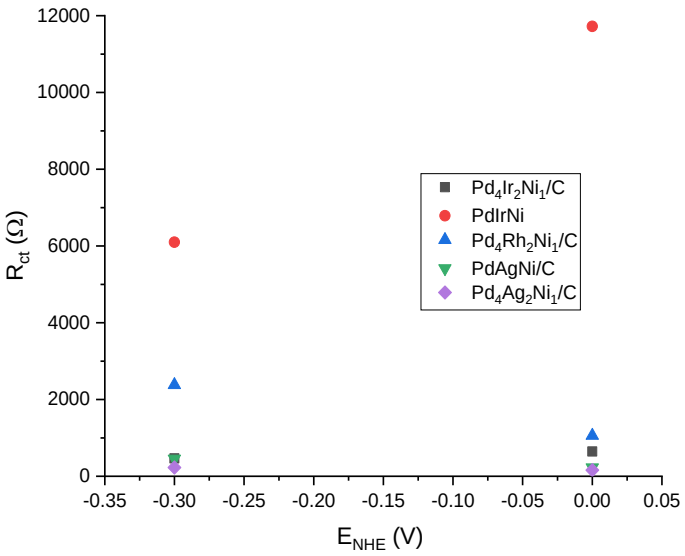

Figure 6-12 Charge transfer resistance (R_{ct}) of PdIrNi/C, PdAgNi/C, $Pd_4Ir_2Ni_1/C$, $Pd_4Ag_2Ni_1/C$, and $Pd_4Rh_2Ni_1/C$ measured at -0.3 V, 0.0 V, and +0.3 V vs NHE

The EIS experiments applying Pd/C and PdRhNi/C were performed using different values of applied potentials as they were prepared at a time distance from the rest of the catalysts. Figure **6-13** shows the charge transfer resistance and EIS spectra of Pd/C and PdRhNi/C. The ethanol oxidation reaction is greatly promoted on Pd/C more than PdRhNi/C by examining the size of the semi-circle arc of EIS scans. Also, the fitted R_{ct} values on PdRhNi are – in general except at the high potential – very high compared to Pd/C. at the lower potential window (-0.5 V to -0.2 V), though, the Rct values are still very high which explains the less OH adsorbed and struggling ethanol oxidation process as most of Pd sites are blocked by some ethoxy molecules. It is interesting that a significant reduction occurs in R_{ct} at the higher potential window (-0.15 V to 0.15 V) which might be explained by the ambiguous role of Rh which may or may not be helping break the C-C bond and promote the full oxidation to CO_2.

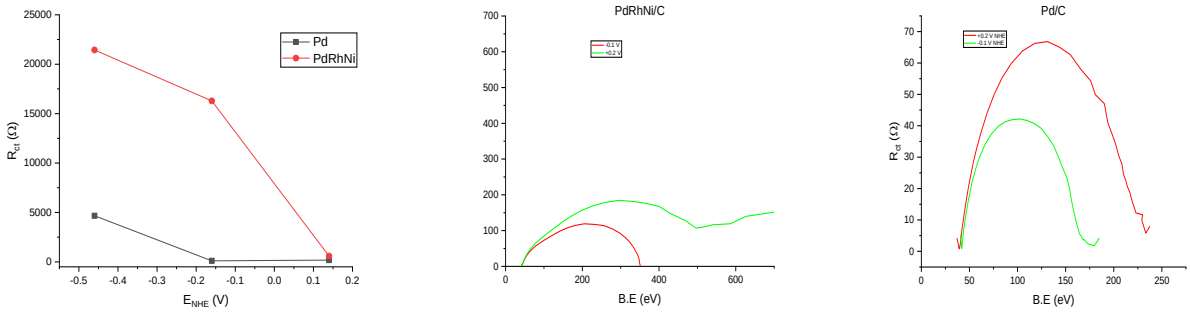

Figure 6-13 R_{ct} values measured -0.46 V, -0.16 V, and +0.14 V vs NHE and EIS spectra of Pd/C and PdRhNi/C

Therefore, the individual metals of Ir, Ni, Ag, and Rh that were prepared applying the SBIPP protocol are not active for ethanol oxidation at applicable applied potential compared to Pd. However, their individual addition to Pd could significantly increase its catalytic potential for ethanol oxidation as widely reported and discussed in section 2.8. Yet, there is short effort pursued on the development of trimetallic combinations of Pd and two other metals and therefore this work could be considered among the first trimetallic catalysts. The physical characterisation reveals interesting findings about each trimetallic catalysts. For example, adding Ag and Ni have given a surface rich in Pd and a core rich in Ag as verified by XPS and EDX. Furthermore, adding Ag has resulted in an alloy structure between Pd and Ag (though the alloying potential is not as strong as that of Pd and Au) and the XRD peaks are shifted to lower diffraction angles. The appearance of individual reduction and oxidation peaks Ag and Ni in the only KOH CV is suggestive of weak alloying among the three metals. Also, the average particle size of both PdAgNi catalysts is larger than that of Pd due to the impact of adding Ag (verified by TEM). The bigger particle size might suggest less active sites exist on the surface generating small current, but the intrinsic enhancement onto the PdAgNi by the d-band structure modification seems have highly promoted the surface catalytic properties and that is why larger currents was actually obtained. The addition of Ir and Ni have led to the enrichment of the surface with Ni and Ir and the Pd seems to have segregated below them in the core of PdIrNi particle as verified by EDX and XPS analyses. As both Ir and Ni are not active on their own for ethanol oxidation, much lower currents are drawn from both PdIrNi catalysts in all the electrochemical tests, This is the situation even though the XRD does not show separate peaks of Ir or Ni which suggests an alloy structured is produced. It is noteworthy that both Ni and Ir would exert a tensile stress and strain on the Pd crystal lattice. This is interesting as it might have downshifted the *d*-band centre of Pd and made it less tolerant for poisoning species. Those two catalysts have very small average particle sizes compared to the other catalysts and still the many active sites available on the surface seem useless for ethanol oxidation as very small current is actually drawn from both of them. Add Rh and Ni into Pd – in PdRhNi and $Pd_4Rh_2Ni_1$ – should be treat with caution. First, both EDX and XPS concentrations of Rh are much less that what is expected and there is a potential that it segregated into the core but such behaviour was not reported and there is no solid evidence to proof. On the other hand, the clear shift of Pd XRD peaks to higher diffraction angles is considered an evidence that Pd and Rh are alloyed in an alloy nanostructure. Furthermore, there is an unresolved controversy surrounding Rh and its potential for breaking the C-C bond in ethanol electrooxidation. This is an advanced issue and the presence of two oxidation peaks (Figure **6-8**) – which does not happen with PdIrNi and PdAgNi systems – could pose a question about the individual species that

are those peaks represent. Is it possible that the lower potential peak if for CO_2 (or one of its derivatives) and the other peak for acetic acid (or one of its derivatives? This question cannot be answered based on the obtained results and it needs a sophisticated in-stiu facility to monitor the reaction mechanism at the each applied potential. Yet, it is evident that both PdRhNi systems are less active and stable than Pd for ethanol oxidation though the question of CO_2 selectivity cannot be addressed.

6.4 Conclusions

In light of the above results and discussion, some conclusions could be drawn. The SBIPP protocol (NaBH4-2-proapanol reduction complex and KBr capping agent) have successfully produced trimetallic PdNiMe (Rh, Ir, and Ag) nanoparticles supported on Vulcan carbon. However, those catalysts do not possess a good potential for ethanol oxidation in fuel cells, unfortunately. The physical characterisations have elucidated information that could be correlated to the respective catalytic performance of each catalyst. For instance, the *repeated* shift to a higher XPS binding energy of Pd 3d – in case of the trimetallics compared to Pd/C – could be interpreted into generally *lower* ethanol catalytic activity. This is probably because of the strong metal-adsorbate bond brought by the modified Pd electronic configuration. The same has also happened for the 3step PdAuNi catalyst and the opposite scenario is valid for the SBEG and SBIPP catalysts in Chapter 5. However, a slightly enhanced ethanol oxidation performance is noted on both PdAgNi systems compared to Pd. Though the alloying results between Ag and Pd are not equivalent to those of Au (according to XRD and CV results), it still expands the Pd lattice and exerts tensile stress/strain on it upshifting the *d*-band centre. Furthermore, Ag has a tendency to segregate into the core and modify the electronic structure of Pd verified by EDX and XPS. Therefore the PdAgNi nanoparticles are more active and stable for ethanol oxidation even though their associated particle sizes are usually larger than those of Pd. This seems to be achieved by the reduction of ethanol activation barrier on PdAgNi further than Pd. Both Ni and Ag show high individual oxidation and reduction peaks in the KOH CV which suggests they could together generate a lot of oxygen species to promote ethanol oxidation on Pd.

On the contrary of that, adding Ir and Ni has a detrimental effect of the ethanol oxidation Pd activity. The reasons are the Ir and Ni tendency to segregate to the surface and contracting the Pd crystal lattice downshifting the *d*-band centre. Pd seems to lose a lot of electrons when prepared with Ir and Ni verified by the big shift Pd 3d XPS peak to a higher binding energy compared to Pd/C. as a result

the catalyst activity deteriorates rapidly upon the start of reaction. Additionally, the surface of PdIrNi systems seems rich in Ir and Ni and poor in Pd driving the possibility of inaccessible Pd sites to ethanol.

The impact of adding Rh and Ni into Pd on ethanol oxidation could not very precisely decided based on the current results. Although less oxidation currents are drawn in the CV and CA and higher R_{ct} is obtained with adding Rh and Ni into Pd in both PdRhNi catalysts, the presence of the two oxidation peaks in the cyclic voltammetry needs further *in-situ* analysis to define the associate reaction species at those potentials. Ultimately, this adds to the controversial debate of Rh capability to break the C-C bond. However, it could be claimed based on the results that adding Rh and Ni into Pd has a detrimental effect on the catalyst activity and stability for ethanol oxidation. This is also understood by the shift of Pd 3d XPS peak to a high binding energy and the XRD peak shift to higher diffraction angles compared to those of Pd/C.

Chapter 7: C-SUPPORTED PD-BASED TRIMETALLIC (AU, RH, AG, IR) CATALYSTS FOR ETHANOL OXIDATION

The current situation of fuel cells – to a large extent – is restricted to a laboratory research. The established commercial applications include stationary application dominated by SOFC systems, transport vehicles dominated by PEMFCs, and recently portable electronics dominated by DMFCs. The overall share of supplied energy by fuel cells is still in the preliminary stages and more energy reliance is prospected on them [52,88,176].This is ascribed to the high costs of their materials and infrastructure (particularly for hydrogen-fed fuel cells). The fuel transport and storage issues could be resolved with introducing liquid alcohols such as methanol and ethanol into the anode replacing the hydrogen gas. There is a considerable potential for the alcohol-fed fuel cells in the sectors of transport, portables, and electronics. For instance, in transport, liquid alcohol fuel cells seem advantageous since the established fuel infrastructure are probably suitable for deploying the liquid ethanol which has been

successfully co-added with gasoline to drive vehicles. Therefore, recharging them with ethanol would be easily available in normal fuel station [2]. Also, small-sized direct methanol fuel cells have shown a commercial potential to supply electronic devices such as laptops and mobile phones[81,85,180]. However, the issue of the noble metal catalyst is still a barrier against the fuel cell wide commercialisation. In this chapter, 6 trimetallic catalysts comprised from Pd and other two metals (Au, Rh, Ag, and Ir) and supported on Vulcan carbon (XC72) are prepared, characterised and tested for ethanol oxidation for the first time. The only exception is PdAuIr which is reported for formic acid oxidation [179]. Those metals are chosen because their individual addition as co-catalysts to Pd for ethanol oxidation was proven beneficial. Therefore, adding two of them to Pd might even duplicate the catalytic benefits. The $NaBH_4$-2-propanol mixture protocol is once again applied. The C-supported catalysts of PdAuRh, PdAuAg, PdAuIr, PdRhIr, PdRhAg, and PdIrAg are physically characterised by XRD, EDX, TEM, and XPS. The metal atomic ratios in all catalysts is 1:1:1 and the total metal loading is 12 wt. %. The electrocatalytic activity is evaluated by CV, CA, Tafel polarisation, and electrochemical impedance spectroscopy (EIS).

7.1 Catalyst Preparation

The applied synthesis is the same SBIPP method explained in Chapter 5 with almost no variation. Briefly, a mixture of water and 2-propanol (v/v: 1/1) was prepared. KBr (1.5 of the total metals in moles) was added to the mixture to work as a capping agent. Then the metal precursors were added and shortly (5 min) sonicated in that mixture. Prior to that, the anhydrous $PdCl_2$ had been solved in NaCl solution and stored. Then, the carbon precursor was added and then the mixture was sonicated for 30 min to disperse the hydrophobic carbon and give a black suspension. Thereafter, the suspension was put into stirring. Then, a freshly prepared $NaBH_4$ solution (0.5M) was added to the mixture in one portion and the $NaBH_4$/metal molar ratio is more than 50:1. The whole mixture was kept under stirring for 30 min. Then, it was left overnight. After that, it was washed using suction filtration. Finally, it was dried in vacuum at 120°C for 3 h. The total anticipated weight of each catalyst powder is 150 mg.

Table 7-1 shows the weights of carbon and metal precursors added to prepare each trimetallic catalysts. After the synthesis, each catalyst was characterised using XRD, EDX, TEM, and

XPS which are all described in Chapter 3. Also, each catalyst was evaluated for ethanol electrooxidation by means of CV, CA, Tafel polarisation, and EIS.

Table 7-1 The carbon and metal precursors' quantities added to prepare PdAuIr/C, and PdIrAg/C, PdAuRh/C, PdRhIr, PdAuAg/C, and PdRhAg/C

Catalyst	C (mg)	$PdCl_2$ (mg)	$AgNO_3$ (mg)	$IrCl_3$ (mg)	$RhCl_3$ (mg)	$AuCl_3$ (mg)
PdRhAg/C	132	10.10	9.68	x	11.94	x
PdRhIr/C	132	7.98	x	13.40	9.41	x
PdAuRh/C	132	7.80	x	x	9.21	13.33
PdAuAg/C	132	7.10	7.64	x	x	13.63
PdAuIr/C	132	6.38	x	10.71	x	10.90
PdIrAg/C	132	8.03	7.48	13.10	x	x

7.2 Physical Analyses

7.2.1 XRD

Figure **7-1**, a) shows the XRD patterns measured for Pd/C, PdAuIr/C, and PdIrAg/C, PdAuRh/C, PdRhIr, PdAuAg/C, and PdRhAg/C between 20° and 85° at a scan rate of 2.5°/min. The crystalline facets of (111), (200), (220), and (311) are shown approximately at 40, 46, 68, and 82°, respectively. The present broad peak at 25°C is due to the turbostatic Vulcan carbon support. Figure **7-1**, b) shows the (111) enlarged to reveal the details of the peak shape for each trimetallic catalyst in comparison to the single Pd/C. As shown some catalysts peaks are shifted to higher – than Pd/C – diffraction angels such as PdIrAg/C and PdRhIr/C. On the other hand, the crystalline peaks of PdAuRh/C, PdAuAg/C, PdAuIr/C, and PdRhAg/C are shifted to lower diffraction angles. The highest shift to the left is noted on PdAuAg/C which is interesting because of the presence of both Ag and Au together with Pd. The reason is that both the individual Ag and Au diffraction peaks are located at smaller diffraction angle that those of Pd. The single Ag/C has shown a strong crystalline nature as confirmed by Figure 6-1, but there are two overlapping peaks at the 200 facet. It could be seen that most of the trimetallic catalysts – as shown in Figure **7-1**, b – convoluted of two three overlapping peaks. This is not completely understood since no individual metal phases are shown separate from the other. To further investigate this peak convolution, Figure **7-2** compares the enlarged (111) peak of each

trimetallic catalyst to the individual peaks of the single constituent metals. This could help explain the presence of asymmetric and overlapping peaks as each shoulder or peak could be correlated to the peak of the individual metal at similar positions.

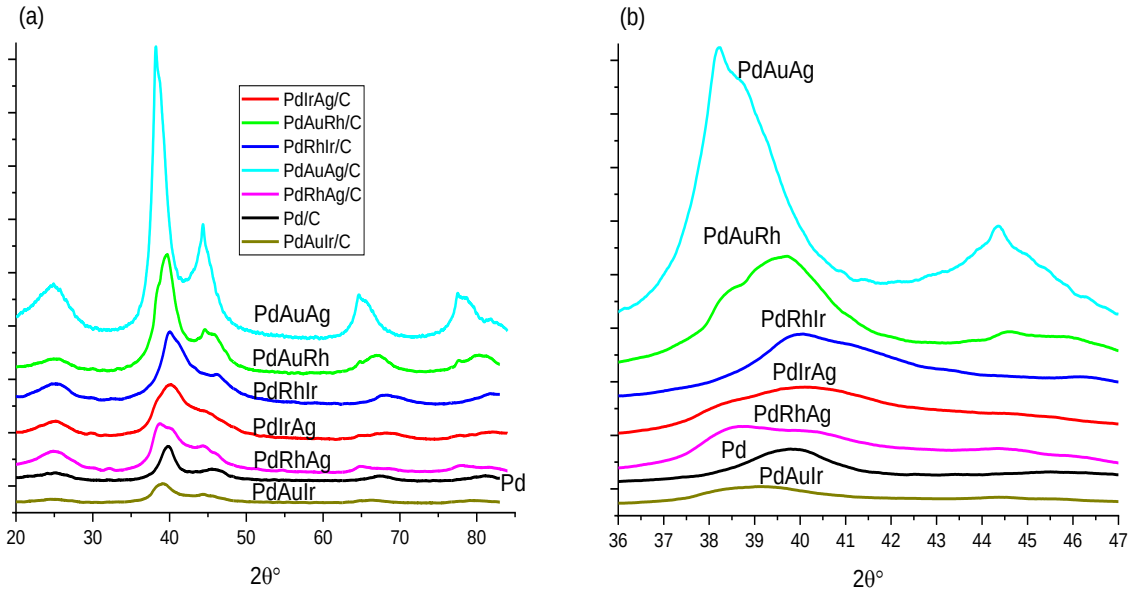

Figure 7-1 (a) X-ray diffraction patterns and (b) enlarged (111) peak of Pd/C, PdAuIr/C, and PdIrAg/C, PdAuRh/C, PdRhIr, PdAuAg/C, and PdRhAg/C

For example, Figure **7-2**, a) compares the (111) peak of PdIrAg to those of Ag, Ir, and Pd. No individual phase of Pd, Ir, or Ag are shown. However, two overlapping peaks could be seen at 38.2° and 40.2°. The smaller-shoulder could attributed to Ag seeing it almost the same diffraction angle of Ag seen in the same graph. Similarly, the higher-angle peak might be ascribed to mainly Pd – and slightly to Ir – seeing it is close to the individual peaks of Pd and Ir. Additionally, Figure **7-2**, b) compares the (111) peak of PdRhAg to those of Ag, Pd, and Ir. Once more, the main PdRhAg peak is located at 38.3° which could be attributed to Ag while the minor shoulder peak is positioned at 40.2° that could be correlated to Pd. The (111) peak of PdAuAg is compared to Ag and Pd in Figure **7-2**, c). Once again, two overlapping peaks are shown at 38.2 (attributed to Ag) and 38.9° which is probably to the PdAu alloy. Figure **7-2**, d) shows the (111) peak of PdAuIr vs Ir and Pd. The impactful Au presence is represented in the shift-to-the-left of PdAuIr although the individual peaks of Pd and Ir are located at higher diffraction angles. Interestingly, no seemingly overlapping peaks are shown in case of PdAuIr. The reason behind this is potentially the good alloying characteristics firstly between Pd and Au and secondly Pd and Ir. Figure **7-2**, e) compares the (111) peak of PdAuRh vs Pd and Rh.

Two clear overlapping peaks of PdAuRh are positioned at 38.5° (reflective of Au) and 40.1° (reflective of Pd). PdRhIr (111) peak is shown in Figure **7-2**, f). two overlapping peaks noted at 40.1° and 41.3° that are attributed to Pd and Ir as could related to the individual pattern of Pd and Ir.

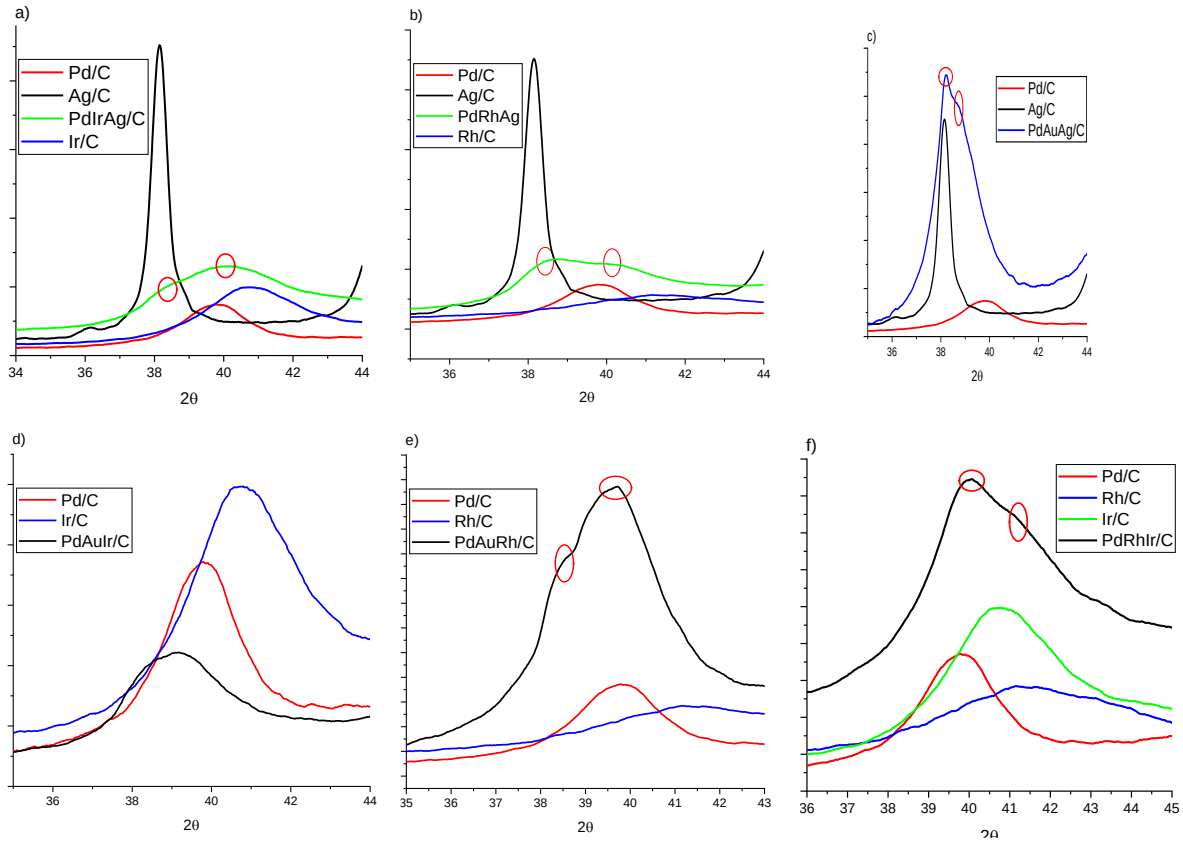

Figure 7-2 Enlarged XRD (111) peaks of a) Pd/C, Ag/C, Ir/C, and PdIrAg/C, b) Pd/C, Ag/C, Rh/C, PdRhAg/C, c) Pd/C, Ag/C, and PdAuAg/C, d) Pd/C, Ir/C, and PdAuIr/C, e) Pd/C, Rh/C, PdAuRh/C, e) Pd/C, Rh/C, PdAuRh/C, and f) Pd/C, Rh/C, Ir/C, PdRhIr/C

Based on the above XRD patterns, it may not be possible to accurately measure the alloy formation potential. The presence of overlapping peaks in one phase is not the same as single peaks in one phase which highly suggests the formation of an alloy. It is, also, not the same as having separate fingerprint peaks of each metal which proves an alloy was not formed. On the other hand, it has been found (in Chapter 5) there is a good alloying potential between Pd, Au, and Ni using the similar SBIPP protocol verified by the single peaks comprising one metal phase of PdAuNi alloy. A smaller success has been attained in the current chapter apart from the PdAuIr which shows only one metallic phase and no overlapping peaks. A similar but not

identical alloying potential was found between Pd, Ag and Ni that has been addressed in Chapter 6. Interpreting the XRD pattern, for a catalyst such as PdRhIr/C, the shift to the right higher angles is farthest from Pd. Once more, both Ir and Rh metals diffract at higher angles than those of Pd as shown in Figure 6-1. Therefore, the crystal peaks of PdRhIr are shifted to higher angles. It is useful to remind that the shift to the left could be beneficial for the catalytic functionality of the catalysts because it means the crystal structure was sub*j*ected to tensile stress and strain by expanding the Pd lattice after the incorporation of larger metal atoms such Au and Ag into it. This lattice expansion up-shifts the *d*-band centre which enhances the catalyst stability by decreasing the Pd-adsorbate bond strength. Also, expanding the lattice and unit cell might mean the surface atoms are less coordinated with the neighbouring ones and eventually they become more active for ethanol oxidation. The opposite claim seems to be valid in case of the shift to higher diffraction angles. It is also worthy to explain the potential effect of peak broadening noted in Figure 7-1. Whilst the highest broadening is noted on PdAuAg, the lowest is noted on PdAuIr. This is very interesting because both catalyst contain Pd and Au but one with added Ag and the other with Ir. That might be attributed to the potential effect of adding Ag to PdAu as it could increase the crystal size of PdAuAg particles. Examining the other Ag-containing catalysts in this chapter and in section 6.2.1 leads to a similar conclusion about the effect of adding Ag. The opposite is true in case of Ir. Au, in particular, is not agreed on whether it would increase or decrease the crystal size but it largely depends on the synthesis method and conditions. Rh is expected to behave in a similar way to Ir. The effects of Au, Ag, Ir, and Rh on the Pd crystal structure have been reported though on bimetallic system [37,103,128,144,158,159,179,180].

7.2.2 EDX

Figure 7-3 shows the EDX quantitative analyses of PdAuIr/C, and PdIrAg/C, PdAuRh/C, PdRhIr, PdAuAg/C, and PdRhAg/C recorded using a Jeol SEM operating at 20 kV and 80 spot size. EDX penetration depth –as was discussed in Chapter 5 – could range from 0.2µm to 2 µm following the mean atomic number and the accelerating voltage. The sample thickness is less than 100µm. Two accelerating voltages were applied: 20 kV and 10 kV. The respective estimated depth of each voltage is 0.5 µm and 1 µm, respectively. Unlike all the PdNiMe systems (Chapters 5 and Chapter 6. EDX maps (Appendix 1) and quantitative analyses at the two voltages show no sign of individual metal segregation into the higher surfaces. Therefore,

only the 20 kV measurements are discussed here. These are acquired from an area of 400 μm^2 from the samples surface. Once more the C-K peak is not shown to distinguish the smaller metal peaks in the spectra but the C concentration is shown for each catalyst. As for the PdRhAg, the Ag has a tendency to escape to the core and that is probably why a small quantity is detected. The three metallic peaks overlap with one another. The Rh quantified (0.35 At%) is much less than what is expected which is probably because either less Rh was reduced during the synthesis or EDX does not detect the Rh at this particular depth especially the other Rh-containing catalyst contain less Rh than expected. For instance, the EDX Rh content in PdRhIr is 0.15 at. % and in PdAuRh is 0.34 At. %. Looking at the PdRhAg spectrum, the Pd peak is the highest and Rh one is the smallest which indicates the Pd weight is highest and Rh is the lowest. The Ir peak, in PdRhIr, is the highest and Rh is the lowest.

PdRhAg/C

Chemic...	mass%	Atom%
C*	65.19	79.73
N*	10.54	11.06
O*	6.43	5.91
Na*	0.62	0.40
Si*	0.45	0.24
S*	1.10	0.50
Rh*	2.48	0.35
Pd*	8.40	1.16
Ag*	4.77	0.65
Total	100.00	100.00

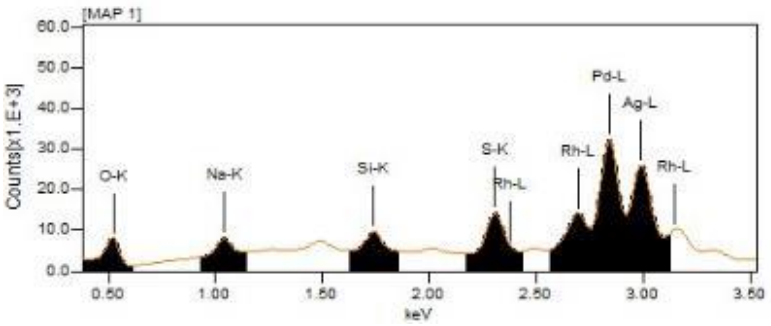

PdRhIr/C

Chemic...	mass%	Atom%
C*	64.41	76.28
N*	14.61	14.83
O*	8.14	7.24
Na*	0.20	0.12
Si*	0.14	0.07
S*	0.54	0.24
Rh*	1.11	0.15
Pd*	4.28	0.57
Ir*	6.58	0.49
Total	100.00	100.00

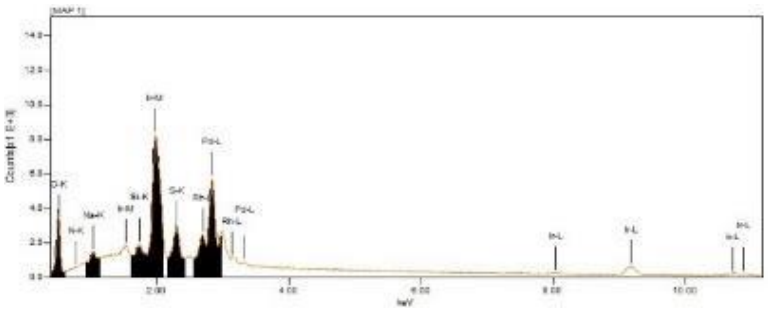

PdAuAg/C

Chemic...	mass%	Atom%
C*	72.85	84.88
N*	9.89	9.88
O*	3.83	3.35
Na*	0.46	0.28
Si*	0.14	0.07
S*	0.88	0.39
Pd*	3.11	0.41
Ag*	1.88	0.24
Au*	6.95	0.49
Total	100.00	100.00

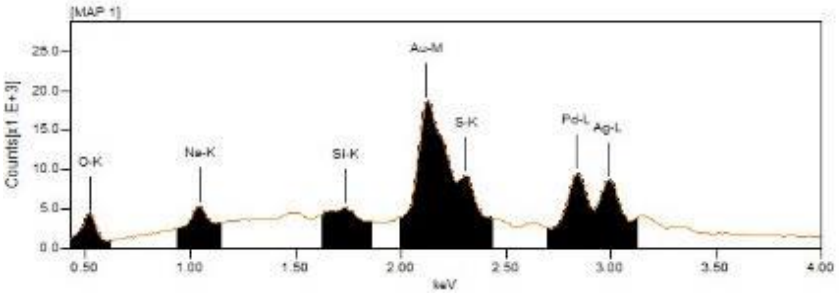

PdAuRh/C

Chemic...	mass%	Atom%
C*	62.93	75.05
N*	14.01	14.33
O*	9.58	8.57
Na*	0.62	0.38
Si*	0.12	0.06
S*	0.89	0.40
Rh*	2.45	0.34
Pd*	2.94	0.40
Au*	6.47	0.47
Total	100.00	100.00

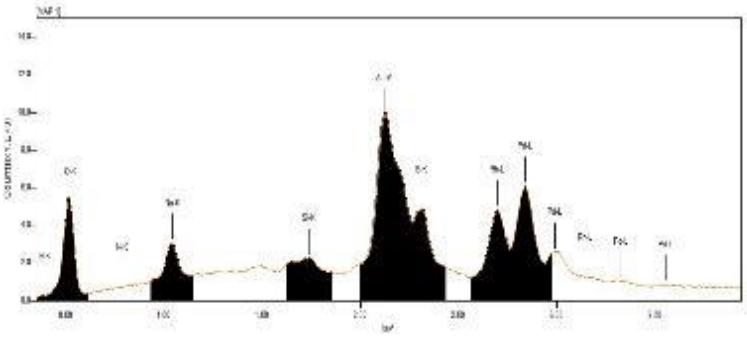

PdIrAg/C

Chemic...	mass%	Atom%
C*	69.82	86.45
N*	7.72	8.19
O*	3.03	2.81
Na*	0.22	0.14
Si*	0.17	0.09
S*	0.82	0.38
Pd*	5.62	0.79
Ag*	2.86	0.39
Ir*	9.73	0.75
Total	100.00	100.00

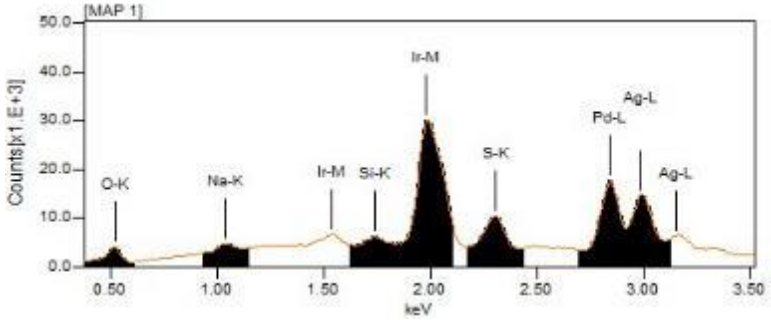

PdAuIr/C

Chemic...	mass%	Atom%
C*	72.54	82.73
N*	6.68	6.53
O*	11.08	9.49
Na*	0.42	0.25
Si*	0.10	0.05
S*	0.53	0.23
Pd*	1.87	0.24
Ir*	3.37	0.24
Au*	3.41	0.24
Total	100.00	100.00

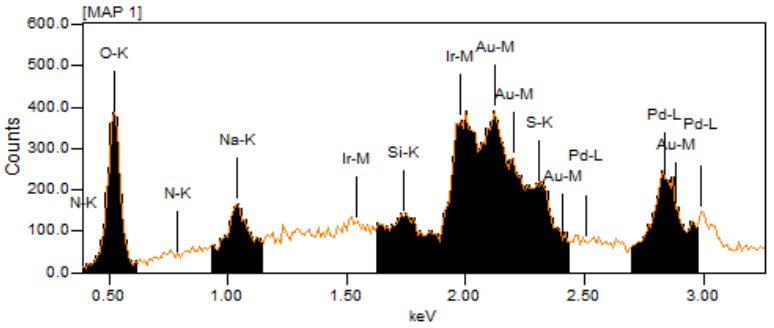

Figure 7-3 EDX quantitative and spectral analyses of PdAuIr/C, and PdIrAg/C, PdAuRh/C, PdRhIr, PdAuAg/C, and PdRhAg/C (C-peak is not shown to clarify the smaller metal peaks)

As for the PdAuAg, the Pd quantity is close to Au, but the Ag one is much less which tends to segregate into the core of PdAuAg. The spectral peaks of Au and Pd are higher than Ag. For the PdAuRh, once more the Au peak (0.47 At. %) is more than Pd (0.40 At. %) and Rh (0.34% At. %) is the lowest. For the PdIrAg, the Ir peak is significantly higher than Pd and Ag (the lowest peak and smallest quantity). The Pd and Ag peaks are in overlap with one another. For the PdAuIr, the spectral peaks of Pd, Au, and Ir are close to one another with an overlap between the Au and Ir peaks. To sum up, for these different combinations of Pd with other two metals, Ag tends to segregate into the core and that is why less quantity is usually detected, Ir

tends to segregate into the surface, Rh is usually detected in small quantities than the nominally added precursor which suggests either the synthesis is method is not very efficient for $RhCl_3$ reduction or the EDX depth does not necessarily reflect the Rh quantity.

7.2.3 TEM

Figure 7-4 shows the micrographs of PdAuIr/C, and PdIrAg/C, PdAuRh/C, PdRhIr, PdAuAg/C, and PdRhAg/C recorded using the C100 Microscope (100 kV). For the PdRhIr/C catalyst, the surface shows high dispersion the PdRhIr particles (1.5 nm to 6 nm) on the carbon (30-60 nm particle size) surface. The average particle size of the metal particles is 2.25 nm. Yet, there is a whole large black area which might be attributed to carbon aggregation during the TEM sample preparation and unlikely due to metal aggregation in larger particles. Similar to PdRhIr/C, the PdAuIr/C micrograph shows high dispersion characteristics although the average particle size of PdAuIr is 0.1 nm higher than that of PdRhIr and that is likely because of the incorporation of Au atoms into the Pd lattice. The PdAuRh achieves higher agglomeration than PdRhIr and PdAuIr and the average particle size is 2.5 nm. It could be concluded the Au addition – unlike adding Rh and Ir – increases the trimetallic particle size which is not uncommon and reported about Au [37,99,103,159,179,180].

PdRhIr/C

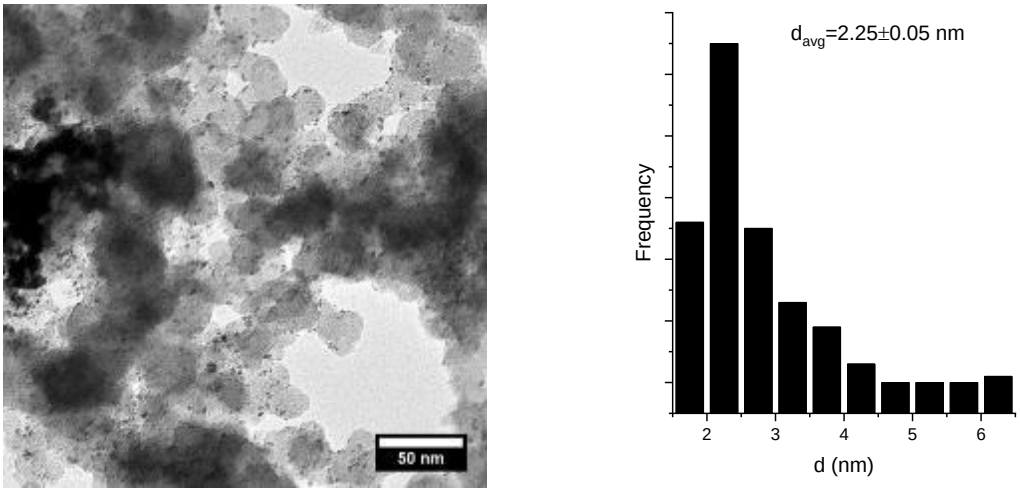

PdAuIr/C

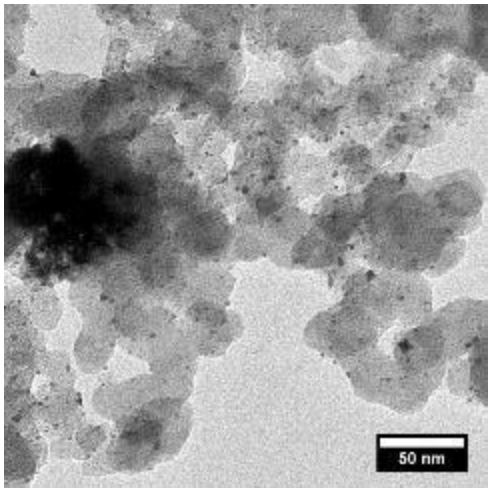

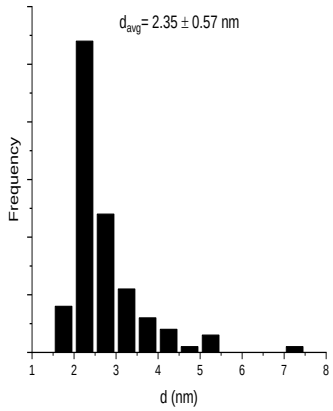

PdAuRh/C

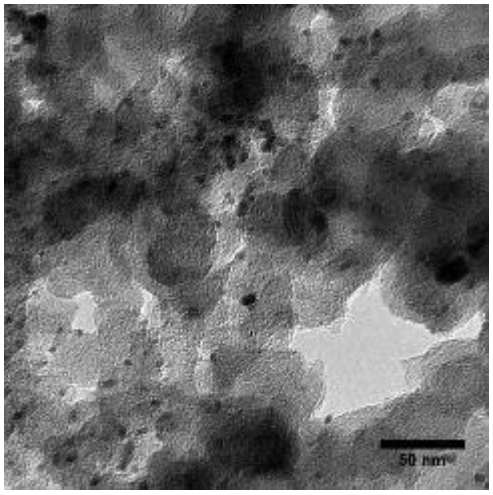

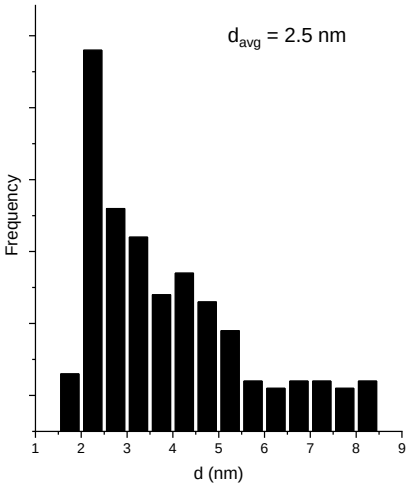

PdAuAg/C

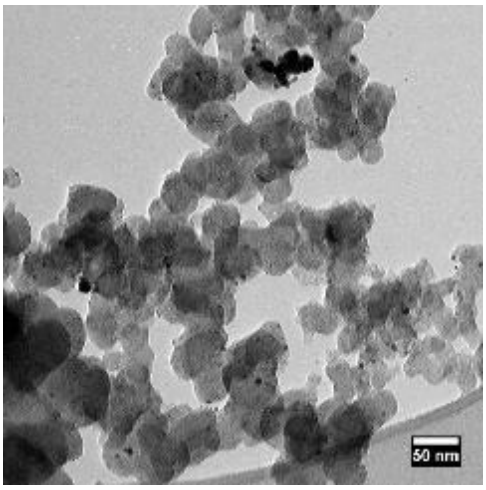

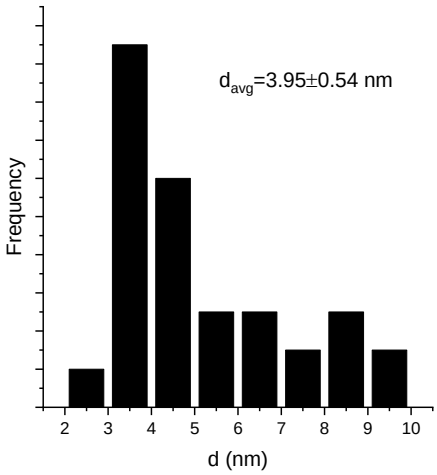

PdIrAg/C

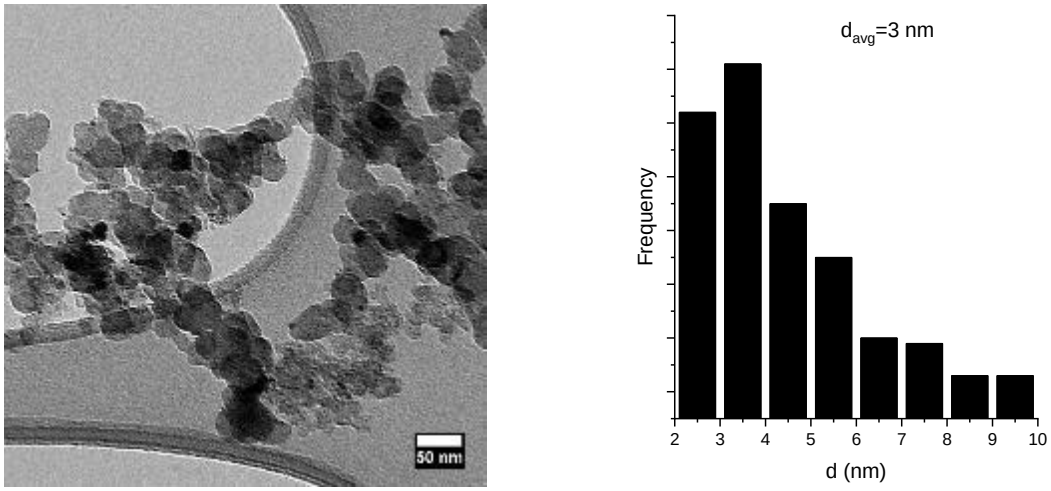

PdRhAg/C

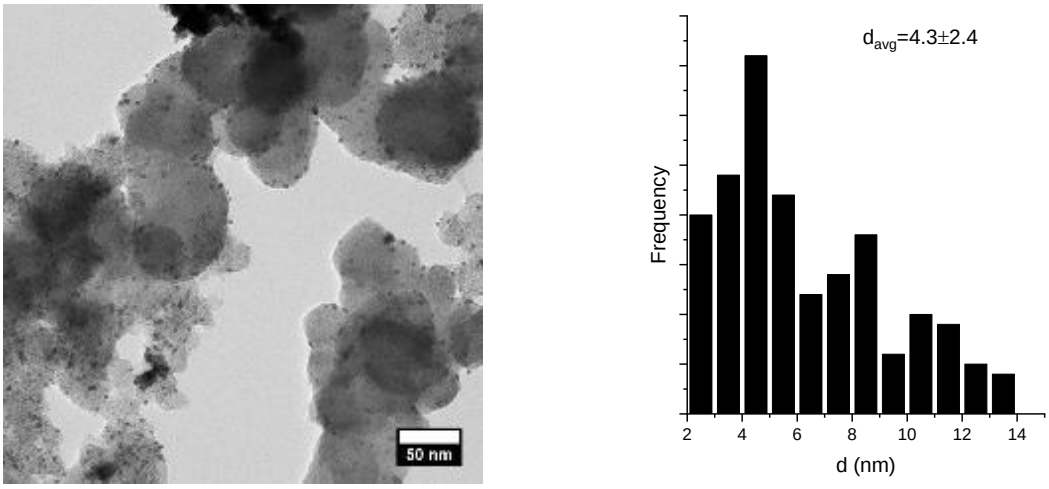

Figure 7-4 TEM Micrographs and particle size distribution of PdAuIr/C, and PdIrAg/C, PdAuRh/C, PdRhIr, PdAuAg/C, and PdRhAg/C

The PdAuAg achieves the second largest average particles size close to 4 nm following PdRhAg. The reason for such size increase are probably because of the addition of Ag which might increase the Pd particle size if added. A few instances of agglomeration could still be seen. In line with the effect of adding Ag, the average of particle size of PdIrAg is 3 nm which is comparatively high compared to PdRhIr for instance. Once more, the potential reason is the addition of Ag which would lead to increase the Pd particle size like Au. It should mentioned the particle size of every catalyst in Figure **7-4** is less than the monometallic Pd/C prepared using the same protocol (Figure **5-4**) except with the Ag- or Au-containing catalysts which achieve higher particle size in this chapter. Other studies confirmed the particle increase by adding Au [37,98–100] and Ag [144].

In general, well dispersion of metallic nanoparticles could be noted in almost all catalysts shown in Figure **7-4**. Also, the $NaBH_4$-2-propanol mixture seems to have a stabilising effect during the nucleation and growth of Pd-based trimetallic nanoparticles. Finally, no high temperature was applied and the high temperature – though speeds up the metal ion reduction – facilitates the metal agglomeration during synthesis.

7.2.4 XPS

Figure **7-5** and Table 7-2 show the XPS elemental peaks and composition of Pd, Au, Ag, Rh, and Ir in the 6 catalysts. As discussed in Chapter 5, the XPS sampling depth is possibly between 1 nm and 30 nm. For the Pd/C, the oxidized Pd existing in this catalyst is 5.37% while the Pd metal is 77.31 %. An important observation is that Pd in case of PdAuRh and PdAuAg is present only in metallic form while there is a little oxide presence in case of PdIrAg, PdRhAg, PdAuIr, and PdRhIr (Table 7-2). The latter oxide presence is also noted on all PdNiMe systems in Chapter 6. However, the three PdAuNi systems in Chapter 5 do not shows any oxide presence of Pd. This could lead to an important conclusion there is small likelihood of PdO formulation when Au is alloyed with Pd as the three PdAuNi systems added to PdAuRh and PdAuAg do not contain any Pd oxide. The Pd satellite peaks are expected due to the shakeup of the unpaired 3d electrons to a higher bound energy level (4s). Therefore, the 2p electron energy is reduced by the excitation of the unpaired 3d electron. Also, there is a noted overlap between the Au 4d peak with the Pd 3d.

PdAuAg/C

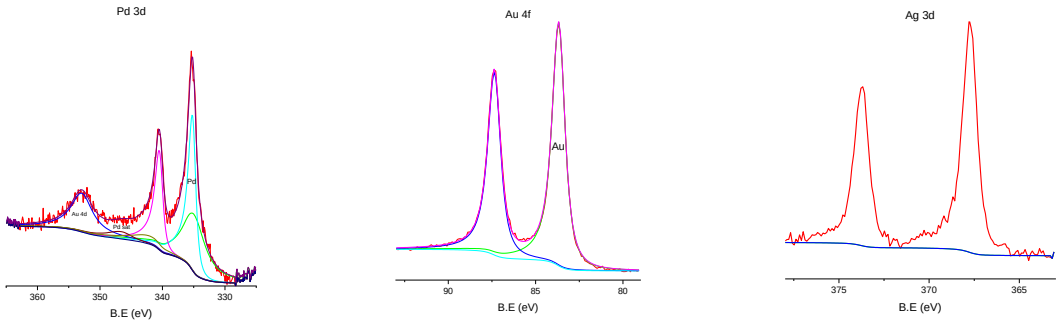

PdIrAg/C

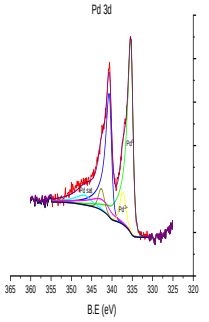

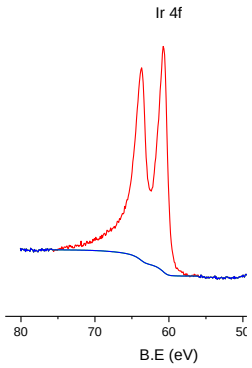

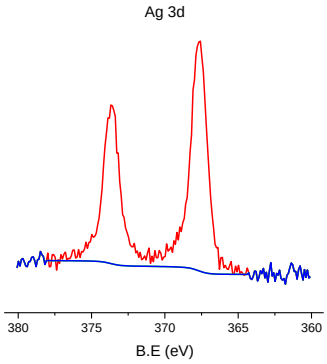

PdAuRh/C

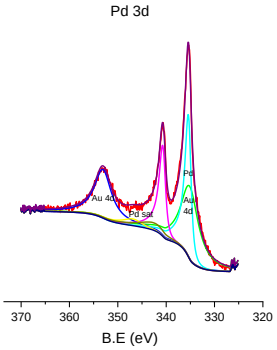

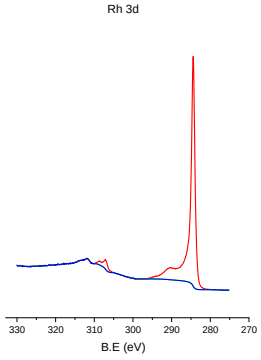

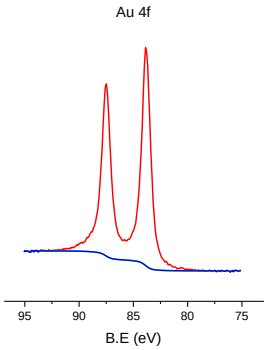

PdRhIr/C

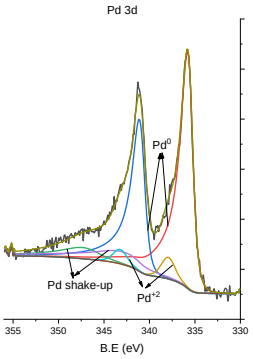

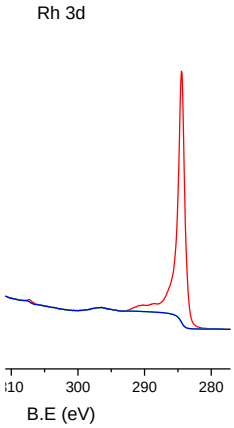

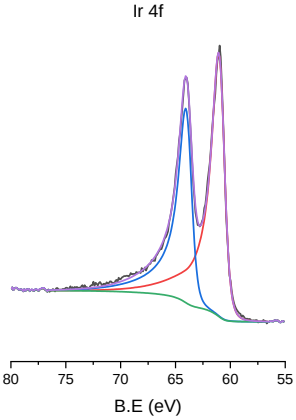

PdRhAg/C

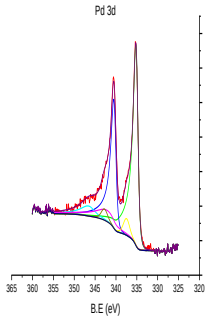

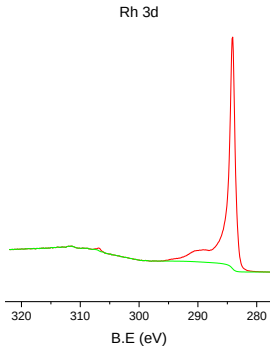

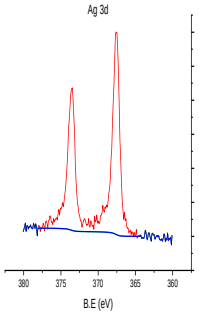

PdAuIr/C

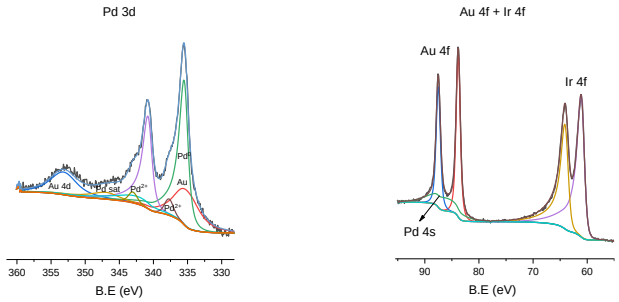

Figure 7-5 XPS spectral metal peaks of PdRhIr/C, PdAuRh/C, PdAuAg/C, PdAuIr/C, PdIrAg/C, PdRhAg/C and Pd/C

Another important observation that all catalyst metals – except Pd – do not contain any oxide as shown in Figure **7-5**. Thus, Ir, Au, Ag, and Rh exist only in metallic form for the current trimetallic catalysts. Furthermore, an interesting measurement about Rh that its XPS concentration in PdAuRh is reasonable with 0.52 At. % but is much less than that in case of PdRhAg and PdIrAg; 0.06 and 0.9 At.%. The Rh small concentration in PdRhAg and PdIrAg cannot be precisely understood especially the respective EDX Rh concentration is also clearly less than their Pd, Ir, Ag counterparts. Like XPS, the EDX measured Rh is reasonably high in both catalysts. Therefore, there is good quantity of Rh in PdAuRh both in the core and external surface layers but the Rh presence on the external surface is very poor in case of PdRhAg and PdIrAg.

The Au 4f peaks are positioned at 83.83 eV and 87.5 eV while the Ir 4f ones are located at 61 eV and 64 eV. It could be noted the higher concentration of Ir (70%) compared to that of Au (30%). That is suggestive the Au segregates to the core of the particles while the Ir segregates into the outer surface. It is also worth mentioning that both metals exist in only metallic states and no oxide has been detected while some Pd oxide was found. This suggests the Pd is more oxyphilic than both Au and Ir. Also, Pd 4s peak is in overlap with Au 4f. While the total atomic concentration of Pd is 0.75%, the Au one is only 0.39%. This confirms the tendency of Au to segregates into the core of PdAu systems while the Pd prefers the surface. Yet, the Ir atomic concentration was proven the highest of the three metals with 0.95% which suggests Ir potential to segregate into the surface more than Pd and Au. The Au concentration (in PdAuRh) is exceptionally high if compared to the Pd and Rh. On the contrary of PdAuRh, the Au concentration in PdAuAg and PdAuIr are significantly small if compared to the concentrations of Ir, Pd, and Ag in a descending order. The Au is known usually to segregate into the core of nanoparticle when impregnated with Pd or Pt [48,104,158,159]. However, the Au

concentration in PdAuRh – quantified by XPS and EDX – is higher than Pd which indicates higher Au presence in the surface. The Ir XPS concentration is generally the highest compared to Pd and the other metals although the theoretically added Ir equals Pd and the 3rd metal. A similar Ir behaviour was reported [123].

For the PdAuRh system, the Pd 3d is shifted to a lower binding energy 0.05 eV which means a net electron gain into it has occurred. According to the Thermo Scientific XPS database, the bulk Rh 3d and Au 4f are located at 307.6 and 84.0 eV, respectively. However, those peaks are located at 307.08 and 83.88 eV, respectively for PdAuRh. This shift to lower binding energies is once again interpreted as a net electron gain into Rh and Au. This gain is the result of both interaction with the carbon support and also interaction with the two other metals. For the PdAuAg catalyst, the Pd 3d is located at 335.17 eV which also implies a net electron gain has occurred into Pd since that of Pd/C is located at 335.43 eV. The Au 4f and Ag 3d peaks are located 83.68 and 367.78 eV, respectively. As the bulk Ag 3d is located at 368.2 eV, therefore both the Ag 3d and Au 4f are shifted to lower binding energies in case of PdAuAg implying a net electron gain has occurred into them. For the PdAuIr, there is 0.05 eV shift to a lower binding energy of Pd 3d peak like PdAuRh. But the Au 7f shift to lower binding energy is higher than PdAuRh. On the contrary, the Ir 4f is shifted 0.28 eV to a higher binding energy which means a net electron loss from Ir unlike Au and Pd. For the PdRhAg, there is a clear shift of 0.29 eV of Pd 3d to lower binding energy compared to Pd/C. Similarly, The Ag 3d and Rh 3d are shifted to lower binding energies. Therefore, a net electron gain is presumably happened into the three metals due to interaction with the carbon support. On the other hand, the PdRhIr Pd 3d is shifted 0.78 eV and 0.35 eV higher than those of bulk Pd and Pd/C which means a high electron loss from Pd. As the Ir shift in this catalysts is smaller than PdAuIr and PdIrAg, it could be assumed a net electron gain into Ir has occurred. The Pd 3d of PdIrAg is shifted 0.11 eV lower than Pd/C. The Ag 3d is similar to that of Pd. The Ir 4f is shifted to a high binding energy compared to the bulk Ir in case of that catalyst.

Table 7-2 XPS surface metal composition of PdRhIr/C, PdAuRh/C, PdAuAg/C, and PdAuIr/C, PdIrAg/C, PdRhAg/C and Pd/C

Catalyst	Pd At. %		Pd $3d_{5/2}$ (eV)	Rh At. %	Rh $3d_{5/2}$ (eV)	Ir At. %	Ir $4f_{7/2}$ (eV)	Ag At. %	Ag $3d_{5/2}$ (eV)	Au At. %	Au $4f_{7/2}$ (eV)
	Pd^0	Pd^{2+}									
Pd/C	1.63	0.45	335.43	x	x	x	x	x	x	x	x
PdAuRh/C	0.55	0.00	335.38	0.52	307.08	x	x	x	x	1.18	83.88
PdAuAg/C	0.83	0.00	335.17	x	x	x	x	0.50	367.78	0.48	83.68
PdAuIr/C	0.87	0.12	335.38	x	x	1.11	61.18	x	x	0.52	83.68
PdRhAg/C	0.87	0.07	335.14	0.06	306.87	x	x	0.52	367.58	x	x
PdRhIr/C	1.12	0.12	335.78	0.09	307.08	1.58	61.08	x	x	x	x
PdIrAg/C	0.80	0.10	335.32	x	x	1.16	60.78	0.52	367.58	x	x

It is noteworthy that the Rh exists only in metallic states while an oxide portion is detected in both PdRhNi and $Pd_4Rh_2Ni_1$/C (Table 6-3and Figure **6-5**). Yet, the Rh concentration in case of PdAuRh is 0.52 which exists in metallic form. This could be explained the Rh air stability is enhanced in presence of the similar precious and noble metals such as Au, Pd, Ag, and Ir. Another interesting finding is that the surface Rh concentration reported in Table 7-2 in PdRhAg and PdRhIr is 0.06 and 0.09 at. %, respectively, which is much less the theoretical concentration. For instance, the Ag and Pd concentrations (in PdRhAg) are 0.52 and 0.87 at. %, respectively. Moreover, the Pd and Ir concentrations in (PdRhIr) are 1.24 and 1.58 at. %, respectively. This might suggest that the Rh was not produced by chemical reduction and is not present in both PdRhAg and PdIrAg catalyst according to Table 7-2. This is supported – to some extent – by the EDX quantitative analyses of both PdRhAg and PdRhIr (Figure **7-3**) which also detects Rh concentrations that comparatively small when compared with Pd, Ir and Ag while the theoretical added concentrations of the four metals are the same. Yet, PdAuRh is unlike PdRhAg and PdIrAg since the detected Rh concentration using XPS and EDX is reasonable. The Ag concentration – in PdAuAg, PdAuIr, and PdIrAg – is almost standard approximately of 0.5 at. % which is comparatively less than Pd and other metals (especially Ir). The small Ag concentration is further supported by the EDX quantitative analysis for the same catalysts. The Ag – in similarity with Au – has a tendency to segregate into the core of PdAg nanoparticles [14,127,129].

7.3 Electrochemical Evaluation

7.3.1 CV

The monometallic Pd-free catalysts (Rh, Ag, and Ir) are prepared to investigate their solo potential for ethanol electrooxidation using the same SBIPP protocol. Figure 7-6 shows the cyclic voltammograms of Rh/C, Ag/C, and Ir/C and compares them to that of Pd. This experiment is done to study how each metal interact with the hydrogen and OH^-, and quantify their electrochemical active surface area. The forward oxidation of adsorbed hydrogen (-0.7 to -0.5 V NHE) is paramount on Rh followed by Ir while it is largely suppressed on Pd and Ag. It seems Rh has a high affinity for hydrogen by checking its high associated peaks in Figure 7-6. Even further to that, hydrogen oxidation was tested applying PtRh system and it was found

that the catalyst would reconstruct its surface according to hydrogen presence/absence. If present, Rh tends to segregate into the surface and if not, Pt segregates into the surface [17]. The OH_{ads} is clearer on Pd than the other metals. With the exception of Ag, the surface oxidation behaviour is similar on Pd, Ir, and Rh. Ag, however, shows a sharp increase in the oxidation current at approximately 400 mV vs NHE. Also, two overlapping peaks could be seen at 470 mV and 550 mV, which is an indicative of two different oxidation processes on Ag. This is also confirmed by looking at the reduction scan and the sharp decrease in current on Ag could be seen at approximately 350 mV. Once more, two peaks – a little one at 220 mV and a shoulder at 50 mV – that suggests two reductive processes occur on Ag. An approximately equivalent peak of PdO could be noted at -120 mV with a very small shoulder at -250 mV. The higher peaks of Pd and Ag reduction are suggestive of a higher electrochemical active surface area attained on both metals. It is noteworthy that another peak on Ag shows up at -100 mV which suggests a third reduction process occurs on Ag. It could be claimed that the distinctively high surface oxidation/reduction peaks on Ag are due to the initial presence of Ag oxide on the catalyst surface which is not corporate by the XPS results in the trimetallic catalysts (no Ag oxide detected). The surface oxide further oxidation – at higher potentials – generates more current than the lower-potential consequent surface metal oxidation. The same could be argued about the reduction which is why the Ag reduction peak at -100 mV is inferior to that at +200 mV. The surface reduction peaks on Ir and Rh are significantly lower than that of Pd.

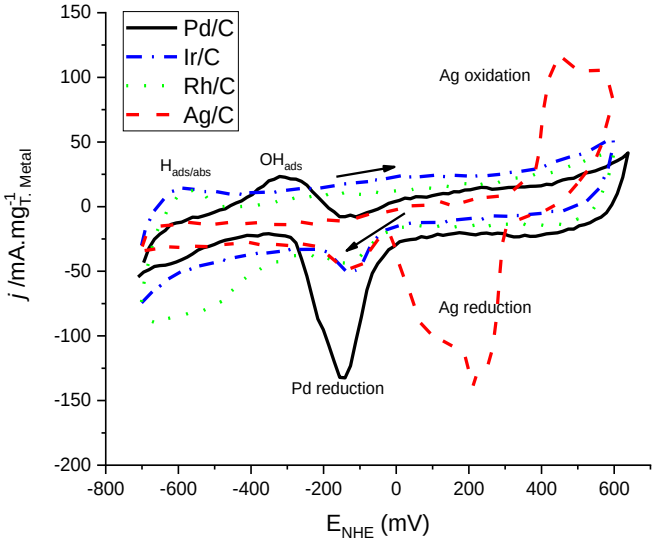

Figure 7-6 Cyclic voltamograms of Pd/C, Rh/C, Ir/C, and Ag/C in 1M KOH at 50 mV/s

Overall, it could be said that the electrochemical active surface area on Pd is much more than that on Ir and Rh. For Ag, however, it seems to have a high ECSA which is comparable to Pd but at a high potential (around +200 mV vs NHE) and it could be noted two reduction processes are occurring following the shoulder peak at 100 mV. As was demonstrated in Figure 6-6, the individual metal catalysts of Rh/C, Ir/C, and Ag/C were tested for ethanol oxidation on their own and have shown no potential compared to Pd/C.

Figure 7-7 shows the cyclic voltammograms obtained for the 6 trimetallic catalysts prepared in addition to the monometallic Pd. The peak of hydrogen absorption and desorption is located around -600 mV vs NHE due to absorption and desorption of hydrogen. This peak is most apparent on PdRhIr, PdAuRh, and followed by PdAuIr while it is supressed for the other catalysts including the monometallic Pd (H is absorbed into the core of Pd). With increasing the applied potential further, the adsorption of OH starts at -400 mV and continues to 0 mV vs NHE.

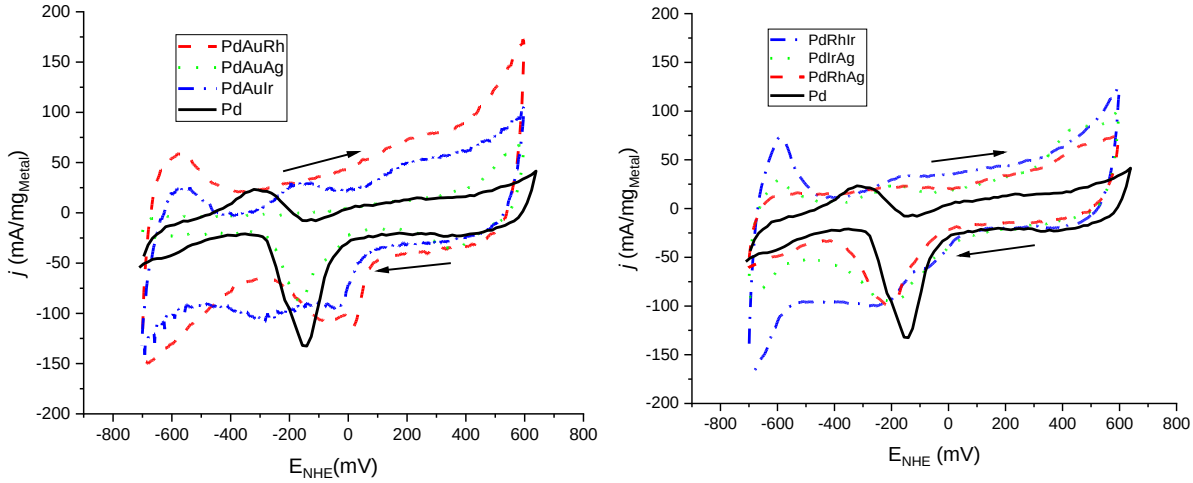

Figure 7-7 CV of (*left*) Pd/C, PdAur/C, PdRhAu/C, PdAuAg/C, (*right*) Pd/C, PdIrAg/C, PdRhIr/C, and PdRhAg/C in 1M KOH at 50 mV/s

The OH_{ads} is likely to overlap with the $H_{abs/des}$ on the trimetallic catalysts. Increasing the applied potential leads to the surface oxidation of the catalyst which continues to the end of the forward scan. In case of the trimetallic catalysts, two surface oxidation peaks could be noted and the potential reason is the consecutive oxidation of the individual metals starting with Pd at 0.0V followed by the other oxidation metals at higher potential such as Ag, Rh, and Ir. In the reverse the most intense PdO reduction is noted on the monometallic Pd from 0V to -300 mV vs NHE.

For all the trimetallic catalysts, this peak is broadened and sometimes overlaps with the reduction peaks Rh and Ir – as reported in [2, 4, 7, and 8] – in the catalyst combinations containing Pd and any of them. This suggests the good alloying characteristics of the three metals and the equal presence of every metal in every particle of the catalyst powder. That suggests with the Pd-Au-Ir system, there is a small potential of metal segregation.

Figure **7-8** shows the cyclic voltammetry scans preformed after adding ethanol (1M) to the KOH solution. The current is divided by the total metal weight. Two graphs are shown: the one on the left one shows the current obtained by PdAuRh, PdAuIr, and PdAuAg versus Pd. The left one shows the current obtained applying PdRhAg, PdIrAg, and PdRhIr versus Pd. The PdAuRh/C, on the other hand, draws higher current values and starts the ethanol oxidation at a lower applied potential than Pd (around -140 mV to the left). What further corporates that is the forward peak potential of Pd which is located at approximately 100 mV while that of PdAuRh is at +60 mV. After normalising the current by the Pd weight, it is found the effective EOR current drawn using PdAuIr and PdAuAg is higher than that of the monometallic Pd. Thus, the three catalysts containing Pd and Au (in addition to Rh, Ir, and Ag) could be assumed containing more Pd active sites for ethanol oxidation than the monometallic Pd. This is primarily due to the effect of adding Au (and secondly Rh and Ag) into Pd.

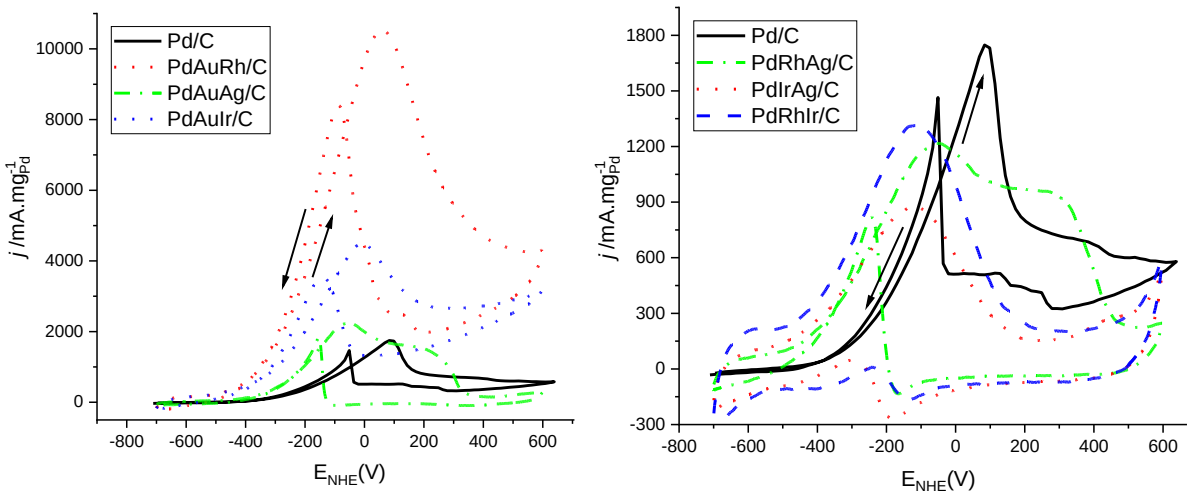

Figure 7-8 CV of (*left*) Pd, PdAuIr, PdRhAu/C, PdAuAg/C, (*right*) Pd/C, PdIrAg/C, PdRhIr/C, and PdRhAg/C in 1M KOH+EtOH at 50 mV/s

The other Au-free Pd trimetallic catalysts (PdRhIr, PdIrAg, PdRhAg) draw smaller current values (normalised and non-normalised) compared to the monometallic Pd. The lower drawn current on those catalysts is suggestive of a smaller rate of ethanol oxidation due to smaller

number of ethanol oxidation active sites. Those catalysts containing Ir which has a high tendency to segregate to the surface of PdIrMe nanoparticle surface decreasing the available Pd active sites on the surface. However, checking the other catalysts, the PdRhIr starts the ethanol oxidation lower than Pd but higher than PdAuRh. A similar finding could be noted about the onset ethanol oxidation potential regarding the PdRhAg which starts at a lower potential than Pd but the active sites on it are significantly less than those on Pd. Figure 7-8 shows that following PdAuRh and PdAuIr, PdAuAg draws the highest current with considerably two overlapping peaks: the high higher peak at lower potential of approximately -100 mV and the smaller peak at higher potential of approximately 200 mV. The higher peak is probably due to the end of OH adsorption and the start of Pd surface oxidation. The other peak is potentially because of the Ag surface oxidation which might (or might not) have contributed to ethanol oxidation. A similar double peak forward scan is noted for PdRhAg at similar potentials.

Unlike PdAuAg and PdRhAg, the PdRhIr and PdIrAg show one single peak in the forward scan and it is worth mentioning the peak is located at a smaller potential that the first peak of noted on PdRhAg and PdAuAg. That is suggestive of smaller onset oxidation potential on PdIrAg and PdRhAg. Also, it is very interesting no high backward peak is noted for PdRhAg and PdAuAg as happening with all other catalysts. The high intensity and sharpness of the backward CV peak signifies the removal of incompletely oxidised intermediates on Pd active sites during the forward sweep. Therefore, the absence of the sharp backward peaks on PdRhAg and PdIrAg may imply less incomplete oxidised intermediates exist on their surfaces during by the end of the forward CV scan. Therefore, it could be assumed the EOR products on both catalysts are probably final (either CH_3COOH or CO_2) and no intermediate products may persist in the backward scan. It is also interesting that both PdIrAg and PdNiRh achieve the lowest oxidation current and the most potential reason is the high coverage of the surface by Ir as confirmed by XPS and EDX measurements. On the contrary of that, the Pd concentration is equivalent to Au in PdAuRh and the particle size is the smallest with 2.5 nm. The PdRhIr particle size is close to that of PdAuRh but it is surface is mainly covered by Ir. The particle size of PdRhAg, PdAuAg, and PdIrAg is 4.3, 3, and 3.95 nm, respectively. The particle size effect is clear especially in case of PdAuRh and PdAuIr.

7.3.2 CA

The chronoamperometry scanning was performed on each catalyst applied for ethanol oxidation at -0.3 V and +0.1 V vs NHE to study the degradation behaviour and catalyst tolerance for reaction intermediates. Figure **7-9** and Figure **7-10** show the two-step chronoamperometry scans performed in 1M KOH+EtOH at -0.3 V and +0.1 V, each for 30 min. At -0.3 V, the initial decay in the current occurs within the first 150 s followed by a steady state decrease in the current. The initial decay takes longer time at +0.1 V in case of Pd, PdAuRh, PdAuAg, and PdAuAg. The higher current drawn at -0.3 V on PdAuIr is indicative of high activity and tolerance for poisoning species. However, at +0.1 V, the PdAuIr current is significantly small even smaller than Pd which indicates a significant loss of the Pd active sites. The reason for this is that the +0.3 V is above the forward oxidation peak potential at which the Pd is oxidised on the surface. A similar finding is noted in case of PdAuRh with fast decaying current to the Pd surface oxidation even though the current drawn on it is significantly high due to the surface enrichment with Pd. The fast decaying current is still due to the growing loss of Pd active ethanol oxidation sites due to the ended OH adsorption. It is noteworthy the current decay in case of Pd at +0.1 V is not very different from -0.3V and the potential reason is that the OH species could still be adsorbed on Pd at potential above +0.3 V vs NHE. The CA current – at +0.3 V – on PdAuAg, PdRhAg, PdIrAg and PdRhIr decays in similar behaviours.

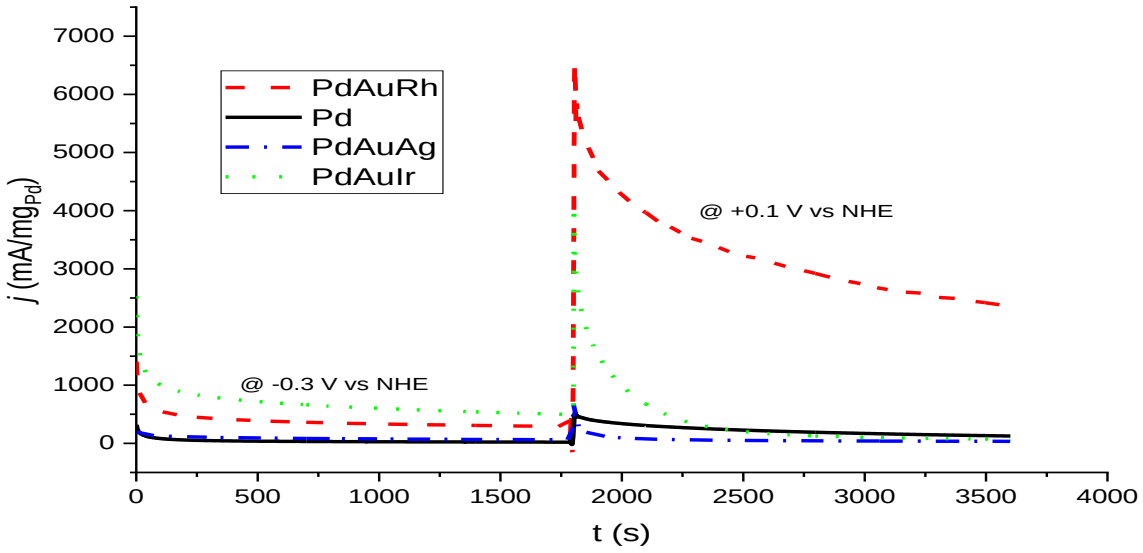

Figure 7-9 Chronoamperometry (CA) scans of PdAuIr/C, PdRhAu/C, PdAuAg/C and Pd/C in 1M KOH+EtOH at -0.3 V and +0.1 V vs NHE

The PdAuAg draws a steady state current that is lower than Pd but higher than PdIrAg, PdRhIr, and PdIrAg. The CA currents drawn on PdAuAg PdRhIr, and PdIrAg at -0.3 V are smaller than those at +0.1 V. The current drawn on PdRhAg at -0.3 V is slightly smaller than that at +0.1 V. Looking at the PdRhAg CV graph, two overlapping peaks exist at those two potentials. The CA steady state decay at +0.1 V of PdRhAg suggests a consistent generation of adsorbed OH promoting the ethanol oxidation and maintaining the CA current over the testing period. A faster decaying current at -0.3 V is suggestive of degrading OH adsorbed on that catalyst. The PdIrAg and PdRhIr CA currents are the lowest at both -0.3 V and +0.1 V which is understandable by looking at the CV graphs.

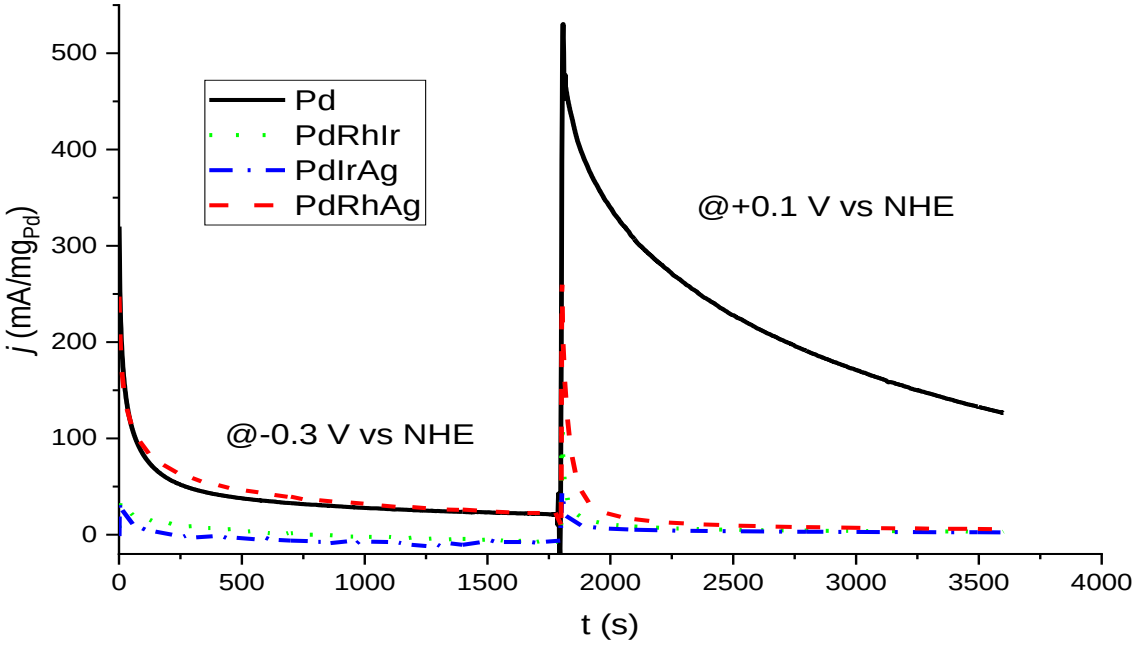

Figure 7-10 Chronoamperometry (CA) scans of PdRhIr/C, PdRhAg/C, PdIrAg/C and Pd/C in 1M KOH+EtOH at -0.3 V and +0.1 V vs NHE

7.3.3 Tafel polarisation

Figure 7-11 shows the Tafel polarisation curves extracted from the potentiodynamic measurements performed between -0.3 V and +0.2 V versus NHE at 0.2 mV/s in 1M EtOH+KOH. The lowest Tafel slope is attained on PdAuRh which indicates the highest rate of

ethanol oxidation. On the far opposite, the highest Tafel slope is obtained on PdRhIr which indicates the slowest reaction of ethanol oxidation occurs on it. Though the small particle size of that catalyst, its XRD pattern shows a shift to higher diffraction angles and also its XPS Pd 3d peaks are shifted to higher binding energies (0.16V). These physical results indicate the PdRhIr surface is mainly covered with Ir followed by Pd. Following PdRhIr, PdIrAg is more active for ethanol oxidation with a smaller Tafel slope. The XRD pattern of that sample shows no difference from the Pd but the XPS and EDX confirm the surface is rich in Ir and poor in Ag. The PdRhAg and PdAuAg catalyst are more active for ethanol oxidation with a lower Tafel slopes than PdRhIr and PdIrAg. Those catalysts surfaces are mainly covered with Pd, as revealed by EDX and XPS. Also, their XRD patterns are shifted to the left and that shift is higher in PdAuAg than PdRhAg. The shift to the lower diffraction angles

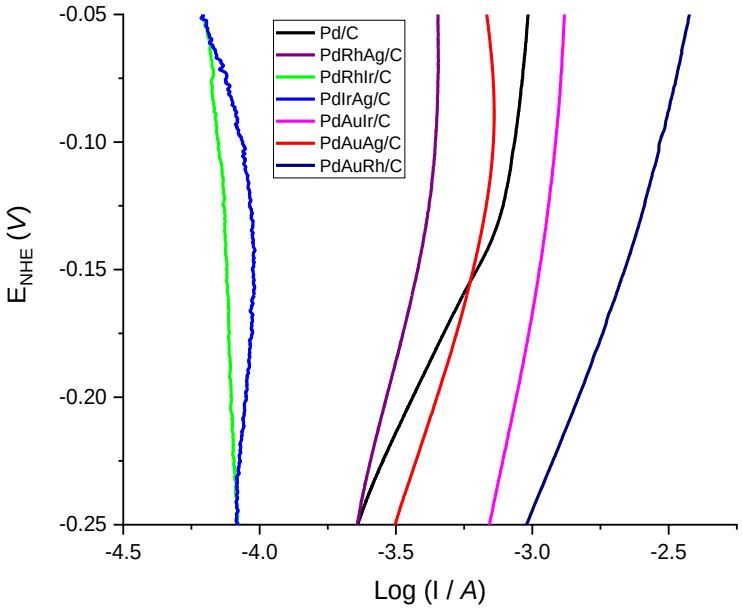

Figure 7-11 Tafel plots of Pd/C, PdAuRh/C, PdIrAg/C, PdRhAg/C, PdAuAg/C, PdAuIr/C, and PdRhAg/C in 1M KOH+EtOH at 0.2 mV/s

7.3.4 EIS

To study the ethanol oxidation mechanism on each catalyst, three different Potentiostatic electrochemical spectroscopy (EIS) measurements have been recorded at -0.3, 0.0, and +0.3 V vs NHE, respectively. The frequency range applied is 10 kHz to 0.2 Hz and the AC amplitude

is 5 mV. Figure **7-12** shows the EIS spectra obtained from every catalyst at the three potentials and it may be reminded the electrolytic solution is the same 1M EtOH + KOH. Looking at the PdAuIr spectra, a smallest impedance arc size is obtained at +0.0 V which indicates the enhanced kinetics at this potential. At -0.3 V, the reaction rate is slower due to the small quantity of adsorbed OH and as a result a slightly bigger arc is noted. However, at +0.3 V, the produced spectrum does not resemble a semi-circle arc and in fact a very high charge transfer resistance is noted at this potential on PdAuIr.

The potential explanation for the three spectra is the highly Ir populated surface more than Pd and make the Pd active sites scarce on the surface especially at the high potential window (0.1 - 0.3 V). Worse than PdAuIr, the PdIrAg presents a very small difference in the impedance arc size by changing the potential from -0.3 to +0.3 V. Also, the three arcs are close to being linear rather than semi-circle. The straight-line EIS plots might suggest a very high charge transfer resistance at high and low frequencies. These suggest the ethanol inactivity encountered on that catalyst surface at all potentials and the potential clarification is the surface enrich of Ir and weak alloying between Ag and Pd. a similar claim could possibly be made from the PdRhAg spectra. However, it is noteworthy in case of the latter, a significant increase in the arc size is noted by increasing the potential to +0.3 V while it is similar both at -0.3 V and +0.0 V. This still suggests this catalyst is more active for ethanol oxidation at certain potentials more than other lower and higher potentials. The reason behind is probably because no Ir is present and the EDX and XPS have detected a smaller (than the theoretical) content of Rh. The eventual outcome is weak mixing of Ag and Pd and losing a considerable quantity of Rh.

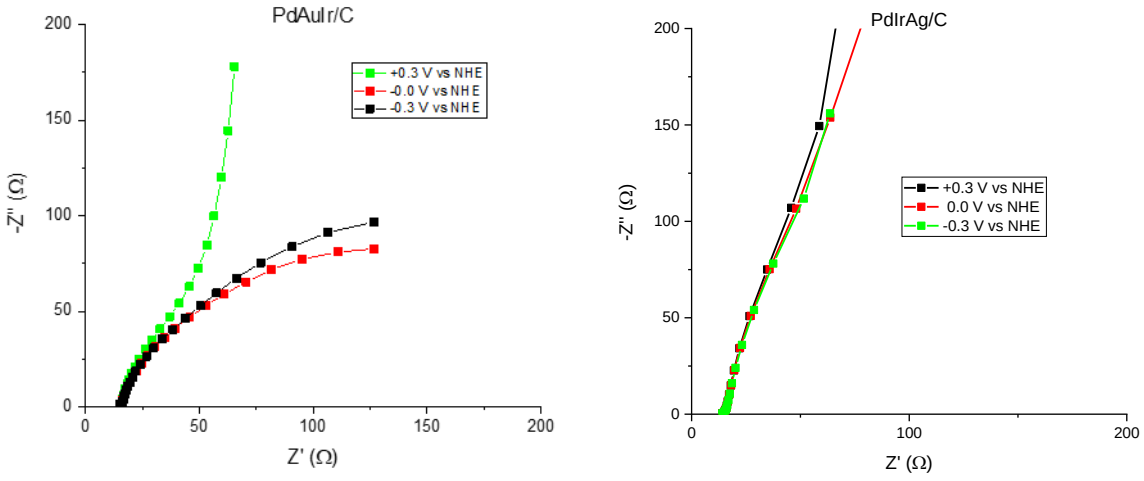

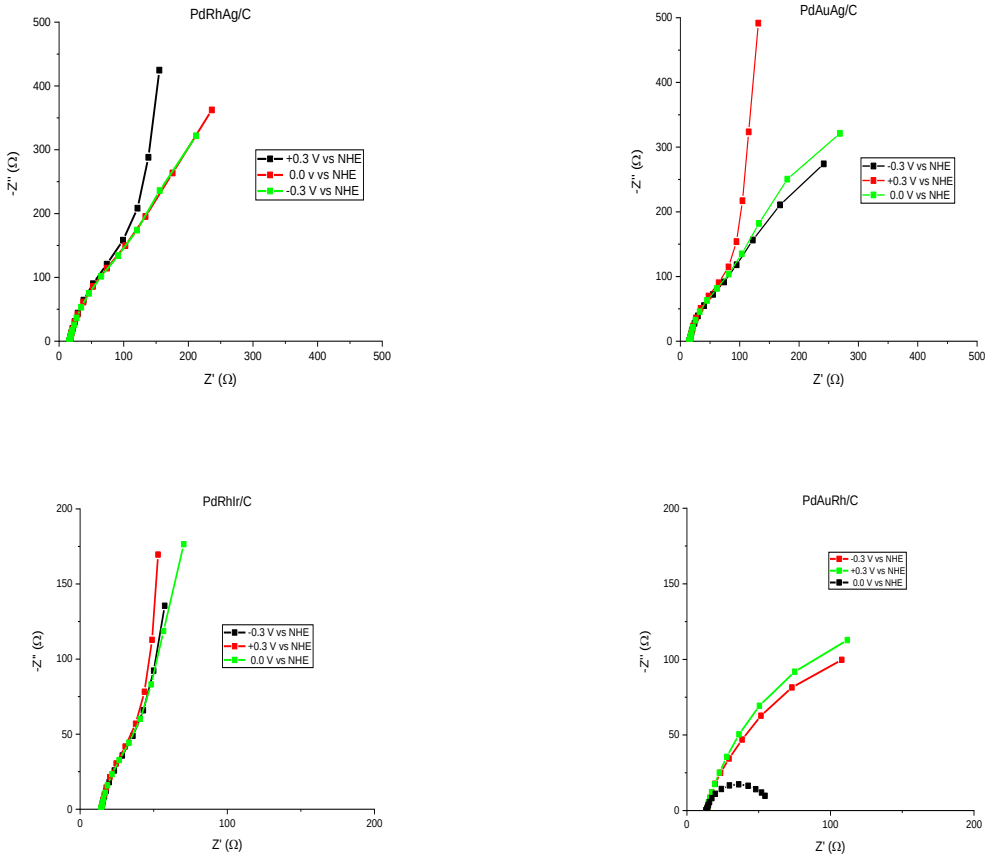

Figure 7-12 EIS spectra of PdAuRh/C, PdIrAg/C, PdRhAg/C, PdAuAg/C, PdAuIr/C, and PdRhAg/C in 1M KOH+EtOH at -0.3, 0.0, +0.3 V vs NHE (frequency 10 kHz - 0.2 Hz)

As for the PdAuAg catalyst, the EIS spectra show similar behaviour to that of PdRhAg. This similarity stems from that both catalyst produce quite similar CV graphs (Figure 7-8) and especially the dual peak in the forward oxidation scan. One main difference, though, the charge transfer resistance (i.e., the arc radius) is more impacted and changed by changing the applied potential. Also, an interesting little observation is the arc radius at -0.3 V is smaller than that at 0.0 V which is counter-default scenario. This could be attributed to the fact at 0.0 V most of Pd surface sites will start to oxidise and therefore the reaction rate decreases significantly. Also, PdRhAg and PdAuAg produce very similar Tafel plots (Figure **7-11**). It might be useful to mention the EDX surface concentration of Pd is equivalent to that of Au but the XPS measured concentration of the latter is higher than the latter. This may suggest that both Ag and Au could have possibly segregated into the bulk PdAuAg causing tensile stress at the core of the particle and to counterbalance that, the Pd-rich surface was subjected to a compressive stress. There is 0.37 eV shift to lower XPS binding energy which could be translated in the mass activity and

onset oxidation potential noted in Figure **7-8**. As for PdRhIr, it is very similar to PdIrAg and it seems logical to assume the Ir influence in both catalysts is dominant. The Ir metal is not active for ethanol oxidation if compared to Pd. Rh, Ag, and Rh are also inactive for ethanol oxidation as shown in Figure **6-6**. Yet, the Ir has a high tendency to segregate into the surface more than Pd and all other metals. Therefore, the PdIrRh and PdIrAg are richest in Ir followed by Pd and finally either Ag or Rh.

Finally, Figure 7-12 also shows the EIS spectra of PdAuRh and the enhancement on the ethanol oxidation on that catalyst is remarkable to all other catalysts. At the three potentials, a semi-circle arc is produced with impedance values much lower those obtained with the other five catalysts. Also, the impact of applied potential on the charge transfer resistance (and the arc radius) cannot be neglected. For instance, at 0.0 V vs NHE, the arc radius is much smaller than it at -0.3 V, which is slightly than it at +0.3 V. this is probably because of the continuous OH adsorption on PdAuRh surface at 0.0 V leading further enhancing the ethanol oxidation rate. The impact of Au is paramount as it shifts the XRD pattern to lower diffraction angles. Furthermore the EDX (Figure 7-3) and XPS (Figure 7-5) results confirm the Au and Pd abundance on the surface. Their co-existence on the surface could be responsible for the remarkable ethanol oxidation performance. Additionally, the highest XPS Pd 3d binding energy to lower value (-0.44 eV) is noted on that catalyst (Table 7-2). All these physical characteristics have played certain roles in the significant current drawn on that catalyst. All the electrochemical results associate the highest performance with PdAuRh for its unique physical characteristics such as the electronic modification of Pd, the tensile stress/strain resulting from the lattice expansion after Au incorporation into the Pd lattice. Figure 7-13 shows the charge transfer resistance (R_{ct}) estimated values after fitting the experimental EIS bod plots using the Gamry EIS 300 software. A general assumption could made the lowest values are obtained at 0.0 V vs NHE followed by those at -0.3 V vs NHE, and finally the highest R_{ct} values at +0.3 V vs NHE. This is understandable as due to the potential of OH adsorption at 0.0 V in comparison to -0.3V. At +0.3 V, there is no OH adsorption but the metal surface is oxidised preventing further fuel oxidation and that is probably the reason for the generally high R_{ct} values.

The R_{ct} is a suitable measure to make a catalytic comparison among the catalysts, and unlike the double layer capacitance (C_{dl}), it is impacted by the applied potential. Two graphs are presented in Figure 7-13: the first of PdAuRh, PdAuIr, PdRhAg, and PdIrAg, and the second with PdRhIr and PdAuAg which record very high R_{ct} values especially at +0.3 V. The catalyst

achieving the lowest R_{ct} is PdAuRh at all potentials R_{ct} is below 150 Ω. The surface Pd abundance in addition to the unique alloying, electronic structure and geometric potential has led to this highest performance. Following PdAuRh is PdAuIr whose Rct values are higher but still below 500 Ω. Apparently the performance decrease is due to the surface being highly covered with Ir more than Pd. Following PdAuIr is PdAuAg whose R_{ct} values at 0.0 V and +0.3 V are strangely high, R_{ct} at 0.0V is higher than that at -0.3 V. This is once more noted PdRhAg and PdIrAg. Probably, these catalysts surface are short of enough Pd (especially PdIrAg), and their alloying potential is not very high (especially between Pd and Ag) using the applied synthesis method. Additionally, some of them have a slightly bigger particle size than the rest of the catalysts. The PdRhIr recorded R_{ct} values are the worst among the catalysts.

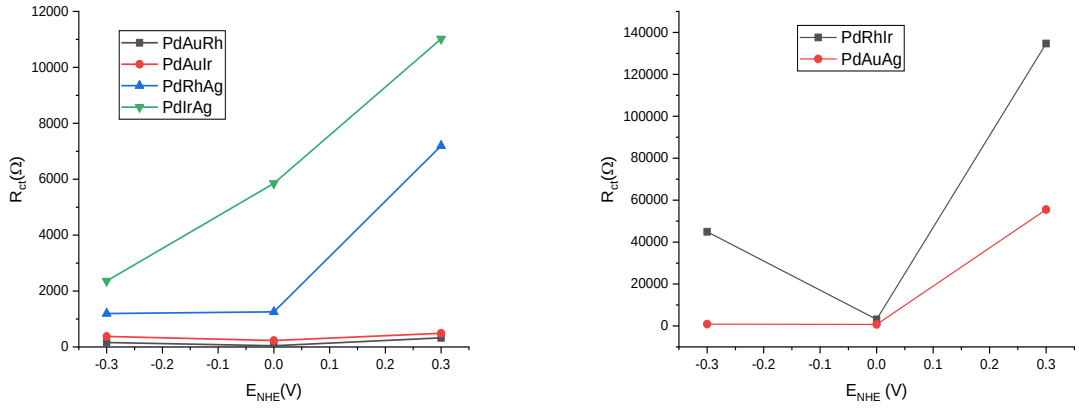

Figure 7-13 Charge transfer resistance values estimated by Gamry EIS 300 fitting models of PdAuIr, PdAuRh, PdAuAg, PdIrAg, PdRhAg, and PdRhIr for ethanol oxidation

The PdAuRh possesses uniquely positive physical characteristics that advocate for its remarkable electrocatalytic oxidation potential. It is XRD patterns shows a well-mixed nanoalloy structure with Pd phase shifted slightly to lower diffraction angles towards Au phase. The absence of any individual Au or Rh peaks is indicative of the incorporation of their atoms into the Pd lattice. This has led to a lattice expansion of Pd (similar PdAuNi/C_{SBIPP} in Chapter 5). Also, the TEM analysis reveals that the catalyst particle size of PdAuRh is very small of 2.5 nm. Additionally, the EDX chemical analysis reveals that the atomic concentration of the three metals are close to one another which supports the good mixing and alloying argument. The XPS results of that catalyst suggests the surface is rich in Au more than Pd and Rh. The Au presence on the surface – noting its high affinity to alloy with Pd – could be very beneficial

for ethanol oxidation as it could activate water and generate oxygen species to improve the CO tolerance. Also, it could enhance the electronic configuration of Pd which is expressed the -0.05 eV shift of Pd 3d binding energy. This shift means a net electron gain into Pd either from Au, Rh, or both of them. It is also interesting no PdO exist in case of PdAuRh. All those excellent physical characteristics could be collectively translated into its remarkable ethanol oxidation activity. Unlike Ag or Ni, no individual oxidation/reduction peaks of Au or Rh show up in the KOH CV of PdAuRh though there is a shoulder peak that seems overlapping with the Pd reduction peak and could be due to Rh reduction. The onset potential of ethanol oxidation on PdAuRh is the lowest of -450 mV vs NHE compared to -380 mV for Pd. the oxidation current peak is remarkable with 10.5 A/mgPd. The ratio of forward/backward current peak is close to 1.2 which indicates a high tolerance for poisoning species. As far as the CA and degradation are concerned, it outperforms all other trimetallic and Pd single catalysts. Although a significant current decay is noted on PdAuRh at the high-potential CA scan, the current obtained is still much higher (for the whole scan duration) than all other catalysts. In the same way, the Tafel slope and charge transfer resistance obtained on PdAuRh are much lower that all other catalysts. The PdAuIr catalyst comes second after PdAuRh in terms of its catalytic potential for ethanol oxidation. Once again, it has an alloy structure and its XRD peaks are shifted to lower diffraction angles towards Au from Pd. The PdAuIr EDX analysis reveals a homogeneous mixture with equivalent concentration for each metal. However, the XPS reveals the top surface is richest in Ir followed by Pd and finally Au. This might help explain the *slightly* high performance for ethanol oxidation as Ir does not seem activate ethanol or generate oxygen species. Furthermore, the binding energy shift is low (-0.05 eV) compared to Pd/C and it is noteworthy that 0.12 At.% of the PdAuIr exist as PdO which might suggest Pd has lost electron in favour of Ir. Yet, it still has a very small particle size of 2.35 nm. As consequence of the moderately good physical characteristics, PdAuIr outperforms Pd and other trimetallic catalysts - except PdAuRh – for ethanol oxidation. With onset potential of -400 mV and oxidation current peak of 3 A/mg_{Pd}, PdAuIr is more active than Pd/C for ethanol oxidation. The ratio of forward to backward current is also satisfactory. It is interesting – as far as the CA concerned – PdAuIr out performs PdAuRh at the lower potential of -0.3 V vs NHE (probably due to the high OH generation potential from Au and Ir at the lower potential). However, the situation is reversed at the higher potential of +0.1 V where the current drawn by PdAuRh is significantly more than all other catalysts. This might be explained at high potential, PdAuIr loses its capacity to generate OH species to help remove the ethoxy and CO species that are

blocking the Pd active sites. Following PdAuIr, the PdAuAg, also, outperforms Pd/C for ethanol oxidation. The XRD peaks of this sample are – unlike other catalysts – asymmetric and that is probably due to the week alloying between Pd and Ag as was found with PdAgNi catalysts in Chapter 6. It is noteworthy that both Au and Ag – unlike Ir, Rh, and Ni - possess geometrical features (lattice parameter and atomic radius) larger than Pd. That is the probable reason the XRD peak shift to lower diffraction angles from Pd phase towards Au (and Ag) phase and the highest shift is in case of PdAuAg. As was seen in Chapter 6, the Ag has a tendency to segregate into the core, the EDX analysis reveals the PdAuAg is richest in Au followed by poorest in Ag though their proportions are close to one another. The situation is slight reversed as far as the XPS is concerned since the Pd concentration is highest. It is noteworthy that no PdO is present on PdAuAg and a high negative binding energy shift (-0.26 eV) - compared to Pd/C - is obtained which suggests Pd has overall gained electrons either from Au, Ag, or both. The drawback, however, is a clear increase in the particle size of PdAuAg (4 nm) compared to other catalysts. This may imply less active sites are present on the surface for ethanol oxidation reaction. Yet, it is interesting that two overlapping oxidation peaks could be seen in the ethanol CV test on PdAuAg (at -0.1 and +0.2 V vs NHE). *In-situ* analysis setup would be useful to identify the associated reaction products at those potentials. As far as catalyst degradation is concerned, PdAuAg shows a promising potential – though the overall current is smaller than PdAuRh and PdAuIr – because a steady and slow current decay could be seen both at -0.3 and +0.1 V vs NHE. The reason for that is probably the consistent generation of oxygen by Au and Ag. After PdAuAg is the PdRhAg in terms of the ethanol oxidation potential. Like PdAuAg, two oxidation peaks appear in the ethanol CV on PdRhAg though the current is less than PdAuAg. Also the potential window of the two peaks is larger than PdAuAg. Once again, the alloying degree between Pd and Ag is not very strong as asymmetric XRD peaks could be seen. Yet, it exerts shifts the Pd peaks towards Ag and expands the unit cell. It is surprising that Rh in this catalyst is barely detected by XPS and EDX. Also a small portion of Pd exist in an oxide state (0.07 %) but the Pd 3d binding energy shift is highest (-0.29 eV). Due to the effect of Ag, the particle size of this catalyst is also higher than most other catalysts (4.3 nm). PdIrAg and PdRhIr are the lowest performing samples for ethanol oxidation. With its established tendency to segregate into the surface more than Pd, Ir could be assumed to have contributed to the lower catalytic activity of both catalysts. Also, the two catalysts are the least stable and easiest to poison by the reaction intermediates. This is probably because both samples are short of oxygen species that are essential to further process

the reaction (even though Ag is present in one of them but it is likely to be buried in the core below Ir and Pd and is inaccessible to the reactants).

7.4 Conclusions

Applying the $NaBH_4$-2-propanol reduction complex complemented by KBr as a capping agent, 6 trimetallic catalyst combinations are prepared and tested for ethanol oxidation for the first time. Unlike Chapter 6, half of the prepared catalysts in this chapter are more active (and presumably more affordable for ethanol oxidation) than the monometallic Pd/C. Adding this to the ease of the synthesis method, the door could be opened for a more viable route to produce large quantities of those catalysts to increase the fuel cell contribution into energy generation. However, the alloying potential of most of those catalysts was not completely attained using the basic XRD test. Some further high-resolution XRD and TEM might help characterise the atomic structure of those catalysts. The PdAuRh is the most active catalyst for ethanol oxidation with a peak current density of more than 10 A/mg_{Pd} which is 5 times higher than the monometallic Pd/C. to a very good extent, there is a high similarity (physically and electrochemically) between this PdAuRh and the $PdAuNi_{SBIPP}$ in Chapter 5. The reasons for this are: the same synthesis method was used and that both Ni and Rh have been proven beneficial addition either into Pd or PdAu. The good alloy structure of PdAuRh and surface modification of Pd by Au and Rh adding to the very small size (2.5 nm) collaborate to produce such remarkable catalytic performance. The other PdAu-containing catalysts (PdAuIr and PdAuAg) still outperforms Pd/C though their activity is much less than PdAuRh. For once, the Ir has a tendency to segregate into the surface (which is noted in PdIrAg too) as could be seen by EDX and XPS while it has no potential for ethanol oxidation on its own or generating oxygen species. Yet, it does not prevent the formation of a sound alloy structure between Pd and Au. Also, the Ag has less potential than Au to form an alloy with Pd which is translated in the separate Ag reduction peak in the KOH CV of PdAuAg. Yet, the Ag clear tendency (verified by EDX and XPS for any Ag-containing catalyst) to segregate into the core below Pd is considered beneficial for promoting its catalytic properties. Yet, the Ag-containing catalysts generally possess larger particle sizes (verified by TEM and XRD) than other catalysts which contributes to the small current obtained on them. The two ethanol oxidation peaks noted on PdAuAg and PdRhAg are suggestive of oxidation of individual ethanol species. The PdRhIr and PdIrAg catalysts give the lowest performance for ethanol oxidation. It could related to the

Ir tendency to segregate into the surface above Pd and other metals and its lack of generating oxygen or activating ethanol. Also, the weak alloying between Ag and Pd could have a detrimental effect on the Pd ethanol oxidation though Ag is active and has a potential to generate oxygen that is used for oxidising the ethanol intermediates.

CONCLUSIONS

This project has aimed to resolve two main challenges of fuel cell ethanol oxidation: the high cost of applying Pt and the particular difficulty of ethanol oxidation requiring a further active catalyst. Twenty-two electrocatalysts (monometallic and trimetallic) have been prepared and investigated for ethanol oxidation. Almost all the trimetallic catalysts in chapter 6 and chapter 7 are reported for ethanol oxidation for the first time as far as the author knows. And based on the obtained results and above discussion, some definite conclusions could be drawn:

The support material is required with certain physicochemical properties. Most of the reported literature have highlighted the importance of both carbon surface area and oxygen functional group content. A few reports have considered the other properties such as mesoporous pore size and crystallinity which are further explored in this project. Vulcan carbon (XC72) remains amongst the most favourable support options for Pd ethanol oxidation. The reasons behind this is its high surface area (230-250 m^2/g), well-developed porous structure (20-nm pores size) and its affordable cost. Yet, it does contain some small micropores that could bury the small metal nanoparticles and make them less accessible to reactants. Another disadvantage, is the prevailing amorphous nature though some crystal arrangements exist proven by the XRD broad peak at 25°. The crystalline carbon is more electronically conductive and more likely to tune in the metal particle size because the crystalline order helps conduct and support small metal species. Other very high-surface-area carbons (AC, C_{s1}, and C_{s2}) tend to have a less developed porous structure with a smaller pore size (10-12 nm). Though they are still considered mesoporous carbon, they provide smaller - than Vulcan carbon - space to accommodate the Pd nanoparticles. Also, their percentage content of small micropores is more than that of Vulcan carbon. Therefore, there is small likelihood the Pd NPs would be fully exposed on the surface and higher likelihood they are buried or surrounded by the carbon texture. As a result, they are less likely to be accessible to the reactants migrating from the bulk solution. Crystalline carbon nanofibres (CNFs) present some potential as a support with reasonable active performance for ethanol oxidation. This is due to their developed porous structure – all of which is mesoporous with a large pore size (21 nm) – and crystalline structure which makes them more conducting to small Pd nanoparticles. However, CNFs do not have a sufficiently high surface area (60

m^2/g) which enhances the chances of particle aggregation. Commercial MWCNT, in addition to the crystalline structure and large pore size – also have a high surface area (close to that of Vulcan carbon) though they are more expensive. Thus, the key conclusion here is that the higher pore size and crystalline nature - added to the high surface area – are very beneficial for the support functionality. After considering the three of them thoroughly, the support cost should be considered as well.

Having seen the Vulcan carbon potential, the attention was then paid to which synthesis method is more likely to produce an active catalyst. Three borohydride reduction routes are used to prepare PdAuNi/C. The $NaBH_4$-ethylene glycol reduction method (SBEG) presents a significantly high agglomeration of the metallic particles on the carbon surface. The surface is largely covered with small metal species that is likely to be Ni hydroxide. Furthermore, the XRD pattern shows an individual peak of $Ni(OH)_2$, which is suggestive of less alloying potential between Ni on one side and PdAu on the other. Also, the CV of this sample presents high oxidation and reduction peaks of $NiOOH/Ni(OH)_2$. Another disadvantage of the SBEG is that it is time consuming (4h for the metal reduction alone). The three step reduction (or core@shell) leads to almost Au-like structure as the XRD peaks are closest to the bulk Au ones. Ni still slightly segregates into the surface and a high particle size is obtained with Au-like structure. Therefore, it gives the lower performance and the potential reason is that separation of each metal nanoparticles has occurred at the nanoscale due to the sequential reduction of each metal. Also the produced Au@Pd on Ni/C does not seem to be active for ethanol oxidation and faces a big activation barrier. The $NaBH_4$-2-propanol (SBIPP) presents the highest catalytic performance towards ethanol oxidation. An alloy structure of PdAuNi with a small particle size (3 nm) is produced. The XPS and EDX confirm the high mixing degree of the three metals as they study different depths of the sample. No individual reduction/oxidation peaks of Ni are noted in the KOH CV. It is noteworthy that the SBIPP is also the easiest and most straightforward approach. Highly enhanced geometric, electronic, and catalytic properties are readily obtained using that simple method. Therefore, this method has a potential for fuel cell catalyst mass production. So the $PdAuNi_{3step}$ with an Au-like structure and largest particle size is the least performing for ethanol. The $PdAuNi_{SBEG}$ with a surface mostly covered with $Ni(OH)_2$ is more active than the monometallic Pd. Finally, the $PdAuNi_{SBIPP}$ with the one XRD phase representing the three metals and highly dispersed metal particles on the carbon surface gives the best activity for ethanol oxidation.

Metal particle size is fairly thought to play a key role to reflect the catalytic performance. Smaller particle size implies a larger reaction surface area. However, in light of the obtained results of the trimetallic catalysts for ethanol oxidation, there are other equivalent contributing factors such as the segregation of certain metals into the surface (Ir and Ni) and other metals into the core (Ag, Au), the geometrical changes of the atomic structure (lattice contraction/expansion), and the electronic configuration tuning of Pd by adding 2 other metals during the synthesis. The PdAgNi systems present a more active and stable performance than the monometallic Pd. Though a higher particle size is obtained for the trimetallic in comparison with Pd, the electronic configuration and geometric tuning brought by adding Ag and Ni into Pd enhances its catalytic activity and stability. The PdIrNi systems give lower activity and less stability towards ethanol oxidation than the monometallic Pd. the potential reasons are the surface enrichment with Ir and Ni while the Pd tends to segregate into the core. Both Ir and Ni do not have a potential to activate ethanol and therefore the lower performance. Also, Ir, unlike Ni, does not have a potential to generate OH species to help oxidise and remove the ethanol reaction intermediates and products. The PdRhNi systems – like PdIrNi ones – also give a less stable and active ethanol oxidation performance than Pd/C. Though the single Pd XRD phase obtained and small particle size, these are not translated into higher oxidation current. Rh and Ni exert compressive strain and stress on the Pd crystal lattice and contracts the unit cell. The surface is still enriched with Ni which is weakly alloyed with Pd. However, two overlapping peaks are noted in the forward CV sweep. Those peaks might belong to different final reaction products (such CO_2 and CH_3COOH). If true, those systems might have a good selectivity for the full oxidation towards CO_2. Yet, as far as this work is concerned these catalysts are less active and stable for ethanol oxidation than Pd. To sum this up, the synergistic effects of PdAgNi, PdRhNi, and PdIrNi trimetallic do not seem very promising for producing an active and stable ethanol oxidation catalysts. Therefore, they could be avoided as trimetallic catalyst candidates for ethanol oxidation. As they is a very few papers investigating them, a recommendation to other research groups could be made about the low potential they present – especially PdIrNi systems.

The less successful PdMeNi systems have inspired to take out Ni – seeing its high tendency to of surface segregation and weak alloying degree with Pd – and try other trimetallic combinations. The PdAuRh system, in particular, presents a remarkably improved performance

towards ethanol oxidation. Various factors have led to such an indispensable activity and stability such as the enhanced crystal structure through the alloying effect with Au. Also, the surface is enriched in Pd and Au which facilitates both the ethanol and OH related reactions. Finally, the obtained particle size is very smallest (2.5 nm). The PdAuIr system also achieves a satisfying electrocatalytic activity and stability though not comparable to that of PdAuRh. Ir seems to segregate into the surface and gain electrons from Pd according to XPS measurements. The benefit of Au and Pd alloying still contributes to the overall catalytic performance. The PdAuAg achieves a slightly enhanced potential activity and stability towards ethanol oxidation in comparison with Pd. It seems Au and Ag are in competition to formulate an alloy with Pd though Au is more favoured. The particle size obtained is comparatively high (close to 4 nm). Yet, there are two peaks noted in the forward ethanol oxidation scan which might be due to the oxidation of two ethoxy species. Also the KOH CV reveals Ag oxidation/reduction peaks due to the lower affinity between Ag and Pd. The other trimetallic systems (PdRhIr, PdIrAg, and PdRhAg) achieve a lower catalytic activity and stability. The apparent reasons include the Ir tendency to segregate into the surface and gain electrons from Pd or the weak alloying potential between Pd and Ag (if compared to PdAu). All of those catalysts are prepared and tested for fuel cell catalysis for the first time. The PdAuRh and PdAuIr catalysts are good candidates for application in direct ethanol fuel cells.

In summary, the critical balance of physical properties and cost of Vulcan carbon make it a suitable support and the pore size and crystallinity are crucial factors upon choosing an alternative. The $NaBH_4$-2-propanol complemented by KBr as a capping agent is a straightforward method to produce various trimetallic alloy nanoparticles some of which (PdAuRh and PdAuNi) are exceptionally active for ethanol oxidation. The studied PdIr catalysts reported in this thesis have found Ir could enhance ethanol oxidation on Pd, but this work has come to conclude that adding Ir to Pd in a trimetallic system, using the current method, does not seem beneficial for ethanol oxidation because it has a high tendency to segregate into the surface above Pd. Nonetheless, Ir has no potential on its own for ethanol activation. Au greatly enhances ethanol oxidation on Pd. A less outcome is obtained with Ag. Although, it has a very little potential for ethanol oxidation on its own, the impact of adding Rh requires further *in-stiu* techniques to analyse the reaction products and intermediates at different potentials.

FUTURE WORK

The current work has aimed to upgrade the catalyst design methodology for ethanol oxidation. This goal was approached through investigating different carbon supports and various trimetallic catalyst combinations. Based on the findings of this study, some further analyses to elucidate better understanding of the ethanol oxidation mechanism and products in a more accurate way are recommended. Also, a deeper analysis of the physical structure to determine the alloying potential is worthy of trial.

Upon choosing a catalyst support for ethanol oxidation, several factors must be thoroughly and critically counted. The balance among the various physiochemical properties and the economic feasibility is a key for the successful functioning of a support. Based on the findings of this study the commercial Vulcan carbon presents a good choice for its high surface and adequate porous structure (pore size close to 20 nm). However, it is not crystalline like carbon nanofibres which constraints its potential functionality. Furthermore, it contains a good part of small micropores that might bury the small metal particles and make them inaccessible to reactants. Finally, although it is relative cheap (when compared to MWCNT for example), it is not the best economic support option especially there is a growing attention paid producing various carbons through renewable and sustainable technologies. Thus, the next step to develop the ethanol oxidation catalyst support is to choose and counter-balance the high surface area, porosity, crystallinity, and costs.

In Chapter 7, most of the trimetallic systems have given XRD patterns with overlapping peaks in one metallic phase. This causes some confusion regarding the potential of an alloy formation of the three metals. Therefore, it is worthy to use and deploy some more sophisticated analysis means to examine that. These technologies might include high-resolution XRD, high-resolution TEM (with electron diffraction) alongside others.

All of the prepared catalysts are investigated in terms of physical structure, and their activity and stability for ethanol oxidation. However, none of them are tested for CO_2 selectivity through breaking the ethanol C-C bond. The most active and stable catalyst is not necessarily the most CO_2 selective one. This requires more specialized techniques in monitoring the

reaction mechanism and the final product yields. These might include special setups of in-situ FTIR, online DEMS, and ionic chromatography.

Finally, the chronoamperometry analyses performed in this study have given some ideas about the individual stability of each catalyst. However, each analysis was performed for a short time period (30 – 60 min) which might not a sufficient time to reveal the exact stable performance over extended operation time periods. Therefore, repeating the analysis for 4 – 5 h is a good method to compare the catalyst stability holistically

REFERENCES

[1] L. Ma, D. Chu, R. Chen, Comparison of ethanol electro-oxidation on Pt/C and Pd/C catalysts in alkaline media, Int. J. Hydrogen Energy. 37 (2012) 11185–11194. https://doi.org/10.1016/j.ijhydene.2012.04.132.

[2] F.B.P. Ryan O'Hayre, Suk-Won Cha, Whitney Colella, Chapter 14: Environmental Impact of Fuel Cells, in: Fuel Cell Fundam., John Wiley & Sons, Inc, Hoboken, NJ, USA, 2016: pp. 481–516. https://doi.org/10.1002/9781119191766.ch14.

[3] A. Chen, C. Ostrom, Palladium-Based Nanomaterials: Synthesis and Electrochemical Applications, Chem. Rev. 115 (2015) 11999–12044. https://doi.org/10.1021/acs.chemrev.5b00324.

[4] H.R. Ellamla, I. Staffell, P. Bujlo, B.G. Pollet, S. Pasupathi, Current status of fuel cell based combined heat and power systems for residential sector, (2015). https://doi.org/10.1016/j.jpowsour.2015.05.050.

[5] K. V. Kordesch, G.R. Simader, Environmental Impact of Fuel Cell Technology, Chem. Rev. 95 (1995) 191–207. https://doi.org/10.1021/cr00033a007.

[6] H.-W. Wu, A review of recent development: Transport and performance modeling of PEM fuel cells, Appl. Energy. 165 (2016) 81–106. https://doi.org/10.1016/J.APENERGY.2015.12.075.

[7] N. Radenahmad, A. Afif, P.I. Petra, M.H. Rahman, S.-G. Eriksson, A.K. Azad, Proton-conducting electrolytes for direct methanol and direct urea fuel cells – A state-of-the-art review, (2016). https://doi.org/10.1016/j.rser.2015.12.103.

[8] G. Hoogers, Fuel Cell Technology Handbook, CRC Press, 2002. https://doi.org/10.1201/9781420041552.

[9] R. O'Hayre, S.-W. Cha, W. Colella, F.B. Prinz, Fuel Cell Fundamentals, John Wiley & Sons, Inc, Hoboken, NJ, USA, 2016. https://doi.org/10.1002/9781119191766.

[10] G. Merle, M. Wessling, K. Nijmeijer, Anion exchange membranes for alkaline fuel cells: A review, J. Memb. Sci. 377 (2011) 1–35. https://doi.org/10.1016/j.memsci.2011.04.043.

[11] E. Antolini, E.R. Gonzalez, Alkaline direct alcohol fuel cells, J. Power Sources. 195

(2010) 3431–3450. https://doi.org/10.1016/j.jpowsour.2009.11.145.

[12] J. Larminie, A. Dicks, Fuel Cell Systems Explained, John Wiley & Sons, Ltd,., West Sussex, England, 2003. https://doi.org/10.1002/9781118878330.

[13] P. Thounthong, B. Davat, S. Raël, Driver Friendly: Fuel Cell/Supercapacitor Hybrid Power Sources for Future Automotive Power Generation, IEEE Power Energy Mag. (2008) 69–76.

[14] L. Li, M. Chen, G. Huang, N. Yang, L. Zhang, H. Wang, Y. Liu, W. Wang, J. Gao, A green method to prepare Pd–Ag nanoparticles supported on reduced graphene oxide and their electrochemical catalysis of methanol and ethanol oxidation, J. Power Sources. 263 (2014) 13–21. https://doi.org/http://dx.doi.org/10.1016/j.jpowsour.2014.04.021.

[15] Modeling Fuel Cells - Digital Engineering 24/7, (n.d.). https://www.digitalengineering247.com/article/modeling-fuel-cells/ (accessed February 4, 2020).

[16] X. Li, Principles of fuel cells. 2006, (n.d.).

[17] G. Centi, S. Perathoner, Problems and perspectives in nanostructured carbon-based electrodes for clean and sustainable energy, Catal. Today. 150 (n.d.) 151–162. https://doi.org/10.1016/j.cattod.2009.09.009.

[18] O.Z. Sharaf, M.F. Orhan, An overview of fuel cell technology: Fundamentals and applications, Renew. Sustain. Energy Rev. 32 (2014) 810–853. https://doi.org/10.1016/j.rser.2014.01.012.

[19] A. Serov, I. V. Zenyuk, C.G. Arges, M. Chatenet, Hot topics in alkaline exchange membrane fuel cells, J. Power Sources. 375 (2018). https://doi.org/10.1016/j.jpowsour.2017.09.068.

[20] F.B.P. Ryan O'Hayre, Suk-Won Cha, Whitney Colella, Chapter 8: Overview of Fuel Cell Types, in: Fuel Cell Fundam., John Wiley & Sons, Inc, Hoboken, NJ, USA, 2016: pp. 269–302. https://doi.org/10.1002/9781119191766.ch8.

[21] S. Mekhilef, R. Saidur, A. Safari, Comparative study of different fuel cell technologies, Renew. Sustain. Energy Rev. 16 (2011) 981–989. https://doi.org/10.1016/j.rser.2011.09.020.

[22] S.L. Suib, T. dos S. Almeida, A.R. De Andrade, Chapter 15 – New Trends in Direct Ethanol Fuel Cells, in: New Futur. Dev. Catal., 2013: pp. 429–452. https://doi.org/10.1016/B978-0-444-53880-2.00020-X.

[23] U. Lucia, Overview on fuel cells, Renew. Sustain. Energy Rev. 30 (2014) 164–169.

https://doi.org/10.1016/j.rser.2013.09.025.

[24] R.F. Service, FUEL CELLS: Shrinking Fuel Cells Promise Power in Your Pocket, Science (80-.). 296 (2002) 1222–1224. https://doi.org/10.1126/science.296.5571.1222.

[25] B.C.H. Steele, A. Heinzel, Materials for fuel-cell technologies, Nature. 414 (2001) 345–352. https://doi.org/10.1038/35104620.

[26] A.M.A.A. Elshekh, Síntese de catalisadores à base de paládio para aplicação em célula à combustível alcalina de etanol direto (DEFC), Federal University of Rio Grande do Sul, 2014. http://hdl.handle.net/10183/98135.

[27] J.M. Andú, F. Segura, Fuel cells: History and updating. A walk along two centuries, (n.d.). https://doi.org/10.1016/j.rser.2009.03.015.

[28] L. An, T.S. Zhao, Transport phenomena in alkaline direct ethanol fuel cells for sustainable energy production, J. Power Sources. 341 (2017). https://doi.org/10.1016/j.jpowsour.2016.11.117.

[29] F.B.P. Ryan O'Hayre, Suk-Won Cha, Whitney Colella, Chapter 3: Fuel Cell Reaction Kinetics, in: Fuel Cell Fundam., John Wiley & Sons, Inc, Hoboken, NJ, USA, 2016: pp. 77–116. https://doi.org/10.1002/9781119191766.ch3.

[30] Terrace ledge kink model, (n.d.). https://en.wikipedia.org/wiki/Terrace_ledge_kink_model (accessed February 4, 2020).

[31] M.A. and W.F.H. Raweewan Klaewkla, A Review of Mass Transfer Controlling the Reaction Rate in Heterogeneous Catalytic Systems, Intech. i (2016) 13. https://doi.org/http://dx.doi.org/10.5772/57353.

[32] How Nanotechnology Maximizes Surface Area, (n.d.). https://www.dummies.com/education/science/nanotechnology/how-nanotechnology-maximizes-surface-area/ (accessed February 4, 2020).

[33] Electric Double Layer, (n.d.). https://web.nmsu.edu/~snsm/classes/chem435/Lab14/double_layer.html (accessed February 4, 2020).

[34] A.C. Fisher, Electrode dynamics, Oxford University Press, 1996.

[35] R. O'Hayre, S.-W. Cha, W. Colella, F.B. Prinz, Chapter 4: Fuel Cell Charge Transport, in: Fuel Cell Fundam., John Wiley & Sons, Inc, Hoboken, NJ, USA, 2016: pp. 117–166. https://doi.org/10.1002/9781119191766.ch4.

[36] D.M. Fadzillah, S.K. Kamarudin, M.A. Zainoodin, M.S. Masdar, Critical challenges in the system development of direct alcohol fuel cells as portable power supplies: An

overview, Int. J. Hydrogen Energy. 44 (2019) 3031–3054. https://doi.org/10.1016/j.ijhydene.2018.11.089.

[37] A.N. Geraldes, D.F. da Silva, E.S. Pino, J.C.M. da Silva, R.F.B. de Souza, P. Hammer, E.V. Spinacé, A.O. Neto, M. Linardi, M.C. dos Santos, Ethanol electro-oxidation in an alkaline medium using Pd/C, Au/C and PdAu/C electrocatalysts prepared by electron beam irradiation, Electrochim. Acta. 111 (2013) 455–465. https://doi.org/10.1016/j.electacta.2013.08.021.

[38] A. Kirubakaran, S. Jain, R.K. Nema, A review on fuel cell technologies and power electronic interface, (n.d.). https://doi.org/10.1016/j.rser.2009.04.004.

[39] A.M.F.R. Pinto, V.B. Oliveira, D.S. Falcão, Introduction to direct alcohol fuel cells, 2018. https://doi.org/10.1016/b978-0-12-811849-8.00001-2.

[40] S.P.S.P.S.S. Badwal, S. Giddey, A. Kulkarni, J. Goel, S. Basu, Direct ethanol fuel cells for transport and stationary applications – A comprehensive review, Appl. Energy. 145 (2015) 80–103. https://doi.org/10.1016/J.APENERGY.2015.02.002.

[41] E. Antolini, Palladium in fuel cell catalysis, Energy Environ. Sci. 2 (2009) 915–931. https://doi.org/10.1039/B820837A.

[42] M.M.O. Thotiyl, T.R. Kumar, S. Sampath, Pd supported on titanium nitride for efficient ethanol oxidation, J. Phys. Chem. C. 114 (2010) 17934–17941. https://doi.org/10.1021/jp1038514.

[43] L. Tsui, C. Zafferoni, A. Lavacchi, M. Innocenti, F. Vizza, G. Zangari, Electrocatalytic activity and operational stability of electrodeposited Pd–Co films towards ethanol oxidation in alkaline electrolytes, J. Power Sources. 293 (2015) 815–822. https://doi.org/10.1016/j.jpowsour.2015.05.121.

[44] M.Z.F. Kamarudin, S.K. Kamarudin, M.S. Masdar, W.R.W. Daud, Review: Direct ethanol fuel cells, Int. J. Hydrogen Energy. 38 (2013) 9438–9453. https://doi.org/10.1016/J.IJHYDENE.2012.07.059.

[45] A. Jablonski, A. Lewera, Improving the efficiency of a direct ethanol fuel cell by a periodic load change, Chinese J. Catal. 36 (2015) 496–501. https://doi.org/10.1016/S1872-2067(14)60226-6.

[46] S. Heysiattalab, M. Shakeri, M. Safari, M.M. Keikha, Investigation of key parameters influence on performance of direct ethanol fuel cell (DEFC), J. Ind. Eng. Chem. 17 (2011) 727–729. https://doi.org/10.1016/j.jiec.2011.05.037.

[47] P. Saisirirat, B. Joommanee, Study on the Performance of the Micro Direct Ethanol Fuel

Cell (Micro-DEFC) for Applying with the Portable Electronic Devices, Energy Procedia. 138 (2017) 187–192. https://doi.org/10.1016/j.egypro.2017.10.148.

[48] J.S. Spendelow, A. Wieckowski, Electrocatalysis of oxygen reduction and small alcohol oxidation in alkaline media., Phys. Chem. Chem. Phys. 9 (2007) 2654–2675. https://doi.org/10.1039/b703315j.

[49] J. Ledesma-garcía, Performance and stability of Pd nanostructures in an alkaline direct ethanol fuel cell, 269 (2014) 370–378. https://doi.org/10.1016/j.jpowsour.2014.06.161.

[50] N. Li, Y.X. Zeng, S. Chen, C.W. Xu, P.K. Shen, Ethanol oxidation on Pd/C enhanced by MgO in alkaline medium, Int. J. Hydrogen Energy. 39 (2014). https://doi.org/10.1016/j.ijhydene.2013.12.122.

[51] A. Zadick, L. Dubau, U.B. Demirci, M. Chatenet, Effects of Pd nanoparticle size and solution reducer strength on Pd/C electrocatalyst stability in alkaline electrolyte, J. Electrochem. Soc. 163 (2016) F781–F787. https://doi.org/10.1149/2.0141608jes.

[52] Y. Wang, S. Zou, W.-B. Cai, Recent Advances on Electro-Oxidation of Ethanol on Pt- and Pd-Based Catalysts: From Reaction Mechanisms to Catalytic Materials, Catalysts. 5 (2015) 1507–1534. https://doi.org/10.3390/catal5031507.

[53] C. Lafforgue, F. Maillard, V. Martin, L. Dubau, M. Chatenet, Degradation of Carbon-Supported Platinum-Group-Metal Electrocatalysts in Alkaline Media Studied by in Situ Fourier Transform Infrared Spectroscopy and Identical-Location Transmission Electron Microscopy, ACS Catal. (2019) 5613–5622. https://doi.org/10.1021/acscatal.9b00439.

[54] J. Friedl, U. Stimming, Model catalyst studies on hydrogen and ethanol oxidation for fuel cells, Electrochim. Acta. 101 (2013) 41–58. https://doi.org/10.1016/j.electacta.2012.12.130.

[55] O.M. Orogbemi, D.B. Ingham, M.S. Ismail, K.J. Hughes, L. Ma, M. Pourkashanian, The effects of the composition of microporous layers on the permeability of gas diffusion layers used in polymer electrolyte fuel cells, Int. J. Hydrogen Energy. 41 (2016) 21345–21351. https://doi.org/10.1016/j.ijhydene.2016.09.160.

[56] E.H. Majlan, D. Rohendi, W.R.W. Daud, T. Husaini, M.A. Haque, Electrode for proton exchange membrane fuel cells: A review, Renew. Sustain. Energy Rev. 89 (2018) 117–134. https://doi.org/10.1016/j.rser.2018.03.007.

[57] P. Kalyani, A. Anitha, Biomass carbon & its prospects in electrochemical energy systems, Int. J. Hydrogen Energy. 38 (2013) 4034–4045. https://doi.org/10.1016/j.ijhydene.2013.01.048.

[58] M.J. Lázaro, L. Calvillo, V. Celorrio, J.I. Pardo, S. Perathoner, R. Moliner, Study and application of Vulcan XC-72 in low temperature fuel cells, in: Carbon Black Prod. Prop. Uses, 2011: pp. 41–68. https://www.researchgate.net/publication/259442510_Study_and_application_of_Vulcan_XC-72_in_low_temperature_fuel_cells.

[59] R.L. McCreery, Advanced carbon electrode materials for molecular electrochemistry, Chem. Rev. 108 (2008) 2646–2687.

[60] E. Antolini, Carbon supports for low-temperature fuel cell catalysts, Appl. Catal. B Environ. 88 (2009) 1–24. https://doi.org/10.1016/J.APCATB.2008.09.030.

[61] E.L. Da Silva, M.R. Ortega Vega, P.D.S. Correa, A. Cuña, N. Tancredi, C.D.F. Malfatti, Influence of activated carbon porous texture on catalyst activity for ethanol electro-oxidation, Int. J. Hydrogen Energy. 39 (2014) 14760–14767. https://doi.org/10.1016/j.ijhydene.2014.07.103.

[62] M. Carmo, M. Brandalise, A.O. Neto, E. V. Spinacé, A.D. Taylor, M. Linardi, J.G. Rocha Poço, J.G. Rocha Poo, Enhanced activity observed for sulfuric acid and chlorosulfuric acid functionalized carbon black as PtRu and PtSn electrocatalyst support for DMFC and DEFC applications, Int. J. Hydrogen Energy. 36 (2011) 14659–14667. https://doi.org/10.1016/j.ijhydene.2011.08.031.

[63] L. Calvillo, V. Celorrio, R. Moliner, M.J.J. Lázaro, Influence of the support on the physicochemical properties of Pt electrocatalysts: Comparison of catalysts supported on different carbon materials, Mater. Chem. Phys. 127 (2011) 335–341. https://doi.org/10.1016/j.matchemphys.2011.02.014.

[64] L.P.R. Moraes, B.R. Matos, C. Radtke, E.I. Santiago, F.C. Fonseca, S.C. Amico, C.F. Malfatti, Synthesis and performance of palladium-based electrocatalysts in alkaline direct ethanol fuel cell, Int. J. Hydrogen Energy. 41 (2016) 6457–6468. https://doi.org/10.1016/j.ijhydene.2016.02.150.

[65] M. Pirjamali, Y. Kiros, Effects of carbon pretreatment for oxygen reduction in alkaline electrolyte, J. Power Sources. 109 (2002) 446–451. https://doi.org/10.1016/S0378-7753(02)00219-7.

[66] M.D. Obradović, G.D. Vuković, S.I. Stevanović, V.V. Panić, P.S. Uskoković, A. Kowal, S.L. Gojković, A comparative study of the electrochemical properties of carbon nanotubes and carbon black, J. Electroanal. Chem. 634 (2009) 22–30. https://doi.org/10.1016/j.jelechem.2009.07.001.

[67] S. Jongsomjit, K. Sombatmankhong, P. Prapainainar, Effect of acid functionalised carbon supports for Pd–Ni–Sn catalyst on ethanol oxidation reaction, RSC Adv. 5 (2015) 61298–61308. https://doi.org/10.1039/C5RA07508D.

[68] C. Yang, X. Hu, D. Wang, C. Dai, L. Zhang, H. Jin, S. Agathopoulos, Ultrasonically treated multi-walled carbon nanotubes (MWCNTs) as PtRu catalyst supports for methanol electrooxidation, J. Power Sources. 160 (2006) 187–193. https://doi.org/10.1016/j.jpowsour.2006.05.015.

[69] H. Murphy, P. Papakonstantinou, T.I.T. Okpalugo, Raman study of multiwalled carbon nanotubes functionalized with oxygen groups, J. Vac. Sci. Technol. B Microelectron. Nanom. Struct. 24 (2006) 715. https://doi.org/10.1116/1.2180257.

[70] T. Maiyalagan, K. Scott, Performance of carbon nanofiber supported Pd–Ni catalysts for electro-oxidation of ethanol in alkaline medium, J. Power Sources. 195 (2010) 5246–5251. https://doi.org/10.1016/j.jpowsour.2010.03.022.

[71] H. Rostami, A.A. Rostami, A. Omrani, An electrochemical method to prepare of Pd/Cu2O/MWCNT nanostructure as an anode electrocatalyst for alkaline direct ethanol fuel cells, Electrochim. Acta. 194 (2016) 431–440. https://doi.org/10.1016/J.ELECTACTA.2016.02.100.

[72] F. Nitze, Synthesis and characterization of palladium based carbon nanostructure-composites and their clean-energy application, 2013.

[73] A.N. Geraldes, D. Furtunato Da Silva, J.C. Martins da Silva, O. Antonio de Sá, E.V. Spinacé, A.O. Neto, M. Coelho dos Santos, Palladium and palladium–tin supported on multi wall carbon nanotubes or carbon for alkaline direct ethanol fuel cell, J. Power Sources. 275 (2015) 189–199. https://doi.org/10.1016/J.JPOWSOUR.2014.11.024.

[74] S.S. Jayaseelan, T.-H. Ko, S. Radhakrishnan, C.-M. Yang, H.-Y. Kim, B.-S. Kim, Novel MWCNT interconnected NiCo2O4 aerogels prepared by a supercritical CO2 drying method for ethanol electrooxidation in alkaline media, Int. J. Hydrogen Energy. 41 (2016) 13504–13512. https://doi.org/10.1016/J.IJHYDENE.2016.05.175.

[75] R.N. Singh, A. Singh, Anindita, Electrocatalytic activity of binary and ternary composite films of Pd, MWCNT and Ni, Part II: Methanol electrooxidation in 1 M KOH, Int. J. Hydrogen Energy. 34 (2009) 2052–2057. https://doi.org/10.1016/J.IJHYDENE.2008.12.047.

[76] E. Taer, M. Deraman, I.A. Talib, A.A. Umar, M. Oyama, R.M. Yunus, Physical, electrochemical and supercapacitive properties of activated carbon pellets from pre-

carbonized rubber wood sawdust by CO2 activation, Curr. Appl. Phys. 10 (2010) 1071–1075. https://doi.org/10.1016/j.cap.2009.12.044.

[77] C. Bianchini, P.K. Shen, Palladium-based electrocatalysts for alcohol oxidation in half cells and in direct alcohol fuel cells, Chem. Rev. 109 (2009) 4183–4206. https://doi.org/10.1021/cr9000995.

[78] J.H. Kim, J.Y. Cheon, T.J. Shin, J.Y. Park, S.H. Joo, Effect of surface oxygen functionalization of carbon support on the activity and durability of Pt/C catalysts for the oxygen reduction reaction, Carbon N. Y. 101 (2016) 449–457. https://doi.org/10.1016/j.carbon.2016.02.014.

[79] A. Jain, C. Xu, S. Jayaraman, R. Balasubramanian, J.Y. Lee, M.P. Srinivasan, Mesoporous activated carbons with enhanced porosity by optimal hydrothermal pre-treatment of biomass for supercapacitor applications, Microporous Mesoporous Mater. 218 (2015) 55–61. https://doi.org/10.1016/j.micromeso.2015.06.041.

[80] X. Chen, R. Paul, L. Dai, Carbon-based supercapacitors for efficient energy storage, Natl. Sci. Rev. 4 (2017) 453–489. https://doi.org/10.1093/nsr/nwx009.

[81] R.S. Amin, R.M.A. Hameed, K.M. El-Khatib, M.E. Youssef, R.M. Abdel Hameed, K.M. El-Khatib, M. Elsayed Youssef, R.M.A. Hameed, K.M. El-Khatib, M.E. Youssef, Electrocatalytic activity of nanostructured Ni and Pd-Ni on Vulcan XC-72R carbon black for methanol oxidation in alkaline medium, Int. J. Hydrogen Energy. 39 (2014) 2026–2041. https://doi.org/10.1016/j.ijhydene.2013.11.033.

[82] M.J.J. Lázaro, V. Celorrio, L. Calvillo, E. Pastor, R. Moliner, Influence of the synthesis method on the properties of Pt catalysts supported on carbon nanocoils for ethanol oxidation, J. Power Sources. 196 (2011) 4236–4241. https://doi.org/10.1016/j.jpowsour.2010.10.055.

[83] S. Carrion-Satorre, M. Montiel, R. Escudero-Cid, J.L.G. Fierro, E. Fatas, P. Ocon, Performance of carbon-supported palladium and palladium-ruthenium catalysts for alkaline membrane direct ethanol fuel cells, Int. J. Hydrogen Energy. 41 (2016) 8954–8962. https://doi.org/10.1016/j.ijhydene.2016.04.053.

[84] G. Sharma, D. Kumar, A. Kumar, H. Al-Muhtaseb, D. Pathania, M. Naushad, G. Tessema Mola, Revolution from monometallic to trimetallic nanoparticle composites, various synthesis methods and their applications: A review, (2017). https://doi.org/10.1016/j.msec.2016.11.002.

[85] J. Calderón Gómez, R. Moliner, M. Lázaro, Palladium-Based Catalysts as Electrodes

for Direct Methanol Fuel Cells: A Last Ten Years Review, Catalysts. 6 (2016). https://doi.org/10.3390/catal6090130.

[86] H. Hei, H. He, R. Wang, X. Liu, G. Zhang, Controlled synthesis and characterization of noble metal nanoparticles., in: Soft Nanosci. Lett., 2012: pp. 34–40. https://doi.org/10.4236/snl.2012.23007.

[87] J.A. Adekoya, E.O. Dare, M.A. Mesubi, A.A. Nejo, H.C. Swart, N. Revaprasadu, Synthesis of polyol based Ag/Pd nanocomposites for applications in catalysis, Results Phys. 4 (2014) 12–19. https://doi.org/10.1016/j.rinp.2014.02.002.

[88] M.A.F.A.F. Akhairi, S.K.K. Kamarudin, Catalysts in direct ethanol fuel cell (DEFC): An overview, Int. J. Hydrogen Energy. 41 (2016) 4214–4228. https://doi.org/10.1016/j.ijhydene.2015.12.145.

[89] S.Y.Y. Shen, T.S.S. Zhao, Q.X.X. Wu, Product analysis of the ethanol oxidation reaction on palladium-based catalysts in an anion-exchange membrane fuel cell environment, Int. J. Hydrogen Energy. 37 (2012) 575–582. https://doi.org/http://dx.doi.org/10.1016/j.ijhydene.2011.09.077.

[90] Z.X. Liang, T.S. Zhao, J.B. Xu, L.D. Zhu, Mechanism study of the ethanol oxidation reaction on palladium in alkaline media, Electrochim. Acta. 54 (2009) 2203–2208. https://doi.org/10.1016/j.electacta.2008.10.034.

[91] A. Ferre-Vilaplana, C. Buso-Rogero, J.M. Feliu, E. Herrero, Cleavage of the C–C Bond in the Ethanol Oxidation Reaction on Platinum. Insight from Experiments and Calculations, J. Phys. Chem. C. 120 (2016) 11590–11597. https://doi.org/10.1021/acs.jpcc.6b03117.

[92] E.A. Monyoncho, S.N. Steinmann, C. Michel, E.A. Baranova, T.K. Woo, P. Sautet, Ethanol Electro-oxidation on Palladium Revisited Using Polarization Modulation Infrared Reflection Absorption Spectroscopy (PM-IRRAS) and Density Functional Theory (DFT): Why Is It Difficult To Break the C–C Bond?, ACS Catal. 6 (2016) 4894–4906. https://doi.org/10.1021/acscatal.6b00289.

[93] S. Beyhan, J.-M. Léger, F. Kadırgan, Understanding the influence of Ni, Co, Rh and Pd addition to PtSn/C catalyst for the oxidation of ethanol by in situ Fourier transform infrared spectroscopy, Appl. Catal. B Environ. 144 (2014) 66–74. https://doi.org/10.1016/j.apcatb.2013.07.020.

[94] C. Rice, S. Ha, R.I. Masel, A. Wieckowski, Catalysts for direct formic acid fuel cells, J. Power Sources. 115 (2003) 229–235. https://doi.org/10.1016/S0378-7753(03)00026-0.

[95] A. Capon, R. Parson, The oxidation of formic acid at noble metal electrodes: I. Review of previous work, J. Electroanal. Chem. Interfacial Electrochem. 44 (1973) 1–7. https://doi.org/10.1016/S0022-0728(73)80508-X.

[96] F. Zhang, D. Zhou, M. Zhou, Ethanol electrooxidation on Pd/C nanoparticles in alkaline media, J. Energy Chem. 25 (2016) 71–76. https://doi.org/10.1016/j.jechem.2015.10.013.

[97] J. Torrero, M. Montiel, M.A. Peña, P. Ocón, S. Rojas, Insights on the electrooxidation of ethanol with Pd-based catalysts in alkaline electrolyte, Int. J. Hydrogen Energy. 4 (2019) 1–8. https://doi.org/10.1016/j.ijhydene.2019.10.124.

[98] C.-H. Liu, R.-H. Liu, Q.-J. Sun, J.-B. Chang, X. Gao, Y. Liu, S.-T. Lee, Z.-H. Kang, S.-D. Wang, Controlled synthesis and synergistic effects of graphene-supported PdAu bimetallic nanoparticles with tunable catalytic properties, Nanoscale. 7 (2015) 6356–6362. https://doi.org/10.1039/C4NR06855F.

[99] Y.-Y. Feng, Z.-H. Liu, Y. Xu, P. Wang, W.-H. Wang, D.-S. Kong, Highly active PdAu alloy catalysts for ethanol electro-oxidation, J. Power Sources. 232 (2013) 99–105. https://doi.org/10.1016/j.jpowsour.2013.01.013.

[100] S. Zhang, M. Qing, H. Zhang, Y. Tian, Electrocatalytic oxidation of formic acid on functional MWCNTs supported nanostructured Pd–Au catalyst, Electrochem. Commun. 11 (2009) 2249–2252. https://doi.org/10.1016/J.ELECOM.2009.10.001.

[101] W. Zhou, J.Y. Lee, Highly active core–shell Au@Pd catalyst for formic acid electrooxidation, Electrochem. Commun. 9 (2007) 1725–1729. https://doi.org/10.1016/J.ELECOM.2007.03.016.

[102] Z. Yin, M. Chi, Q. Zhu, D. Ma, J. Sun, X. Bao, Supported bimetallic PdAu nanoparticles with superior electrocatalytic activity towards methanol oxidation, J. Mater. Chem. A. 1 (2013) 9157. https://doi.org/10.1039/c3ta11592e.

[103] L.Y. Chen, N. Chen, Y. Hou, Z.C. Wang, S.H. Lv, T. Fujita, J.H. Jiang, A. Hirata, M.W. Chen, Geometrically Controlled Nanoporous PdAu Bimetallic Catalysts with Tunable Pd/Au Ratio for Direct Ethanol Fuel Cells, ACS Catal. 3 (2013) 1220–1230. https://doi.org/10.1021/cs400135k.

[104] B.T.X. Lam, M. Chiku, E. Higuchi, H. Inoue, Preparation of PdAg and PdAu nanoparticle-loaded carbon black catalysts and their electrocatalytic activity for the glycerol oxidation reaction in alkaline medium, J. Power Sources. 297 (2015) 149–157. https://doi.org/10.1016/J.JPOWSOUR.2015.07.086.

[105] A.M. Sheikh, E.L. Silva, L. Moares, L.M. Antonini, M.Y. Abellah, C.F. Malfatti, Pd-based Catalysts for Ethanol Oxidation in Alkaline Electrolyte, 2 (2014) 64–69. https://doi.org/10.12691/ajmm-2-4-1.

[106] M.D. Obradović, Z.M. Stančić, U.Č. Lačnjevac, V.V.V.R. Radmilović, A. Gavrilović-Wohlmuther, V.V.V.R. Radmilović, S.L. Gojković, Electrochemical oxidation of ethanol on palladium-nickel nanocatalyst in alkaline media, Appl. Catal. B Environ. 189 (2016) 110–118. https://doi.org/10.1016/J.APCATB.2016.02.039.

[107] Z. Zhang, L. Xin, K. Sun, W. Li, Pd–Ni electrocatalysts for efficient ethanol oxidation reaction in alkaline electrolyte, Int. J. Hydrogen Energy. 36 (2011) 12686–12697. https://doi.org/10.1016/j.ijhydene.2011.06.141.

[108] S. Karim Hassaninejad-Darzi, M. Gholami-Esfidvajani, Electrocatalytic oxidation of ethanol using modified nickel phosphate nanoparticles and multi-walled carbon nanotubes paste electrode in alkaline media for fuel cell, (2016). https://doi.org/10.1016/j.ijhydene.2016.09.091.

[109] Y. Feng, D. Bin, B. Yan, Y. Du, T. Majima, W. Zhou, Porous bimetallic PdNi catalyst with high electrocatalytic activity for ethanol electrooxidation, J. Colloid Interface Sci. 493 (2017) 190–197. https://doi.org/10.1016/j.jcis.2017.01.035.

[110] K.-W.W. Yu-Chen Wei, Chen-Wei Liu, Wei-Da Kang, Chien-Ming Lai, Li-Duan Tsai, Electro-catalytic activity enhancement of Pd–Ni electrocatalysts for the ethanol electro-oxidation in alkaline medium: The promotional effect of CeO2 addition, J. Electroanal. Chem. 660 (2011) 64–70. https://doi.org/10.1016/J.JELECHEM.2011.06.006.

[111] A. Maksić, M. Smiljanić, Š. Miljanić, Z. Rakočević, S. Štrbac, Ethanol Oxidation on Rh/Pd(poly) in Alkaline Solution, Electrochim. Acta. 209 (2016) 323–331. https://doi.org/10.1016/J.ELECTACTA.2016.05.096.

[112] L.A. Soares, C. Morais, T.W. Napporn, K.B. Kokoh, P. Olivi, Beneficial effects of rhodium and tin oxide on carbon supported platinum catalysts for ethanol electrooxidation, J. Power Sources. 315 (2016) 47–55. https://doi.org/10.1016/j.jpowsour.2016.03.013.

[113] A.B. Delpeuch, T. Asset, M. Chatenet, C. Cremers, Electrooxidation of Ethanol at Room Temperature on Carbon-Supported Pt and Rh-Containing Catalysts: A DEMS Study, J. Electrochem. Soc. 161 (2014) F918–F924. https://doi.org/10.1149/2.0731409jes.

[114] J. Piwowar, A. Lewera, On the Lack of Beneficial Role of Rh Towards C-C Bond Cleavage During Low Temperature Ethanol Electrooxidation on Pt-Rh Nanoalloys,

(n.d.). https://chemrxiv.org/articles/On_the_Lack_of_Beneficial_Role_of_Rh_Towards_C-C_Bond_Cleavage_During_Low_Temperature_Ethanol_Electrooxidation_on_Pt-Rh_Nanoalloys/6281264 (accessed December 10, 2018).

[115] F.H.B. Lima, D. Profeti, W.H. Lizcano-Valbuena, E.A. Ticianelli, E.R. Gonzalez, Carbon-dispersed Pt-Rh nanoparticles for ethanol electro-oxidation. Effect of the crystallite size and of temperature, (2008). https://doi.org/10.1016/j.jelechem.2008.01.024.

[116] A. Kowal, M. Li, M. Shao, K. Sasaki, M.B. Vukmirovic, J. Zhang, N.S. Marinkovic, P. Liu, A.I. Frenkel, R.R. Adzic, Ternary Pt/Rh/SnO2electrocatalysts for oxidizing ethanol to CO2, Nat. Mater. 8 (2009) 325–330. https://doi.org/10.1038/nmat2359.

[117] A.B. Delpeuch, F. Maillard, M. Chatenet, P. Soudant, C. Cremers, A. Bach Delpeuch, F. Maillard, M. Chatenet, P. Soudant, C. Cremers, Ethanol oxidation reaction (EOR) investigation on Pt/C, Rh/C, and Pt-based bi- and tri-metallic electrocatalysts: A DEMS and in situ FTIR study, Appl. Catal. B Environ. 181 (2016) 672–680. https://doi.org/10.1016/J.APCATB.2015.08.041.

[118] A. Bach Delpeuch, Mechanistic study of the ethanol oxidation reaction on carbon supported Pt-, Rh-and SnO2-based electrocatalysts in acidic medium, n.d. https://tel.archives-ouvertes.fr/tel-01304234 (accessed December 10, 2018).

[119] M. Li, A. Kowal, K. Sasaki, N. Marinkovic, D. Su, E. Korach, P. Liu, R.R. Adzic, Ethanol oxidation on the ternary Ptâ€“Rhâ€“SnO2/C electrocatalysts with varied Pt:Rh:Sn ratios, Electrochim. Acta. 55 (2010) 4331–4338. https://doi.org/10.1016/j.electacta.2009.12.071.

[120] F. Zhang, D. Zhou, Z. Zhang, M. Zhou, Q. Wang, Preparation of Rh/C and its high electro-catalytic activity for ethanol oxidation in alkaline media, RSC Adv. 5 (2015) 91829–91835. https://doi.org/10.1039/C5RA16859G.

[121] M.H.M.T. Assumpção, S.G. Da Silva, R.F.B. De Souza, G.S. Buzzo, E. V. Spinacé, M.C. Santos, A.O. Neto, J.C.M. Silva, Investigation of PdIr/C electrocatalysts as anode on the performance of direct ammonia fuel cell, J. Power Sources. 268 (2014) 129–136. https://doi.org/10.1016/j.jpowsour.2014.06.025.

[122] A.O. Neto, S.G. Da Silva, G.S. Buzzo, R.F.B. De Souza, M.H.M.T. Assumpção, E. V Spinacé, J.C.M. Silva, Ethanol electrooxidation on PdIr/C electrocatalysts in alkaline media: electrochemical and fuel cell studies, (n.d.). https://doi.org/10.1007/s11581-014-

1201-5.

[123] S.Y. Shen, Y.G. Guo, G.H. Wei, L.X. Luo, F. Li, J.L. Zhang, A perspective on the promoting effect of Ir and Au on Pd toward the ethanol oxidation reaction in alkaline media, (n.d.). https://doi.org/10.1007/s11708-018-0586-7.

[124] B. Miao, Z. Wu, H. Xu, M. Zhang, Y. Chen, L. Wang, Ir catalysts: Preventing CH3COOH formation in ethanol oxidation, Chem. Phys. Lett. (2017). https://doi.org/10.1016/j.cplett.2017.09.045.

[125] L. Cao, G. Sun, H. Li, Q. Xin, Carbon-supported IrSn catalysts for a direct ethanol fuel cell, Electrochem. Commun. 9 (2007) 2541–2546. https://doi.org/10.1016/j.elecom.2007.07.031.

[126] Y.-G. Jo, S.-M. Kim, J.-W. Kim, S.-Y. Lee, Composition-tuned porous Pd-Ag bimetallic dendrites for the enhancement of ethanol oxidation reactions, J. Alloys Compd. 688 (2016) 447–453. https://doi.org/10.1016/j.jallcom.2016.07.227.

[127] M.C. Oliveira, R. Rego, L.S. Fernandes, P.B. Tavares, Evaluation of the catalytic activity of Pd–Ag alloys on ethanol oxidation and oxygen reduction reactions in alkaline medium, J. Power Sources. 196 (2011) 6092–6098. https://doi.org/10.1016/j.jpowsour.2011.03.062.

[128] J. Qi, N. Benipal, C. Liang, W. Li, PdAg/CNT catalyzed alcohol oxidation reaction for high-performance anion exchange membrane direct alcohol fuel cell (alcohol = methanol, ethanol, ethylene glycol and glycerol), Appl. Catal. B Environ. 199 (2016) 494–503. https://doi.org/10.1016/j.apcatb.2016.06.055.

[129] Y. Zhang, Q. Yi, Z. Deng, X. Zhou, H. Nie, Excellent Electroactivity of Ternary Pd-Ag-Sn Nanocatalysts for Ethanol Oxidation, Catal. Letters. 148 (1234) 1190–1201. https://doi.org/10.1007/s10562-018-2335-2.

[130] F. Zhu, M. Wang, Y. He, G. Ma, Z. Zhang, X. Wang, A comparative study of elemental additives (Ni, Co and Ag) on electrocatalytic activity improvement of PdSn-based catalysts for ethanol and formic acid electro-oxidation, Electrochim. Acta. 148 (2014) 291–301. https://doi.org/10.1016/j.electacta.2014.10.062.

[131] A. Dutta, J. Datta, Outstanding Catalyst Performance of PdAuNi Nanoparticles for the Anodic Reaction in an Alkaline Direct Ethanol (with Anion-Exchange Membrane) Fuel Cell, J. Phys. Chem. C. 116 (2012) 25677–25688. https://doi.org/10.1021/jp305323s.

[132] P.P.-C. Su, H.-S.H. Chen, T.T.-Y. Chen, C.-W.C. Liu, C.-H. Lee, J.-F. Lee, T.-S. Chan, K.-W. Wang, Enhancement of electrochemical properties of Pd/C catalysts toward

ethanol oxidation reaction in alkaline solution through Ni and Au alloying, Int. J. Hydrogen Energy. 38 (2013) 4474–4482. https://doi.org/10.1016/J.IJHYDENE.2013.01.173.

[133] F. Zhu, G. Ma, Z. Bai, R. Hang, B. Tang, Z. Zhang, X. Wang, High activity of carbon nanotubes supported binary and ternary Pd-based catalysts for methanol, ethanol and formic acid electro-oxidation, J. Power Sources. 242 (2013) 610–620. https://doi.org/10.1016/j.jpowsour.2013.05.145.

[134] V.L. Martins, R.M. Torresi, A.J.R. Rennie, Design considerations for ionic liquid based electrochemical double layer capacitors, Electrochim. Acta. 270 (2018) 453–460. https://doi.org/10.1016/J.ELECTACTA.2018.03.094.

[135] Y. Leng, X-Ray Diffraction Methods, in: Mater. Charact., John Wiley & Sons, Ltd, Chichester, UK, n.d.: pp. 45–77. https://doi.org/10.1002/9780470823002.ch2.

[136] D.G. Brandon, W.D. Kaplan, Wiley InterScience (Online service), Microstructural characterization of materials, John Wiley, 2008. https://www.wiley.com/en-gb/Microstructural+Characterization+of+Materials%2C+2nd+Edition-p-9780470027851 (accessed November 28, 2018).

[137] Y. Leng, X-Ray Spectroscopy for Elemental Analysis, in: Mater. Charact., John Wiley & Sons, Ltd, Chichester, UK, n.d.: pp. 171–196. https://doi.org/10.1002/9780470823002.ch6.

[138] Yang Leng, Transmission Electron Microscopy, in: Mater. Charact., John Wiley & Sons, Ltd, Chichester, UK, n.d.: pp. 79–119. https://doi.org/10.1002/9780470823002.ch3.

[139] A. Dutta, J. Datta, Energy efficient role of Ni/NiO in PdNi nano catalyst used in alkaline DEFC, J. Mater. Chem. A. 2 (2014) 3237. https://doi.org/10.1039/c3ta12708g.

[140] Y. Leng, Thermal Analysis, in: Mater. Charact., John Wiley & Sons, Ltd, Chichester, UK, n.d.: pp. 301–331. https://doi.org/10.1002/9780470823002.ch10.

[141] Y. Leng, Electron Spectroscopy for Surface Analysis, in: Mater. Charact., John Wiley & Sons, Ltd, Chichester, UK, n.d.: pp. 197–224. https://doi.org/10.1002/9780470823002.ch7.

[142] M.M. Antxustegi, A.R. Pierna, N. Ruiz, Chemical activation of Vulcan® XC72R to be used as support for NiNbPtRu catalysts in PEM fuel cells, Int. J. Hydrogen Energy. 39 (2014) 3978–3983. https://doi.org/10.1016/j.ijhydene.2013.04.061.

[143] G. Zhang, Y. Wang, X. Wang, Y. Chen, Y. Zhou, Y. Tang, L. Lu, J. Bao, T. Lu,

Preparation of Pd – Au / C catalysts with different alloying degree and their electrocatalytic performance for formic acid oxidation, "Applied Catal. B, Environ. 102 (2011) 614–619. https://doi.org/10.1016/j.apcatb.2010.12.049.

[144] A.J. Armenta-González, R. Carrera-Cerritos, M. Guerra-Balcázar, L.G. Arriaga, J. Ledesma-García, Comparative study of carbon-supported Pd and PdAg catalysts synthesised by the polyol process and reverse micelles methods, J. Appl. Electrochem. 45 (2015) 33–41. https://doi.org/10.1007/s10800-014-0776-x.

[145] Y.-H. Qin, Y. Li, R.-L. Lv, T.-L. Wang, W.-G. Wang, C.-W. Wang, Pd-Au/C catalysts with different alloying degrees for ethanol oxidation in alkaline media, Electrochim. Acta. 144 (2014) 50–55. https://doi.org/10.1016/J.ELECTACTA.2014.08.078.

[146] H. An, L. Pan, H. Cui, B. Li, D. Zhou, J. Zhai, Q. Li, Synthesis and performance of palladium-based catalysts for methanol and ethanol oxidation in alkaline fuel cells, Electrochim. Acta. 102 (2013) 79–87. https://doi.org/10.1016/j.electacta.2013.03.142.

[147] H. Rostami, A. Omrani, A.A. Rostami, On the role of electrodeposited nanostructured Pd–Co alloy on Au for the electrocatalytic oxidation of glycerol in alkaline media, Int. J. Hydrogen Energy. 40 (2015) 9444–9451. https://doi.org/10.1016/J.IJHYDENE.2015.05.154.

[148] Table of Electrical Resistivity and Conductivity, (n.d.). https://www.thoughtco.com/table-of-electrical-resistivity-conductivity-608499 (accessed February 15, 2019).

[149] B. Ulas, A. Caglar, O. Sahin, H. Kivrak, Composition dependent activity of PdAgNi alloy catalysts for formic acid electrooxidation, J. Colloid Interface Sci. 532 (2018) 47–57. https://doi.org/10.1016/j.jcis.2018.07.120.

[150] J.R.H. Ross, Heterogeneous catalysis : fundamentals and applications, Elsevier, 2012.

[151] R.M. Modibedi, T. Masombuka, M.K. Mathe, Carbon supported Pd-Sn and Pd-Ru-Sn nanocatalysts for ethanol electro-oxidation in alkaline medium, Int. J. Hydrogen Energy. 36 (2011) 4664–4672. https://doi.org/10.1016/j.ijhydene.2011.01.028.

[152] R.M. Modibedi, T. Mehlo, K.I. Ozoemena, M.K. Mathe, Preparation, characterisation and application of Pd/C nanocatalyst in passive alkaline direct ethanol fuel cells (ADEFC), Int. J. Hydrogen Energy. 40 (2015) 15605–15612. https://doi.org/10.1016/j.ijhydene.2015.08.113.

[153] P. Kim, J.B. Joo, W. Kim, J. Kim, I.K. Song, J. Yi, NaBH4-assisted ethylene glycol reduction for preparation of carbon-supported Pt catalyst for methanol electro-oxidation,

J. Power Sources. 160 (2006) 987–990. https://doi.org/10.1016/j.jpowsour.2006.02.050.

[154] R.S. Henrique, J.M.S. Ayoub, R.M. Piasentin, M. Linardi, M.C. Santos, Preparation of Pt / C-In 2 O 3 . SnO 2 Electrocatalysts by Borohydride Reduction Process for Ethanol Electro-Oxidation, Int. J. Electrochem. Sci. 7 (2012) 2036–2046. https://doi.org/10.1007/s11581-013-0955-5.

[155] A.O. Neto, M.M. Tusi, N.S. De Oliveira Polanco, S.G. Da Silva, M. Coelho Dos Santos, E. V. Spinacé, PdBi/C electrocatalysts for ethanol electro-oxidation in alkaline medium, Int. J. Hydrogen Energy. 36 (2011) 10522–10526. https://doi.org/10.1016/j.ijhydene.2011.05.154.

[156] C. Zhu, D. Wen, M. Oschatz, M. Holzschuh, W. Liu, A.-K.K. Herrmann, F. Simon, S. Kaskel, A. Eychmüller, Kinetically controlled synthesis of PdNi bimetallic porous nanostructures with enhanced electrocatalytic activity, Small. 11 (2015) 1430–1434. https://doi.org/10.1002/smll.201401432.

[157] ao A.N. Geraldes, D.F. da Silva, L.G. de A. e Silva, E.V. Spinacé, A.O. Neto, M.C. dos Santos, A. Napole, ao A.N. Geraldes, D. Furtunato da Silva, L. Gondim de Andrade Silva, E. Vit orio Spinac, A. Oliveira Neto, M. Coelho dos Santos, Binary and ternary palladium based electrocatalysts for alkaline direct glycerol fuel cell, J. Power Sources. 293 (2015) 823–830. https://doi.org/10.1016/j.jpowsour.2015.06.010.

[158] Y.-H. Qin, Y. Jiang, D.-F. Niu, X.-S. Zhang, X.-G. Zhou, L. Niu, W.-K. Yuan, Carbon nanofiber supported bimetallic PdAu nanoparticles for formic acid electrooxidation, J. Power Sources. 215 (2012) 130–134. https://doi.org/10.1016/J.JPOWSOUR.2012.05.008.

[159] Y. Suo, I. Hsing, Synthesis of bimetallic PdAu nanoparticles for formic acid oxidation, Electrochim. Acta. 56 (2011) 2174–2183. https://doi.org/10.1016/j.electacta.2010.12.037.

[160] N. Li, W.Y. Xia, C.W. Xu, S. Chen, Pt/C and Pd/C catalysts promoted by Au for glycerol and CO electrooxidation in alkaline medium, J. Energy Inst. 90 (2017). https://doi.org/10.1016/j.joei.2016.07.005.

[161] A. Dutta, A. Mondal, P. Broekmann, J. Datta, Optimal level of Au nanoparticles on Pd nanostructures providing remarkable electro-catalysis in direct ethanol fuel cell, J. Power Sources. 361 (2017) 276–284. https://doi.org/10.1016/J.JPOWSOUR.2017.06.063.

[162] In EDAX analysis, how much X-ray can penetrate in surface of sample?, (n.d.).

https://www.researchgate.net/post/in_EDAX_analysis_how_much_X-ray_can_penetrate_in_surface_of_sample (accessed August 12, 2019).

[163] What is the depth resolution of Energy Dispersive Spectroscopy?, (n.d.). https://www.researchgate.net/post/What_is_the_depth_resolution_of_Energy_Dispersive_Spectroscopy (accessed August 12, 2019).

[164] H.L. Skriver, N.M. Rosengaard, Surface energy and work function of elemental metals, Phys. Rev. B. 46 (1992) 7157. https://doi.org/10.1103/PhysRevB.46.7157.

[165] How can I make XPS measurements more surface sensitive?, (n.d.). https://www.researchgate.net/post/How_can_I_make_XPS_measurements_more_surface_sensitive (accessed August 12, 2019).

[166] J. Kawai, H. Adachi, Y. Kitajima, K. Maeda, S. Hayakawa, Y. Gohshi, Inelastic Mean Free Path of Photoelectrons in Ag Determined by Total Reflection X-Ray Photoelectron Spectroscopy, 1997. https://www.jstage.jst.go.jp/article/analsci1985/13/5/13_5_797/_pdf (accessed August 12, 2019).

[167] S. Merzlikin aus Kharkiv, Depth Profiling by X-ray Photoelectron Spectroscopy, 2007. https://d-nb.info/987575090/34 (accessed August 12, 2019).

[168] XPS Interpretation of Palladium, (n.d.). https://xpssimplified.com/elements/palladium.php (accessed March 25, 2019).

[169] W. Chen, Y. Zhang, X. Wei, Catalytic performances of PdNi/MWCNT for electrooxidations of methanol and ethanol in alkaline media, Int. J. Hydrogen Energy. 40 (2015) 1154–1162. https://doi.org/10.1016/j.ijhydene.2014.11.069.

[170] S. Shen, T.S. Zhao, J. Xu, Y. Li, High performance of a carbon supported ternary PdIrNi catalyst for ethanol electro-oxidation in anion-exchange membrane direct ethanol fuel cells, Energy Environ. Sci. 4 (2011) 1428. https://doi.org/10.1039/c0ee00579g.

[171] Y. Wang, K. Jiang, W.-B. Cai, Enhanced Electrocatalysis of Ethanol on Dealloyed Pd-Ni-P Film in Alkaline Media: an Infrared Spectroelectrochemical Investigation, Electrochim. Acta. 162 (2015) 100–107. https://doi.org/10.1016/J.ELECTACTA.2014.11.182.

[172] T. Ramulifho, K.I. Ozoemena, R.M. Modibedi, C.J. Jafta, M.K. Mathe, Fast microwave-assisted solvothermal synthesis of metal nanoparticles (Pd, Ni, Sn) supported on sulfonated MWCNTs: Pd-based bimetallic catalysts for ethanol oxidation in alkaline medium, Electrochim. Acta. 59 (2012) 310–320.

https://doi.org/10.1016/j.electacta.2011.10.071.

[173] Y. Holade, N. Sahin, K. Servat, T. Napporn, K. Kokoh, Recent Advances in Carbon Supported Metal Nanoparticles Preparation for Oxygen Reduction Reaction in Low Temperature Fuel Cells, Catalysts. 5 (2015) 310–348. https://doi.org/10.3390/catal5010310.

[174] J. Piwowar, A. Lewera, On the lack of beneficial role of Rh towards C-C bond cleavage during low temperature ethanol electrooxidation on Pt-Rh nanoalloys, (2018) 1–7. https://doi.org/10.26434/chemrxiv.6281264.

[175] C.R. Zanata, P.S. Fernández, H.E. Troiani, A.L. Soldati, R. Landers, G.A. Camara, A.E. Carvalho, C.A. Martins, Rh-decorated PtIrO x nanoparticles for glycerol electrooxidation: Searching for a stable and active catalyst, "Applied Catal. B, Environ. 181 (2016) 445–455. https://doi.org/10.1016/j.apcatb.2015.08.021.

[176] G.L. Soloveichik, G.L. Soloveichik Review, Liquid fuel cells, Beilstein J. Nanotechnol. 5 (2014) 1399–1418. https://doi.org/10.3762/bjnano.5.153.

[178] F.A. Zakil, S.K. Kamarudin, S. Basri, Modified Nafion membranes for direct alcohol fuel cells: An overview, (2016). https://doi.org/10.1016/j.rser.2016.07.040.

[179] A.O. Neto, J. Nandenha, R.F.B. De Souza, G.. Buzzo, J.C.M. Silva, E.V. Spinacé, M.H.M.T. Assumpção, Anodic oxidation of formic acid on PdAuIr/C-Sb2O5·SnO2 electrocatalysts prepared by borohydride reduction, J. Fuel Chem. Technol. 42 (2014) 851–857. https://doi.org/10.1016/S1872-5813(14)60037-2.

[180] M. Brandalise, Preparation and characterization of electrocatalysts based on palladium for electro-oxidation of alcohols in alkaline medium, 2008.

APPENDICES

Appendix 1

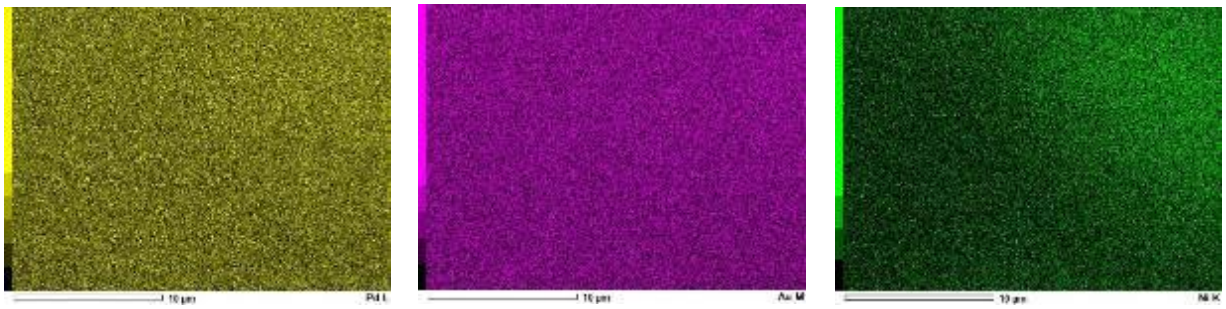

EDX Elemental (Pd, Au, Ni) Maps of PdAuNi/C_{3step}

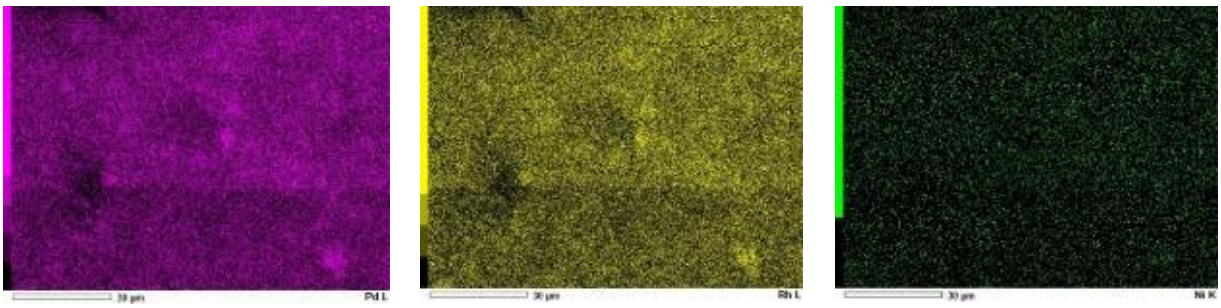

EDX Elemental maps of $Pd_4Rh_2Ni_1/C$

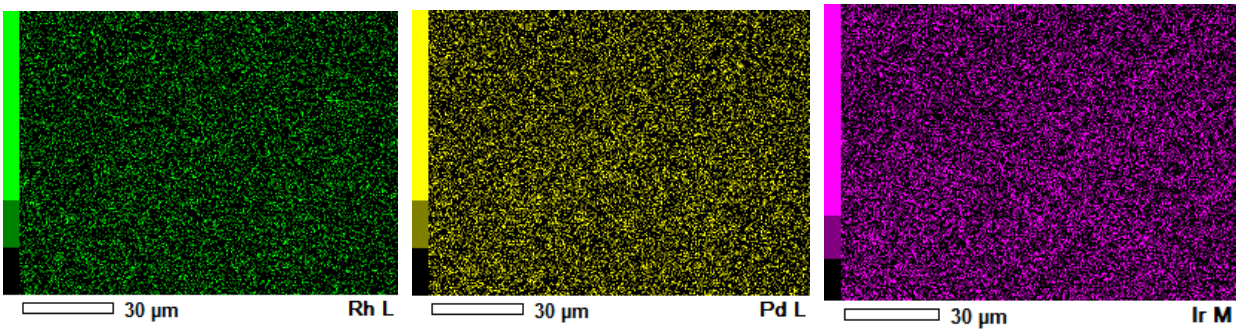

EDX Elemental maps of PdRhIr/C

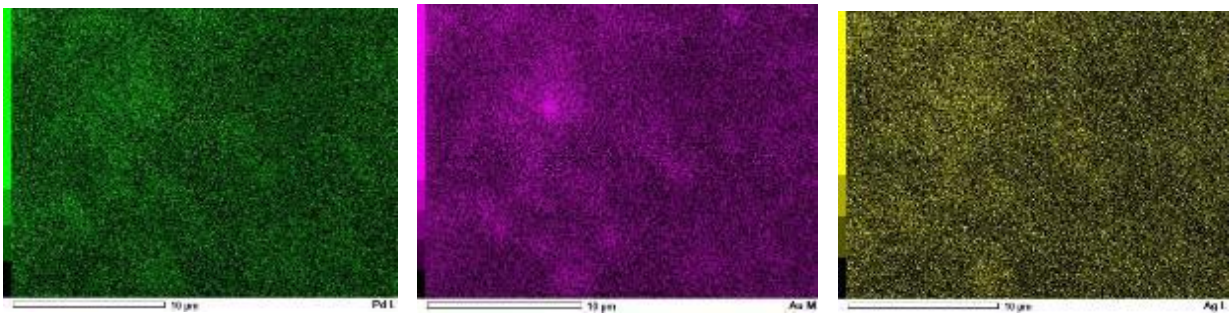

EDX Elemental maps of PdAuAg/C

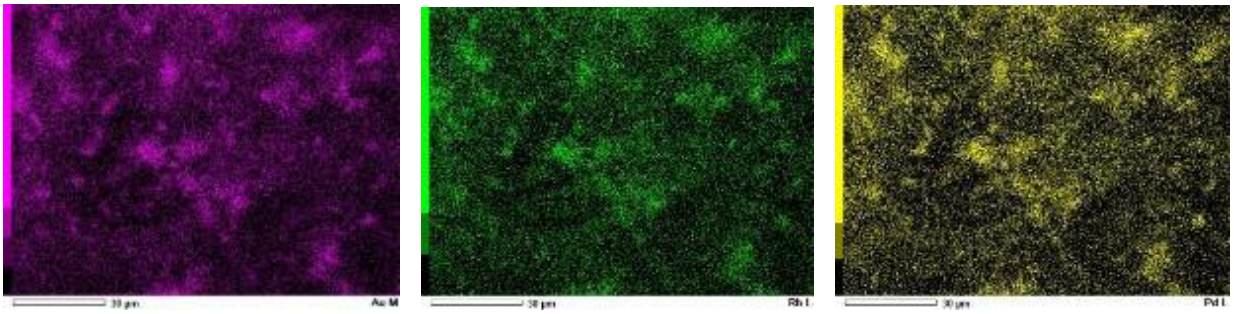

EDX Elemental maps of PdAuRh/C

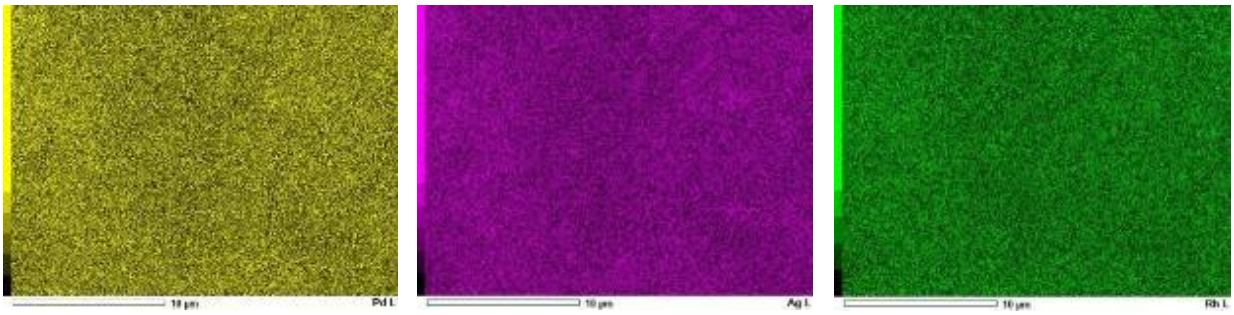

EDX Elemental (Pd, Ag, Rh) Maps of PdAgRh/C

Appendix 2

XPS spectral peaks of C 1s and O 1s + Pd 3p of Pd/C_v, Pd/C_{vf}, Pd/C_{s1}, Pd/C_{s2}, Pd/CNF, and Pd/AC

Peaks	Pd/C_v	Pd/C_{vf}	Pd/C_{s1}	Pd/C_{s2}	Pd/CNF	Pd/AC
C 1s	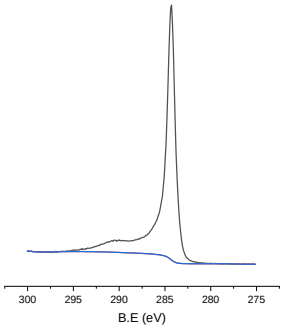	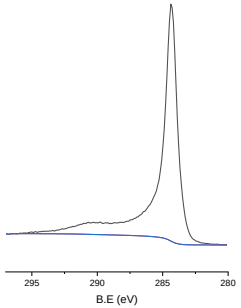	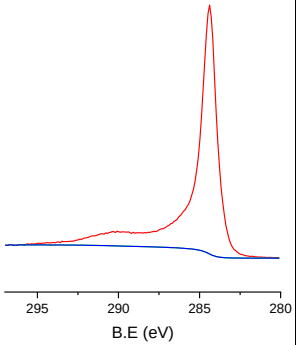	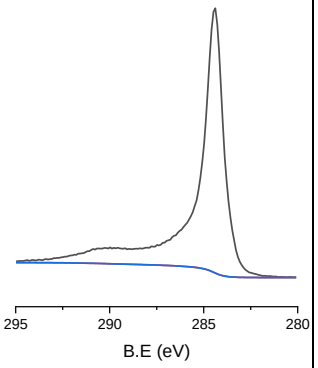	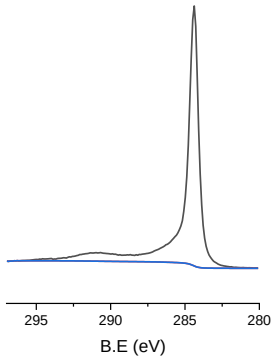	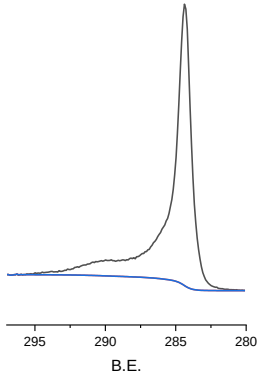
O 1s + Pd 3p	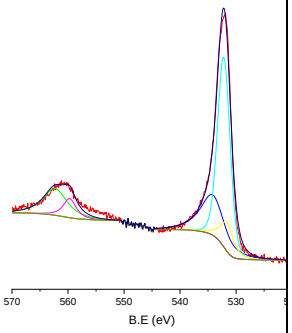	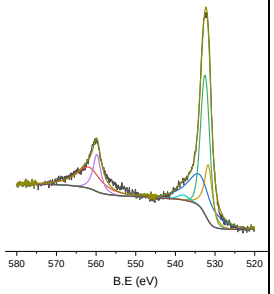	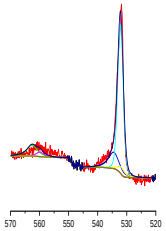	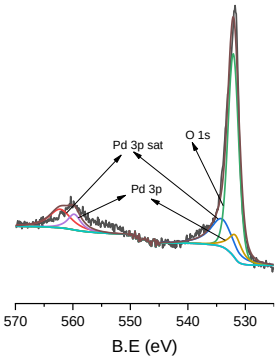	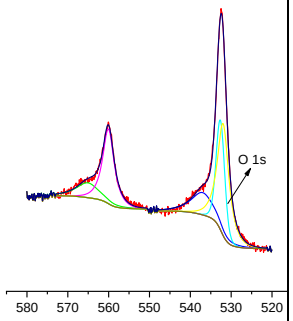	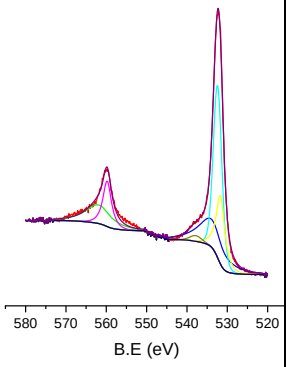

XPS spectral peaks of Pd 3d, Ni 2p, Rh 3d, Ir 4f, and Ag 3d in $Pd_4Rh_2Ni_1/C$, $Pd_4Ir_2Ni_1/C$, and $Pd_4Ag_2Ni_1/C$

$Pd_4Rh_2Ni_1/C$

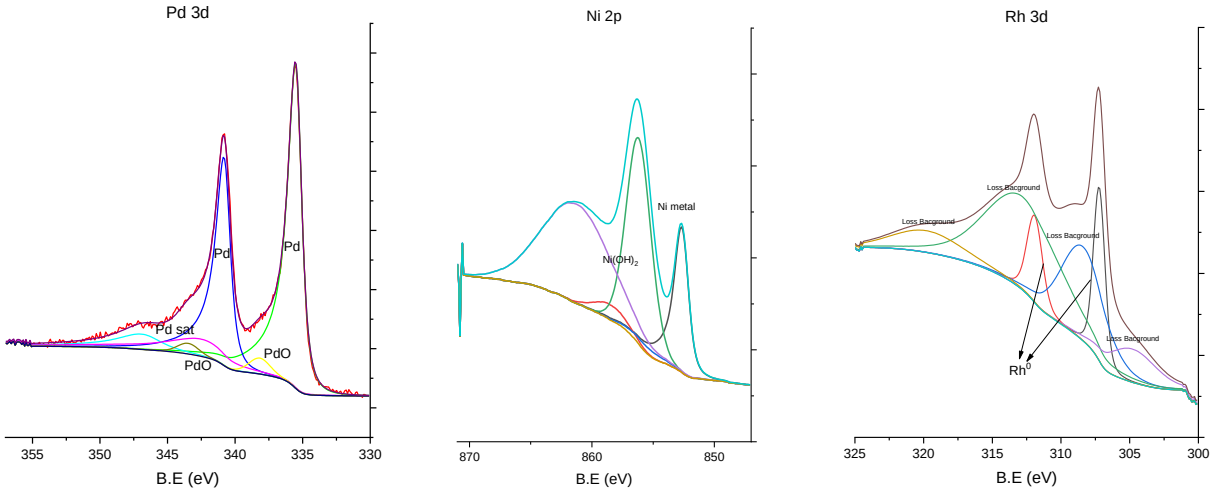

$Pd_4Ir_2Ni_1/C$

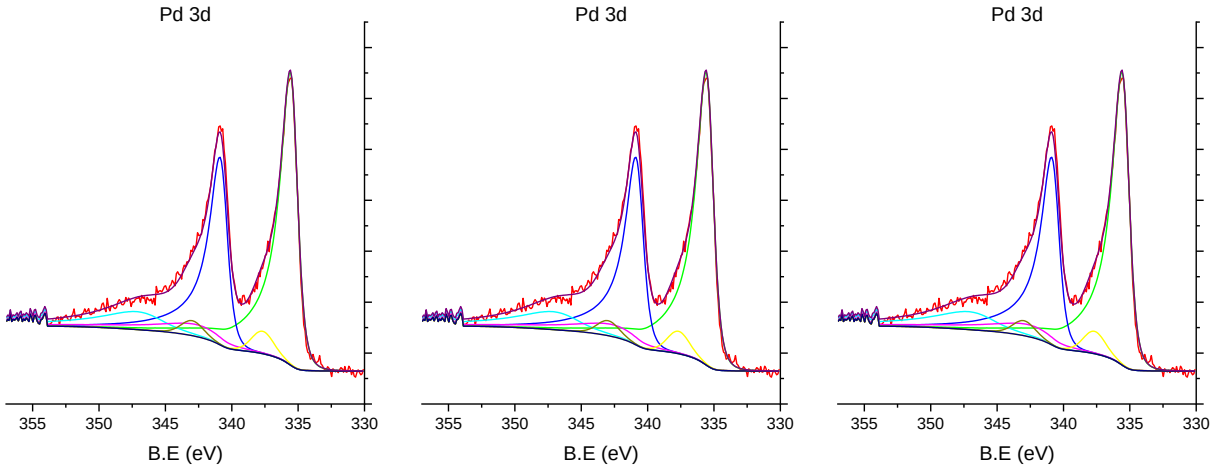

$Pd_4Ag_2Ni_1/C$

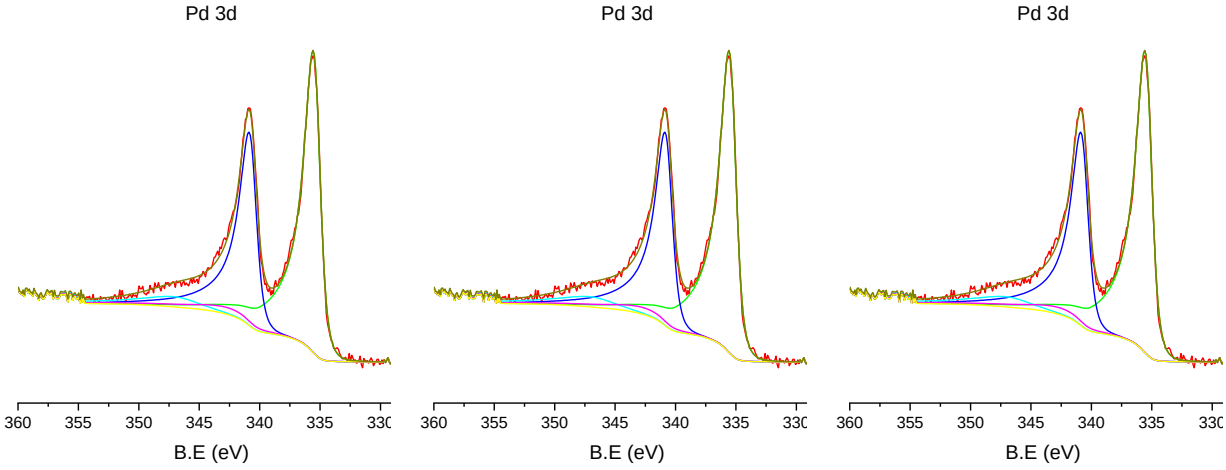

Appendix 3: Publication Record

Available online at www.sciencedirect.com

ScienceDirect

Energy Procedia 151 (2018) 79–83

Energy Procedia

www.elsevier.com/locate/procedia

3rd Annual Conference in Energy Storage and Its Applications, 3rd CDT-ESA-AC, 11–12 September 2018, Sheffield, UK

Influence of physicochemical characteristics of carbon supports on Pd ethanol oxidation catalysts

Ahmed Elsheikh[a,b], Vitor L. Martins[c], James McGregor[a]

[a]*Chemical and Biological Engineering Department, University of Sheffield, Mappin Street, Sheffield S1 3JD, UK*
[b]*Mechanical Engineering Department, South Valley University, ElMadares Street, Qena 83521, Egypt*
[c]*Depto. Química Fundamental, Instituto de Química, Universidade de São Paulo, Av. Prof. Lineu Prestes 748, 05508-000 São Paulo, SP, Brasil*

Abstract

Direct ethanol fuel cells (DEFCs) have the potential to play a valuable role in the conversion of energy from sustainable sources. DEFCs need a support matrix, typically carbon, for the noble metal catalyst. In this work, two distinct carbon supports are compared and their electrochemical efficacy is related to their physicochemical characteristics. Specifically, Vulcan (C_V) is compared to Selectivity (C_S) as a support for Pd nanoparticles to catalyze ethanol electrooxidation. Characterisation data show that C_S has potentially favorable properties such as a high surface area. However, Pd/C_V exhibits a superior catalytic performance due to the higher adequacy of C_V texture that meets the particular needs of DEFC support in terms of pore size distribution. Additionally, synthesis of Pd nanoparticles on both carbons has decreased their surface areas and increased their pore sizes.

Selection and peer-review under responsibility of the 3rd Annual Conference in Energy Storage and Its Applications, 3rd CDT-ESA-AC.

Keywords: carbon, mesoporous, ethanol electrooxidation, Pd

[In Press Chapter] Catalytic Carbon Materials from Biomass

Gareth Davies, Ahmed Elsheikh, Catherine Collet, Ibrahim Yakub and James McGregor

August 2020

In book: Emerging Carbon Materials for Catalysis

Publisher: Elsevier

External Collaboration Paper

A03-0164: Trimetallic Carbon-Supported Catalysts for Borohydride Oxidation and Oxygen Reduction in Alkaline Solutions

Thursday, 25 July 2019
11:30 - 11:50
Scottish Event Campus - Alsh 2

Borohydrides present a particularly attractive option for alkaline liquid fuel systems, having high energy densities, a low standard potential for its oxidation, and good stability in alkaline conditions. A key area in the success of a fuel cell utilizing borohydride is the development of an anode, which can make use of the full 8-electron oxidation, directly oxidising the borohydride with as little of the undesired hydrolysis reaction occurring as possible. This is in addition to the common requirements of high activity, high stability, good electronic conductivity and effective transport of reactants and products. Here we present new studies on the oxidation of borohydride and reduction of oxygen in alkaline media under various conditions for a selection of trimetallic carbon-supported catalysts based on Pd, prepared by quick and straightforward synthetic routes. The prepared catalysts were characterised by cyclic voltammetry, chronoamperometry, and RDE based procedures. Notably, PdAuNi/C prepared via a $NaBH_4$-2-propanol complex presents highly dispersed trimetallic alloy particles, as determined by XRD, XPS and TEM. The best performing electrodes under characterisation conditions were tested in a direct borohydride fuel cell under several different conditions. The influence of experimental parameters (temperature, borohydride concentration, as well as NaOH concentration) on the electrical behaviour of the fuel cell were studied and optimized. These results show that Pd-based trimetallic catalysts supported on carbon provide a ready route to successfully operate borohydride based fuel cells.

Acknowledgements: A. Elsheikh acknowledges a Newton-Mosharafa Scholarship (Reference no. NMJ8/15) for funding. The Portuguese Foundation for Science and Technology (FCT, Portugal) is acknowledged for PhD grant no. SFRH/BD/137470/2018 (R.C.P. Oliveira), contract no. IST-ID/156/2018 (B. Šljukić) and contract no. IF/01084/2014/CP1214/CT0003 under IF2014 Programme (D.M.F. Santos).

Keywords: Palladium, trimetallic catalysts, nanomaterials, borohydride oxidation, oxygen reduction, fuel cell, kinetic parameters.

Authors

Ahmed MAA Elsheikh
University of Sheffield

Raisa Costa Paes Oliveira
CeFEMA, Instituto Superior Técnico, ULisboa

Biljana Sljukic
CeFEMA, Instituto Superior Técnico, ULisboa

Diogo M.F. Santos
CeFEMA, Instituto Superior Técnico, ULisboa

Cesar A.C. Sequeira
CeFEMA, Instituto Superior Técnico, ULisboa

James McGregor
University of Sheffield

الخلاصة

تعتبر خلايا الوقود أجهزة تحويل طاقة يتم تغذيتها بوقود ومؤكسد لكي تولد كهرباء. وحديثا لاقي لاقى وقود الايثانول اهتمام الباحثين كوقود لتغذية الخلية بدلا من الهيدروجين نظرا لطبيعته السائلة واستدامة وجوده. ولكن التحدي امامه هو البطء الشديد في تفاعل اكسدته داخل الخلية. لذا من الملح إيجاد حفاز نشط جدا لتحفيز اكسدة الايثانول لوقت طويل نسبيا. يعرف معدن البلاتين بأنه انشط المعادن لتحفيز تفاعلات خلايا الوقود ولكن ندرته الشديدة تجعل تسويق خلايا الوقود تجاريا غير مجدي. أيضا فان معدن البلاتين لا يقام السموم الكربونية التي قد توجد على شكل شوائب او تنتج اثناء التفاعلات في خلايا الوقود مما يجعل عمر الحفاز الفعلي قصير جدا. على الجانب الآخر معدن البلاديوم يقدم بديل مناسب للبلاتين حيث انه اقل ندرة من البلاتين في القشرة الأرضية و يعمل بكفاءة تناظر البلاتين. إضافة الي ذلك فان عمر حفاز البلاديوم أطول من البلاتين نظرا لقدرة الأول على مقاومة التسمم بالعينات الكربونية. في هذه الرسالة جسيمات البلاديوم النانوية تم تحضيرها بالاختزال الكيمياء و تم تثبيتها على خمسة أنواع كربون مختلفة كل منهم تم تحليه فيزيائيا و كيميائيا و تم تطبيقها لأكسدة الايثانول. نظرا لتداخل تأثيرات الخواص الفيزوكيميائية مثل المساحة السطحية والمسامية ودرجة التبلور فان الكربون من نوع فولكان 72 قدم افضل أداء هندسي كحامل لحفاز البلاديوم لأكسدة الايثانول يعرف من خلال شدة التيار الكهربي الناتج من التفاعل. العديد من الدراسات السابقة توصلت الى ان إضافة عنصر آخر الي البلاديوم يحقق مصلحة مزدوجة برفع الكفاءة و تقليل الكمية المستهلكة من معدن البلاديوم النبيل. و لكن القليل من الدراسات ركز على دراسة إضافة عنصرين الي البلاديوم بدلا من عنصر واحد. لذا الهدف في هذا العمل هو فحص تركيبات محفزة مختلفة من ثلاث معادن (بلاديوم إضافة الى معدنين اخرين) وطرق تحضير مختلفة. ثلاث طرق اختزال باستخدام البوروهيدريد تم تطبيقاها لانتاج ثلاث حفازات ثلاثية من البلاديوم و الذهب و النيكل. الحفاز المنتج باستخدام تركيبة بوروهيدريد الصوديوم و البوروبانول الثنائي هو اعلاهم أداء بكثافة تيار 9 امبير/مجم (بلاديوم) و جهد بدأ أكسدة -0.36 فولت بينما الحفازي الأحادي من البلاديوم اعطي فقط 2 امبير/مجم (بلاديوم) و ابتدء اكسدة الايثانول مع فرق جهد -0.26 فولت. التشخيص الفيزيائي لهذا الحفاز بينية انشائية محسنة من سبيكة البلاديوم و الذهب و النيكل. و بنفس طريقة التحضير تم تحضير 12 حفاز ثلاثى اخري من البلاديوم و معدنين اخرين و معدل تحميل المعدن على الكربون يكافئ 12% بالوزن. بصفة عامة الحفازات التي تحتوي على بلاديوم و ذهب إضافة الى معدن اخر تقدم أداء محسن تجاه اكسدة الايثانول اكثر من الحفازات الأخرى. انشط هؤلاء هو الحفاز الذي يحتوي على بلاديوم و ذهب و روديوم و الذي انتج كثافة تيار مرتفعة بقيمة 10 امبير/مجم (بلاديوم) و بدأ أكسدة الايثانول عند تطبيق جهد -0.4 فولت. ان هذا الحفاز الثلاثي و أيضا الحفاز المحتوي على بلاديوم و ذهب و نيكل يقدمون بدائل ناجحة و جدية لاستبدال البلاتين و يمكنهم تسهيل الانتقال الي تقنية منعدمة الكربون لإنتاج الكهرباء بشكل مستدام.

تطوير حفازات محمولة جديدة لخلايا وقود الايثانول المباشر

أحمد محمد على الشيخ

كلية الهندسة

معهد كروتو للأبحاث

قسم الهندسة الكيميائية والبيولوجية

جامعة شفيلد

هذه الاطروحة مقدمة لنيل درجة الدكتوراه في الهندسة

يوليو 2017